รายงานวิจัยฉบับสมบูรณ์

โครงการ การศึกษากลไกวิศวกรรมชีวภาพดินสำหรับการเพิ่มเสถียรภาพของลาดดิน

โดย ศาสตราจารย์ ดร.สุเชษฐ์ ลิขิตเลอสรวง

มิถุนายน 2561

สัญญาเลขที่ RSA5880023

รายงานวิจัยฉบับสมบูรณ์

โครงการ การศึกษากลไกวิศวกรรมชีวภาพดินสำหรับการเพิ่มเสถียรภาพของลาดดิน

ศาสตราจารย์ ดร.สุเชษฐ์ ลิขิตเลอสรวง
ภาควิชาวิศวกรรมโยธา คณะวิศวกรรมศาสตร์
จุฬาลงกรณ์มหาวิทยาลัย

สนับสนุนโดยสำนักงานกองทุนสนับสนุนการวิจัยและ
จุฬาลงกรณ์มหาวิยาลัย

Abstract (บทคัดย่อ)

Project Code: RSA5880023

(รหัสโครงการ)

Project Title: A Study of the Mechanism of Soil Bioengineering for Slope Stabilisation

(ชื่อโครงการ) การศึกษากลไกวิศวกรรมชีวภาพดินสำหรับการเพิ่มเสถียรภาพของลาดดิน

Investigator: Prof. Suched Likitlersuang, Geotechnical Research Unit, Department of Civil Engineering, Faculty of Engineering, Chulalongkorn University

(ชื่อนักวิจัย) ศ.ดร.สุเชษฐ์ ลิขิตเลอสรวง หน่วยปฏิบัติการวิจัยธรณีเทคนิค ภาควิชาวิศวกรรมโยธา คณะวิศวกรรมศาสตร์ จุฬาลงกรณ์มหาวิทยาลัย

E-mail Address: fceslk@eng.chula.ac.th

Project Period: 3 years

(ระยะเวลาโครงการ) 3 ปี (1 ก.ค. 2558 – 30 มิ.ย. 2561)

การวิบัติของลาดดินส่วนใหญ่ในธรรมชาติมักเกิดจากการกระตุ้นจากการไหลของน้ำใต้ดินและ/หรือน้ำฝน วิธีวิศวกรรมชีวภาพดินเป็นวิธีที่เป็นมิตรกับสิ่งแวดล้อมซึ่งใช้พืชในการเสริมแรงโดยเฉพาะบริเวณพื้นที่ลาดชัน พืชจะมีส่วนร่วมต่อการเพิ่มเสถียรภาพลาดดินใน 2 ด้าน คือ การเสริมกำลังและการปรับปรุงอุทกวิทยา งานวิจัยนี้ศึกษาผลของรากพืชต่อการเพิ่มเสถียรภาพดินทางด้านกำลังเป็นหลัก โดยเลือกใช้หญ้าแฝกที่ปลูกต่ำกว่า 1 ปี เป็นตัวอย่างพืชในการศึกษา ขั้นตอนการศึกษาประกอบไปด้วย การสังเกตการเจริญเติบโตของราก การทดสอบกำลังรับแรงเฉือน และการทดสอบแบบจำลองหมุนเหวี่ยง มีการวัดอัตราการเจริญเติบโตและค่าอัตราส่วนพื้นที่รากหญ้าแฝก ตลอดจนมีการวัดค่าพารามิเตอร์ความเชื่อมแน่นและมุมแรงเสียดทานภายในจากการทดสอบด้วยเครื่องมือเฉือนทางตรง มีการศึกษาผลของรากพืชต่อการวิบัติของลาดดินภายใต้เงื่อนไขการไหลของน้ำใต้ดินและการกระทำของน้ำฝนด้วยการทดสอบแบบจำลองหมุนเหวี่ยง ผลการศึกษาชี้ให้เห็นว่ารากหญ้าแฝกสามารถเจริญเติบโตได้อย่างรวดเร็วภายใน 1 ปีและกลุ่มรากหญ้ายังเพิ่มกำลังให้กับดินอย่างมีนัยสำคัญ นอกเหนือจากนั้นกลุ่มรากหญ้ายังช่วยชะลอการเคลื่อนตัวของมวลดินภายใต้การสูญเสียเสถียรภาพของลาดดิน

Keywords: Slopes; Vegetation; Laboratory tests; Field investigation; Numerical modelling

(คำหลัก): ลาดดิน; พืช; การทดสอบในห้องปฏิบัติการ; การสำรวจภาคสนาม; แบบจำลองเชิงตัวเลข

1. บทนำ

ปัญหาดินถล่มเป็นภัยธรรมชาติที่เกิดจากอิทธิพลของน้ำฝน เป็นหนึ่งในปัญหาที่สำคัญในงานด้านวิศวกรรมธรณีเทคนิค เนื่องจากดินถล่มก่อให้เกิดผลกระทบต่าง ๆ ทั้งความสูญเสียต่อชีวิตและความเสียหายด้านเศรษฐกิจ ที่ผ่านมาการขาดเสถียรภาพของลาดดินในธรรมชาติมีแนวโน้มที่สูงขึ้นโดยเฉพาะในพื้นที่มรสุมเขตร้อน เช่น ประเทศในแถบเอเชียตะวันออกเฉียงใต้ ปัจจัยที่ทำให้เกิดการวิบัติของลาดดินมีหลากหลายสาเหตุ เช่น การเคลื่อนไหวทางธรณีวิทยา อิทธิพลทางด้านอุทกวิทยาและการกระทำของมนุษย์ อย่างไรก็ตามปัจจัยหลักที่ทำให้เกิดการวิบัติได้แก่ น้ำฝน เนื่องจากการซึมผ่านของน้ำฝนที่เข้าสู่ดินสามารถเพิ่มระดับน้ำใต้ดิน และเพิ่มแรงดันน้ำในโพรงหรือลดแรงดูดของดิน ซึ่งส่งผลให้กำลังรับแรงเฉือนของดินลดลง

ที่ผ่านมาได้มีกระบวนการทางวิศวกรรมหลากหลายวิธีได้ถูกเสนอขึ้นเพื่อเพิ่มเสถียรภาพของลาดดิน เช่น การติดตั้งสลักยึดดิน การใช้วัสดุปูผิวใยสังเคราะห์ และการใช้คอนกรีตพ่น อย่างไรก็ตามเทคนิคที่กล่าวมาข้างต้นมีราคาค่อนข้างสูง และอาจไม่เหมาะกับการเพิ่มเสถียรภาพของลาดดินในธรรมชาติ ที่ผ่านมาการปลูกพืชคลุมดินเพื่อลดการกระเซาะหน้าดินและเพิ่มเสถียรภาพของลาดดินเป็นที่รู้จักกันในวงกว้าง เทคนิคทางวิศวกรรมชีวภาพเป็นหนึ่งในเทคนิคที่เป็นมิตรกับสิ่งแวดล้อม โดยมีสองกระบวนการที่สำคัญในการปลูกพืชคลุมดินที่ส่งผลต่อเสถียรภาพของลาดดิน คือ กระบวนการเปลี่ยนแปลงทางอุทกวิทยาและเชิงกล

หญ้าแฝกเป็นพืชที่มีความสามารถในการช่วยป้องกันการวิบัติของลาดดินและชะลอการไหลบ่าของน้ำผิวดิน โดยในประเทศไทยได้มีการส่งเสริมให้ใช้หญ้าแฝกเพื่อการอนุรักษ์ดินและน้ำโดยหน่วยงานภาครัฐ เนื่องจากหญ้าแฝกมีการเจริญเติบโตอย่างรวดเร็วและต้องการการดูแลไม่มากนัก นอกจากนี้รากของหญ้าแฝกยังสามารถหยั่งลึกได้ถึง 2.0-3.5 เมตร โดยปกติแล้วการวิบัติแบบตื้นเกิดขึ้นในพื้นที่ที่มีฝนตกหนักอย่างยาวนาน ส่วนมากเกิดขึ้นที่ระดับความลึกที่ 1.0-1.5 เมตรจากผิวดิน ดังนั้นการวิบัตินี้อาจสามารถป้องกันได้ด้วยการปลูกหญ้าแฝก เนื่องจากรากของหญ้าแฝกจะเพิ่มการยึดเกาะระหว่างอนุภาคของดิน โดยงานวิจัยนี้จะทำการศึกษาคุณสมบัติในด้านกำลังของระบบรากหญ้าแฝกในการป้องกันการวิบัติและพังทลายของดิน

นอกเหนือจากนี้ งานวิจัยที่ผ่านมาได้มีการจำลองเสถียรภาพของลาดดินที่ถูกเสริมกำลังด้วยรากพืช โดย Sonnenberg et al.(2010) ที่ใช้การจำลองสถานการณ์ด้วยเครื่องหมุนเหวี่ยง (centrifuge) โดยมีแรงหนีศูนย์กลางที่ 15 เท่าของแรงโน้มถ่วงโลก และทำการเพิ่มระดับน้ำใต้ดินในแบบจำลองอย่างต่อเนื่อง (model slope) ผลของการเสริมกำลังโดยรากพืชถูกคำนวณย้อนกลับโดยขึ้นอยู่กับการไหลของผิวดินที่มีการวิบัติ ต่อมา Takahashi et al. (2014) ได้ทำการศึกษาผลกระทบของการปลูกพืชคลุมดินที่มีต่อการวิบัติโดยการชักนำจากการไหลซึมผ่านของน้ำใต้ดิน (seepage-induced) โดยใช้การจำลองด้วยเครื่องหมุนเหวี่ยงที่มีแรงหนีศูนย์กลาง 50 เท่าของแรงโน้มถ่วงมาตรฐาน และ Eab et al. (2014) ได้ทำการศึกษาต่อจาก Takahashi et al. (2014) โดยเน้น

การศึกษาการเสริมกำลังลาดดินโดยการใช้รากพืช ในกรณีที่มีการซึมผ่านของน้ำฝน โดยใช้การจำลองน้ำฝนภายในแบบจำลองด้วยเครื่องหมุนเหวี่ยง

2. วัตถุประสงค์

1) เพื่อศึกษาพฤติกรรมการเสริมกำลังของรากหญ้าแฝกสำหรับเพิ่มเสถียรภาพของลาดดินโดยใช้กระบวนการทดสอบในห้องปฏิบัติการ
2) เพื่อศึกษาตัวแปรที่มีผลของรากต่อกำลังรับแรงเฉือนของดิน (direct shear test) โดยการใช้เครื่องทดสอบกำลังรับแรงเฉือน สำหรับหญ้าแฝกหนึ่งต้น และ เครื่องทดสอบแรงเฉือนขนาดใหญ่ (large direct shear test) สำหรับหญ้าแฝกแบบกลุ่ม
3) เพื่อศึกษาการเจริญเติบโตของรากหญ้าแฝกและอัตราส่วนของรากหญ้าแฝกต่อพื้นที่ ด้วยการวัดโดยตรง และการใช้เทคนิคการวิเคราะห์ด้วยภาพถ่าย (image processing) ตามลำดับ
4) จำลองปัญหาลาดดินโดยแบบจำลองด้วยเครื่องหมุนเหวี่ยงโดยใช้การไหลของน้ำและการจำลองปริมาณน้ำฝนเพื่อศึกษาประสิทธิภาพของรากพืชที่มีผลต่อการเพิ่มเสถียรของลาดดิน

3. วิธีการศึกษา

3.1 การทดลองในห้องปฏิบัติการเพื่อศึกษาการเจริญของราก และทดสอบการต้านแรงเฉือนของราก

ในการทดลองนี้ หญ้าแฝกถูกปลูกเพื่อเจริญเติบโตใน 3 สภาวะ ได้แก่ (1) การเจริญของหญ้าแฝก ในระบบไฮโดรโปนิกส์ (hydroponic) ดังรูปที่ 1 (2) การเจริญของหญ้าแฝกหนึ่งต้นในท่อทึบแสง ดังรูปที่ 2(a) และ (3) การเจริญของหญ้าแฝกแบบกลุ่มในกล่อง ดังรูปที่ 2(b)

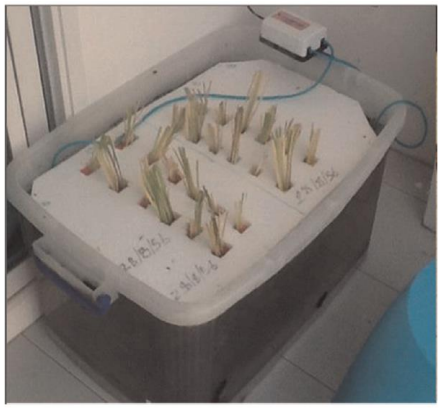

รูปที่ 1 การเจริญของหญ้าแฝกในระบบไฮโดรโปนิกส์ (hydroponic)

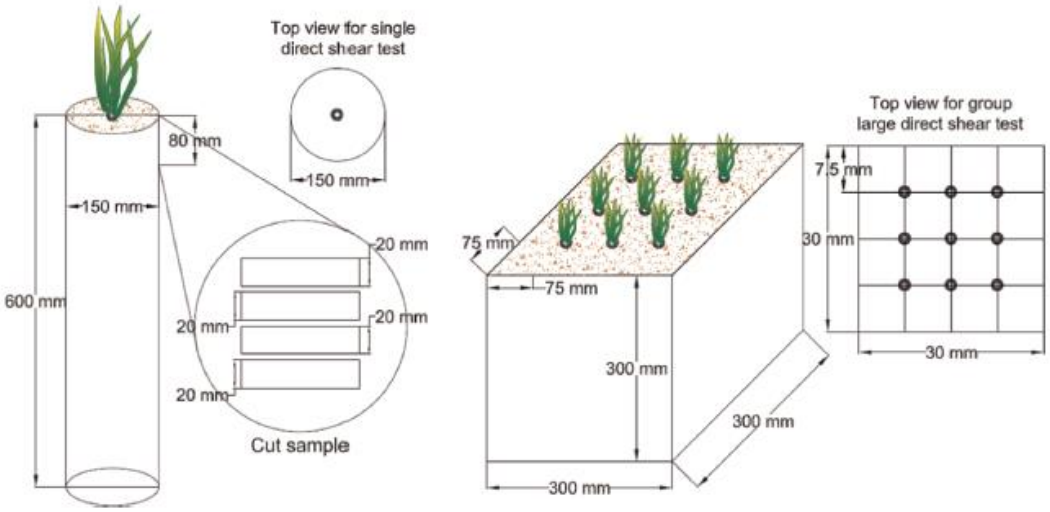

(a) (b)

รูปที่ 2 การเตรียมตัวอย่างหญ้าแฝกเพื่อทดสอบแรงเฉือนของราก (a) การปลูกหญ้าแฝกเชิงเดี่ยว 4 เดือนสำหรับการทดสอบแรงเฉือนแบบมาตรฐาน (b) การปลูกหญ้าแฝกแบบกลุ่ม 6 เดือนเพื่อทดสอบแรงเฉือนด้วยเครื่องทดสอบแรงเฉือนขนาดใหญ่

ปลูกหญ้าแฝกในระบบไฮโดรโปนิกส์ ซึ่งไม่ใช้ดิน เป็นเวลา 6 เดือน เพื่อศึกษาและเก็บข้อมูลการเจริญเติบโตของราก ความยาวราก ความหนาของราก และรัศมีของรากที่แผ่ในแต่ละตัวอย่าง

สำหรับการทดลองในสภาวะที่ 2 หญ้าแฝกถูกปลูกในดินที่ถูกบรรจุอยู่ในท่อ PVC ทึบ ซึ่งมีขนาดเส้นผ่านศูนย์กลาง 150 มิลลิเมตร ยาว 600 มิลลิเมตร เมื่อสิ้นสุดการทดลอง นำชุดการทดลองไปทดสอบแรงเฉือน โดยเฉือนในส่วนบนที่ความหนา 20 มิลลิเมตร ดังรูปที่ 3(a) โดยมีอัตราการเฉือนที่ 1.5 มิลลิเมตรต่อนาที

ในส่วนของการทดลองในสภาวะที่ 3 หญ้าแฝก 9 ต้นถูกปลูกในกล่องที่มีขนาด 300 ตารางที่มิลลิเมตร โดยมีระยะห่างระหว่างต้นเท่ากับ 7.5 มิลลิเมตร ดังรูปที่ 2(b) เพื่อทดสอบด้วยเครื่องทดสอบแรงเฉือนขนาดใหญ่ ตัวอย่างถูกเตรียมขึ้น 3 ตัวอย่าง โดยเตรียมตัวอย่างให้พอดีกับกล่องทดสอบขนาด 300 มิลลิเมตร x 300 มิลลิเมตร x 200 มิลลิเมตร ดังรูปที่ 3(b) นอกจากนี้การปลูกหญ้าแฝกแบบกลุ่มได้มีการติดตามเก็บข้อมูลการเจริญเติบโตของรากโดยการวิเคราะห์จากภาพถ่ายเพื่อหาสัดส่วนของรากต่อพื้นที่

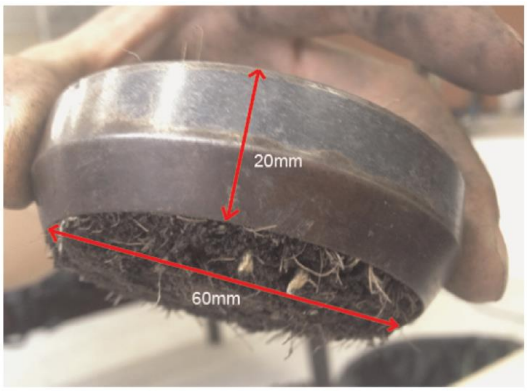

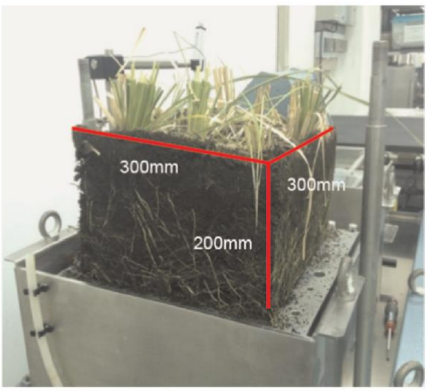

(a) (b)

รูปที่ 3 แสดงตัวอย่างสำหรับการทดสอบแรงเฉือน (a) อุปกรณ์สำหรับการทดสอบแรงเฉือนขนาดเส้นผ่านศูนย์กลาง 60 มิลลิเมตร (b) เครื่องมือสำหรับการทดสอบแรงเฉือนขนาดใหญ่ (ขนาด 300 มิลลิเมตร x 300 มิลลิเมตร x 200 มิลลิเมตร)

3.2 การจำลองแบบหมุนเหวี่ยง (centrifuge modelling)

การทดสอบแบบจำลองย่อส่วนในเครื่องหมุนเหวี่ยง เป็นการจำลองที่รู้จักและใช้กันอย่างแพร่หลายในการวิจัยและออกแบบทางวิศวกรรมธรณีเทคนิค เนื่องด้วยเสถียรภาพของลาดดินเป็นปัญหาที่เกี่ยวข้องกับแรงโน้มถ่วง ดังนั้นข้อดีของหลักของการใช้การจำลองแบบหมุนเหวี่ยงคือ นักวิจัยสามารถลดขนาดของปัญหาลง ในขณะที่สามารถจำลองความเค้นได้อย่างถูกต้องโดยการเพิ่มแรงหนีศูนย์กลาง ซึ่งในการทดลองนี้จะใช้ค่าความเร่งแรงหนีศูนย์กลางเท่ากับ 50 เท่าของแรงโน้มถ่วงโลก วิธีการเร่งความเร็วด้วยการหมุนเหวี่ยงถูกใช้เพื่อจำลองการเกิดปัญหาในด้านเสถียรภาพของลาดดิน โดยได้มีการทดสอบ 2 ประเภท (1) การจำลองปัญหาการไหลของน้ำใต้ดิน (seepage tests) และ (2) การจำลองปัญหาจากการกระทำของน้ำฝน (rainfall tests)

4. ผลการศึกษา

4.1 การสังเกตการเจริญของราก

รูปที่ 4 ได้แสดงค่าเฉลี่ยของความยาวรากและขนาดเส้นผ่านศูนย์กลางของรากจากการปลูกพืชในระบบไฮโดรโปนิกส์ เป็นระยะเวลา 6 เดือน ความสัมพันธ์ระหว่างความยาวรากและรัศมีของมัดรากแสดงดังรูปที่ 4(a) อัตราการเจริญของรากสามารถหาได้จากความยาวของรากกับเวลาที่ทดสอบแสดงดังรูปที่ 4(b) จากผลการทดสอบพบว่ารากของหญ้าแฝกสามารถขยายรัศมีของมัดรากได้ถึง 1.7 เซนติเมตร และรากสามารถเจริญเติบโตได้ถึง 180 เซนติเมตรภายในระยะเวลา 6 เดือน ดังนั้นอัตราการเจริญเติบโตของรากเฉลี่ยโดยประมาณเท่ากับ 30 เซนติเมตรต่อเดือน นอกจากนี้จากการผลการทดสอบพบว่าอัตราการเจริญเติบโตของหญ้าแฝกมีค่าสูงกว่างานวิจัยของ Kaewsaeng (2000) โดยความแตกต่างที่เกิดขึ้นนี้อาจเกิดจากสภาวะของการปลูกพืชและวิธีการตรวจวัด

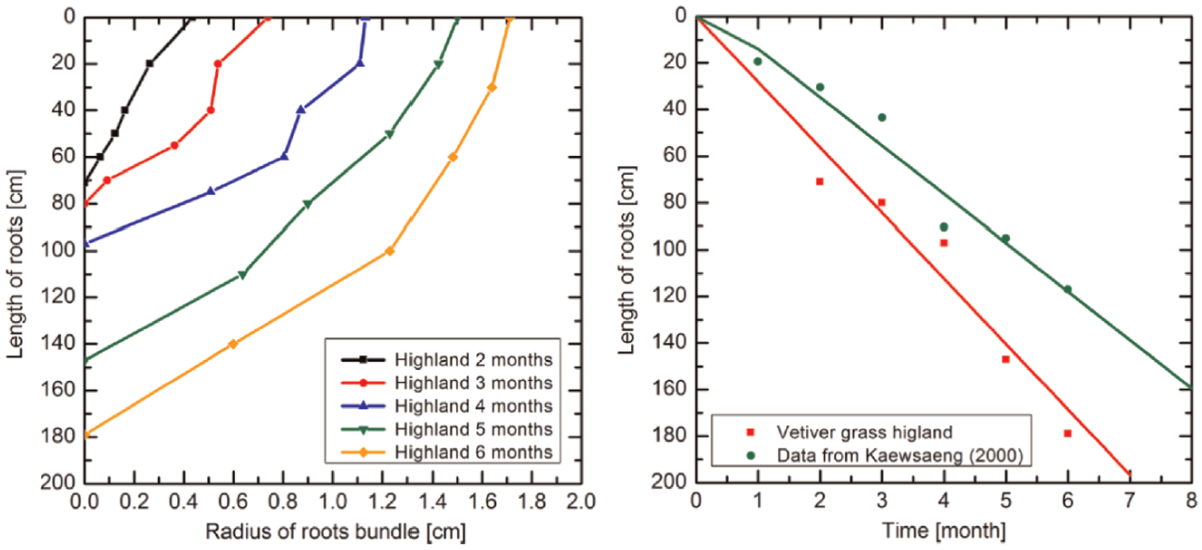

(a) (b)

รูปที่ 4 ค่าเฉลี่ยจากการวัดรากหญ้าแฝก (a) ความสัมพันธ์ระหว่างความยาวรากและรัศมีของมัดราก (b) อัตราการเจริญเติบโตของราก

นอกจากนี้ อัตราส่วนของรากต่อพื้นที่ยังสามารถสังเกตได้จากการปลูกหญ้าแฝกแบบกลุ่ม ซึ่งค่านี้มีความสำคัญต่อค่าความเค้นเฉือน อย่างไรก็ตาม การหาอัตราส่วนของรากต่อพื้นที่ตามแนวราบซึ่งตั้งฉากกับทิศทางการเจริญของรากพืชนั้นทำได้ยาก และอีกทั้งยังเปลี่ยนแปลงตามความลึก ดังนั้นในการทดลองนี้จึงใช้การวัดแบบแนวขนานซึ่งสามารถทำได้ง่ายกว่า Alsheimer and Hughes (2007) รายงานว่าการถ่ายภาพเพื่อสังเกตการกระจายของรากในตัวอย่างที่ใช้ในการทดสอบหาแรงเฉือนขนาดใหญ่ รูปที่ถ่ายของรากและดินถูกบันทึกด้วยกล้องดิจิตอลและเปลี่ยนเป็น binary images โดยฟังก์ชัน histogram ในโปรแกรม Photoshop โดยความแตกต่างระหว่างรากพืชและดินสามารถจำแนกได้จากสีขาวและดำ ซึ่งอัตราส่วนระหว่าง pixel ของรากกับจำนวน pixel รวมทั้งหมด แสดงถึงอัตราส่วนของรากต่อพื้นที่ ผลการทดลองแสดงค่าเฉลี่ยของอัตราส่วนรากต่อพื้นที่ของหญ้าแฝกที่ 4 เดือนและ 6 เดือนมีค่า 2.44% และ 4.37% ตามลำดับ รูปที่ 5(b) แสดง binary images สำหรับการประเมินค่าอัตราส่วนรากต่อพื้นที่ซึ่งขึ้นอยู่กับสีในภาพ

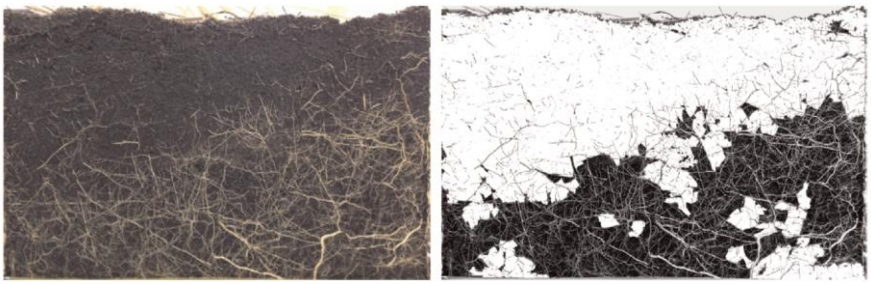

(a) (b)

รูปที่ 5 การคำนวณอัตราส่วนรากต่อพื้นที่ (a) ภาพถ่ายของรากหญ้าแฝกที่เจริญเติบโต 6 เดือน (b)

binary images กับอัตราส่วนรากพื้นที่ 4.56%

4.2 แรงเฉือนของรากหญ้าแฝก

การเสริมกำลังด้วยรากของหญ้าแฝก ศึกษาโดยใช้การทดสอบแรงเฉือน การทดสอบนี้ดำเนินการในห้องปฏิบัติการเนื่องจากสามารถควบคุมความหนาแน่นและความชื้นในดินให้อยู่ที่ระหว่าง 20-25% สำหรับดินเปล่าและดินที่ปลูกพืช เป็นผลให้สามารถลดผลกระทบจากความแตกต่างของค่าแรงดูดน้ำใต้ดิน ระหว่างการทดสอบได้มีการเพิ่มขึ้นของกำลังต้านทานแรงเฉือนจากการเสริมกำลังโดยรากของหญ้าแฝก ซึ่งสังเกตได้จากการเปรียบเทียบกับดินเปล่าที่มีความหนาแน่นและปริมาณความชื้นเท่ากับตัวอย่างชุดการทดลอง

ตารางที่ 1 ผลการทดลองจาก direct shear test

การทดสอบ	**ตัวอย่าง**	**ตัวแปรที่มีผลต่อค่ากำลังต้านทางแรงเฉือน**	**การเพิ่มขึ้นของค่าแรงยึดเหนี่ยว (kPa)**
การทดสอบแรงเฉือน	ดินเปล่า	c = 6.8 kPa; $\varnothing$ = 22.8°	6.8
	หญ้าแฝกเชิงเดี่ยวอายุ 4 เดือน	c = 13.6 kPa; $\varnothing$ = 29.7°	
การทดสอบด้วยเครื่องทดสอบแรงเฉือนขนาดใหญ่	ดินเปล่า	c = 2.5 kPa; $\varnothing$ = 21.8°	6.0
	หญ้าแฝกแบบกลุ่มอายุ 6 เดือน	c = 8.5 kPa; $\varnothing$ = 29.2°	

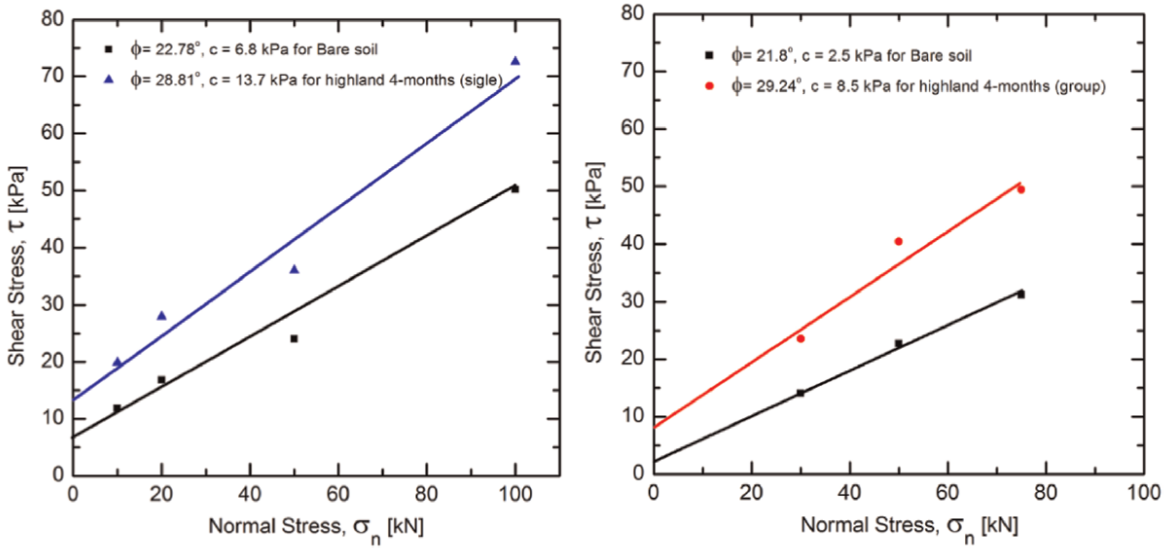

(a) (b)

รูปที่ 6 แรงเฉือนของรากหญ้าแฝกกับดิน: (a) หญ้าแฝกเชิงเดี่ยว 4 เดือนโดยการทดสอบแรงเฉือนแบบมาตรฐาน (b) การปลูกหญ้าแฝกแบบกลุ่ม 6 เดือนโดยเครื่องทดสอบแรงเฉือนขนาดใหญ่

กำลังต้านทานของแรงเฉือนของดินที่ถูกเสริมกำลังด้วยรากหญ้าแฝกอายุ 4 เดือนและดินเปล่า แสดงในรูปที่ 6(a) และค่าแรงยึดเหนี่ยว และมุมเสียดทานภายในดิน สามารถคำนวณจากสมการวิบัติของมอร์-คูลอมบ์ (Mohr-Coulomb failure criterion) ดังแสดงในตารางที่ 1 จากผลการทดสอบพบว่ารากของหญ้าแฝกช่วยเพิ่มกำลังในดิน อีกทั้งยังเพิ่มค่ากำลังยึดเหนี่ยวจากแรงเฉือน ประมาณ 7 kPa ซึ่งสอดคล้องกับการทดลองของ Ali and Osman (2008) ที่รายงานว่าค่ากำลังยึดเหนี่ยวจากแรงเฉือนเพิ่มขึ้นประมาณ 11 kPa จากการเสริมกำลังโดยรากของหญ้าแฝก

หญ้าแฝกอายุ 6 เดือนถูกเตรียมขึ้นในลักษณะของตัวอย่างแบบกลุ่มในกล่อง และทดสอบด้วยเครื่องทดสอบแรงเฉือนขนาดใหญ่ ด้วยอัตรา 30, 50, และ 75 kPa ทุกตัวอย่างถูกเฉือนจนถึงระยะสูงสุดที่ 50 มิลลิเมตร ผลของการทดสอบด้วยเครื่องทดสอบแรงเฉือนขนาดใหญ่แสดงดัง*รูปที่ 6* (b) จากผลการทดลองพบว่า ค่าความเชื่อมแน่น (cohesion) ของดินเพิ่มขึ้นในการปลูกหญ้าแฝกแบบเดี่ยวมากกว่าแบบกลุ่ม ซึ่งความแตกต่างอาจจะเกิดขึ้นจากการกระจายตัวของรากหญ้าแฝกซึ่งอธิบายได้จากค่าอัตราส่วนของรากต่อพื้นที่ ทั้งนี้ยังอาจจะเกิดจากผลกระทบของขนาดในการทดสอบ

4.3 การจำลองปัญหาลาดดินด้วยแบบจำลองหมุนเหวี่ยง (centrifuge modelling)

แบบจำลองหมุนเหวี่ยงถูกใช้อย่างแพร่หลายในงานวิจัยด้านธรณีเทคนิค โดยเสถียรภาพของลาดดินมีปัจจัยที่ขึ้นอยู่กับแรงโน้มถ่วงของโลก ซึ่งข้อดีของการใช้แบบจำลองหมุนเหวี่ยงคือผู้วิจัยสามารถลดขนาดของแบบจำลองลดได้ในขณะที่ยังใช้ค่าความเค้นที่ถูกต้องโดยการเพิ่มค่าแรงโน้มถ่วง

ในการทดลองนี้ได้ใช้ 50 เท่าของแรงโน้มถ่วงมาตรฐาน ในการจำลองปัญหาของลาดดิน ซึ่งการทดลองแบ่งออกเป็น 2 ประเภท ได้แก่ (1) การจำลองปัญหาการไหลของน้ำใต้ดิน (seepage tests) และ (2) การจำลองปัญหาจากการกระทำของน้ำฝน (rainfall tests)

4.3.1 คุณสมบัติของวัสดุที่ใช้ในแบบจำลอง

ดินทรายที่ใช้ในแบบจำลองเป็นทรายอิโดเซกิ (Edosaki sand) ซึ่งเป็นทรายมาตรฐานญี่ปุ่น ชนิดทรายเม็ดละเอียด (fine sand) และมีเส้นใยสังเคราะห์ (fiber) 2 ชนิดที่ถูกใช้ในการศึกษาครั้งนี้ (1) เส้นเอ็นตกปลา (fishing line) ที่มีขนาดเส้นผ่านศูนย์กลาง 0.33 มิลลิเมตร และมีความยาว 10 มิลลิเมตร และ (2) เส้นใยโพลีเอสเตอร์ (polyester fiber) ที่มีขนาดเส้นผ่านศูนย์กลาง 39 μm และมีความยาว 10 มิลลิเมตร โดยจะผสมเส้นเอ็นตกปลากับดินให้มีความหนา 20 มิลลิเมตร ในปริมาณ 1% โดยมวล (เทียบเท่ากับความหนาชั้นดิน 1 เมตร ในขนาดแท้จริง) ในทำนองเดียวกันจะผสมเส้นใยโพลีเอสเตอร์ปริมาณ 2% โดยมวลให้มีความหนา 40 มิลลิเมตร (เทียบเท่ากับความหนาชั้นดิน 2 เมตรในขนาดแท้จริง) ซึ่งการจำลองนี้สามารถเทียบเท่ากับการเจริญเติบโตของหญ้าแฝกที่มีอายุเท่ากับ 6 เดือน โดย รูปที่ 7 แสดงรูปที่ของเส้นเอ็นตกปลาและเส้นใยโพลีเอสเตอร์ก่อนและหลังการผสมกับทราย

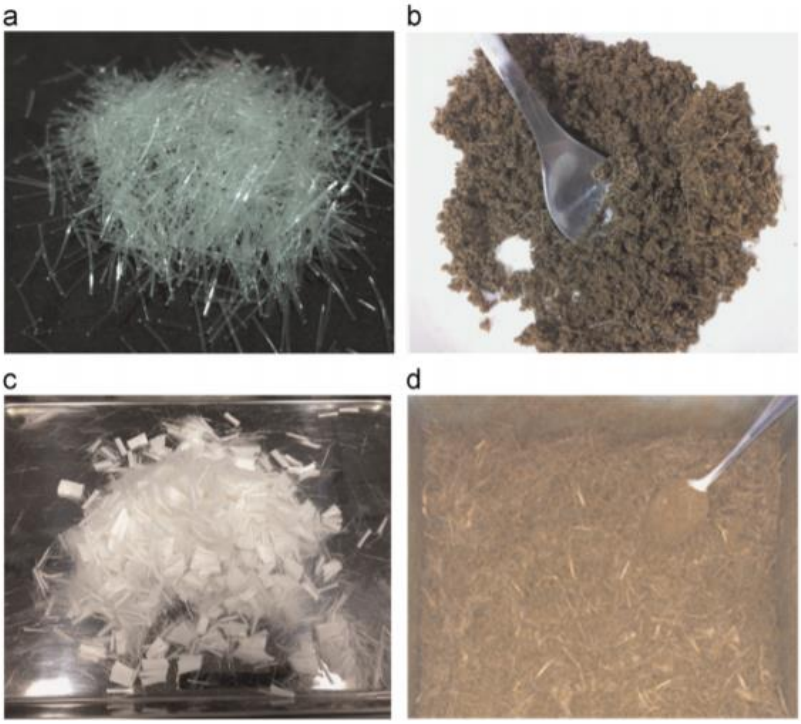

รูปที่ 7 รูปที่ของเส้นใยก่อนและหลังการผสมกับทราย: (a) ลักษณะของเส้นเอ็นตกปลา และ (c) ลักษณะของเส้นใยโพลีเอสเตอร์ (a) เส้นเอ็นตกปลาก่อนทำการผสม (b) เส้นเอ็นตกปลาหลังทำการผสมกับดิน (c) เส้นใยโพลีเอสเตอร์ก่อนทำการผสม (d) เส้นใยโพลีเอสเตอร์หลังทำการผสมกับดิน

จากการสังเกตผลการทดสอบพบว่า เส้นใยไม่มีการเปลี่ยนแปลงรูปที่ร่างแม้กระทั่งหลังจากการทดลองสิ้นสุดลง ดังนั้นผลกระทบของการเปลี่ยนแปลงรูปที่ร่างของเส้นใยที่มีต่อค่ากำลังรับแรง

เฉือน มีค่าน้อยมากเมื่อเทียบกับเปอร์เซ็นต์ในการผสม และแรงยึดเหนี่ยวระหว่างวัสดุที่แตกต่างกัน โดยเส้นใยกับดิน รูปที่ 8 แสดงผลการเปรียบเทียบจากผลการทดสอบแรงเฉือน ผลการทดลองพบว่า การผสมเส้นเอ็นตกปลาปริมาณ 1% จะเพิ่มค่าแรงยึดเหนี่ยวของดินประมาณ 2 kPa และค่ามุมเสียดทานภายในประมาณ 8º ในขณะที่การผสมเส้นใยโพลีเอสเตอร์ปริมาณ 2% สามารถเพิ่มค่าแรงยึดเหนี่ยว ของดินประมาณ 14 kPa และค่ามุมเสียดทานภายในประมาณ 3º ความแตกต่างที่เกิดขึ้นน่าจะเป็นผลกระทบจากชนิดและปริมาณของเส้นใยสังเคราะห์ เมื่อพิจารณาการเพิ่มขึ้นของค่าแรงยึดเหนี่ยว ประมาณ 6-7 kPa เนื่องจากการปลูกหญ้าแฝก สามารถกล่าวได้ว่าค่ากำลังรับแรงเฉือน ของดินผสมเส้นเอ็นตกปลา และดินผสมเส้นใยโพลีเอสเตอร์สามารถนำมาใช้ในจำลองพฤติกรรมของการเพิ่มกำลังของดินโดยหญ้าแฝกได้ ดังนั้นเส้นใยทั้งสองชนิดถูกเลือกใช้ในการจำลองแบบหมุนเหวี่ยง

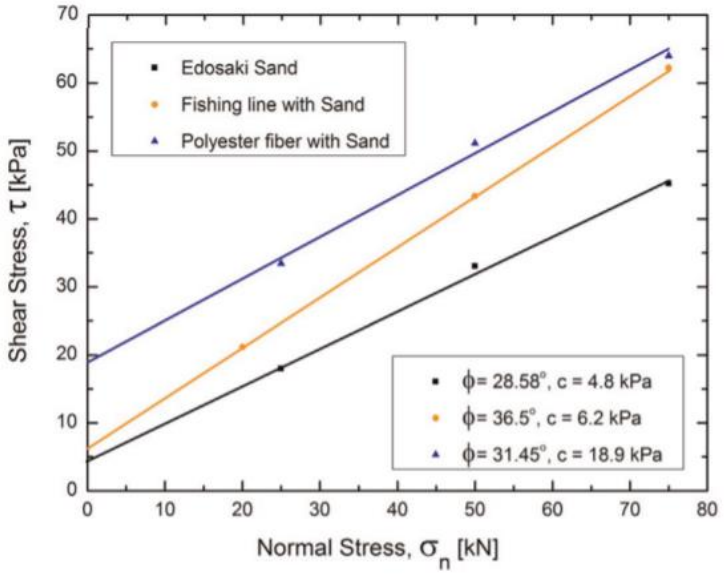

รูปที่ 8 ผลการทดสอบแรงเฉือนของดินทรายอิโดเซกิ ดินทรายผสมเส้นเอ็นตกปลา และดินทรายผสมเส้นใยโพลีเอสเตอร์

4.3.2 แบบจำลองลาดดินและกระบวนการทดสอบ

แบบจำลองแบบหมุนเหวี่ยง ถูกจำลองขึ้น 2 สภาวะ (1) การจำลองปัญหาการไหลของน้ำใต้ดิน (seepage tests) และ (2) การจำลองปัญหาจากการกระทำของน้ำฝน (rainfall tests) การทดสอบสองแบบนี้ได้จำลองกระบวนการวิบัติของลาดดิน แบบจำลองถูกเตรียมขึ้นในกล่องที่มีขนาด 450 มิลลิเมตร x 150 มิลลิเมตร x 270 มิลลิเมตร และประกอบด้วยสองส่วน ส่วนแรกคือส่วนของชั้นหิน (bedrock) ดังแสดงในรูปที่ 9 และส่วนที่สองเป็นการจำลองลาดดินด้วยทรายอิโดเซกิ ซึ่งแบ่งออกเป็น 4 ชั้น มีความหนารวม 80 มิลลิเมตร ในกรณีของการจำลองปัญหาการไหลของน้ำใต้ดิน จะติดตั้งทรานสดิวเซอร์วัดแรงดันน้ำ (PWP transducers) จำนวน 10 ตัว และอุปกรณ์วัดความเร่ง (accelerometers) จำนวน 4 ตัว ส่วนในกรณีของการจำลองปัญหาจากการกระทำของน้ำฝน

ทรานสดิวเซอร์วัดแรงดันน้ำจำนวน 8 ตัว และอุปกรณ์วัดความเร่ง 6 ตัวถูกติดตั้งในแบบจำลอง โดยอยู่ในตำแหน่งดังที่แสดงในรูปที่ 9

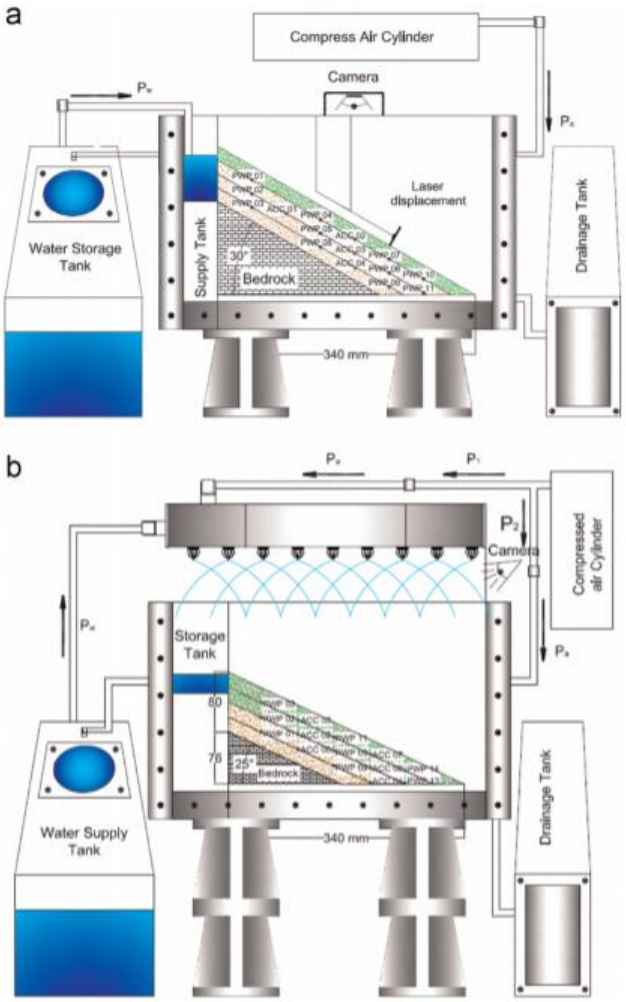

รูปที่ 9 แบบจำลองหมุนเหวี่ยง (a) seepage model test และ (b) rainfall model test

จากผลจากการจำลองแบบหมุนเหวี่ยงแสดงให้เห็นถึงความแตกต่างของเส้นระดับผิวน้ำ (phreatic line) ภายในลาดดิน ในการทดสอบปัญหาการไหลของน้ำใต้ดิน เส้นระดับผิวน้ำขนานกับความชันของชั้นหินและลาดดิน ในทางตรงกันข้ามเส้นระดับผิวน้ำสูงขึ้นที่ด้านล่างของลาดดินในการทดสอบปัญหาจากการกระทำของน้ำฝน นอกจากนี้เส้นระดับผิวน้ำ ในการทดสอบแบบฝนตกของกรณีดินที่เสริมกำลังจากรากมีการลดลง ซึ่งการลดลงนี้อาจจะเกิดเนื่องมาจากเส้นใยโพลีเอสเตอร์ มีส่วนช่วยในการป้องกันการเพิ่มขึ้นของระดับน้ำใต้ดิน นอกจากนี้ผลการการวัดแรงดันน้ำจาก PWPs ในการทดสอบแบบจำลองน้ำฝนชี้ให้เห็นว่าลาดดินมีลักษณะไม่อิ่มตัวด้วยน้ำ

ผลจากการจำลองแบบหมุนเหวี่ยงสามารถสังเกตถึงรอยแยกของลาดดินเล็กน้อยได้ที่ขั้นตอนการวิบัติในกรณีที่ไม่มีการเพิ่มกำลังของดินเท่านั้น และในกรณีที่มีการเพิ่มกำลังของดินด้วยรากไม่พบการไหลบ่าของน้ำ และการกัดเซาะของดิน

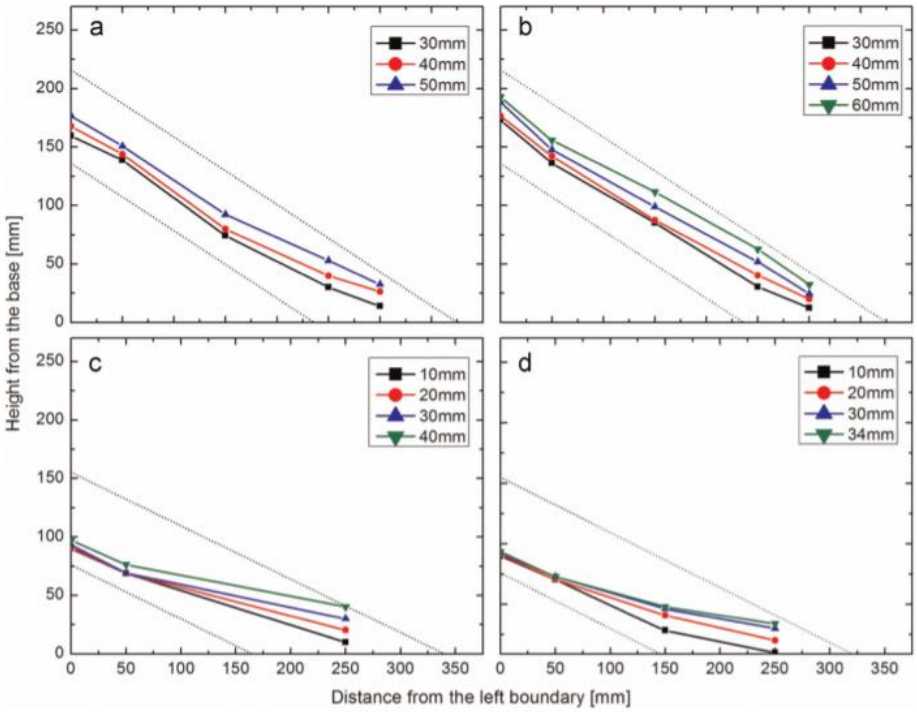

รูปที่ 10 ความแตกต่างของเส้นระดับผิวน้ำ (phreatic line) ระหว่างการทดสอบ: (a) ปัญหาการไหลของน้ำใต้ดินกรณีไม่เสริมแรง; (b) ปัญหาการไหลของน้ำใต้ดินกรณีเสริมแรงด้วยราก 20 มิลลิเมตร; (c) ปัญหาการกระทำจากน้ำฝนกรณีไม่เสริมแรง; และ (d) ปัญหาการกระทำจากน้ำฝนกรณีเสริมแรงด้วยราก 40 มิลลิเมตร

รูปที่ 11 แสดงภาพถ่ายดิจิตอลของลาดดินหลังจากการทดสอบในปัญหาการไหลของน้ำใต้ดิน การพังทลายของดินเริ่มที่ด้านล่างเมื่อแรงดันน้ำ (pressure head) ที่ปลายลาดดินมีค่าความสูงประมาณ 30 มิลลิเมตร สำหรับทั้งในกรณีที่ไม่มีการเสริมและมีการเสริมแรงด้วยราก ในกรณีของลาดดินที่เสริมแรงด้วยรากที่ 20 มิลลิเมตร พบว่าไม่มีการไถลของหน้าดินที่ตรงกึ่งกลาง นอกจากนี้การเปลี่ยนแปลงที่เกิดขึ้นถูกจำกัดอยู่ในบริเวณด้านล่างของกรณีที่มีการเสริมแรงของดินด้วยราก ในขณะที่กรณีที่ไม่มีการเสริมแรงจะเกิดการวิบัติขึ้นที่บริเวณกึ่งกลาง ซึ่งสามารถพิจารณาได้ว่าเป็นผลของเส้นใยสังเคราะห์ในผิวดิน ในการทดสอบโดยการจำลองน้ำฝนพบว่าลาดดินเริ่มวิบัติจากด้านล่างและเลื่อนสูงขึ้นจนกระทั่งความแรงดันน้ำใต้ดินใกล้เคียง 40 มิลลิเมตร

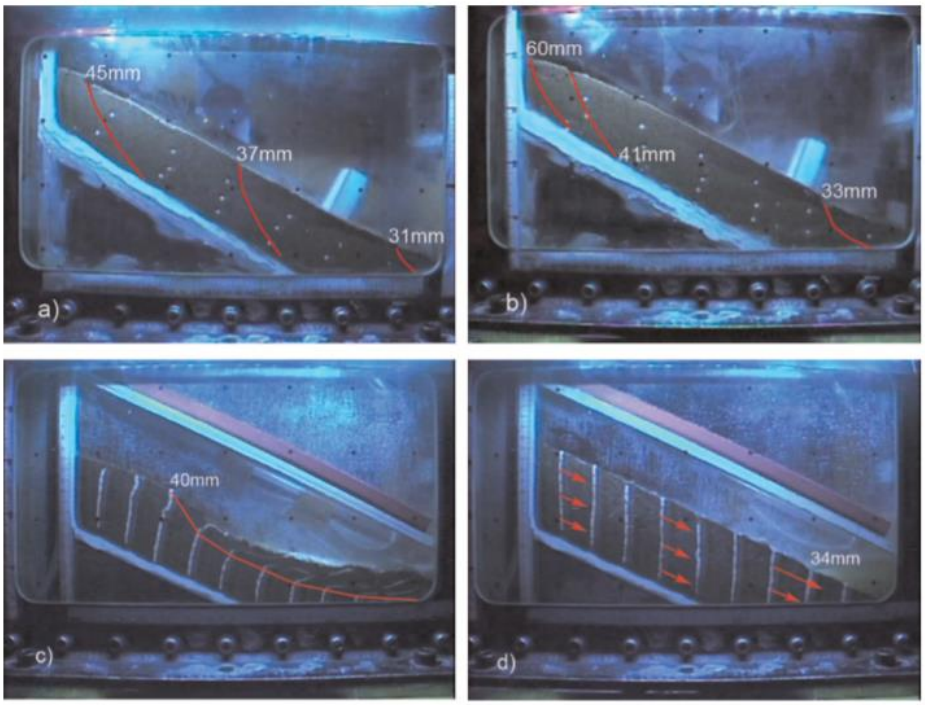

รูปที่ 11 เส้นโค้งการวิบัติของลาดดิน (slip surface line): (a) ปัญหาการไหลของน้ำใต้ดินกรณีไม่เสริมแรง; (b) ปัญหาการไหลของน้ำใต้ดินกรณีเสริมแรงด้วยราก 20 มิลลิเมตร; (c) ปัญหาการกระทำจากน้ำฝนกรณีไม่เสริมแรง; และ (d) ปัญหาการกระทำจากน้ำฝนกรณีเสริมแรงด้วยราก 40 มิลลิเมตร

การเคลื่อนตัวของลาดดินสามารถคำนวณได้จากเครื่องวัดความเร่งดังแสดงในรูปที่ 12 ค่าความชันในการจำลองน้ำฝนในกรณีที่ไม่มีการเสริมกำลังของดินด้วยราก แสดงถึงการทรุดตัวอย่างมากประมาณ 16 มิลลิเมตร เมื่อค่าแรงดันน้ำด้านล่างมีค่าใกล้กับ 50 มิลลิเมตร ส่วนในกรณีที่มีการเพิ่มกำลังของราก การทรุดตัวของลาดดินมีค่าลดลงถึงที่ 8 มิลลิเมตรที่ค่าแรงดันน้ำ 60 มิลลิเมตร ในทางกลับกันลาดดินมีการพังทลายลงเนื่องจากกรณีที่มีฝนตกหนักถูกแสดงดังรูปที่ 12 (c) ค่าการทรุดตัวในกรณีของแบบจำลองน้ำฝนมีปริมาณอยู่ที่ 15 มิลลิเมตร เมื่อค่าแรงดันน้ำที่ใกล้ด้านล่างของลาดดินมีค่าใกล้กับ 30 มิลลิเมตร จากการประยุกต์ใช้เส้นใยในการเพิ่มกำลังของลาดดินที่ผิวดิน พบว่าการเปลี่ยนแปลงของหน้าดินลดลงน้อยกว่า 3 มิลลิเมตรโดยไม่มีการพังทลายดังแสดงในรูปที่ 12 (d)

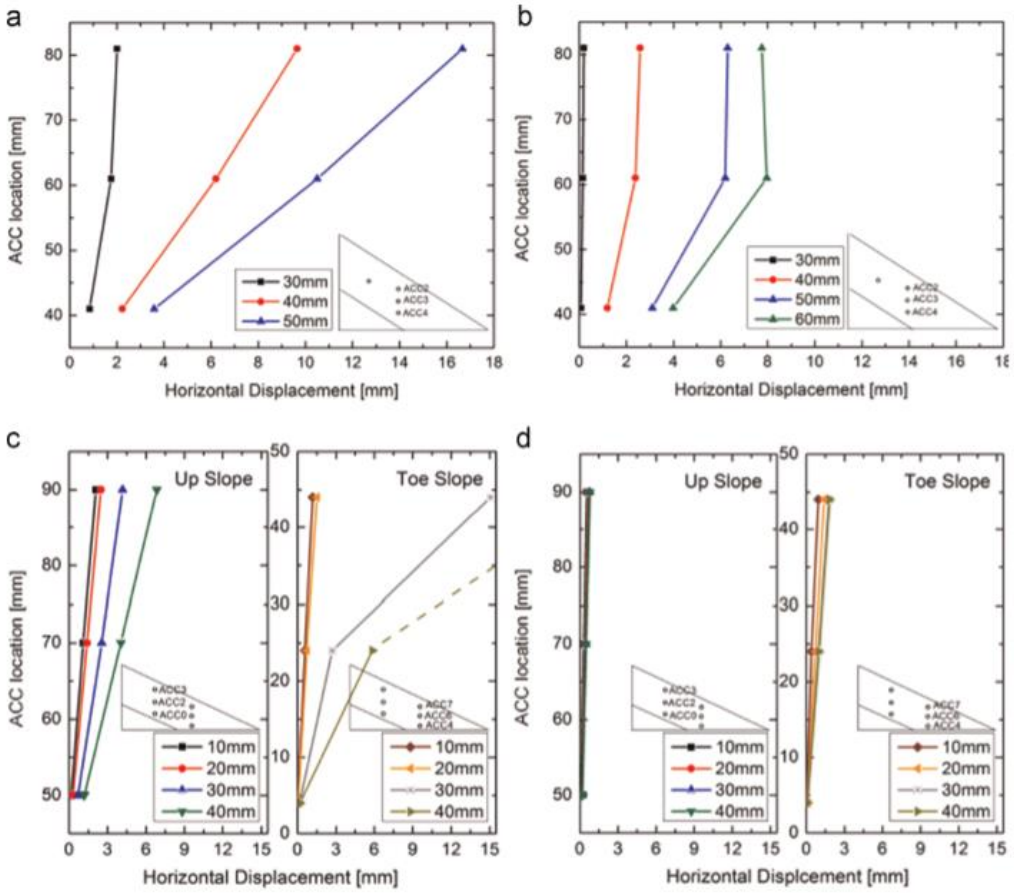

รูปที่ 12 การเคลื่อนตัวที่คำนวณได้จาก accelerometers: (a) ปัญหาการไหลของน้ำใต้ดินกรณีไม่เสริมแรง; (b) ปัญหาการไหลของน้ำใต้ดินกรณีเสริมแรงด้วยราก 20 มิลลิเมตร; (c) ปัญหาการกระทำจากน้ำฝนกรณีไม่เสริมแรง; และ (d) ปัญหาการกระทำจากน้ำฝนกรณีเสริมแรงด้วยราก 40 มิลลิเมตร

4.4 การวิเคราะห์เสถียรภาพด้วยแบบจำลองเชิงตัวเลข

จากผลการทดลองด้วยแบบจำลองหมุนเหวี่ยงพบว่าการวิบัติของลาดดินในกรณีที่ไม่มีการเสริมกำลังเกิดขึ้นเนื่องจากการเพิ่มสูงขึ้นของระดับน้ำใต้ดิน ทั้งนี้สามารถสังเกตได้ว่าการเคลื่อนตัวของลาดดินเกิดขึ้นที่ด้านล่างก่อนที่จะขยายไปถึงด้านบนของคันดิน สำหรับกรณีการเสริมแรงด้วยรากส่งผลให้ลาดดินเกิดการเคลื่อนตัวเพียงเล็กน้อยแต่ไม่เกิดการพังทลาย ผลการทดสอบแบบจำลองหมุนเหวี่ยงสรุปไว้ดังแสดงในตารางที่ 2 ซึ่งผลการทดลองบ่งชี้ว่าการมีอยู่ของรากช่วยในการเพิ่มความแข็งแรงของดินและลดอัตราการไหลซึมของน้ำฝนลงสู่ดิน ซึ่งเป็นผลในการชะลอการเปลี่ยนแปลงระดับน้ำใต้ดิน หรือสามารถกล่าวได้ว่ารากสามารถชะลอการพังทลายของลาดดิน

ตารางที่ 2 สรุปผลการทดลองจากการจำลองแบบหมุนเหวี่ยง

กรณี	ชนิดของแบบจำลอง	คำอธิบาย	ระยะเวลาที่ทดสอบ (ชั่วโมง)	หมายเหตุ
1	ไม่มีการเสริมกำลัง	ดินเปล่า	18	เกิดการวิบัติของลาดดิน
2	การเสริมกำลังของดินด้วยเส้นใยหนา 20 มิลลิเมตร	ความยาวรากลึก 1 เมตร	35	เกิดการเปลี่ยนแปลงของลาดดินปานกลาง (ไม่มีการวิบัติ)
3	การเสริมกำลังของดินด้วยเส้นใยหนา 40 มิลลิเมตร	ความยาวรากลึก 2 เมตร	40	เกิดการเปลี่ยนแปลงของลาดดินเล็กน้อย (ไม่มีการวิบัติ)

ในการศึกษานี้ จะนำผมการศึกษาด้วยแบบจำลองหมุนเหวี่ยง ไปดำเนินการวิเคราะห์การไหลสองมิติ (seepage analysis) และการวิเคราะห์สเถียรภาพของลาดดิน (slope stability analysis) ด้วยโปรแกรม GEO-SLOPE โดยตัวแปรที่นำเข้าได้แก่ เส้นโค้งลักษณะเฉพาะของดินและน้ำ (soil-water characteristic curve, SWCC) และ ฟังก์ชันการนำน้ำ (hydraulic conductivity function) โดยรูปที่ 13 แสดงค่า SWCC และ hydraulic conductivity function ที่ใช้ในการศึกษาในครั้งนี้ และรูปที่ 14 แสดงขอบเขตทางเรขาคณิต และค่าความดันของน้ำเริ่มต้นในการวิเคราะห์

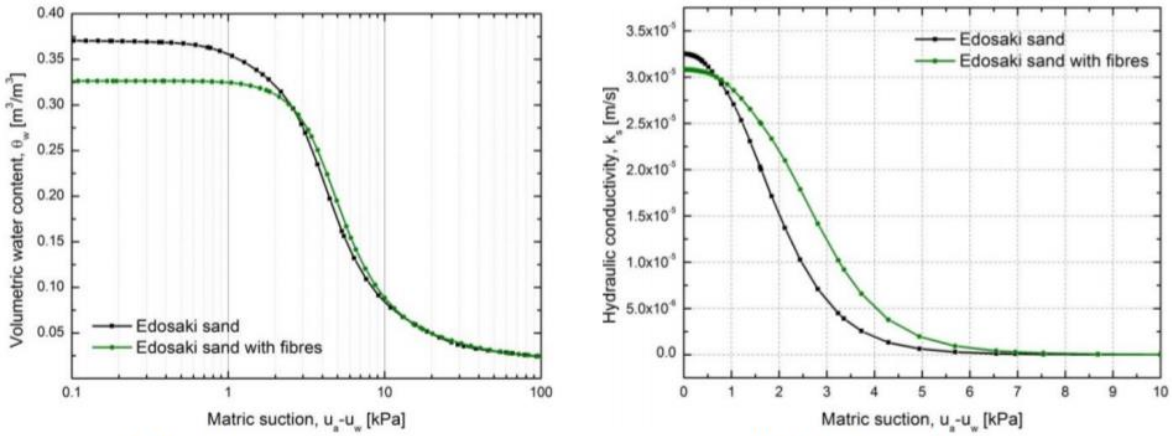

(a) Soil water characteristic curve (b) Hydraulic conductivity

รูปที่ 13 Input soil water characteristic curve และ hydraulic conductivity สำหรับการวิเคราะห์การไหลของน้ำ

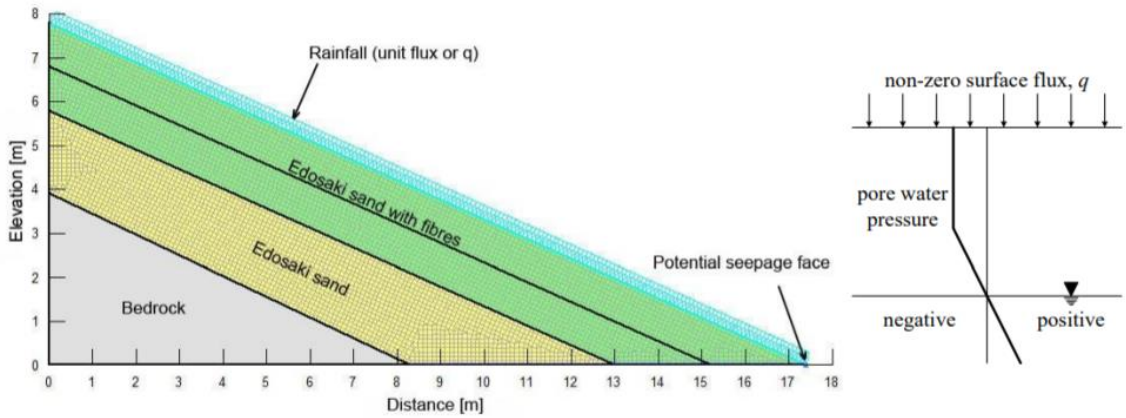

(a) Geometry boundary condition (b) Initial pore water pressure condition

รูปที่ 14 ขอบเขตทางเรขาคณิต และค่าความดันของน้ำเริ่มต้นในการวิเคราะห์

4.4.1 การกระจายตัวของแรงดันน้ำในลาดดิน (Pore water pressure distribution)

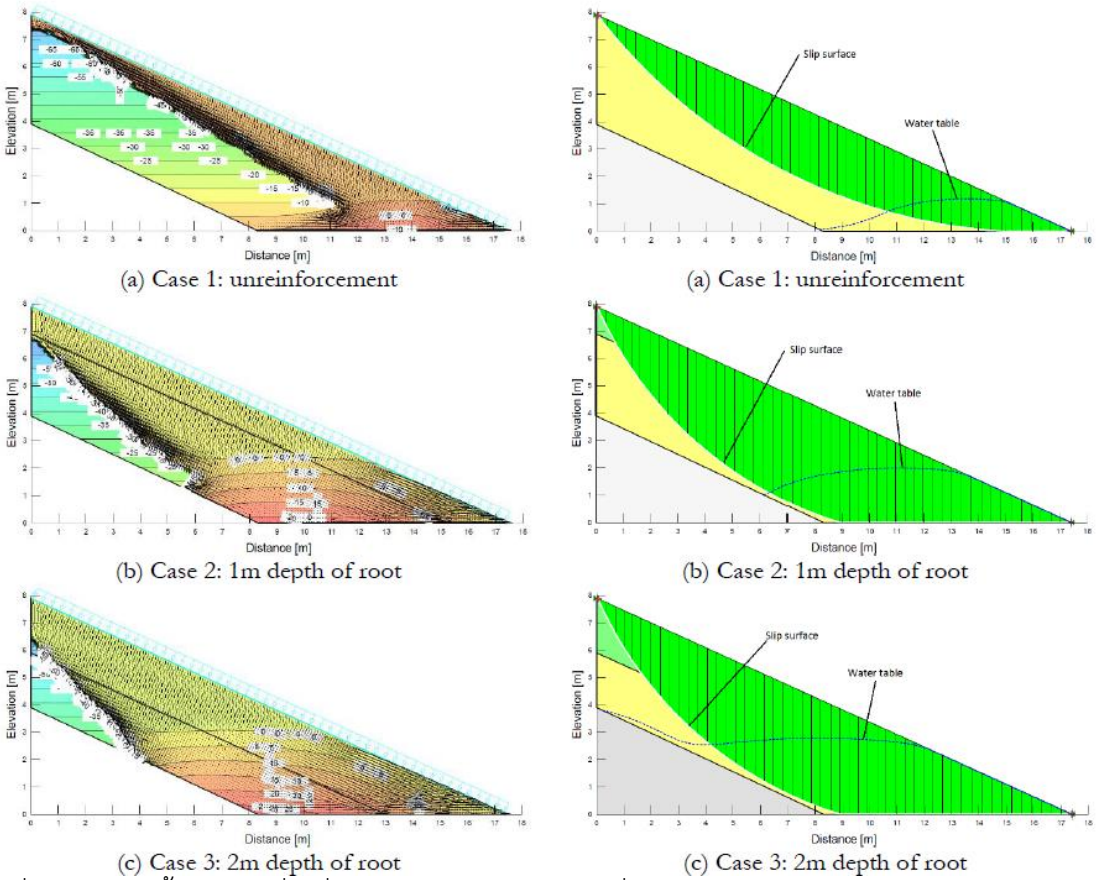

(a) Case 1: unreinforcement (a) Case 1: unreinforcement

(b) Case 2: 1m depth of root (b) Case 2: 1m depth of root

(c) Case 3: 2m depth of root (c) Case 3: 2m depth of root

รูปที่ 15 แรงดันน้ำในโพรงที่เปลี่ยนแปลงไปหลังจากการทดสอบ

รูปที่ 16 การไถลของผิวดินหลังจากการทดสอบ

รูปที่ 15 แสดงค่าการกระจายของแรงดันน้ำในโพรงดินในลาดดินที่ถูกจำลองขึ้น โดยใช้การวิเคราะห์การไหลของน้ำสำหรับทั้ง 3 สภาวะ ผลการทดลองพบว่าในระหว่างที่ฝนตก ค่าแรงดันน้ำในโพรงเริ่มต้นจากค่าที่เป็นลบ (แรงดูด) และเปลี่ยนไปทางค่าบวก รูปที่ 15(a) แสดงผลของการเสริม

กำลัง ในขณะที่ค่าแรงดันน้ำในโพรงเพิ่มขึ้น 10 kPa ที่ส่วนปลายสุด ในขณะที่แรงดันน้ำส่วนบนยังคงอยู่ที่ค่าลบหลังจากผ่านไป 18 ชั่วโมงในช่วงระยะเวลาที่ฝนตก สำหรับในกรณีของการปลูกพืชคลุมดินที่ความลึก 1 เมตร ดังแสดงดังรูปที่ 16(b) จำนวนน้ำฝนที่ซึมผ่านทางลาดและมีผลต่อการเปลี่ยนแปลงของค่าแรงดันน้ำในโพรงจากค่าลบเป็นบวกที่ 20 kPa หลังจากผ่านไป 35 ชั่วโมง สำหรับกรณีที่ปลูกพืชคลุมดินที่ระดับความลึก 2 เมตร แสดงในรูปที่ 16(c) ค่าแรงดันน้ำในโพรงเพิ่มขึ้นถึง 25 kPa หลังจาก 40 ชั่วโมง จากผลการทดลองพบว่าค่าแรงดันน้ำในโพรงเพิ่มขึ้นถึงค่าวิกฤติเมื่อลาดดินเริ่มวิบัติหรือเคลื่อนตัวไป

4.4.2 ระนาบวิบัติ (slip surface) และแฟกเตอร์ความปลอดภัย (factor of safety, FS)

รูปที่ 16 แสดงค่าความเป็นไปได้ของหน้าดินที่มีการไหลและระดับน้ำใต้ดิน ซึ่งจำลองโดยโปรแกรม SLOPE/W เนื่องจากการเพิ่มขึ้นของค่าแรงยึดเหนี่ยว โดยการเสริมกำลังโดยรากของหญ้าแฝก ซึ่งระนาบวิบัติในกรณีการเสริมกำลังโดยหญ้าแฝกถูกปรับปรุงในบริเวณด้านล่าง โดยเฉพาะในกรณีที่มีการปลูกพืชที่ความลึก 2 เมตร เมื่อเปรียบเทียบการไถลของหน้าดินของลาดดินที่ไม่มีการเสริมกำลัง ซึ่งเกิดมาจากการที่ค่าความเค้นเฉือนของดินและรากที่บริเวณด้านบนมีค่าสูงกว่าดินที่บริเวณด้านล่าง นอกจากนี้ผลการทดลองพบว่าค่าแฟกเตอร์ความปลอดภัย (FS) มีค่าเพิ่มขึ้นเล็กน้อยเมื่อเพิ่มกำลังของลาดดินดังแสดงในตารางที่ 3 จากผลการทดลองพบว่าค่ากำลังรับแรงเฉือนในชั้นดินที่ไม่อิ่มตัวมีค่าลดลงและส่งผลให้ค่า FS ของลาดดินมีค่าลดลงในขณะที่ฝนตก และเมื่อเปรียบเทียบค่า FS ในช่วงระยะเวลาเดียวกันพบว่าค่า FS เพิ่มสูงขึ้นตามความลึกของรากที่ช่วยเสริมกำลังให้ดิน

ตารางที่ 3 ค่าแฟกเตอร์ความปลอดภัยจากการวิเคราะห์เสถียรภาพของลาดดิน

กรณีทดสอบ		วิธีการวิเคราะห์เสถียรภาพ	ระยะเวลาที่ฝนตก (ชม.)		
			18 ชั่วโมง	35 ชั่วโมง	40 ชั่วโมง
ไม่มีการเพิ่มกำลังของลาดดิน		Bishop	1.76	-	-
		Morgenstern-Price	1.77	-	-
มีการเพิ่มกำลังของลาดดิน	ความลึก 1 เมตร	Bishop	2.05	1.82	-
		Morgenstern-Price	2.09	1.87	-
	ความลึก 2 เมตร	Bishop	2.29	2.01	1.89
		Morgenstern-Price	2.31	2.01	1.90

4.5 การเปรียบเทียบผลการทดลองจากแบบจำลองแบบหมุนเหวี่ยงและแบบจำลองเชิงตัวเลข

รูปที่ 17 แสดงการเปรียบเทียบค่าแรงดันน้ำในโพรงจากผลการทดสอบแบบหมุนเหวี่ยงและจากผลการวิเคราะห์แบบเชิงตัวเลข ค่าแรงดันน้ำในโพรงสามารถวัดค่าได้โดย PWP13 และ PWP14 ที่ถูกติดตั้งอยู่ในบริเวณใกล้กับด้านล่างของลาดดิน ค่าแรงดันน้ำที่เพิ่มขึ้นสามารถบ่งชี้ผลของเวลาที่มีต่อการพังทลายของลาดดินดังที่แสดงในตารางที่ 2 การเพิ่มขึ้นของค่าแรงดันน้ำในโพรงในกรณีที่ไม่มีการเสริมกำลังของดินเกิดขึ้นอย่างรวดเร็วเมื่อเทียบกับกรณีที่มีการเสริมกำลัง สำหรับกรณีที่ไม่มีการเสริมกำลัง ค่าแรงดันน้ำในโพรงที่วัดได้จากแบบจำลองแบบหมุนเหวี่ยงมีค่าสูงกว่าการวิเคราะห์เชิงตัวเลข ดังนั้นค่า FS ที่ได้จากการคำนวณด้วยแบบจำลองเชิงตัวเลขจึงมีค่าสูงกว่าที่คาดไว้ ซึ่งอาจเกิดจากการที่ผลของการวิเคราะห์ขึ้นอยู่กับค่าตัวแปรที่นำเข้าและเงื่อนไขขอบ ถึงอย่างไรก็ตามการเปรียบเทียบระหว่างแบบจำลองแบบหมุนเหวี่ยงและแบบจำลองเชิงตัวเลขแสดงความสอดคล้องที่สมเหตุสมผล ยกเว้นค่าที่เป็นลบที่วัดได้จาก PWP14

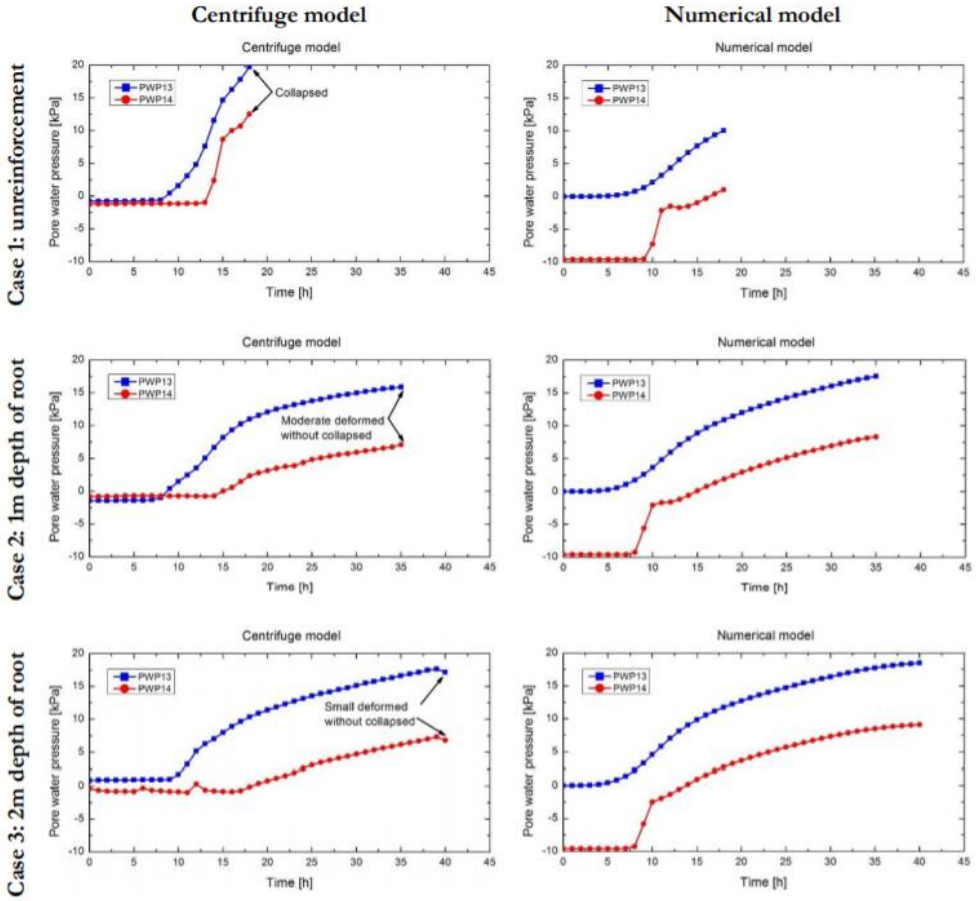

รูปที่ 17 แสดงการเปรียบเทียบค่าแรงดันน้ำในโพรงที่เปลี่ยนแปลงไประหว่างการทดสอบแบบหมุนเหวี่ยงและการวิเคราะห์ด้วยวิธีเชิงตัวเลข

จากการทดลองในครั้งนี้ผลที่ได้จากแบบจำลองทั้งสองทำให้ผู้วิจัยสามารถเข้าใจได้ถึงกระบวนการของระบบรากที่มีส่วนช่วยในการเพิ่มกำลังรับของดินในขณะที่ฝนตก อีกทั้งยังช่วยชะลอการเพิ่มสูงขึ้นของระดับน้ำใต้ดินและทำให้ค่า FS ของลาดดินมีค่าสูงขึ้น

5. สรุป

จากการสังเกตรากหญ้าแฝกพบว่า มีการเจริญเติบโตที่สูงกว่าพืชชนิดอื่นๆ (Lyr and Hoffman, 1967) โดยรากหญ้าแฝกสามารถเจริญลึกลงได้ถึง 200 เซนติเมตรในช่วงปีแรก ผลการทดลองที่ได้จากการทดสอบแรงเฉือนพบว่า รากหญ้าแฝกมีส่วนช่วยในการเพิ่มค่ากำลังรับแรงเฉือนของดินโดยเฉพาะการเพิ่มการยึดติดของดิน ซึ่งผลการทดลองนี้สอดคล้องกับ Ali and Osman (2008) อย่างไรก็ตาม การเพิ่มขึ้นของการยึดเกาะสำหรับการปลูกหญ้าแฝกหนึ่งต้นมีค่าสูงกว่าการปลูกหญ้าแฝกแบบกลุ่มซึ่งอาจเป็นผลมาจากขนาดของตัวอย่าง นอกจากนี้ ผลจากแบบจำลองหมุนเหวี่ยงบ่งชี้ว่า การมีอยู่ของรากบนพื้นผิวของลาดดินมีผลต่อการพังทลายของลาดดิน โดยสามารถเพิ่มเสถียรภาพของลาดดินทั้งในกรณีของการทดสอบระดับน้ำและจำลองปริมาณน้ำฝน ในกรณีของการไหลซึมของน้ำ การเสริมกำลังด้วยรากหญ้าแฝกช่วยในการป้องกันการพังของหน้าดิน นอกจากนี้ ในกรณีของการจำลองปริมาณน้ำฝนยังพบว่า เกิดการเคลื่อนที่ของลาดดินเพียงเล็กน้อย ทั้งยังไม่เกิดการพังทลายเนื่องจากการเสริมกำลังของรากหญ้าแฝก

จากการทดลองในครั้งนี้พบว่า ความยาวและรัศมีของกลุ่มรากเป็นตัวแปรที่สำคัญที่จะช่วยในการป้องกันการพังทลายของลาดดินโดยการเพิ่มการยึดเกาะ นอกจากนี้ ยังพบว่าการวิบัติของลาดดินมีผลจากการเพิ่มขึ้นของระดับน้ำใต้ดิน และเริ่มมีการเปลี่ยนแปลงจากด้านล่างของลาดดิน การเพิ่มขึ้นของค่าแรงดันน้ำในโพรงส่งผลให้ค่าความเค้นประสิทธิผล และค่ากำลังรับแรงเฉือนของดินมีค่าลดลง การประยุกต์ใช้เส้นใยประเภทโพลีเอสเตอร์เพื่อจำลองการเสริมกำลังโดยรากบนลาดดินพบว่ารากพืชมีส่วนช่วยในการป้องกันการแตกของหน้าดิน ช่วยชะลอการซึมของน้ำฝนและชะลอการเพิ่มระดับของน้ำใต้ดิน อีกทั้งความลึกของรากสามารถเพิ่มกำลังของดินบริเวณที่เสริมแรงและลดการเกิดการเคลื่อนที่ของลาดดินได้ ผลการทดลองที่ได้จากแบบจำลองหมุนเหวี่ยงสอดคล้องกับผลการวิเคราะห์จากแบบจำลองเชิงตัวเลข ซึ่งแฟกเตอร์ความปลอดภัยที่ได้มีค่าสูงขึ้นเมื่อความยาวของรากเพิ่มขึ้น การผสมดินกับเส้นใยของรากเพิ่มค่ากำลังรับแรงเฉือนของดิน ซึ่งทำให้สรุปได้ว่ารากหญ้าแฝกสามารถใช้ในการปรับปรุงเสถียรภาพของดินได้

6. เอกสารอ้างอิง

Ali, F.H., Osman, N., 2008. Shear strength of a soil containing vegetation roots. Soils Found. 48(4), 587–596.

Alsheimer, L., Hughes, B.O., 2007. “Ch 4 – Black and White in Photoshop” Black and White in Photoshop CS3 and Photoshop Light room: Create Stunning Monochromatic Images in Photoshop CS3, Photoshop Light-room, and Beyond. Elsevier 91–139.

Eab, K.H., Takahashi, A., Likitlersuang, S., 2014. Centrifuge modelling of root-reinforced soil slope subjected to rainfall infiltration. Geotech. Lett. 4, 211–216.

Kaewsaeng, W., 2000. Engineering Properties of Weathered Clay Soil Reinforced with Prachuap Khiri Khan Vetiveria memoralis A. Camus Root for Slope Protection (Thesis report). King Mongkut's University of Technology, Thonburi, Thailand.

Sonnenberg, R., Bransby, M.F., Hallett, P.D., Bengough, A.G., Mickovski, S.B., Davies, M.C.R., 2010. Centrifuge modelling of soil slopes reinforced with vegetation. Can. Geotech. J. 47, 1415–1430.

Takahashi, A., Nakamura, K., Likitlersuang, S., 2014. On the seepage-induce failure of vegetation-stabilised slopes. In: C. Gaudin, D. White (Eds.), Pro-ceedings of the 8th International Conference on the Physical Modelling in Geotechnic. Taylor&Francis Group, London, pp.1233–1239. ISBN:978-1-138-00152-7.

Lyr, H., Hoffmann, G., 1967. Growth rates and growth periodicity of tree roots. Int. Rev. For. Res. 2, 181–236.

Output จากโครงการวิจัยที่ได้รับทุนจาก สกว.

1. ผลงานตีพิมพ์ในวารสารวิชาการนานาชาติ (ระบุชื่อผู้แต่ง ชื่อเรื่อง ชื่อวารสาร ปี เล่มที่ เลขที่ และหน้า) หรือผลงานตามที่คาดไว้ในสัญญาโครงการ

1.1 ชื่อเรื่อง Laboratory and modelling investigation of root-reinforced system for slope stabilisation

วารสาร Soils and Foundation

ปี 2015 ฉบับ Vol. 55, No. 5 หน้า 1270 – 1281

Eab, K.H., Likitlersuang, S. and Takahashi, A. (2015) “Laboratory and modelling investigation of root-reinforced system for slope stabilisation” Soils and Foundations, Vol. 55, No. 5, pp. 1270–1281. DOI:10.1016/j.sandf.2015.09.025 (IF2017 = 1.599)

1.2 ชื่อเรื่อง Laboratory investigation of the performances of cement and fly ash modified asphalt concrete mixtures

วารสาร International Journal of Pavement Research and Technology

ปี 2016 ฉบับ Vol. 9, No. 5 หน้า 337 – 344

Likitlersuang, S. and Chompoorat, T. (2016) “Laboratory investigation of the performances of cement and fly ash modified asphalt concrete mixtures” International Journal of Pavement Research and Technology, Vol. 9, No. 5, pp. 337–344. DOI:10.1016/j.ijprt.2016.08.002 (SCOPUS)

1.3 ชื่อเรื่อง Modeling of Root-reinforced Soil Slope under Rainfall Condition

วารสาร Engineering Journal

Likitlersuang, S., Takahashi, A. and Eab, K.H. (2017) “Modeling of Root-reinforced Soil Slope under Rainfall Condition” Engineering Journal, Vol. 21, No. 3, pp. 123–132. DOI: 10.4186/ej.2017.21.3 (SCOPUS, ESIC)

1.4 ชื่อเรื่อง Deformation characteristics and stress responses of cement-treated expansive clay under confined one-dimensional swelling

วารสาร Applied Clay Sciences

Por, S., Nishimura S. and Likitlersuang, S. (2017) “Deformation characteristics and stress responses of cement-treated expansive clay under confined one-dimensional

swelling" Applied Clay Sciences, Vol. 146, pp. 316 – 324 DOI:10.1016/j.clay.2017.06.022 (IF2017 = 3.641)

1.5 ชื่อเรื่อง Influence of the spatial variability of shear strength parameters on rainfall induced landslides: a case study of sandstone slope in japan
วารสาร Arabian Journal of Geosciences
Nguyen T.S., Likitlersuang, S., Ohtsu H. and Kitaoka, T. (2017) "Influence of the spatial variability of shear strength parameters on rainfall induced landslides: a case study of sandstone slope in japan" Arabian Journal of Geosciences, Vol. 10, Issue 16, Article 369, pp. 1 – 12 DOI:10.1007/s12517-017-3158-y (IF2017 = 0.860)

1.6 ชื่อเรื่อง Underground excavation behaviour in Bangkok using three-dimensional finite element method
วารสาร Computers and Geotechnics
Chheng, C. and Likitlersuang, S. (2018) "Underground excavation behaviour in Bangkok using three-dimensional finite element method" Computers and Geotechnics Vol. 95, March, pp. 68-81. DOI:10.1016/j.compgeo.2017.09.016 (IF2017 = 3.138)

1.7 ชื่อเรื่อง Stability analysis of vegetated residual soil slope under rainfall conditions
วารสาร Environmental Geotechnics
Nguyen, T.S., Likitlersuang, S. and Jorisankasa (2018) "Stability analysis of vegetated residual soil slope in Thailand under rainfall conditions" Environmental Geotechnics (Ahead of print) DOI:10.1680/jenge.17.00025 (IF2017 = 1.200)

2. การนำผลงานวิจัยไปใช้ประโยชน์
2.1 เชิงพาณิชย์ (มีการนำไปผลิต/ขาย/ก่อให้เกิดรายได้ หรือมีการนำไปประยุกต์ใช้โดยภาคธุรกิจ/บุคคลทั่วไป): สามารถส่งเสริมให้เกษตรกรหรือชุมชนท้องถิ่นการใช้หญ้าแฝกในการป้องกันภัยดินถล่มโดยผ่านองค์ความรู้ที่ดำเนินการวิจัย
2.2 เชิงนโยบาย (มีการกำหนดนโยบายอิงงานวิจัย/เกิดมาตรการใหม่/เปลี่ยนแปลงระเบียบข้อบังคับหรือวิธีทำงาน): อาจสามารถผลักดันเพื่อส่งเสริมการใช้หญ้าแฝกในการป้องกันภัยดินถล่มในเชิงนโยบายผ่านหน่วยงานภาครัฐที่เกี่ยวข้อง เช่น กรมพัฒนาที่ดิน กรมทรัพยากรธรณี หรือ กรมป้องกันและบรรเทาสาธารณภัย
2.3 เชิงสาธารณะ (มีเครือข่ายความร่วมมือ/สร้างกระแสความสนใจในวงกว้าง): สร้างเครือข่ายความร่วมมือกับหน่วยงานภาครัฐและเอกชนที่ให้การสนับสนุนการนำหญ้าแฝกไปใช้ป้องกันเสถียรภาพของลาดดิน เช่น มหาวิทยาลัยเกษตรศาสตร์ มูลนิธิชัยพัฒนา มูลนิธิพลังที่ยั่งยืน

2.4 เชิงวิชาการ (มีการพัฒนาการเรียนการสอน/สร้างนักวิจัยใหม่): มีการนำเอาองค์ความรู้ไปใช้ในการเรียนการสอนระดับชั้นป.ตรี และเป็นหัวข้องานวิจัยที่เป็นส่วนหนึ่งของหัวข้อวิทยานิพนธ์ในระดับบัณฑิตศึกษคือ

- นายอดิเทพ วังบุญคง นิสิตปริญญาโท หัวข้อวิทยานิพนธ์ “การศึกษาพฤติกรรมการเสริมแรงของรากพืชเพื่อป้องกันการพังทลายของลาดดิน” จบการศึกษา พฤษภาคม พ.ศ.2557
- นายเกร็งฮัฟ เอบ นิสิตปริญญาเอก หัวข้อวิทยานิพนธ์ “กลไกวิศวกรรมชีวภาพดินสำหรับการเพิ่มเสถียรภาพลาดดินในสภาวะไม่อิ่มตัวด้วยน้ำ” จบการศึกษา สิงหาคม พ.ศ.2558
- นายกิตติคุณ คงอยู่ นิสิตปริญญาโท หัวข้อวิทยานิพนธ์ “การศึกษาปรับปรุงคันดินทดสอบด้วยวัสดุใยสังเคราะห์ผสมซีเมนต์และหญ้าแฝกเพื่อควบคุมการกัดเซาะ” กำลังศึกษา

3. อื่นๆ (เช่น ผลงานตีพิมพ์ในวารสารวิชาการในประเทศ การเสนอผลงานในที่ประชุมวิชาการ หนังสือ การจดสิทธิบัตร)

การเสนอผลงานในที่ประชุมวิชาการ:

<u>ระดับชาติ</u>

- อดิเทพ วังบุญคง นวพล คำคง ธนกร คำเฝ้า และ สุเชษฐ์ ลิขิตเลอสรวง (2556), “การศึกษาพฤติกรรมด้านกำลังของรากหญ้าแฝกสำหรับป้องกันการพังทลายของลาดดิน” เอกสารการประชุมวิชาการวิศวกรรมโยธาแห่งชาติครั้งที่ 18 ระหว่าง 8 – 10 พฤษภาคม 2556 เล่มที่ 1 หน้าที่ GTE 51 – 54 จัดโดยมหาวิทยาลัยเชียงใหม่ โรงแรมดิเอ็มเพรส เชียงใหม่
- กิตติคุณ คงอยู่ และ สุเชษฐ์ ลิขิตเลอสรวง (2561), “การตรวจวัดการกัดเซาะหน้าดินระยะสั้นจากคันดินทดสอบที่ปรับปรุงด้วยวัสดุซีเมนต์ใยสังเคราะห์และหญ้าแฝกภายใต้การกระทำของน้ำฝน” เอกสารการประชุมวิชาการวิศวกรรมโยธาแห่งชาติครั้งที่ 23 ระหว่าง 18 – 20 กรกฎาคม 2561 จัดโดยโรงเรียนนายร้อยพระจุลจอมเกล้า และมหาวิทยาลัยศรีนครินทรวิโรฒ ณ หอประชุม โรงเรียนนายร้อยพระจุลจอมเกล้า อำเภอเมือง จังหวัดนครนายก (*ได้รับรางวัลบทความดีเด่น)

<u>ระดับนานาชาติ</u>

- Vangbunkong, A., Likitlersuang, S. and Takahashi, A. (2013), “Inversitgation of Root Induced Shear Strength of Vetiver Grass Reinforced Soil”, Proceeding of the 26th KKHTCNN Symposium on Civil Engineering, November 18 - 20, 2013, Singapore.
- Eab, K.H., Likitlersuang, S. and Takahashi, A. (2014) “Assessing the Effect of Vegetation to Slope Stability using Limit Equilibrium Analysis” Proceeding of the

27th KKHTCNN Symposium on Civil Engineering, November 9 - 12, 2014, Shanghai, China.

- Likitlersuang, S., Lohwongwatana. B., Vanno, S., and Boonyananta, S. (2015) "Laboratory Investigation of Vetiver Root Reinforcement for Slope Protection" Proceeding of the 6th International Conference on Vetiver, May 5-8, 2015, Da Nang, Vietnam. (*Awarded Certificate of Excellence the King of Thailand Vetiver Awards 2015 – An Outstanding Research in the Field of Non-agricultural Application)
- Kounyou, K. and Likitlersuang, S. (2016) "A study of test embankment improved by geosynthetic cementitious composite mat and vetiver grass on surface erosion" the 30th KKHTCNN Symposium on Civil engineering, November 2 – 4, 2017, Taipei, Taiwan
- Wasino, R., Junjaroen, D.S. and Likitlersuang, S. (2016) "Investigation of the extraction of heavy metals (Pb, Zn, and Cd) from contaminated soils by vetiver" the 30th KKHTCNN Symposium on Civil engineering, November 2 – 4, 2017, Taipei, Taiwan

Soils and Foundations 2015;55(5):1271–1282

The Japanese Geotechnical Society

Soils and Foundations

www.sciencedirect.com
journal homepage: www.elsevier.com/locate/sandf

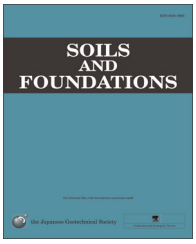

Laboratory and modelling investigation of root-reinforced system for slope stabilisation

Kreng Hav Eab[a], Suched Likitlersuang[c,*], Akihiro Takahashi[b]

[a]Department of Civil Engineering, Faculty of Engineering, Chulalongkorn University, Bangkok 10330, Thailand
[b]Department of Civil Engineering, Tokyo Institute of Technology, Tokyo, Japan
[c]Geotechnical Research Unit, Department of Civil Engineering, Faculty of Engineering, Chulalongkorn University, Bangkok 10330, Thailand

Received 23 June 2013; received in revised form 13 May 2015; accepted 23 June 2015

Abstract

Most natural slope failures are induced by seepage and/or rainfall. Soil bioengineering is an environmentally friendly method which employs vegetation to reinforce the soil in sloping terrain. The vegetation can contribute to slope stability in two ways, mechanical and hydrological. This paper demonstrates the effect of a vegetation root matrix on a soil slope and focuses on mechanical reinforcement using an example of vetiver grass. Vetiver grass (*Vetiveria nemoralis A. Camus*) specimens, grown for under a year, were used in this study. The investigation programme includes root observations, direct shear tests and centrifuge model tests. The growing rate of the vetiver roots and the root area ratios were observed during the tests. The cohesion and angle of internal friction of root-reinforced soils were determined from a standard direct shear apparatus and a large direct shear apparatus. A series of centrifuge tests was carried out to demonstrate the effect of vegetation on seepage- and rainfall-induced slope failures. The results indicate that the vetiver roots showed rapid growth within a year and that the shear strength of the root-reinforced soil was significantly increased by the bundle of roots. The results also reveal that the bundle of root fibres in the centrifuge model tests helped to reduce the deformation of the soil slope due to instability by increasing the shear strength of the slope.

Keywords: Centrifuge modelling; Laboratory tests; Slopes; Vegetation

1. Introduction

Landslides are one of the most widespread earth processes which involve the failure of sloping earth material. Landslides are considered to be one of the most important problems in geotechnical engineering. This is because landslides are usually among the most costly natural disasters in terms of human fatalities and economic loss. In recent years, natural slope instability has increased especially in tropical monsoon zones, such as Southeast Asian countries. There are several factors that can cause natural slope failures, such as geological activity, hydrological influence and human interference, but seepage and rainfall are the main factors. The infiltration of rain water can cause a rise in the groundwater level and an increase in pore water pressure or a decrease in the matric suction of the soil. In addition, the physical process of rainfall infiltration into the ground and its seepage through the soil layers have been studied by hydrogeologists, soil scientists and geotechnical engineers (Ng and Shi, 1998).

To increase slope stability, several methods have been used, such as soil nails, retaining structures, geosynthetic

*Corresponding author.
E-mail addresses: krenghav_eab@yahoo.com (K.H. Eab), fceslk@eng.chula.ac.th (S. Likitlersuang), takihiro@cv.titech.ac.jp (A. Takahashi).
Peer review under responsibility of The Japanese Geotechnical Society.

http://dx.doi.org/10.1016/j.sandf.2015.09.025

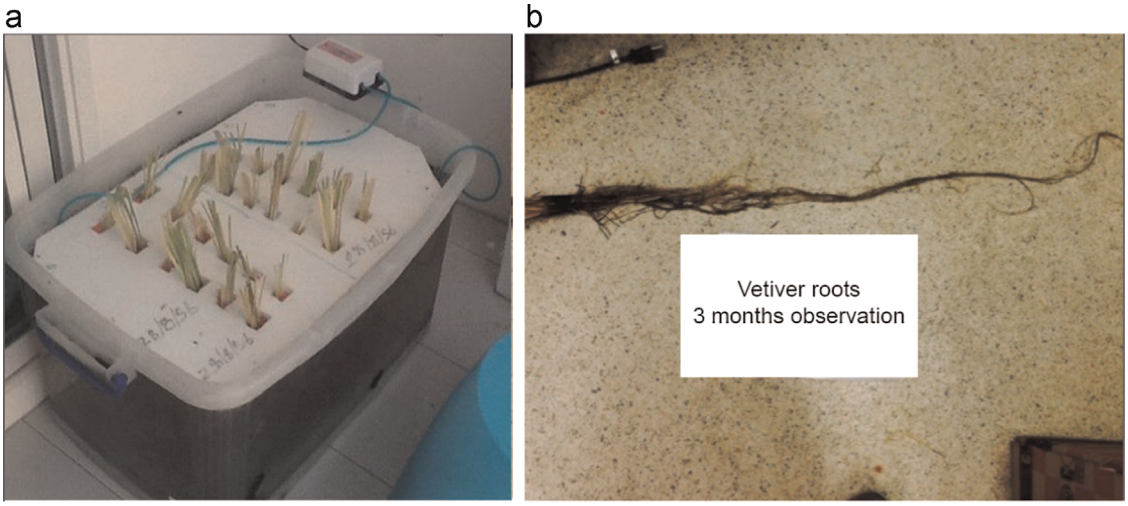

Fig. 1. (a) Vetiver specimens grown in hydroponic conditions and (b) root observation.

Table 1
Chemical test results of planted soil.

Test	Value	Level
Alkaline–acidity (pH)	6.7	Medium
Organic (O)	12.13%	High
Phosphorus (P)	61 mg/kg	High
Calcium (Ca)	7859 mg/kg	High
Magnesium (Mg)	974 mg/kg	High
Potassium (K)	1996 mg/kg	Very high

reinforcements and shotcrete. However, these methods are costly and may not be suitable for natural slopes. In ancient times, the use of vegetation in soil slopes and earthen covers for landfill was well recognised, and it is still well-known that the effect of vegetation plays an important role in increasing soil slope stability. Soil bioengineering is an environmentally friendly alternative that uses vegetation for improving slope failure. There are two main contributions whereby vegetation can affect slope stability, i.e., hydrological and mechanical processes. Firstly, changing the soil moisture regime and drawing the water from the soil via evapotranspiration (Ali and Osman, 2008) can increase soil suction. Secondly, the roots of vegetation can enhance slope stability by increasing the shear strength of the soil (Gray and Sotir, 1996; Wu et al., 1979). The role of vegetation in slope stability has been defined by Greenway (1978), Coppin and Richards (1990) and Wu (1995). In addition, this method is applied to prevent shallow failure as well as soil surface erosion in natural slopes.

Vetiver grass (*Vetiveria nemoralis A. Camus*), was promoted to help prevent soil erosion and water runoff or infiltration by the World Bank in the 1980s, and is important in soil bioengineering (Greenfield, 1996). Recently, the Chaipattana Foundation and the Office of the Royal Development Projects Board, Thailand, have promoted the use of vetiver grass for soil and water conservation for many royal projects in Thailand. Vetiver grass is fast growing and requires low maintenance. The length of vetiver roots has been seen to grow up to 2–3.5 m (Chinapan et al., 1997). Vetiver roots can penetrate deep into the ground to form a net-like barrier capable of filtering silt and containing top soil. Normally, shallow failure is a typical failure mode of soil slopes in regions with prolonged and heavy rainfall; it always occurs 1–1.5 m in depth from the surface (Gray and Leiser, 1982). Hence, shallow failure of natural slopes could be prevented by the rooting depth of the vetiver grass which interlocks with the soil particles. Previous research has investigated the tensile root strength properties of vetiver grass for resisting shallow failure and superficial erosion (Hengchaovanich and Nilaweera, 1998).

Recently, the stability of model soil slopes that were reinforced by plant roots has been investigated by Sonnenberg et al. (2010) at 15*g* using a centrifuge. By continuously raising the groundwater table in model slopes, contributions of mechanical root reinforcement were back-analysed based on observed slip surfaces at failure. Takahashi et al. (2014) studied the effect of vegetation structures on seepage-induced slope failure using a 50*g* centrifuge model. Eab et al. (2014) continued the study of Takahashi et al. (2014) focusing on a root-reinforced slope subjected to rainfall infiltration using a rainfall simulator in the centrifuge.

The aim of this paper is to present an investigation programme of the vetiver root-reinforced system for slope stabilisation using a laboratory technique. The shear strength parameters of root-reinforced soils were determined using standard direct shear tests for single vetiver and large direct shear tests for a group of vetiver. The growing rate of the vetiver roots and the root-area ratios were observed by direct measurement and an image processing technique, respectively. Finally, a series of centrifuge model tests using a seepage and rainfall simulator to demonstrate the effectiveness of roots in shallow depths against slope instability was also performed.

2. Experimental investigation

In the soil bioengineering approach, the selection of suitable vegetation is the first important step. Vetiver grasses have been

selected based on the type of soil and the type of environment which could help them survive for a long period of time. Thailand's Land Development Department (LDD, 1998) suggested that the roots of vetiver grass can penetrate deep into the ground and that vetiver grass is suitable for arid areas. However, research on the engineering aspects of vetiver grass is still limited and on-going. In this study, observations of vetiver grasses have been performed in both field and laboratory tests. In the field, vetiver grasses were planted along a slope to observe the rate of growing and to make a comparison with the vetiver specimens grown in the laboratory. In the laboratory, the vetiver specimens were grown under three conditions: (1) vetiver specimens grown under hydroponic conditions; (2) a single vetiver specimen planted in a cylindrical container; and (3) a group of vetiver specimens planted in a cubic box.

2.1. Vetiver specimen preparation

In this study, the vetiver specimens were grown under three conditions. The first condition is hydroponics. Twelve identical single vetiver specimens were grown in a container with a liquid nutrient (without soil). An air pump was also installed in the container to provide oxygen, as shown in Fig. 1(a). This experiment was used to investigate the growing rate of vetiver roots without destroying the roots. Measurements were taken continuously, for over 6 months, of the length of the root and the radius of the root bundle for each specimen (Fig. 1(b)).

For the second and third conditions, the vetiver grasses were grown in soil. The soil used in this study was collected from a typical slope area. The chemical properties of the soil were tested and are reported in Table 1. The results show that the various nutrients remained relatively high and were similar to those used for planting purposes. In other words, this kind of soil can be used for cultivation on agriculture land. The single vetiver specimens were planted in plastic bags and placed in PVC tubes, having a diameter of 150 mm and a length of 600 mm, in preparation for the standard direct shear tests. Fig. 2(a) shows a schematic of planting vetiver grass for single specimens. Four samples were prepared by cutting at the upper part from the up–down direction with a thickness of 20 mm for each tested sample to fit the direct shear box, as shown in Figs. 2(a) and 3(a).

For the group specimens, the vetiver grasses were grown by planting them in a 300-mm^3 wooden box. Nine vetiver specimens were planted with a spacing of 75 mm, as shown in Fig. 2(b). These group vetiver specimens were prepared for the large direct shear tests. Three samples were prepared for the tests by trimming them to fit the large direct shear mould, 300 mm × 300 mm × 200 mm, as shown in Fig. 3(b). In addition, this group of vetiver grass specimens was prepared for image processing to define the root area ratio as well. It is noted that the group vetiver specimens were planted in the same soil which was used for the single vetiver specimens.

2.2. Vetiver root observation

Fig. 4 presents the average values for the root length and the root bundle diameter from the hydroponic vetiver specimens. The results have been observed and measured continuously for 2–6 months. The relationship between the length of the roots and the radius of the root bundle is shown in Fig. 4(a). The growing rate of the roots can be determined from a plot of the length of the roots with respect to time, as shown in Fig. 4(b). According to the results, it is indicated that the roots of the grass have spread the radius of the root bundle up to 1.7 cm (Fig. 4(a)) and that the roots can grow up to 180 cm within 6 months (b). The average growth rate of roots is approximately 30 cm/month. As shown on the plot in Fig. 4(b), the current study has shown a slightly higher growth rate of

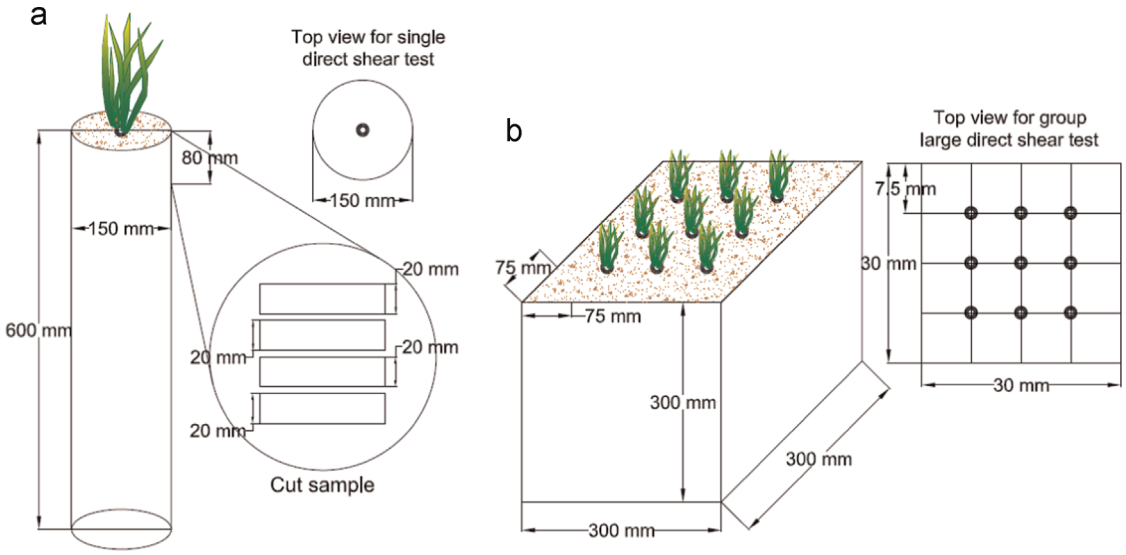

Fig. 2. Vetiver grass specimens prepared for shear tests: (a) 4-month-old single vetiver grass for standard shear tests and (b) 6-month-old group vetiver grass for large direct shear tests.

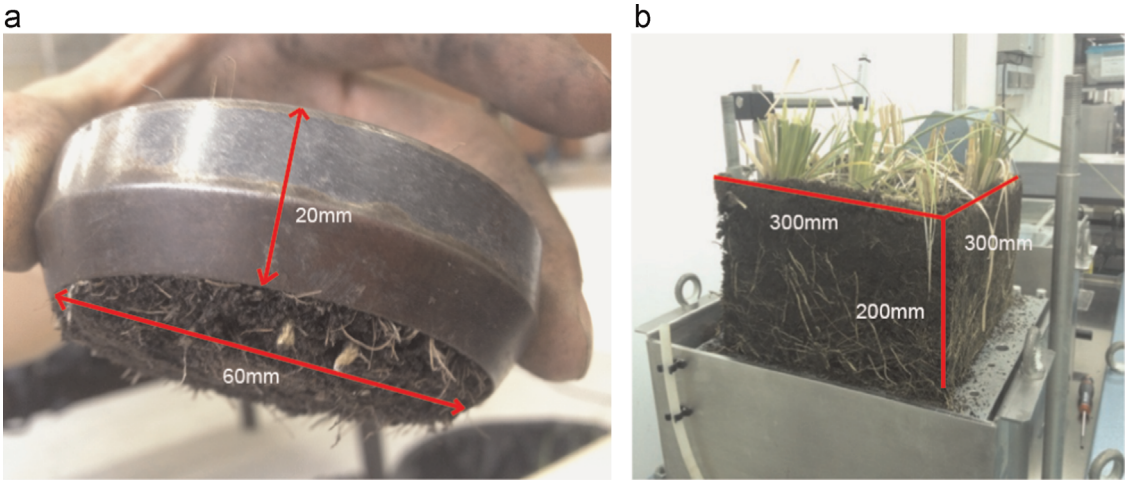

Fig. 3. Tested samples for direct shear tests: (a) 60-mm-diameter direct shear apparatus and (b) 300 mm × 300 mm large direct shear apparatus.

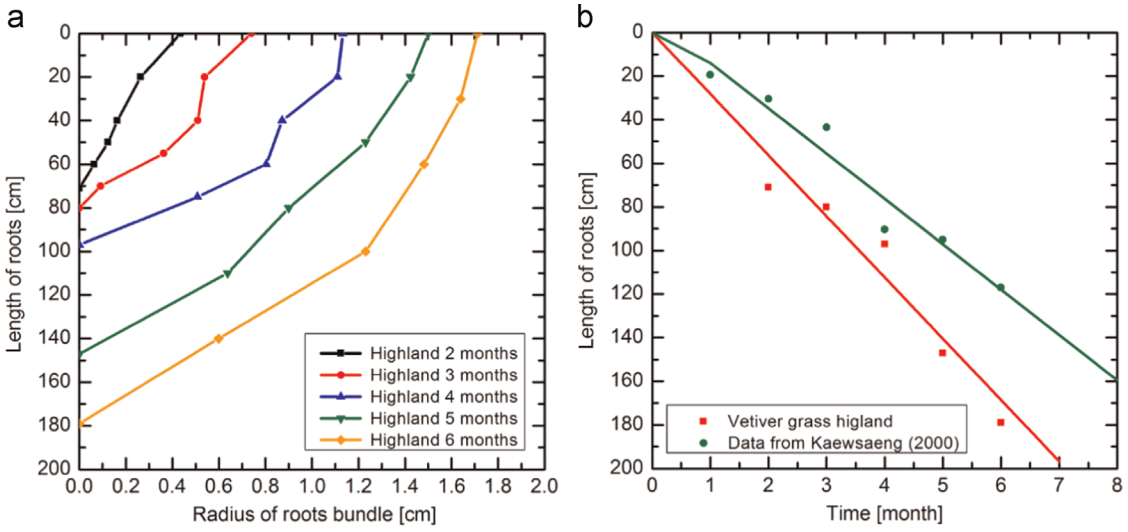

Fig. 4. Average values for vetiver root measurements: (a) relationship between length of roots and radius of root bundle and (b) growing rate of roots.

vetiver compared to that in the data by Kaewsaeng (2000). The difference is probably caused by the planting conditions and the measurement methods. The data by Kaewsaeng (2000) were taken from the specimens planted in soil and measurements of the roots required the removal of the plant.

Moreover, observations of the group vetiver roots can be defined by a root area ratio. The term root area ratio refers to the fraction of the total cross-sectional area of a soil that is occupied by roots (Gary and Sotir, 1996). The root area ratio plays an important role in the contribution of the root fibres to the shear strength when it is directly defined by the cross-sectional area in the shear plane. However, the root area ratio measured in the plane perpendicular to the root-growth direction is really difficult to determine and it varies with depth. The parallel plane measurement of the root area ratio, which is easier to observe and represents an average of the root fibre contribution in the soil, was used in this study. Alsheimer and Hughes (2007) have reported the technique of using image processing to observe root distribution in a large direct shear specimen. Photographs of roots and soil were taken with a digital camera and transferred to binary images via the histogram function of Photoshop software. The black and white pixels of the images could be distinguishably counted between the soil and the roots. The ratio between the pixels of the roots and the total pixels can be loosely defined as the root area ratio. The results show that the average root area ratio of the group vetiver at 4 months and 6 months are 2.44% and 4.37%, respectively. Fig. 5(b) shows the binary image for the method used to estimate the root area ratio based on the colour in the image. For example, the white and black colours represent the soil and the void space, respectively, while the grey colour represents the root area. Hence, the root area ratio can be determined by the total pixels of the roots and the total pixels. The root area ratio for the 6-month group vetiver root was 4.56% (Fig. 5).

2.3. Shear strength of vetiver roots

In this study, the reinforcements of the vetiver root system were studied using direct shear tests in the laboratory.

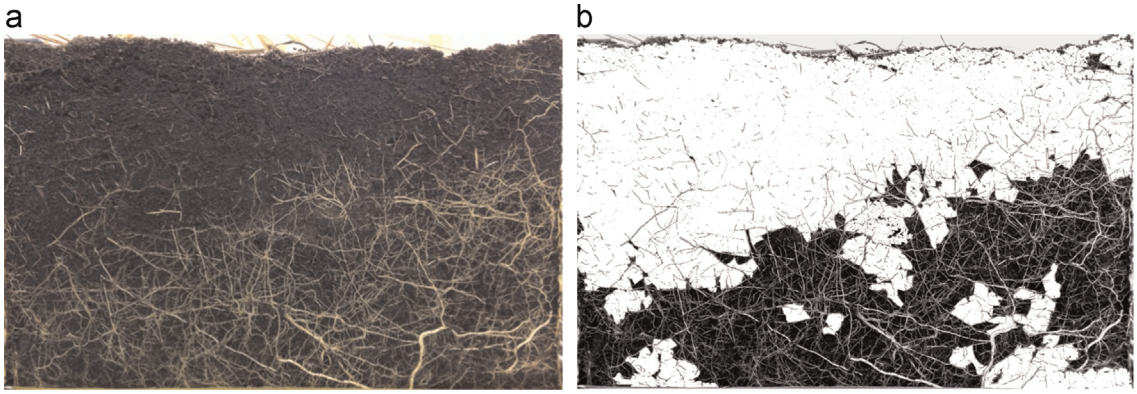

Fig. 5. Determination of root area ratio: (a) root photograph taken from 6-month group vetiver and (b) binary image with results of root area ratio of 4.56%.

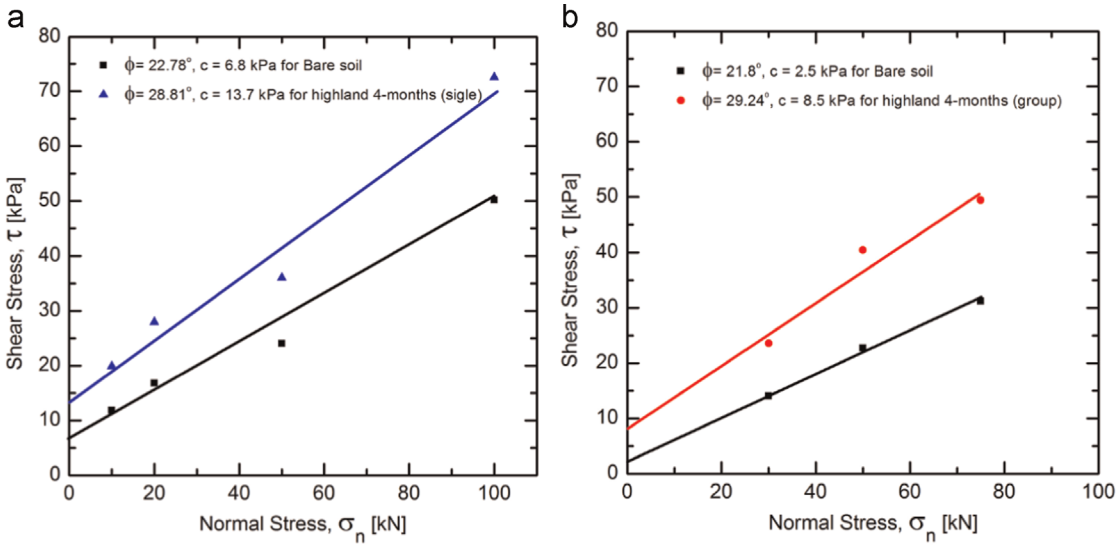

Fig. 6. Shear strength of roots with soil: (a) 4-month-old single vetiver from direct shear tests and (b) 6-month-old group vetiver from large direct shear tests.

Laboratory tests were chosen instead of field tests; hence, the vetiver sample could be simply prepared and the density and the water content of the soil could be controlled between 20% and 25% for the bare soil and vetiver grass specimens. This could minimise the effect of the differences in matric suction during the tests. Two types of specimens were prepared in this study, i.e., single and group vetiver. Four-month-old single vetiver specimens (Fig. 2(a)) were prepared for the standard direct shear tests. On the other hand, six-month-old group vetiver specimens (Fig. 2(b)) were prepared for the large direct shear tests. To observe the increase in shear strength from the vetiver-root reinforcement, bare soil with the same density and water content for the four-month and six-month specimens were prepared for the direct shear tests as well.

Four-month-old single vetiver grass was individually prepared in the cylindrical plastic bags and put into PVC tubes to ensure that the roots of the vetiver could grow vertically into the soil, as shown in Fig. 2(a). A 60-mm-diameter cylindrical mould was used to perform the direct shear tests for the four-month-old single specimens, as shown in Fig. 3(a). The tests were performed by following the ASTM D3080 (1998) (similar to JGS 0561) standard with the shear rate of 1.5 mm/min. Normal stress rates of 10, 20, 50 and 100 kPa were applied for each test. All specimens were sheared until they reached the peak point, started showing fairly constant shear stress or a maximum horizontal displacement of 6 mm. The shear strength of the four-month-old vetiver root reinforced soil and the bare soil was obtained as presented in Fig. 6 (a). The cohesion intercept and the friction angle were determined according to the Mohr–Coulomb failure criterion, as presented in Table 2. The presence of the vetiver roots has improved the strength of the soil. As a result, the vetiver grass was able to increase the cohesion of shear strength by almost 7 kPa. Ali and Osman (2008) reported the increase in cohesion of the shear strength of soil by vetiver roots. The results show that the cohesion of the soil was increased to around 11 kPa from the average values for a rooted zone 1 m in depth.

Six-month-old vetiver grass was prepared as a group specimen in the cubic box, as shown in Fig. 2(b). The large direct shear apparatus was chosen to perform direct shear tests for the group vetiver specimens, as shown in Fig. 3(b). The tests were performed following the ASTM D3080 (1998) standard. Normal stress rates of 30, 50 and 75 kPa were applied by the hydraulic pressure system. The side friction between the

Table 2
Results of direct shear tests.

Test	Specimen	Shear strength parameters	Increase in cohesion (kPa)
Standard direct shear test	Bare soil	$c=6.8$ kPa; $\phi=22.8^\circ$	6.8
	4-Month-old single vetiver	$c=13.6$ kPa; $\phi=29.7^\circ$	
Large direct shear test	Bare soil	$c=2.5$ kPa; $\phi=21.8^\circ$	6.0
	6-Month-old group vetiver	$c=8.5$ kPa; $\phi=29.2^\circ$	

sample and the shear box was minimised by applying some oil. All the data from the displacement transducer and the load cell were acquired by an automatic data logging system. All samples were sheared to reach the maximum horizontal displacement at 50 mm. The large direct shear test results are plotted in Fig. 6(b). The friction angles were determined based on the Mohr–Coulomb failure criterion as presented in Table 2.

According to the results, the increase in cohesion of the soil for the single vetiver specimen was higher than the group specimen (see Table 2). The difference is probably caused by the contribution of the Vetiver root loosely defined by the root area ratio. In addition, another difference is also caused by the scale effect of the tests. Cerato and Lutenegger (2006) have reported the results of tests using three different specimen sizes and the scale effect of direct shear tests on sands. Their results indicate that the friction angle decreases as the specimen size increases.

3. Centrifuge modelling

Centrifuge modelling is a physical model test that is now widely used in geotechnical research or design. Since slope stability is a gravity-dependent problem, the major advantage of using centrifuge modelling is to enable researchers to test reduced-scale physical models at the correct stress level by increasing the g-level (Taylor, 1995). The centrifuge facility at the Tokyo Institute of Technology was used for this study. The soil slope models were prepared in a steel box. In this study, a 50*g* centrifugal acceleration was used to model the slope stability problem. Two types of tests were conducted: (1) seepage tests and (2) rainfall tests. A brief summary of the experimental details are given in the following sections.

3.1. Properties of materials used in the model

According to JGS0051 (a Japan Geotechnical Society standard), Edosaki sand is defined as a fine sand and was employed to prepare the slope models. The grain size distribution curve of Edosaki sand is shown in Fig. 7 and its

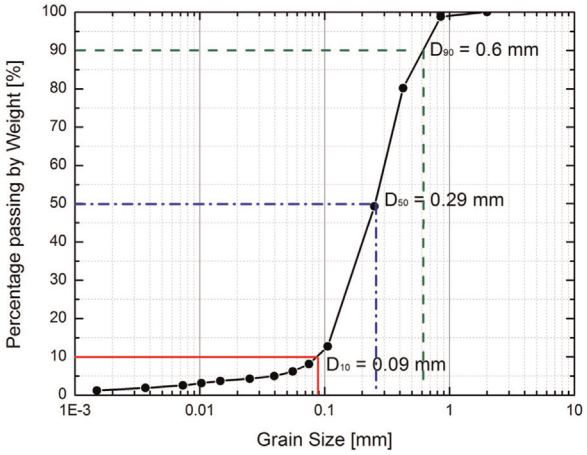

Fig. 7. Grain size distribution curve of Edosaki sand.

Table 3
Properties of compacted soils used in centrifuge models.

Soil type	Edosaki sand	Edosaki sand+1% by mass of fishing line	Edosaki sand+2% by mass of polyester fibre
Specific gravity, G_s	2.65	–	–
Maximum dry unit weight, γ_d (kN/m^3)	12.9	13.5	12.9
Optimum water content, w_{opt} (%)	15.2	15.8	17.3
Total unit weight, γ_t (kN/m^3)	14.9	15.4	15.2
Cohesion intercept, c (kPa)	4.8	6.2	18.9
Angle of shearing resistance, ϕ (deg)	28.6	36.5	31.5

engineering properties are described in Table 3. Two types of fibre were used in this study: (1) a fishing line with a diameter of 0.33 mm and a length of 10 mm and (2) polyester fibre (Teijin RA04FN, size of 17 dtex) with a diameter of 39 μm and a length of 10 mm. In the model tests, the 1% by mass (approximately 3% by volume) of the 20-mm-deep fishing line, mixed with sand in model scale equivalent to 1 m in prototype scale, was able to represent the 4-month-old vertiver grass, as shown in Fig. 4. Similarly, the 2% by mass (around 7% by volume) of the polyester fibre, with a depth of 40 mm and mixed in model scale equivalent to 2 m in prototype scale, was able to represent the 6-month-old vetiver grass. It is noted that the values of 3–7% by volume are slightly higher than the root area ratio of 4.56% observed from the 6-month-old vetiver group specimen. However, it is still comparable to the typical values for the root area ratio of 3–5% for other small vegetations observed in literatures (Wu, 1995; Gary and Sotir, 1996). Fig. 8 presents photos of the fishing line and the polyester fibre before and after being mixed with the sandy soil. The engineering properties of the soil mixed with 1% fishing line and 2% polyester fibre are also summarised in Table 3.

The shear strength of the soils was examined by standard direct box shear tests. The soil specimen was prepared in a

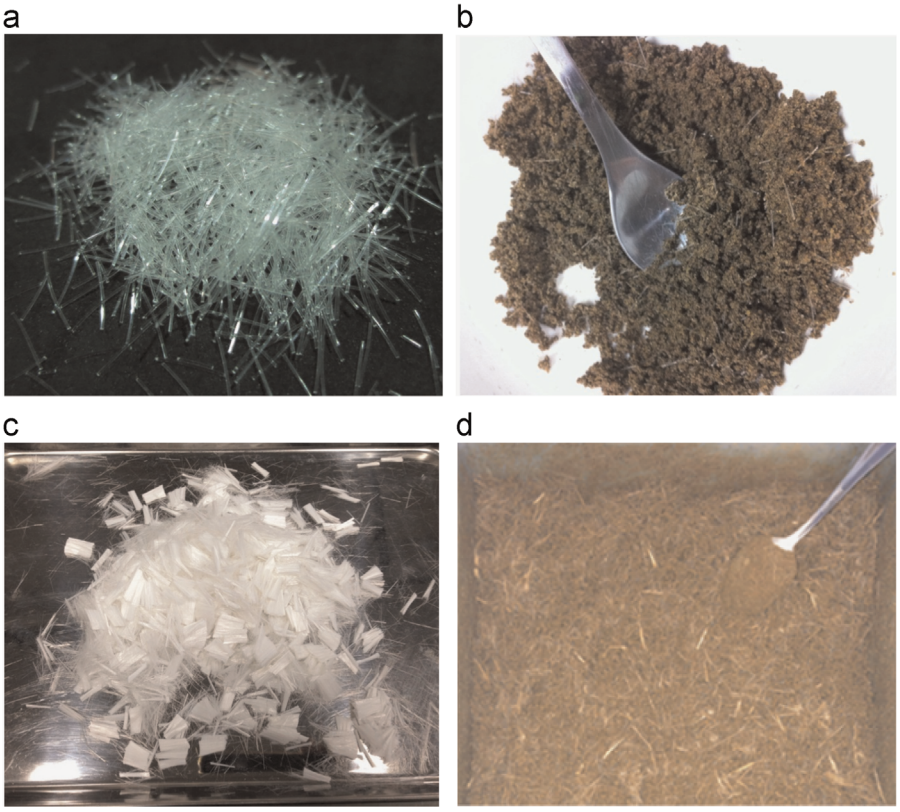

Fig. 8. Photos of fibre before and after mixing: (a) 1% by mass of finishing line and (c) 2% by mass of polyester. (a) Before mixing fishing line, (b) after mixing fishing line, (c) before mixing polyester fibre, and (d) after mixing polyester fibre.

cylindrical shape to have a diameter of 60 mm and a height of 20 mm. The observation after the tests revealed that the fibre was randomly oriented even after the tests. Therefore, the effect of fibre orientation on the shear strength is small compared to the percent of mixing and adhesion mobilised by the fibre with the soil. In the tests, Edosaki sand with a water content of 15% was compacted to achieve a degree of compaction of 80%. In the case with the fishing line, a water content of 15% was needed to mix with 1% fishing line, and in the case with the polyester fibre, a water content of 17% was needed to mix with 2% fibre to reach the final water content of 15%. The direct shear tests were carried out to obtain the angle of shearing resistance (ϕ) and the cohesion intercept (c) of the soils. Fig. 9 compares the results of the direct shear tests for the soils. The results indicate that with 1% fishing line added, the cohesion of the soil increased just around 2 kPa and the friction angle around 8°, while with 2% polyester fibre added, the cohesion of the soil increased around 14 kPa and the friction angle around 3°. Consequently, the fibre has increased the cohesion of the soil by 1.4 kPa and 14 kPa for fishing line and polyester fibre, respectively. The difference is likely caused by the type and the amounts of materials, as summarised in Table 3. Considering the fact that the increase in the cohesion of the soil reinforced by the real vetiver grass was 6–7 kPa, it can be said that the shear strength of the soil with fishing line and polyester fibre exhibits similar shear behaviour to the soil reinforced with vetiver grass (Fig. 6), which could increase the shear strength of the soil mainly from the cohesion. Thus, both materials can be reasonably selected to model the vetiver grass in centrifuge model tests.

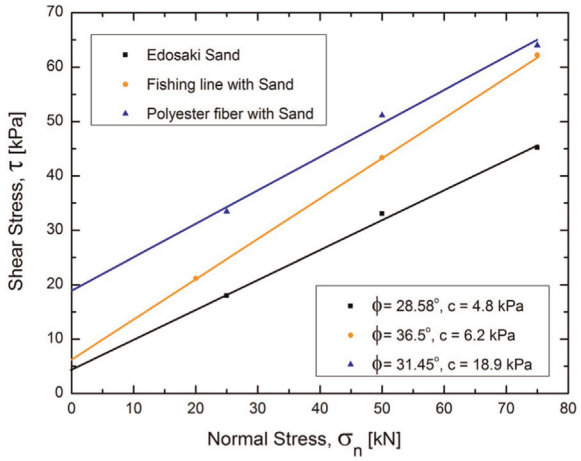

Fig. 9. Direct shear results of Edosaki sand, fishing line, and polyester fibre mixed with Edosaki sand.

3.2. Slope model and testing procedure

In the centrifuge tests, the slope models were conducted under two conditions: (1) seepage tests – the tests were conducted to define the mechanism of slope failure during the groundwater flow from the far area where the rain had fallen, and (2) rainfall tests – the tests were conducted to

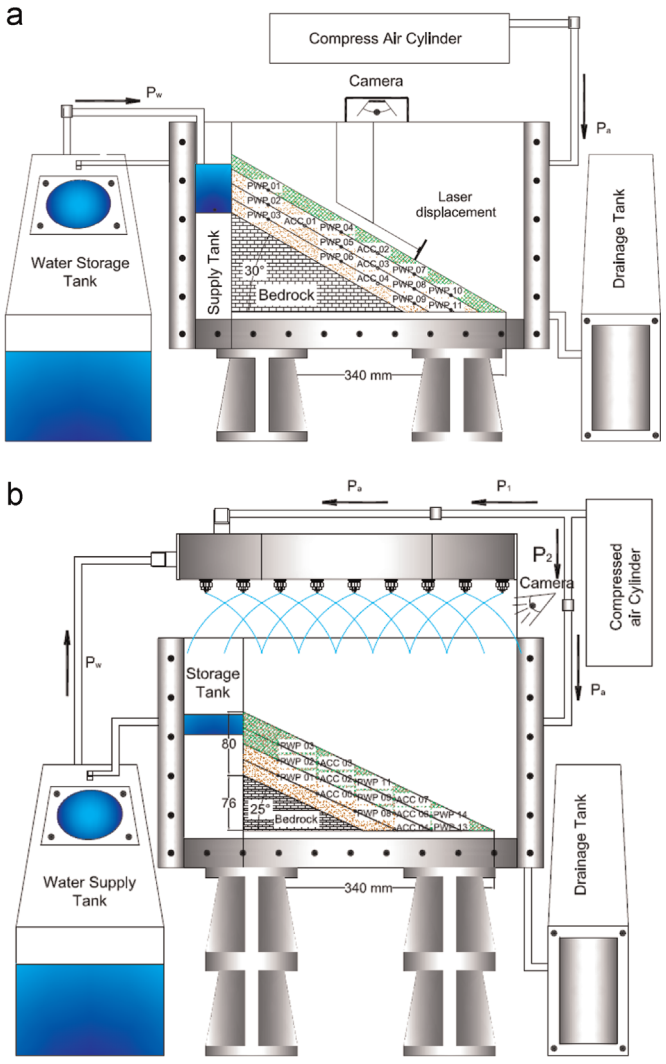

Fig. 10. Schematic of centrifuge system: (a) seepage model tests and (b) rainfall model tests.

examine the effect of run-off on the slope surface. These two tests were carried out to simulate the mechanism of the slope failure. The model slopes were prepared inside a steel box, 450 mm in width, 150 mm in breadth, and 270 mm in depth, and consisted of two parts, one a bedrock part that was made of aluminium plates and was placed on a 10 mm-thick acrylic plate, as shown in Fig. 10, and the other a soil part which was made of Edosaki sand and consisted of four layers that had a total thickness 80 mm in height in the model scale. Fig. 10 shows the schematic system for both seepage and rainfall model tests. During the tests, pore-water pressure transducers (PWPs) and accelerometers (ACCs) were installed in the soil layers during compaction to measure the pore water pressure and the soil slope displacement, respectively. In the seepage cases, 10 PWP transducers and 4 accelerometers were installed in the model tests and, in rainfall cases, 8 PWP transducers and 6 accelerometers were installed in the model tests. The locations of the PWP transducers and the accelerometers are presented in Fig. 10. The pore water pressure transducers used are SSK Micro Pore Water Pressure Transducers Model P303AV-2 with a diameter of 6 mm and a length of 8.5 mm (diameter of wiring = 1.3 mm). The accelerometers used are SSK Micro Accelerometers Model A5-50 with dimensions of $5 \times 5 \times 15$ mm^3 (diameter of wiring = 1.6 mm). If the wiring of these sensors had been in the vertical direction, perhaps the wiring could have been rainwater infiltration paths and could have restrained the slope deformation. To avoid such conditions, the wiring was extended in the horizontal direction. The slope displacement was calculated by integrating the inclination of the accelerometers along the depth. A digital camera was installed in front of the transparent window to observe the displacement and/or the deformation of the slope failure during the tests.

3.2.1. . *Seepage tests*

For the seepage tests, a 50-mm-wide water supply tank was installed inside the steel box on the left side to provide seepage flow from the upslope during the tests. A filter was installed between the vertical side wall of the tank and the slope model to make sure that only water could seep through to the slope model. In addition, a laser displacement transducer was installed on the top of the soil slope to measure the slope displacement, and one small digital camera was installed at the middle-top of the steel box to observe the slope surface cracking. Therefore, the deformations of the soil slope were clearly observed by video recording and the laser displacement transducer as well as by the accelerometers. The model slope consisted of two parts, one bedrock, with a length of 236 mm, a height of 136 mm and an angle of 30°, between the slope surface and the bottom plate, and the other the soil part, as shown in Fig. 10(a). During the centrifuge operation, the groundwater level in the model slope was controlled by changing the water level in the water supply tank. In the seepage tests, two cases were conducted, i.e., (1) the case of a soil slope without reinforcement, to be used as reference, and (2) the case of a soil slope reinforced at the surface by a 20-mm fishing line. The purpose of the latter was to simulate the mechanism of shallow roots at the top of surface which are similar to 4-month-old vetiver grass.

3.2.2. . *Rainfall tests*

For the rainfall tests, heavy rainfall conditions were chosen to impose over the slope model. An array of pneumatic spray nozzles (H. Ikeuchi & Co., BIMV45075) was selected to simulate the heavy rainfall in the centrifuge. The rainfall simulator consisted of nine spray nozzles and was placed above the steel box at a distance of 80 mm. On the left side of the steel box, a small tank, 80 mm in width, was installed as a water storage tank and was used as a rain gauge to estimate the precipitation on the slope. In addition, one small digital camera was installed at the top-right side of the steel box to observe the slope failure at the toe. After soil compaction was complete, Japanese noodles were installed between the model slope and the front transparent window so that the deformation of the slope could be clearly observed. Thus, the soil displacements were measured by both the accelerometers and the video recording taken through the front transparent window of the steel box. The bedrock part of this model is

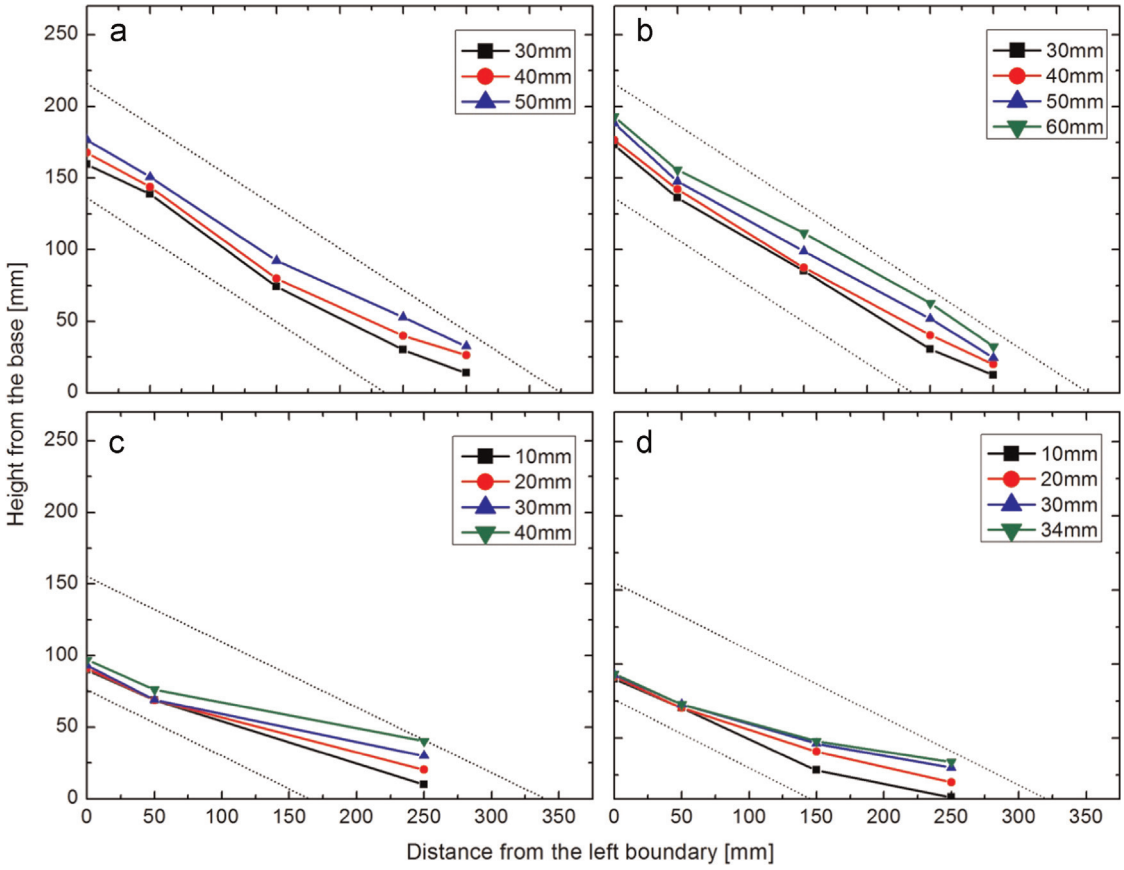

Fig. 11. Variation in phreatic lines: (a) unreinforced slope under seepage; (b) 20-mm root-reinforced slope under seepage; (c) unreinforced slope under rainfall; and (d) 40-mm root-reinforced slope under rainfall.

165 mm in length, 76 mm in height and the slope angle of 25°, as shown in Fig. 10(b). The surface of the model bedrock was roughened by attaching sand paper to it. During the tests, rainfall intensity of 1000 mm/h (20 mm/h in the prototype) was used by spraying rain drops over the slope surface. Two cases were performed for these rainfall tests, i.e., (1) an unreinforced soil slope used for reference and (2) a soil slope reinforced at the surface by 40-mm polyester fibre. The 40-mm fibre-reinforced model is similar to the case of the six-month-old vetiver grass.

3.3. Results of centrifuge model tests

Fig. 11 shows the variations in phreatic lines within the soil slope. The positions of the phreatic lines are calculated from the pore-water pressure measured by the PWPs at the toe in both seepage and rainfall tests. According to these results, the phreatic lines for the seepage tests (Fig. 11(a) and (b)) were approximately parallel to the slope between the boundary of the soil and the bedrock. In contrast, the phreatic lines in the rainfall tests (Fig. 11(c) and (d)) were raised at the toe. In addition, the phreatic lines for the rainfall tests in the root-reinforced case decreased. This decrease may have been caused by the polyester fibres which helped prevent the rising up of the groundwater table. Moreover, the results from PWPs in the rainfall case (Fig. 11(c) and (d)) indicate that the soil slope was not fully saturated. The results of the centrifuge model showed that small soil erosions were observed at the near failure stage only in the un-reinforced case and that no runoff or soil erosion was observed in the reinforced case. Hence, the effect of runoff and soil erosion could not account for the slope surface in this study.

Fig. 12 shows digital snapshots of the slopes after the tests together with the slip surface formation timing in terms of the pressure head near the toe. In the seepage tests, the slope failure started in the toe area when the pressure head at the toe has approximately reached 30 mm for both the unreinforced and the root-reinforced cases (Fig. 12(a) and (b)). By presenting the 20-mm root-reinforced case in the soil slope, there is no slip surface in the middle of the slope (Fig. 12(b)). Deformation is limited around the toe in the root-reinforced case, while it is extended to the middle in the unreinforced case (Fig. 12(a)). This is attributed to the effects of the root fibres on the soil surface. In the rainfall tests, the slope started to collapse from the toe and progressively moved upward until the pressure head near the toe reached around 40 mm (Fig. 12(c)). There is no slip surface beside the small deformation at the toe slope in the 40-mm root-reinforced case in the soil slope (Fig. 12(d)).

The displacements of the soil slope can be calculated from the accelerometers, as presented in Fig. 13. The plots show the horizontal displacement of each accelerometer, where the values in the legend represent the pressure head near the toe

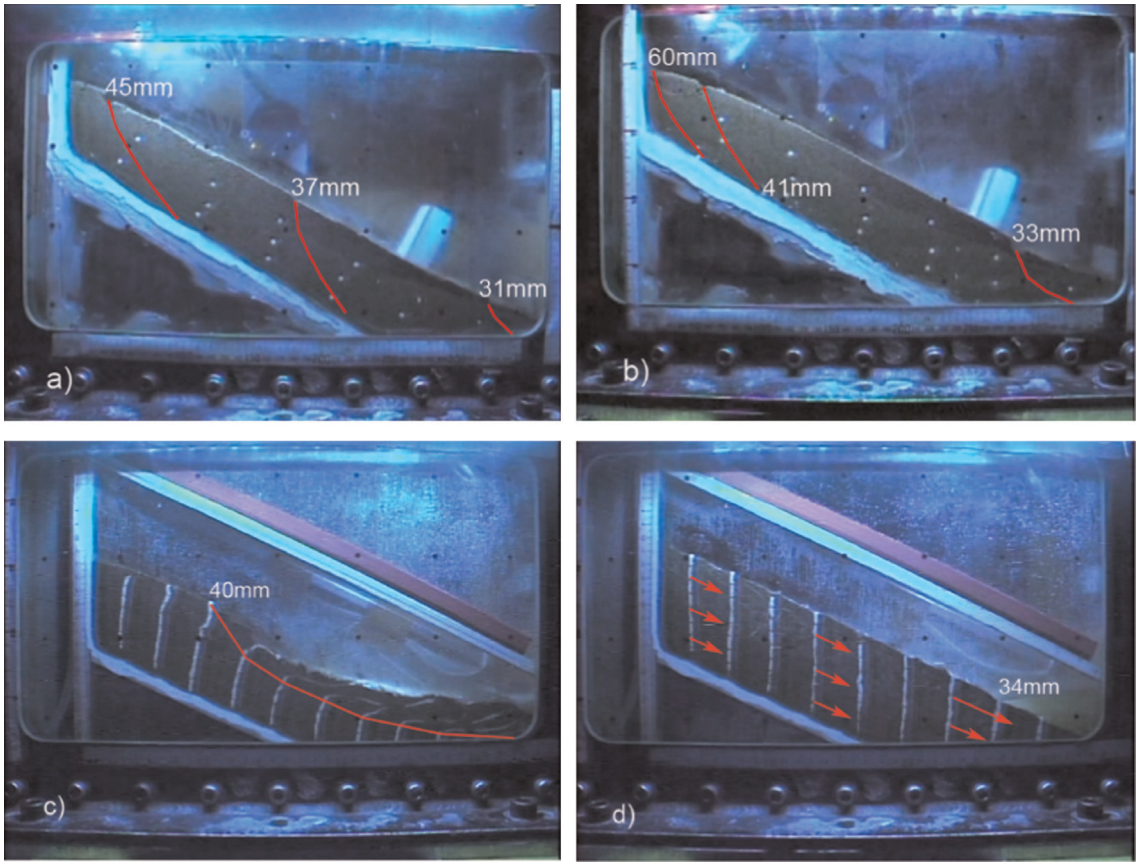

Fig. 12. Variation in slip surface lines: (a) unreinforced slope under seepage; (b) 20-mm root-reinforced slope under seepage; (c) unreinforced slope under rainfall; and (d) 40-mm root-reinforced slope under rainfall.

slope. In the seepage tests (Fig. 13(a) and (b)), the slope present a large displacement around 16 mm once the pressure head near the toe reaches around 50 mm in the unreinforced case, as depicted in Fig. 13(a). For the root-reinforced case in Fig. 13(b), the slope displacement decreases to 8 mm with a high pressure head of 60 mm. On the other hand, the slope collapsed due to the heavy rainfall condition, as shown in Fig. 13(c). The displacement in the rainfall case reached 15 mm when the pressure head near the toe reached 30 mm. By applying fibre reinforcement on the top surface, the deformation of soil was reduced less than 3 mm without collapse as depicted in Fig. 13(d). Table 4 summarises the comparison of slope displacements for each tests.

4. Result and discussions

According to the root observation results, the growth rate of vetiver roots is relatively high compared to others (Lyr and Hoffmann, 1967). The maximal depth of development of vetiver root systems can go up to 200 cm in the first year and the average daily increment in roots is approximately 10 mm. The direct shear test results indicate that vetiver roots significantly enhance the shear strength of soil especially the cohesion of the soil. These results agree well with the observation by Ali and Osman (2008). However, the increase in cohesion for the single vetiver specimen is higher than that for the group specimen due to the scale effect of the specimen size. The results in Fig. 6 show that the friction angle and cohesion decreased due to the increase in specimen size.

In addition, the centrifuge results indicate that the presence of root fibre on the surface of a soil slope was able to enhance the slope stability in both seepage and rainfall-induced slope failure problems. In the seepage tests, the root reinforcement was able to improve the soil slope by preventing cracks on the slope surface. Moreover, the results for the root-reinforced slope in the rainfall tests show a small deformation of the soil slope at the toe of the slope without collapses.

The results from this study indicate that the length and the radius of the root bundle are important parameters which can help prevent slope instability by increasing the cohesion of the soil. Therefore, vetiver roots are seen to have a great effect on the strengthening of the surface soil where the root length and the radius of root bundle are generally high.

5. Concluding remarks

According to the concepts of soil bioengineering and the observation results for vetiver grass, vegetation roots can increase the shear strength of soil by mechanical reinforcement. The present research confirms a significant contribution

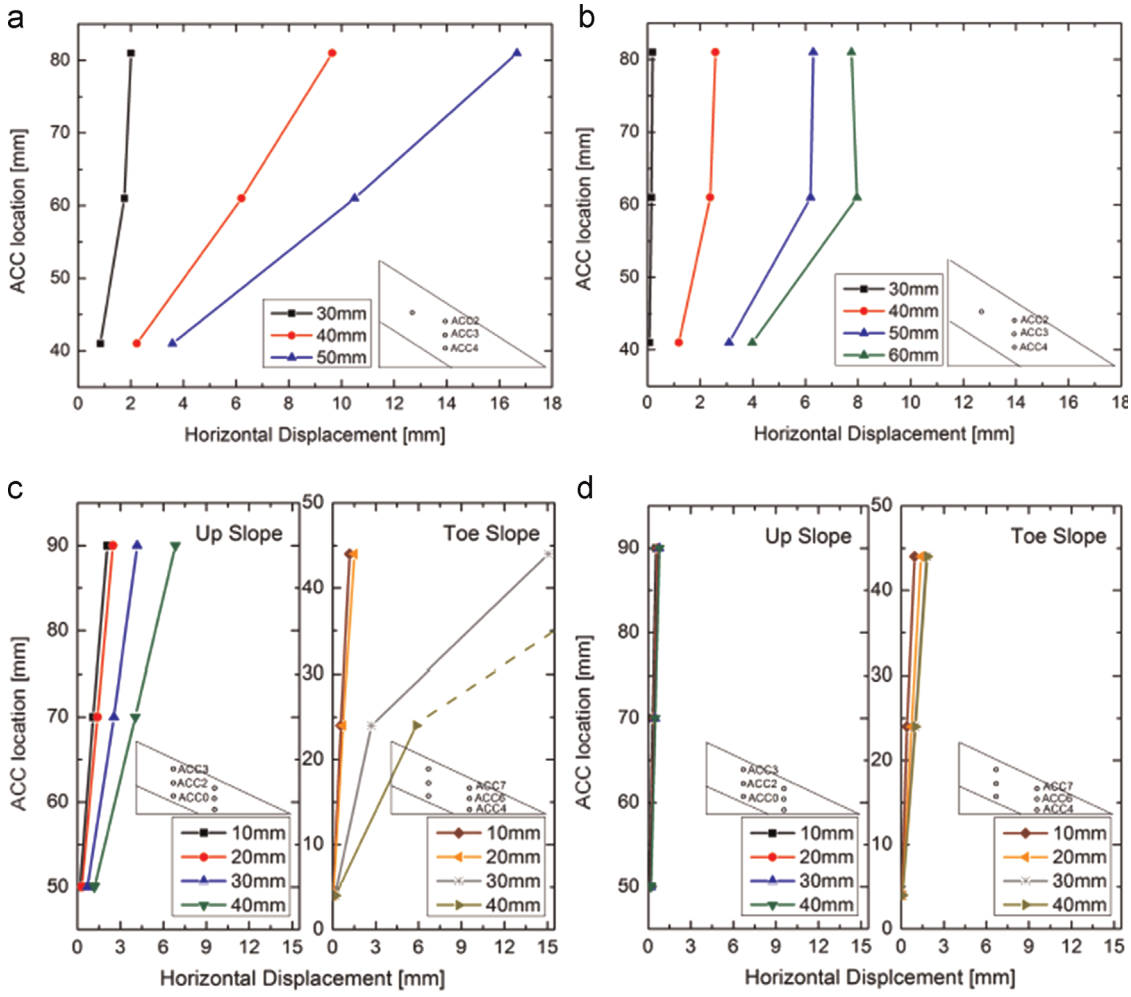

Fig. 13. Soil displacement calculated from ACCs: (a) unreinforced slope under seepage; (b) 20-mm root-reinforced slope under seepage; (c) unreinforced slope under rainfall; and (d) 40-mm root-reinforced slope under rainfall.

Table 4
Summary of centrifuge test.

Tests	Model case	Real case	Displacement (mm)	Slope deformation
Seepage				
1	Un-reinforced	Bare soil	16	Collapsed
2	Fishing line with 20-mm-deep reinforced zone	1-m-deep vetiver grass (4 months old)	8	Collapsed; fewer cracks on surface
Rainfall				
1	Unreinforced	Bare soil	15	Collapsed
2	Polyester fibres with 40-mm-deep reinforced zone	2-m-deep vetiver grass (6 months old)	3	Small deformation; without collapse

of the vegetation root to slope stability. A series of centrifuge model tests on a slope whose surface is reinforced by model roots was conducted to understand the mechanism of the vegetation reinforcement against seepage and rainfall-induced shallow failure. The conclusions of this study are as follows:

(1) The results from direct shear tests confirmed that the roots significantly increased the shear strength of the soil. The shear strength of the root-reinforced soil depended on the root length and the root area ratio.

(2) The centrifuge model tests illustrated that slope failure due to seepage and heavy rainfall is triggered by the rising of the water table and starts around the toe of the slope. The rise in the water table causes the effective stress to decrease and results in a decrease in the shear strength of the soil.

(3) It was confirmed from the centrifuge model tests that the presence of root fibres on the slope surface helps prevent cracking on the soil slope.

(4) The centrifuge model with rainfall simulator tests demonstrated an important role of vegetation roots in slope

stability, namely, the ability to delay both the infiltration rate into the ground and the rising of the groundwater table.

Acknowledgement

This research was supported by the Thailand Research Fund under the TRF Research Scholar Award Grant no. RSA-5880023. The first author would like to acknowledge the AUN/SEED-Net (JICA) for his Ph.D. scholarship during his study. The work was also conducted under the research and development project on landslide prevention and protection according to the Royal Initiatives of the Chaipattana Foundation.

References

Ali, F.H., Osman, N., 2008. Shear strength of a soil containing vegetation roots. Soils Found. 48 (4), 587–596.

Alsheimer, L., Hughes, B.O., 2007. "Ch 4 – Black and White in Photoshop" Black and White in Photoshop CS3 and Photoshop Lightroom: Create Stunning Monochromatic Images in Photoshop CS3, Photoshop Lightroom, and Beyond. Elsevier91–139.

ASTM D3080, 1998. Standard Test Method for Direct Shear Test of Soil under Consolidated Drained Conditions. American Society for Testing and Materials (ASTM), 100 bar Harbor Drive, PO Box C700, West Conshohocken, PA, 5.

Cerato, A.B., Lutenegger, A.L., 2006. Specimen size and scale effect of direct shear box tests of sands. Geotech. Test. J. 29 (6), 1–10.

Chinapan, W., Sukhasem, A., Moncharoen, L., 1997. A Study on the Ecotype Comparison of Vetiver Grass in Thailand. Land Development Department, Ministry of Agriculture and Cooperatives, Thailand.

Coppin, N.J., Richards, I.G., 1990. Use of Vegetation in Civil Engineering Construction Industry and Research Information Association (CIRIA). Butterworths, London.

Eab, K.H., Takahashi, A., Likitlersuang, S., 2014. Centrifuge modelling of root-reinforced soil slope subjected to rainfall infiltration. Geotech. Lett. 4, 211–216.

Gray, D.H., Leiser, A.T., 1982. Biotechnical Slope Protection and Erosion Control. Van Nostrand Reinhold, New York, NY.

Gray, D.H., Sotir, R.B., 1996. Biotechnical and Soil Bioengineering Slope Stabilization: A Practical Guide for Erosion Control. John Wiley & Sons, New York.

Greenfield, J.C., 1996. Vegetative vs. mechanical soil conservation system as they affect moisture conservation and sustained production. In: Proceedings of the First International Conference on Vetiver. Office of the Royal Development Projects Board, Bangkok, pp. 1–7.

Greenway, D.R., 1978. Vegetation and slope stability. In: Anderson, M.G., Richards, K.S. (Eds.), Slope Stability. John Wiley and Sons, New York, NY.

Hengchaovanich, D., Nilaweera, N., 1998. An assessment of strength properties of vetiver grass roots in relation to slope stabilization. In: Proceedings of the First International Conference on Vetiver. Office of the Royal Development Projects Board, Bangkok, pp. 153–158.

Kaewsaeng, W., 2000. Engineering Properties of Weathered Clay Soil Reinforced with Prachuap Khiri Khan *Vetiveria memoralis A. Camus* Root for Slope Protection (Thesis report). King Mongkut's University of Technology, Thonburi, Thailand.

LDD, 1998. Vetiver Grass Overview. Land Development Department, Ministry of Agriculture and Coorperatives, Bangkok.

Lyr, H., Hoffmann, G., 1967. Growth rates and growth periodicity of tree roots. Int. Rev. For. Res. 2, 181–236.

Ng, C.W.W., Shi, Q., 1998. A numerical investigation of the stability of unsaturated soil slope subjected to transient seepage. Comput. Geotech. 22 (1), 1–28.

Sonnenberg, R., Bransby, M.F., Hallett, P.D., Bengough, A.G., Mickovski, S. B., Davies, M.C.R., 2010. Centrifuge modelling of soil slopes reinforced with vegetation. Can. Geotech. J. 47, 1415–1430.

Takahashi, A., Nakamura, K., Likitlersuang, S., 2014. On the seepage-induce failure of vegetation-stabilised slopes. In: C. Gaudin, D. White (Eds.), Proceedings of the 8th International Conference on the Physical Modelling in Geotechnic. Taylor & Francis Group, London, pp. 1233–1239. ISBN: 978-1-138-00152-7.

Taylor, R.N., 1995. Geotechnical Centrifuge Technology. Geotechnical Engineering Research Center, Citi University, London. Blackie Academic & Professional, An Imprint of Chapman & Hall Wester Cleddens Road, Bishopbriggs, Glasgow G64 2N2.

Wu, T.H., McKinnell, W.P., Swanston, D.N., 1979. Strength of tree roots and landslides on Prince of Wales Island, Alaska. Can. Geotech. J. 16, 19–33.

Wu, T.H., 1995. Slope stabilization. In: Morgan, R.P.C., Rickson, R.J. (Eds.), Slope Stabilization and Erosion Control. E & FN Spon, London.

Available online at www.sciencedirect.com

ScienceDirect

International Journal of Pavement Research and Technology 9 (2016) 337–344

www.elsevier.com/locate/ijprt

Laboratory investigation of the performances of cement and fly ash modified asphalt concrete mixtures

Suched Likitlersuang [a], Thanakorn Chompoorat [b,*]

[a] Geotechnical Research Unit, Department of Civil Engineering, Faculty of Engineering, Chulalongkorn University, Thailand
[b] Department of Civil Engineering, School of Engineering, University of Phayao, Thailand

Received 11 May 2016; received in revised form 12 July 2016; accepted 3 August 2016
Available online 12 August 2016

Abstract

The influence of filler materials on volumetric and mechanical performances of asphalt concrete was investigated in this study. The AC60/70 asphalt binder incorporating with cement and fly ash as filler materials was mixed with limestone following the Marshall mix design method. The filler contents of cement and/or fly ash were varied. The non-filler asphalt concrete mixtures of the AC60/70 and the polymer modified asphalt were prepared for the purpose of comparison. The investigation programme includes the indirect tensile test, the resilient modulus test and the dynamic creep test. The tests are conducted under the humid temperate environments. All tests were then carried out under standard temperature (25 °C) and high temperature (55 °C) by using a controlled temperature chamber via the universal testing machine. The wet-conditioned samples were prepared to investigate the moisture susceptibility. Results show that cement and/or fly ash were beneficial in terms of improved strength, stiffness and stripping resistance of asphalt mixture. In addition, the combined use of cement and fly ash can enhance rutting resistance at wet and high temperature conditions. The results indicate that the strength, stiffness and moisture susceptibility performances of the asphalt concrete mixtures improved by filler are comparable to the performance of the polymer modified asphalt mixture.

Keywords: Asphalt concrete; Filler; Resilient modulus; Dynamic creep test; Moisture susceptibility

1. Introduction

Materials broadly employed to construct the surface layer of flexible pavement is an asphalt concrete, which is the composite material mixed from aggregates and asphalt binder. While the aggregates conduce resistance to support traffic loads, the asphalt binder contributes viscous-elastic behaviour to help with the adhesion of aggregate particles. The practicable size range of aggregate is from 50 mm to 0.075 mm. From this range the fine aggregates are defined to be smaller than 4.75 mm and the coarse aggregates are bigger than 4.75 mm. Even though particle size of the filler is less than 0.075 mm, it is well-known that the filler plays an important role in providing better packing conditions between the coarse and fine aggregates. It also leads to the greater stability within asphalt concrete and the reduction of optimum asphalt content.

Filler is categorised as a fine material which can be used to modify the properties of asphalt binder and asphalt concrete mixture. To this point, Portland cement, hydrated lime, fly ash, limestone dust, and clay particles are counted as fillers. The filler is not considered as a part of the aggregates. It is a modifier to improve the temperature susceptibility and durability of the asphalt binder as well as the asphalt concrete mixture [1]. The moisture susceptibility

* Corresponding author.
E-mail addresses: fceslk@eng.chula.ac.th (S. Likitlersuang), thanakorn.ch@up.ac.th (T. Chompoorat).
Peer review under responsibility of Chinese Society of Pavement Engineering.

http://dx.doi.org/10.1016/j.ijprt.2016.08.002

can be reduced by using the mineral fillers, for instance, hydrated lime [2,3]. In addition to utilisation of mineral fillers, the strength and stiffness of asphalt concrete can be increased [4]. The purpose of studying the characteristics of mineral filler is to enhance the performance of asphalt concrete in particular to increase the stability and durability against rutting and shoving. Lesueur et al. [3] presented that the durability of asphalt concrete mixtures can be increased by 2–10 years when the 1–1.5% of hydrated lime is used in the mixture. It is also found that Portland cement utilised as the filler can improve the anti-stripping properties of asphaltic concrete [5,6]. Additionally, the significant improvement on the moisture resistance characteristics can be observed when fly ash is employed to replace the cement and hydrated lime in producing asphalt concrete mixtures [7,8].

The key factors separating the fillers are particle shape and size, void content, surface area, mineral, chemical properties, and other physical properties [9]. By this reason different kinds of fillers replaced in the asphalt mixture lead to various asphalt mixture performances. This research aims to study the influence of filler types and fractions on the asphalt concrete mixture's properties. The materials selected to be the filler for this study are cement and fly ash. The contents of cement, fly ash and their combination were varied in the mixtures. The performance characteristics of the asphalt concrete mixture containing different types and fractions of filler were evaluated by various laboratory tests. The tests are conducted under the humid temperate environments of Thailand. To reach the standard test requirement, a minimum of three specimens was evaluated in each test.

2. Materials and testing programme

2.1. Materials

Most pavements in Thailand are constructed using asphalt mixes, consisting of AC60/70 penetration grade asphalt cement and aggregates. Mineral fillers such as limestone dust and cement are used to enhance the stability and durability of the asphalt concrete mixture. There is still no specification of filler material approved by the Thailand's Department of Highways (DOH). In the study, a local asphalt mix design based on the standard of the DOH commonly used in a flexible paving project was employed. In order to compare the performance of filler mixtures, the typical hot mix asphalt (HMA) without fillers and the polymer modified asphalt (PMA) mixtures were also prepared. Therefore, the locally-produced AC60/70 asphalt binder and the polymer modified asphalt were chosen in this study. The limestone aggregate used in the lab mixes was also obtained from an approved paving project. The aggregate particles were sieved according to the required size ranges in preparation to blend the considered asphalt mix with the approved gradation as shown in Fig. 1. Basic properties of aggregate were tested and summarised in Table 1. The two main variables in the specimens are the type and content of the filler. The filler used in this research are Portland cement type I and fly ash class C. The Portland cement type I is a common construction material locally made and consumed in the country. The fly ash is a by-product of lignite-fired power generation from the Mae Moh Power Plant in Lampang province. The chemical component and physical properties of cement and fly ash are summarised in Tables 2 and 3, respectively. The results of scanning electron micrograph of cement and fly ash are presented in Fig. 2.

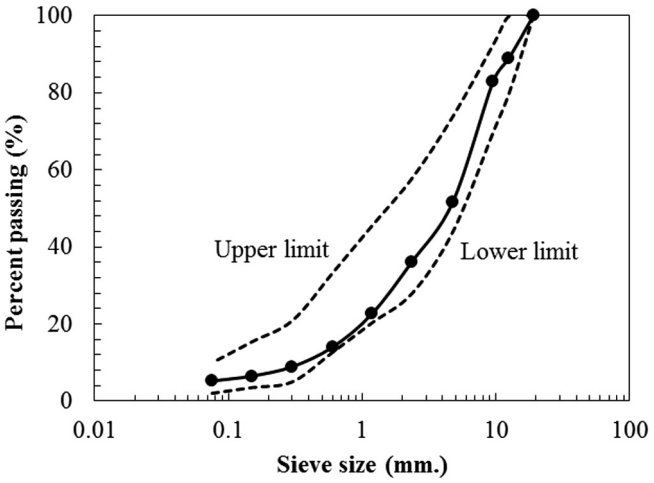

Fig. 1. Grain size distribution of aggregate.

Table 1
Properties of aggregate.

Aggregate type	Limestone
Bulk specific gravity	2.70
Flakiness index (%)	33
Asphalt absorption (%)	0.25
LA abrasion value (%)	
Aggregate 3/4″	22.70
Soundness (%)	
Weight loss aggregate 3/4″	1.0
Fine aggregate	3.2
Sand equivalent	64

Table 2
Chemical composition of materials from X-ray fluorescence (XRF) test (after Ref. [10]).

Chemical composition (%)	Portland cement	Fly ash
SiO_2	20.90	30.90
Al_2O_3	4.76	17.60
Fe_2O_3	3.41	14.80
CaO	65.41	23.24
MgO	1.25	2.12
SO_3	2.71	3.87
Na_2O	0.24	1.50
K_2O	0.35	2.73
LOI	0.96	1.20

Table 3
Basic properties of Portland cement and fly ash.

Material	Retained on sieve #325 (%)	Blaine fineness (cm^2/g)	Mean particle size (d_{50}, μm)	Specific gravity
Portland cement	13	3,420	11	3.15
Fly ash	29	3,602	19	2.12

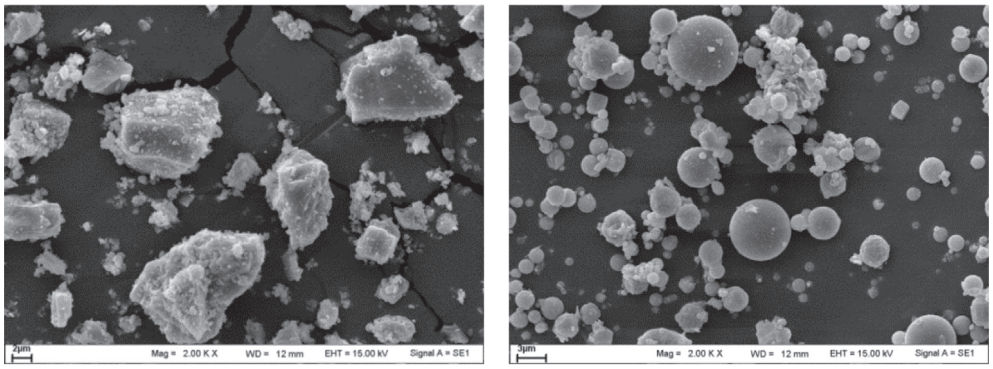

(a) Portland cement (b) Fly ash

Fig. 2. Scanning electron micrographs of fillers with 2000× magnification (after Ref. [10]).

2.2. Asphalt concrete mixture preparation

Asphalt cement together with a 12.5-mm nominal maximum aggregate size of limestone were employed to prepare asphalt mixes. The mixture specimens were designed according to the Marshall method which is also used by the Thailand's Department of Highways. In this study, a total of 11 mixtures were prepared as summarised in Table 4. The HMA and PMA are the mixtures without filler, which are fabricated from the AC60/70 and the polymer modified asphalt binder, respectively. The letter C and F refer to the mixtures with cement and fly ash added as filler, respectively, and the number after the letter means the percentage of filler by weight of the aggregate. For example, C1.5F1.5 refers to the mix with 1.5% cement + 1.5% fly ash added by weight of the aggregate. The optimum asphalt content of 5% was determined from the HMA mix according to the Marshall design method [11]. In this study, the asphalt content of 5% was fixed for all mixes.

All materials were prepared in accordance the Marshall method (ASTM D6926) [12]. Before the mixing process, the aggregates were heated at 100 °C for 24 h to ensure moisture-free conditions and continued to be heated for 2 h at a mixing temperature of 150 °C. The asphalt was also heated at 150 °C in the oven. The specimens with dimensions of approximately 102 mm (4 inch) diameter and 64 mm (2.5 inch) height were compacted by using Marshall hammer compaction at 135 °C. The specimens were compacted at 75 blows per side according to heavy traffic conditions. After a 24-hour curing period for the Marshall specimens, volumetric measurement was conducted for all specimens. The results of volumetric properties of all mixes are summarised in Table 4.

Table 4
Volumetric properties of all mixtures.

Mix	Bulk specific gravity (G_{mb}, −)	Voids in the total mix (VTM, %)	Voids in the mineral aggregate (VMA, %)	Voids filled with asphalt (VFA, %)
HMA	2.418	4.0	14.7	72.8
C1	2.461	2.5	13.3	81.2
C3	2.462	2.8	13.4	79.1
C5	2.453	3.5	13.9	74.8
F1	2.467	2.0	12.8	84.4
F3	2.468	1.7	12.3	86.2
F5	2.471	1.3	11.7	88.9
C0.5F0.5	2.465	2.2	13.0	83.1
C1.5F1.5	2.466	2.2	12.8	82.8
C2.5F2.5	2.470	2.1	12.5	83.2
PMA	2.419	4.0	14.7	72.8

Remark: HMA = Hot Mix Asphalt (without filler), PMA = Polymer Modified Asphalt (without filler), C = Cement, F = Fly ash (e.g. C1.5F1.5 = 1.5% cement + 1.5% fly ash mixture).

2.3. Testing programme

The experimental tests including the Marshall stability (ASTM D6927) [13], the indirect tensile test (IDT) (ASTM D4867) [14], the resilient modulus (Mr) test (ASTM D4123) [15], and the dynamic creep test (BS DD226) [16] were carried out through this research as summarised in Table 5. Following the Marshall stability test, the specimens were soaked at 60 °C for 24 h, and then the conditioned specimens were loaded to failure at a constant rate of 1.65 mm/min. The ratio of the stability to flow, which is stated as the Marshall quotient (MQ), indicates the stiffness of the specimen. For the indirect tensile, the resilient modulus, and the dynamic creep tests, a controlled temperature and humidity chamber is used to manage the

Table 5
Experimental programme.

Test	Temperature (°C)	Mix	Conditions
Stability and flow (ASTM D6927)	60	HMA, PMA, C1, F1, C0.5F0.5, C3, F3, C1.5F1.5, C5, F5, C2.5F2.5	Wet
Indirect tensile test (ASTM D4867)	25, 55	HMA, PMA, C1, F1, C0.5F0.5, C3, F3, C1.5F1.5, C5, F5, C2.5F2.5	Dry/Wet
Resilient modulus test (ASTM D4123)	25, 55	HMA, PMA, C1, F1, C0.5F0.5, C3, F3, C1.5F1.5, C5, F5, C2.5F2.5	Dry/Wet
Dynamic creep test (BS DD226)	25, 55	HMA, PMA, C1, F1, C0.5F0.5, C3, F3, C1.5F1.5, C5, F5, C2.5F2.5	Dry/Wet

temperatures desired for the testing samples at 25 °C and 55 °C. In order to examine the moisture sensitivity, the conditioned specimens were soaked at 55 °C for 24 h prior to the test started. The details of testing conditions are summarized in Table 5.

For the indirect tensile test, the cylindrical specimens are subjected to monotonically compressive loads, which act parallel to the vertical diametric plane, by using the 200 kN Universal Testing Machine (UTM). This type of loading produces a relatively uniform tensile stress acting perpendicular to the applied load plane and the specimen usually fails by splitting along with the loaded plane. The indirect tensile strength (ITS) is then defined as the maximum strength. The test method has been carried out similar to the previous research by the authors [17]. The 14 kN cyclic UTM was employed in the resilient modulus and the dynamic creep tests. To evaluate the mixture's resilient modulus, 10% of indirect tensile strength (ITS) values at each temperature are used for the resilient modulus test. The specimens are continuously loaded by 1 Hz frequency (loading period for 0.1 s and rest period for 0.9 s) with 155 cycles, which the first 150 cycles are for preloaded conditions and the last 5 cycles are for measuring the resilient modulus. The dynamic creep test or the permanent deformation test was performed according to the British Standard [16], a deviator stress of 100 kPa was used in the unconfined test, and the loading frequency of 1 Hz (loading period for 0.5 s and rest period for 0.5 s) with 1800 cycles or until the specimen is failed was applied.

3. Results and discussion

3.1. Material characterisation

The limestone used for coarse and fine aggregates was relatively clean and free from deleterious material, and the particle shape was relatively flaky and irregular. The properties of limestone such as flakiness index, LA abrasion, soundness and sand equivalent satisfy the Thailand's Department of Highways requirement for asphalt concrete mixture application [18]. It is noted that the Thailand's Department of Highways standards are rather similar to the ASTM and AASHTO standards [19–21]. The properties of cement and fly ash are shown in Table 3. The specific surface area (the surface area per unit mass) was tested by Blaine fineness. The specific surface area of fly ash is slightly higher than that of cement. The fine particle size (i.e., sieve No.325 with an opening size of 0.044 mm) and the mean particle size (d_{50}) were tested and reported. The particle size of fly ash is higher than that of cement. The specific surface can be correlated with particle size and linked to physical and mechanical properties of the mixture. The specific gravity of cement is greater than that of fly ash. The particle shape, size and morphology of the cement and fly ash were examined by using scanning electron microscopy (SEM) as shown in Fig. 2. The SEM images show that the cement is irregular in shape and its particle size is around 2 μm, whereas the fly ash shape is relatively spherical and approximately 3 μm in size. It is because the specific gravity of fly ash is lower than cement. It can be deduced that the fly ash particle is bigger and has a more specific surface area than cement particle. Therefore, the information shown in SEM images is consistent with the Blaine fineness test and d_{50} data in Table 3.

3.2. Volumetric properties of the mixture

In this study, the effect of the amount and type of filler on the volumetric properties of the mixture was examined. The asphalt content of 5.0% was fixed for all the mixes. The results of volumetric properties of all specimen designs are summarised in Table 4. The bulk specific gravity (G_{mb}) values of the mixtures with filler added are higher than those of the HMA and PMA mixes. The HMA and PMA specimens have higher the total voids in the mix (VTM) and the voids in mineral aggregate (VMA), but lower the voids filled by asphalt (VFA) than those of the mixtures with filler added. This is because the filler can fill the void and increase the density of the mixture.

Comparing among the mixtures with filler added, the fly ash provides the denser properties than the cement, in which the mix with 5% fly ash has the highest G_{mb} and lowest the VTM. The mix with both cement and fly ash has the intermediate values of the volumetric properties. It is possible that filler, for a certain size range, would fill up voids among the aggregates, thereby decreasing the VMA. The decrease in the VMA could indirectly lead to the decrease in the VTM even though the asphalt content of all mixes is fixed. Certain fillers require more asphalt to wrap onto its surface because of the relatively higher specific surface area, thus resulting in a higher VFA.

3.3. Strength and stiffness of the mixture

3.3.1. Marshall stability

The Marshall stabilities and flows of all asphalt concrete specimens were tested. The ratio of stability (kN) to flow (mm), stated as the Marshall quotient (MQ), and as an

Table 6
Experimental results.

Specimen	MQ (kN/0.25 mm)	ITS (kPa)			TSR 55 °C (%)	Mr (MPa)			Accumulated strain @ 1800 cycles (%)			Accumulated strain rate		
		dry		wet		dry		wet	dry		wet	dry		wet
		25 °C	55 °C	55 °C		25 °C	55 °C	55 °C	25 °C	55 °C	55 °C	25 °C	55 °C	55 °C
HMA	0.74	603	86	57	66.28	3,247	240	153	1.43	1.62	2.38	0.1004	0.1954	0.2172
C1	0.74	683	109	119	109.17	3,372	344	163	1.18	1.28	1.23	0.0902	0.1479	0.1342
C3	0.79	687	120	126	105.00	3,553	399	193	1.16	1.12	1.00	0.1059	0.1378	0.0851
C5	0.87	684	129	138	106.98	3,280	396	192	0.65	1.20	1.14	0.0651	0.1291	0.0878
F1	0.72	631	112	91	81.25	4,005	340	224	1.12	1.37	0.98	0.1114	0.1612	0.1004
F3	0.75	657	127	126	99.21	3,325	324	174	0.55	1.50	0.94	0.0611	0.1593	0.0948
F5	0.72	663	132	125	94.70	3,284	334	149	1.31	1.25	1.26	0.1511	0.1447	0.1310
C0.5F0.5	0.75	647	95	94	98.95	3,758	310	225	1.38	1.45	1.39	0.1162	0.1755	0.1267
C1.5F1.5	0.91	653	132	110	83.33	4,005	368	354	0.47	1.35	0.92	0.0546	0.1599	0.0918
C2.5F2.5	0.93	675	159	132	83.02	3,967	309	275	0.81	1.11	0.94	0.0938	0.1144	0.0870
PMA	0.99	747	165	130	78.79	3,839	439	377	0.62	0.80	0.83	0.0594	0.0493	0.0546

empirical indication of the stiffness of the mixes is reported in Table 6. It is well-recognised that the MQ is a measure of the material's resistance to shear stresses, permanent deformation, and hence rutting. The high MQ values indicate a high stiffness mix and resistance to creep deformation. Fig. 3 illustrates the MQ for all mixtures. The results indicated that the PMA has highest MQ value and the more cement added the higher MQ can be observed. Conversely, the fly ash has less influence to the MQ value. However, the combination of cement and fly ash as fillers can significantly increase the MQ value of the mixture. The filler content is in the range of 3–5%, in which the mixture with 2.5% cement + 2.5% fly ash provides the MQ value almost closed to the PMA mix.

3.3.2. Indirect tensile strength

The indirect tensile tests (IDT) were carried out on unconditioned (dry) and conditioned (wet) specimens at standard temperature (25 °C) and hot temperature (55 °C). The test results are summarized in Table 6 and

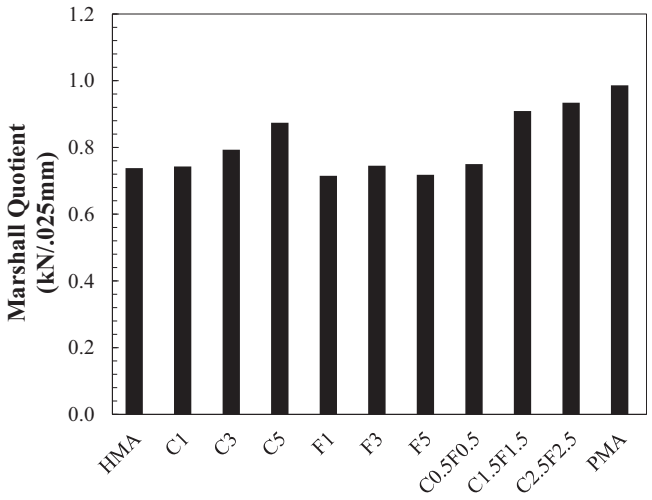

Fig. 3. Marshall quotient values of asphalt mixtures.

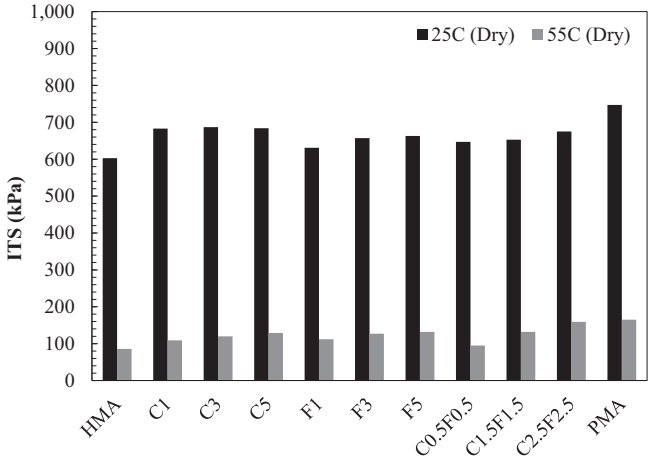

Fig. 4. Indirect tensile strength (ITS) values of asphalt mixtures in dry conditions.

plotted as shown in Figs. 4 and 5. The IDT is normally conducted to determine the tensile properties of the asphaltic concrete, which can be further related to the cracking properties of the pavement. Fig. 4 illustrates the average indirect tensile strength (ITS) under dry conditions of the asphalt specimens treated with filler material. The result indicates that the use of cement and fly ash result in increasing in the ITS comparing to the HMA mix around 10–15% at 25 °C and almost 50% at 55 °C. However, the ITSs of all filler mixtures are still lower than the ITS of PMA mix.

Fig. 5 presents a comparison of the average ITS of the unconditioned and conditioned specimens at 55 °C. The tensile strength ratio (TSR), defined as the ratio between the ITS of conditioned and unconditioned sample at 55 °C, is an indicator for moisture susceptibility. The results show that both cement and fly ash can significantly increase the ITS of conditioned specimens at 55 °C, especially the 5% cement and 5% fly ash specimens offer the ITS values as good as the PMA specimen. It is noted that the TSR at 55 °C for the mixes C1, C3 and C5 are slightly greater

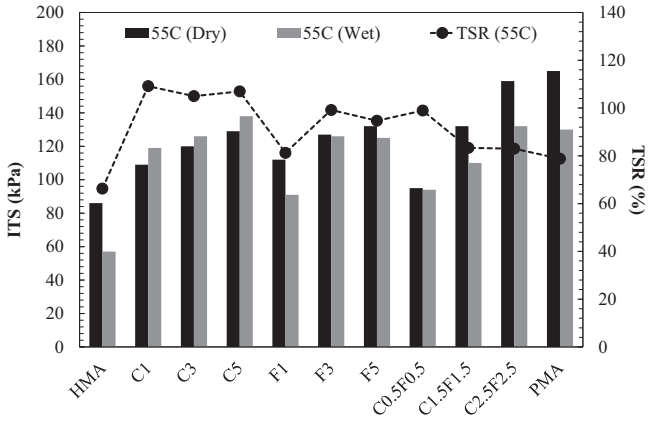

Fig. 5. Indirect tensile strength (ITS) and tensile strength ratio (TSR) values of asphalt mixtures at 55 °C.

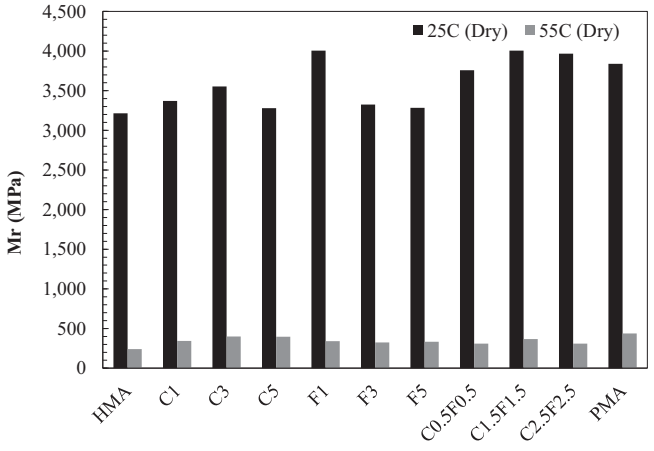

Fig. 6. Resilient modulus (Mr) values of asphalt mixtures in dry conditions.

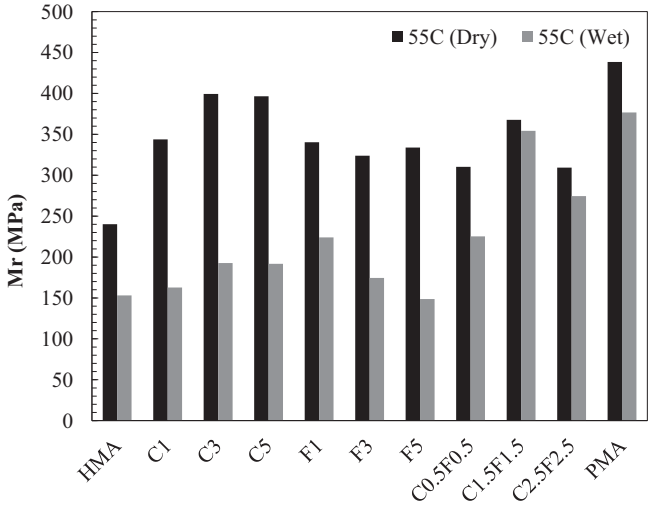

Fig. 7. Resilient modulus (Mr) of asphalt mixtures at 55 °C.

than 100%. This might be from the influence of cementation in the first 24 h. The samples were better curing when soaked in the water than air-dried conditions.

3.3.3. Resilient modulus

Similar to the ITS, the cement and fly ash can improve the stiffness of asphalt concrete. The resilient modulus (Mr) is a significant parameter for pavement design as indicated by the material stiffness. The test results of resilient modulus are also summarised in Table 6 and plotted as shown in Figs. 6 and 7. Fig. 6 shows that the Mr values are increased by cement and fly ash. The presence of filler may modify the viscoelastic properties of the asphalt mastic and affect the mixture's stiffness. However, an excessive amount of filler could reduce the viscous behaviour of asphalt mastic and result in decreasing the Mr value. In this study, the suitable amount of cement and/or fly ash was found to be in the range of 1–3%.

3.4. Dynamic creep performance

Rutting is the major distress found in flexible pavement. It is the permanent deformation in the transverse profile in the wheel patch, starting at zero rut depth and increasing with the number of loading repetitions. A repetitive uniaxial compressive load on cylindrical specimen from the dynamic creep test provides a reasonable simulation of asphalt pavement subjected to repetitive axle loads. In this study, all mixture specimens were firstly performed in dry conditions at 25 °C according to BS DD226 [16]. To evaluate the moisture susceptibility, the dynamic creep tests for all mixture specimens were conducted in dry and wet conditions at hot temperature (55 °C). The dynamic creep test results known as creep curves were plotted as shown in Figs. 8–10 for dry-conditioned at 25 °C, dry-conditioned at 55 °C and wet-conditioned at 55 °C, respectively. Two parameters, the accumulated strain at 1800 cycles and the accumulated strain rate, were determined from the curves as reported in Table 6.

The results indicate that the cement and fly ash can improve the resistance to performance deformation. The 5% cement, 3% fly ash and 1.5% cement + 1.5% fly ash are the mixtures that can provide resistance to permanent deformation as similar to the PMA mix. The fillers can

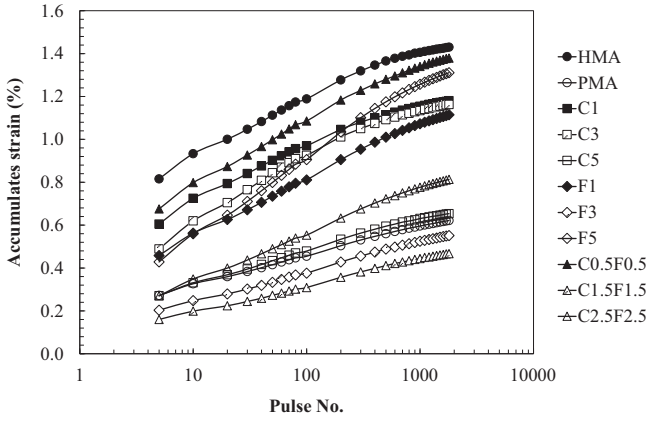

Fig. 8. Creep behaviour of asphalt mixture at 25 °C under dry conditions.

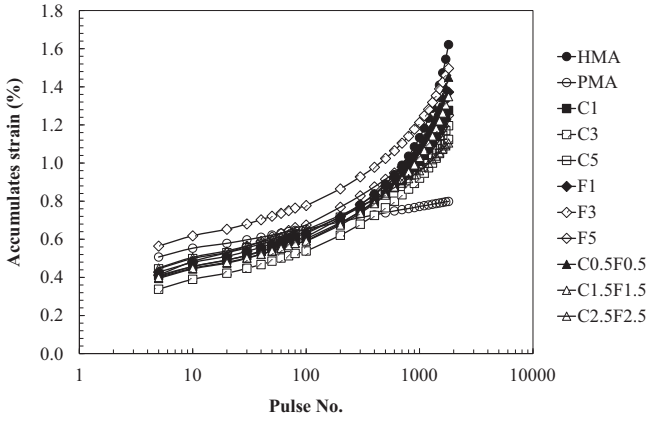

Fig. 9. Creep behaviour of asphalt mixtures at 55 °C under dry conditions.

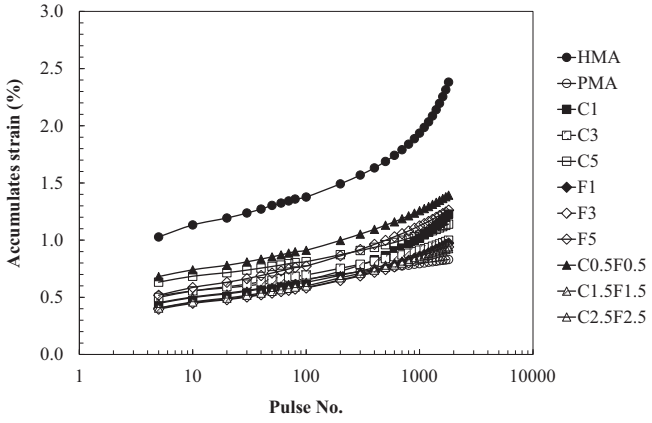

Fig. 10. Creep behaviour of asphalt mixtures at 55 °C under wet conditions.

enhance the rutting resistance of asphalt concrete, especially at high temperature, when the asphalt behaves softly.

3.5. Moisture susceptibility

In tropical countries like Thailand, moisture susceptibility is one of the most important distress mechanisms leading to premature failure of asphalt pavements. There are many researchers trying to study and develop the methods of testing [11,22]. In this study, the test results of the conditioned specimens can be used to indicate the moisture susceptibility. Basically, higher values of ITS, Mr and accumulated strains of conditioned samples may indicate greater resistance to moisture damage. The indirect tensile strength ratio (TSR) is a common parameter to evaluate moisture susceptibility. The TSR for all mixes are reported in Table 6 and Fig. 5. The results indicate that the cement and fly ash as filler can enhance the moisture susceptibility of the asphalt concrete. The 1% cement mixture gives the highest number of the TSR. However, the 1.5% cement + 1.5% fly ash mixture offers the highest Mr and accumulated strain values in wet conditions, which is similar to the values of PMA mix. It seems that the combination of the cement and fly ash as filler can increase the moisture susceptibility of the HMA as good as the PMA mix.

4. Discussion and conclusion

Filler is usually added to asphalt concrete mixtures as a stiffening and void-filling material. This study evaluated totally 11 groups of specimens with various cement and/or fly ash contents and a 5% asphalt content. The hot mix asphalt (HMA) and polymer modified asphalt (PMA) mixtures without filler added were prepared for a sake of comparison. The mechanical properties of these mixtures were determined at 25 °C and 55 °C and moisture susceptibility tests were conducted at 55 °C to determine their moisture damage potential. The influence of cement and fly ash as filler materials on the performance of asphalt concrete can be discussed as follows:

(1) It is obvious that the filler can fill the void and increase the density of the mixture. It is resulting in increasing the bulk specific gravity (G_{mb}) and reducing the voids in the total mix (VTM). However, the fly ash provides denser properties than cement because the fly ash has greater specific surface area. The more specific surface area the more asphalt to wrap its surface, thus resulting in a higher void filled with asphalt (VFA). Moreover, the filler can perform as a tiny roller during the compaction process. If the filler has a large enough diameter and a regular shape, it will act as a friction-lubricating agent [9]. The relationship between types of fillers and voids of mineral aggregates directly affects the work ability of the mixture. The bigger size and more regular shape of fly ash particle may act as rollers that facilitate less friction in the mastic during compaction, thereby resulting in a tighter packing and a lower void in the mineral aggregate (VMA).
(2) Results from this study shows that cement and/or fly ash were beneficial in terms of improved strength, stiffness and stripping resistance of asphalt mixture. Mechanical properties and moisture damage testing results indicated that the use of 1.5% cement + 1.5% fly ash improves the resilient modulus (Mr) of the mix at low and high temperature. Since cement increases the strength of asphalt concrete [4] and fly ash increases the stripping resistance of mix [23], the combined use of both cement and fly ash might be the optimum filler solution.
(3) For pavement distress, the addition of cement and/or fly ash in asphalt concrete mixture significantly reduces the permanent deformation of the mix, especially in wet and high temperature. The results show that the mix of 1.5% cement + 1.5% fly ash provides the best rutting resistance.

In this study, investigation of volumetric and mechanical properties of asphalt concrete mixtures revealed that

cement and/or fly ash imparted different enhancements to mixtures. It is concluded that the filler interacted with other constituent materials in the asphalt concrete mixture contributes to the mixture's performance. The combination of cement and fly ash mixture exhibited better strength, stiffness and moisture damage resistance. It is well-known that the PMA considerably increases mechanical performances and work ability of the asphalt concrete mixture [22,24]. Therefore, an alternative of using filler to improve the conventional HMA might be the optimal solution in the practice. It is noted that some more research would be suggested to be conducted in future, such as the influence of the optimum asphalt content and the fatigue performance.

Acknowledgement

This research was supported by the Thailand Research Fund under the TRF Research Scholar Award Grant No. RSA-5880023. The authors would like to thank Phitayuth Pholkainuwatra for his assistance throughout the tests. The authors are most grateful to the Thailand's Department of Highway staff for their kindness in providing data related to this research.

References

[1] C. Gorkem, B. Sengoz, Predicting stripping and moisture induced damage of asphalt concrete prepared with polymer modified bitumen and hydrated lime, Constr. Build. Mater. 23 (6) (2009) 2227–2236, http://dx.doi.org/10.1016/j.conbuildmat.2008.12.001.

[2] R. Taha, A. Al-Rawas, A. Al-Harthy, A. Qatan, Use of cement bypass dust as filler in asphalt concrete mixtures, J. Mater. Civ. Eng. 14 (4) (2002) 338–343, http://dx.doi.org/10.1061/(ASCE)0899-1561(2002) 14:4(338).

[3] D. Lesueura, J. Petitb, H.J. Ritterc, The mechanisms of hydrated lime modification of asphalt mixtures: a state-of-the-art review, Road Mater. Pavement Des. 14 (1) (2013) 1–16, http://dx.doi.org/10.1080/14680629.2012.743669.

[4] A.H. Aljassar, S. Metwali, M.A. Ali, Effect of filler types on Marshall stability and retained strength of asphalt concrete, Int. J. Pavement Eng. 5 (1) (2004) 47–51, http://dx.doi.org/10.1080/10298430410001733491.

[5] S.D. Ramswamy, M.A. Aziz, Assessment of effect of filler on the stripping of bituminous mix, The 4th Conference of the Road Engineering Association of Asia and Australasia, 1983, pp. 159–170.

[6] S.D. Ramswamy, M.A. Aziz, Effect of filler type and shape of aggregates on the stability of bituminous mixes, The 4th Conference of the Road Engineering Association of Asia and Australasia, 1983, pp. 171–177.

[7] J.C. Rosner, R.D. Pavlouich, J.G. Chehovits, Fly ash as a mineral filler and anti-strip agent for asphalt concrete, Report No. FHWA-AZ-81/173, 1981, USA.

[8] M. Pasetto, N. Baldo, Resistance to permanent deformation of road and airport high performance asphalt concrete base courses, Adv. Mater. Res. 723 (2013) 494–502, 10.4028/www.scientific.net/AMR.723.494.

[9] A. Zulkati, Y. Diew, D.S. Delai, Effects of fillers on properties of asphalt–concrete mixture, J. Transp. Eng. 138 (7) (2012) 902–910, http://dx.doi.org/10.1061/(ASCE)E.1943-5436.0000395.

[10] T. Chompoorat, S. Likitlersuang, Assessment of shrinkage characteristic in blended cement and fly ash admixed soft clay, 15th Asian Regional Conference on Soil Mechanics and Geotechnical Engineering, Japanese Geotechnical Society Special Publication 2(6), 2015, pp. 311–316. doi: http://doi.org/10.3208/jgssp.THA-01.

[11] T. Chompoorat, S. Likitlersuang, Laboratory investigation of hot mix asphalt behaviour for mechanistic-empirical pavement design in tropical countries, Geotech. Eng. J. SEAGS AGSSEA 46 (1) (2015) 37–44.

[12] ASTM D6926, American Society for Testing and Materials, Standard practice for preparation of bituminous specimens using Marshall apparatus, 2010, Washington, DC.

[13] ASTM D6927, American Society for Testing and Materials, Standard test method for Marshall stability and flow of asphalt mixtures, 2015, Washington, DC.

[14] ASTM D4867, American Society for Testing and Materials, Standard test method for effect of moisture on asphalt concrete paving mixtures, 2009, Washington, DC.

[15] ASTM D4123, American Society for Testing and Materials, Standard test method for indirect tension test for resilient modulus of bituminous mixtures, 1995, Washington, DC.

[16] BS DD226, Method for Determining Resistance to Permanent Deformation of Bituminous Mixtures Subject to Unconfined Dynamic Loading, British Standards Institution, UK, 1996.

[17] T. Chompoorat, S. Likitlersuang, An influence of asphalt binder on time-temperature shift function for asphalt concrete at large strains, KSCE J. Civil Eng. (Online) (2016), http://dx.doi.org/10.1007/s12205-016-0665-4.

[18] DH-S 408, 2532, Asphalt Concrete or Hot-Mix Asphalt, Standard of the Department of Highways, Thailand, 1989 (in Thai).

[19] ASTM D692, American Society for Testing and Materials, Standard specification for coarse aggregate for bituminous paving mixtures, 2015, Washington, DC.

[20] M. Aashto, American Association of State Highway and Transportation Officials, Standard specification for fine aggregate for bituminous paving mixtures, 2012, Washington, DC.

[21] M. Aashto, American Association of State Highway and Transportation Officials, Standard specification for mineral filler for bituminous paving mixtures, 2011, Washington, DC.

[22] K. Kanitpong, N. Charoentham, S. Likitlersuang, Investigation on the effects of gradation and aggregate type to moisture damage of warm mix asphalt modified with Sasobit, Int. J. Pavement Eng. 13 (5) (2012) 451–458, http://dx.doi.org/10.1080/10298436.2011.565058.

[23] N. Ali, J.S. Chan, S. Simms, R. Bushman, A.T. Bergan, Mechanistic evaluation of fly ash asphalt concrete mixtures, J. Mater. Civ. Eng. 8 (1) (1996) 19–25, http://dx.doi.org/10.1061/(ASCE)0899-1561.

[24] M. Pasetto, N. Baldo, Influence of the aggregate skeleton design method on the permanent deformation resistance of stone mastic asphalt, Mater. Res. Innovations 18 (S3) (2014) S96–S101, http://dx.doi.org/10.1179/1432891714Z.000000000588.

ENGINEERING JOURNAL

Article

Modeling of Root-reinforced Soil Slope under Rainfall Condition

Suched Likitlersuang[1,*], Akihiro Takahashi[2], and Kreng Hav Eab[1]

1 Geotechnical Research Unit, Department of Civil Engineering, Faculty of Engineering, Chulalongkorn University, 254 Phayathai Road, Wang-Mai, Pathumwan, Bangkok 10330, Thailand
2 Department of Civil Engineering, Tokyo Institute of Technology, M1-3, 2-12-1, Ookayama Meguro-ku Tokyo 152-8552, Japan
*E-mail: fceslk@eng.chula.ac.th (Corresponding author)

Abstract. This paper presents the results of geotechnical centrifuge and numerical modeling study of root-reinforced systems on soil slopes. The centrifuge models were designed to simulate a soil slope reinforced by vetiver grass root system commonly grows in Southeast Asian countries. Unreinforced and root-reinforced soil slope models were subjected to heavy rainfall using a rainfall simulator designed for a geotechnical centrifuge. Results of the study show that the root system causes a reduction of rainwater infiltration rate, delay in the response of groundwater table, and increasing in soil shear strength. The results were validated by comparing centrifuge modeling test results with numerical modeling analyses based on limit equilibrium and finite element methods. The transient seepage analysis results were employed in the slope stability analysis. The numerical analysis shows a good agreement in failure mechanisms with the observations from centrifuge modeling tests.

Keywords: Centrifuge modeling, slope stability, seepage analysis, landslides, vegetation.

ENGINEERING JOURNAL Volume 21 Issue 3
Received 27 September 2016
Accepted 14 December 2016
Published 15 June 2017
Online at http://www.engj.org/
DOI:10.4186/ej.2017.21.3.123

DOI:10.4186/ej.2017.21.3.123

1. Introduction

Landslides induced by rainfall are one of most serious and common disasters worldwide. In recent years, natural slope instability has increased especially in the tropical monsoon zone such as Southeast Asian countries including Thailand. There are several factors that could cause the natural slope failure, such as geological activity, hydrological influence and human interference, but rainfall is usually the main factor. This is because the change of pore water pressures can be induced by ground water rising or infiltration from the rain water. The increase in pore water pressure shall reduce the matric suction and hence decrease the shear strength of soil in unsaturated zone. The physical process of rainfall infiltration into the ground and its seepage through the soil layers have been studied by hydrogeologists, soil scientist and geotechnical engineers [1].

Vegetation along a slope plays a major role in preventing failure as it can provide both hydrological and mechanical benefits to the stability of natural soil slopes. The role of vegetation on slope stability has been defined by Greenway (1978) [2], Coppin and Richard (1990) [3], Wu (1995) [4] and Gray and Sotir (1996) [5]. For the hydrological process, changing the soil moisture regime and drawing the water from the soil via evapotranspiration [6] could increase the soil suction. For mechanical process, the roots of vegetation could enhance slope stability by increasing the shear strength of the soil [5, 7]. The benefits of vegetation along natural soil slopes are to prevent shallow failure and soil surface erosion. However, research to understand fundamental mechanisms of root-reinforced soil slopes is limited, particularly for the study of root reinforcement effects on slope stability.

Vetiver grass (*Vetiveria nemoralis A. Camus*), has been implemented to prevent soil erosion, water runoff, and infiltration by the World Bank in the 1980s [8]. In Thailand, the Chaipattana Foundation and the Office of the Royal Development Projects Board has promoted the use of vetiver grass for soil and water conservation for many royal projects. Vetiver grass is fast growing, cost effective, and requires low maintenance. Chinapan et al. (1997) [9] observed the length of vetiver roots to be up to 2-3.5 m. The vetiver roots can penetrate deep into the ground to form a net-like barrier capable of filtering silt and preserving top soil. In Thailand, slope failure due to prolonged and heavy rainfall typically occurs at shallow depth of approximately 1-1.5 m from the ground surface. As a result, the use of the vetiver grass root system as slope reinforcement is suitable for preventing slope failure. Root area ratio defined as the ratio between the cross-sectional area of root in the shear plane area and the total area of shear plane, plays an important role contributing to the increase of soil shear strength [5]. Eab et al. (2015) [10] correlated the root area ratio of the vetiver roots with the increase of soil shear strength. The root area ratios of the 4-6 month growth group vetiver were in the range of 2.44 – 4.56%. The shear strength of soil with vetiver root system was measured by direct shear tests. Results showed that the cohesion of the reinforced soil was increased approximately 11 kPa compared to unreinforced soil.

Centrifuge modeling was implemented in this study because the centrifuge allows modeling of soil slopes with full-scale stress conditions. Few researchers have investigated the mechanism of vegetation for slope stability through the use of a centrifuge. These models simulated the slope failure by continuously raising the groundwater table (e.g. Sonnenberg et al., 2010, 2012) [11, 12]. Some previous researches have investigated the mechanism of rainfall-induced slope failure based on laboratory tests and filed monitoring [13]. However, it is difficult to model the rainfall in a centrifuge. Recently, centrifuge modeling has been used to model rainfall induced landslides to provide a better understanding of the triggering mechanisms of landslides due to rainfall [14–16]. Eab et al. (2015) [10] focused on the application of root-reinforced system to slope stabilization using a rainfall simulator in the centrifuge. In addition, Ng et al., (2014, 2015) [17, 18] and Kamchoom et al. (2014) [19] studied the effects of root on transpiration-induced soil suction using centrifuge model.

This paper presents the results of centrifuge and numerical modeling of root-reinforced systems on soil slopes. The results of centrifuge tests carried out by Eab et al. (2014, 2015) [16, 10] were validated by comparing with numerical modeling simulations. The pore water pressure generation due to transient seepage was used for the slope stability analysis. Input parameters used for the numerical analysis, including volumetric water content, hydraulic conductivity, and shear strength parameters, were obtained from laboratory testing results. Discussions of results from centrifuge and numerical modeling are provided in this paper.

2. Centrifuge Model Tests

Centrifuge modelling is a physical model test and is now widely used in many geotechnical applications. Since slope stability is a gravity-dependent problem, the major advantage of using centrifuge modelling is to enable researchers to test reduced-scale physical models at the correct stress level by increasing g-level [20]. The centrifuge model tests were conducted at Tokyo Institute of Technology in Japan. The tests were performed at a centrifugal acceleration of 50g. To simulate a heavy rainfall in the centrifuge, a pneumatic nozzle system was designed to spray water over the model slope. Figure 1 shows the schematic of the rainfall simulation system for this study. A brief summary of the experimental details is explained below. More detailed information of centrifuge model tests can be found in Eab et al. (2014, 2015) [16, 10].

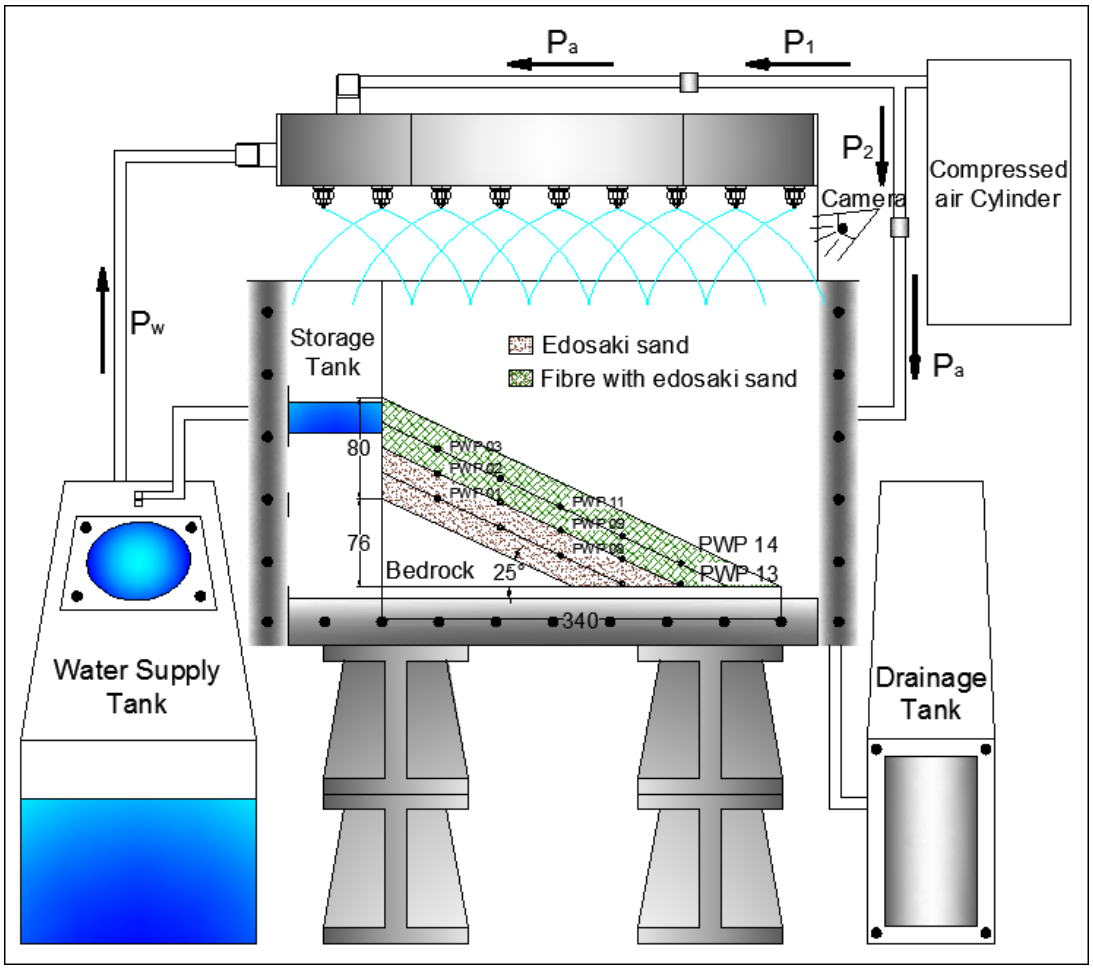

Fig. 1. Schematic centrifuge model with a rainfall simulator system (After Eab et al., 2014) [16].

2.1. Material Properties

The Japan Geotecnical Society (JGS) Standard fine sand called Edosaki Sand was used in the model slopes. The engineering properties of the Edosaki sand are summarized in Table 1. The polyester fibers with approximately 39μm in diameter and 10mm in length were used to model the root fibers. In the model tests, the 2% by mass of polyester fibers were randomly mixed with the sandy soil to model the vegetated slope surface. The 2% fiber mixing by mass is approximately 7% by volume, which is slightly higher than the root area ratio of vetiver root at 6-months growth reported by Eab et al. (2015) [10]. It is noted that the typical values of the root area ratio of 3 – 5% for small vegetation are reported by Gray and Sotir (1996) [5]. The engineering properties of soil mixed with 2% of polyester fiber are summarized in Table 1.

Table 1. Properties of compacted soils (After Eab et al., 2014) [16].

Soil type	Edosaki Sand	Edosaki Sand + 2% by mass of polyester fiber
Specific gravity, G_s	2.65	-
Maximum dry unit weight, γ_d (kN/m^3)	12.9	12.9
Optimum water content, w_{opt} (%)	15.2	17.3
Degree of saturation, S_r (%)	39.9	-
Total unit weight, γ_t (kN/m^3)	14.9	15.2
Void ratio, e	1.01	-
Maximum void ratio, e_{max}	1.29	-
Minimum void ratio, e_{min}	0.87	-
Saturated hydraulic conductivity, Ksat (cm/s)	3.25×10^{-5}	3.08×10^{-5}
Cohesion intercept, c (kPa)	4.8	18.9
Angle of shearing resistance, ϕ (^{o})	28.6	31.5

Shear strength of soil was examined by a standard 60-mm diameter direct shear apparatus. Edosaki sand was prepared to achieve a relative density of 80% and water content of 15%. For a mixture of sand and fiber roots, the sample was prepared at the same degree of compaction but at a water content of 17%. The direct shear tests were carried out to determine the angle of shearing resistance (ϕ) and the cohesion intercept (c) of the Edosaki sands with and without fibers. By adding 2% of polyester fiber into the sand, the cohesion and friction angle of the mixture are increased by approximately 14kPa and 3^o respectively as presented in Table 1. It is noted that the sands were prepared in unsaturated state. Therefore, the shear strength parameters reported in Table 1 are the "apparent" shear strength parameters. However, this result is comparable with the direct shear test results of vetiver root system from Eab et al. (2015) [10]. It is also observed that the coefficient of permeability of the soil and fiber mixture was slightly lower than that of the soil without fibers.

2.2. Slope Model Tests

The slope model was constructed inside a 450mm×150mm×270mm steel box. The model design is schematically illustrated in Fig. 1. Three model cases, i.e., Case 1: without reinforcement, Case 2: with 20-mm fiber reinforcement and Case 3: with 40-mm fiber reinforcement, were conducted and summarized in Table 2.

Table 2. Summary of centrifuge tests (After Eab et al., 2014) [16].

Case No.	Model Description	Setup	Test duration (hr)	Remarks
1	Unreinforced	Bare soil	18	Slope collapsed
2	20-mm thick of fiber-reinforced surface layer	1-m depth of vegetation root	35	Moderate deformed (Not collapsed)
3	40-mm thick of fiber-reinforced surface layer	2-m depth of vegetation root	40	Small deformed (Not collapsed)

To examine the reinforcing effect of the roots against slope failure, the rooting depth is selected as a parameter. The slope model consists of bedrock and soil slope. The bedrock with 165mm in length (8.25m in the prototype), 76mm in height (3.8m in the prototype) and slope angle of 25^o was made of aluminum plates and placed on a 10mm-thick acrylic plate. The surface of bedrock was roughened by attaching a sand

paper. The soil slope consists of four layers of Edosaki sand with a total thickness of 80mm. Pore water pressure transducers (PWPs) and accelerometers (ACCs) were installed in the soil layers during the compaction to measure the pore water pressure and the soil slope displacement. The soil displacements were measured and a testing video was recorded through the transparent front side of the model container. During the test, a rainfall intensity of 1000mm/h (20mm/h in the prototype) classified as heavy rainfall [21] was applied to simulate rainfall over the slope surface. Pore water pressure and soil displacement were continuously recorded during the test. It is noted that the tests were stopped when the collapse of slope or dam-up water at the toe slope was observed.

2.3. Results of Centrifuge Tests

Results showed that the unreinforced slope failed due to the rising groundwater table. It was observed that the failure started to deform from the toe and progressively propagate upward to the top of the slope. Both root-reinforced slopes deformed but did not collapse. The tests were terminated when the failure of the slope was observed or the pressure head at the toe slope reached the critical value. The centrifuge test results are summarized in Table 2. Results indicated that the existence of root fibers helps increase the soil strength and reduce the infiltration rate of rainfall into the ground, resulting in a delayed response in the groundwater table. In other words, roots can delay slope failure and slow movement of a soil slope could provide a first early warning of failure. More detailed discussions of the centrifuge results can be found in Eab et al. (2014) [16].

3. Slope Stability Analysis

Numerical analysis is commonly carried out to validate the results of physical modeling tests and to better understand the effect of suction loss due to rainfall infiltration on slope stability. In this study, the three cases similar to the centrifuge tests were modeled. Each model was performed by using transient analysis to define the pore water pressure change in the soil slope. Based on the pore water pressure information, the factor of safety of the soil slope was calculated using the limit equilibrium methods.

3.1. Seepage and Slope Stability Modeling

Two-dimensional seepage and slope stability analyses were performed using GEO-SLOPE software [22]. Simplified homogenous slope profiles for each soil layer were used in the study. For a transient analysis in seepage, the soil-water characteristic curve (SWCC) and the hydraulic conductivity function are required input parameters. The estimation method to determine the SWCC proposed by Aubertin et al. (2003) [23] was chosen in this analysis. The proposed model assumes that soil-water characteristic results from the combined effect of capillary and adhesion forces. The SWCC can be evaluated from the negative pore water pressure and material property information such as particle-size distribution. In addition, the hydraulic conductivity function can also be estimated using several predictive methods that utilize either a grain-size distribution or a measured volumetric water content function and the saturated hydraulic conductivity (Ksat). In SEEP/W, a built-in predictive method can be used to estimate the hydraulic conductivity function once the volumetric water content function and a Ksat value have been specified. More details of the assumptions of the predictive methods to estimate the SWCC and the hydraulic conductivity function can be seen in the SEEP/W manual [22]. Figures 2(a) and 2(b) present the SWCC and the hydraulic conductivity function used in this study.

The initial total head was defined by specifying the initial water table position at the base of the toe slope. The negative pore water pressure in the unsaturated zone above the water table varies in a linear manner from zero at the base of the toe slope to the maximum value at the surface. For the rainfall simulation, the flux boundary, q equal to the desired rainfall intensity of 20 mm/hr was applied to the surface of the slope. The potential seepage face was also applied at the toe of the slope model. Figure 3 presents the geometry boundary and the initial water pressure conditions for the seepage and slope stability analyses. The pore water pressures were calculated for every time step at each node of the finite-element mesh. The pore water pressure results from SEEP/W were then incorporated into the SLOPE/W model. Slope stability analyses were performed using Bishop's simplified and Morgenstern-Price methods. The input parameters from the direct shear tests shown in Table 1 were used for the slope stability analyses.

DOI:10.4186/ej.2017.21.3.123

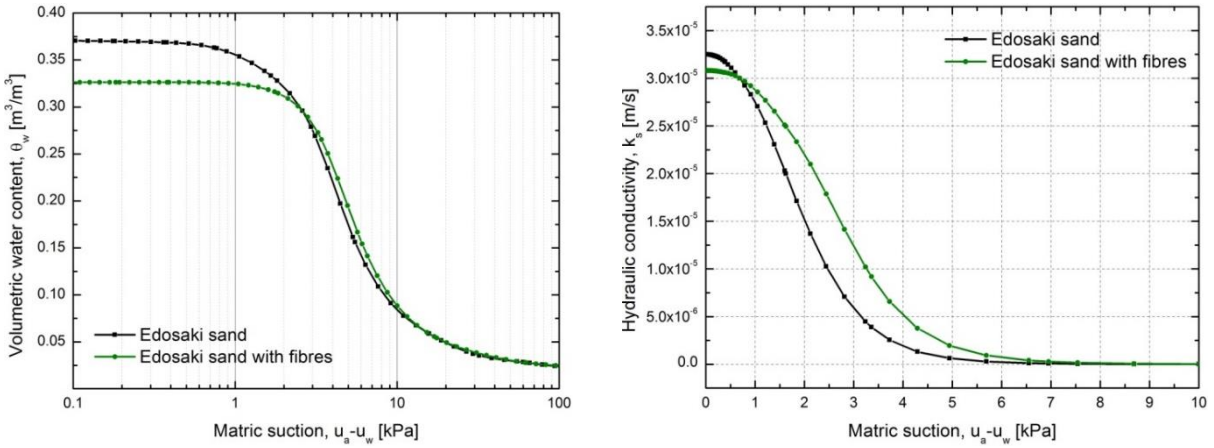

(a) Soil water characteristic curve (b) Hydraulic conductivity

Fig. 2. Input soil water characteristic curve and hydraulic conductivity for seepage analysis

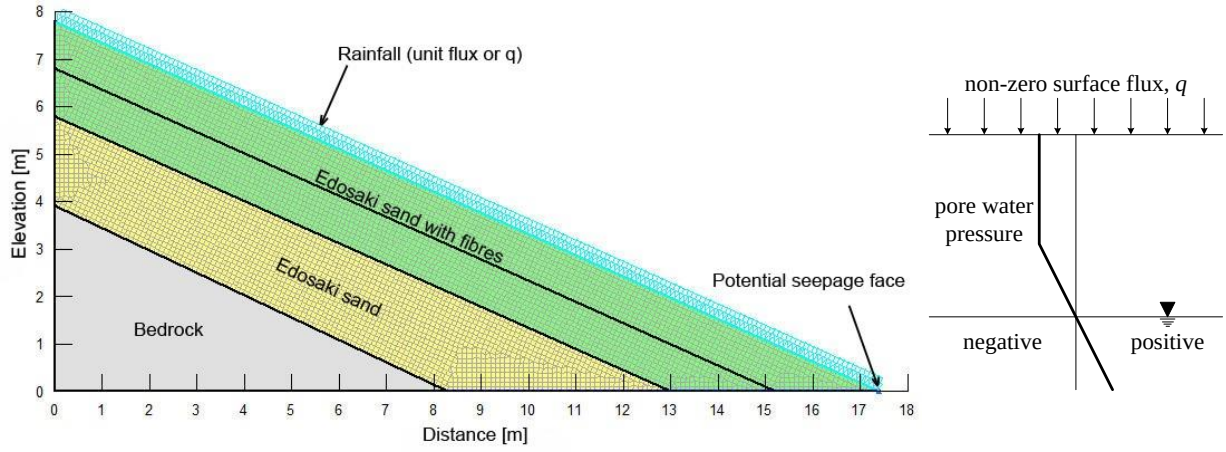

(a) Geometry boundary condition (b) Initial pore water pressure condition

Fig. 3. Boundary and initial conditions for seepage and stability analyses

4. Results and Discussion

4.1. Pore Water Pressure Distribution

Figure 4 shows the pore water pressure contour distribution in the soil slope simulated by the seepage analysis for the three different cases. Results showed that during rainfall, pore water pressure in the soil slope initially started from negative and then moved gradually towards positive values. Figure 4(a) shows the result of the unreinforced case, where the pore water pressure increased by 10kPa at the toe of the slope while at the top slope pressure remained negative after an 18hr duration of rainfall. For the case of 1-m depth of vegetation, shown in Fig. 4(b), the large amount of rainwater infiltrated into the slope and changed the pore water pressure from negative to positive value of 20kPa after 35hr. For the case of 2-m depth of vegetation, shown in Fig. 4(c), pore water pressure increased up to 25kPa after 40hr. Based on these results, it is observed that pore water pressure increased to the critical values when the slope started to fail or deform significantly.

4.2. Slip Surface for Factor of Safety

Figure 5 shows the potential slip surface and ground water table simulated by SLOPE/W. Due to the increase of cohesion by the root reinforcement, the slip surface for the root-reinforced slope was mostly

developed near the bedrock, especially for the case of 2-m depth of vegetation (Fig. 5(c)), in comparison with the slip surface of the unreinforced slope that was developed at shallower depth (Fig. 5(a)). The reason of this occurs is because the shear strength of the soil and root fiber at the top layer is higher than the soil only at the bottom layer. In addition, it was found that the factor of safety (FS) is slightly increased for the reinforced soil slopes as summarized in Table 3. According to the results, the shear strength of unsaturated zone decreased and consequently the FS of the slope reduced during the rainfall. Comparing the FS at the same duration of rainfall, the FS increases with the depth of roots for the root-reinforced cases.

Table 3. Factors of safety from numerical analysis

Case		Circular failure method	Duration of rainfall (hr)		
			18 hr	35 hr	40 hr
Unreinforced slope		Bishop	1.76	-	-
		Morgenstern-Price	1.77	-	-
Root-reinforced slope	1-m depth	Bishop	2.05	1.82	-
		Morgenstern-Price	2.09	1.87	-
	2-m depth	Bishop	2.29	2.01	1.89
		Morgenstern-Price	2.31	2.01	1.90

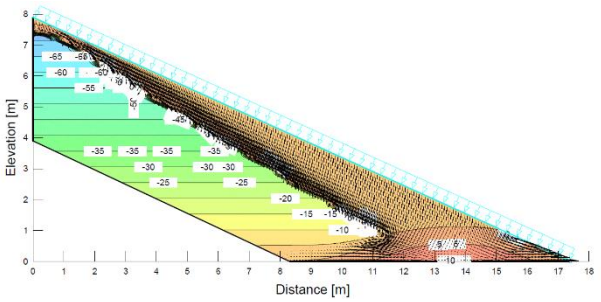

(a) Case 1: unreinforcement

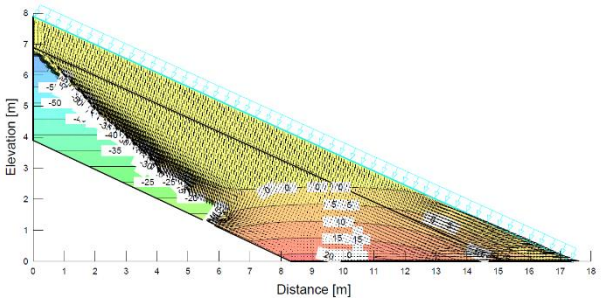

(b) Case 2: 1m depth of root

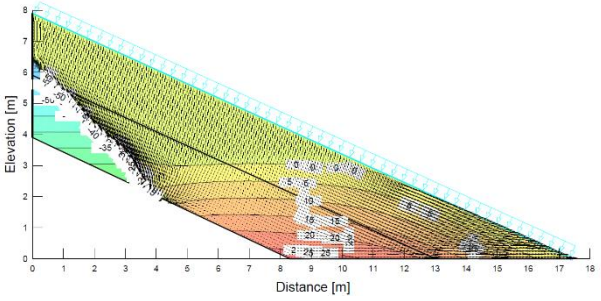

(c) Case 3: 2m depth of root

Fig. 4. Results pore water pressure change at the end of test.

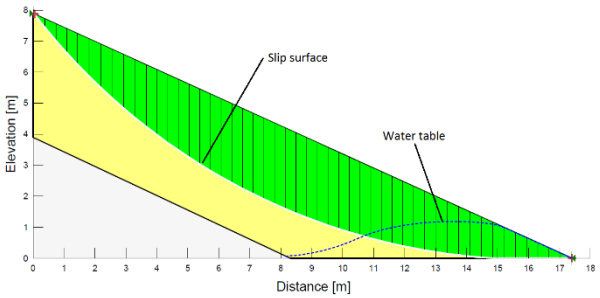

(a) Case 1: unreinforcement

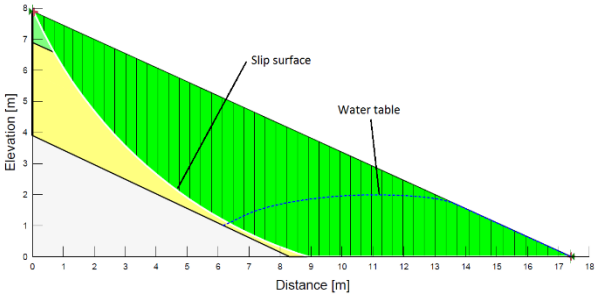

(b) Case 2: 1m depth of root

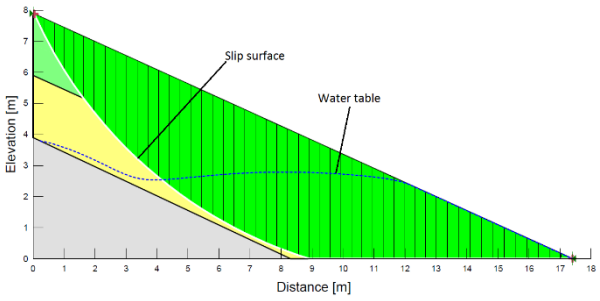

(c) Case 3: 2m depth of root

Fig. 5. Results slip surface at the end of test.

DOI:10.4186/ej.2017.21.3.123

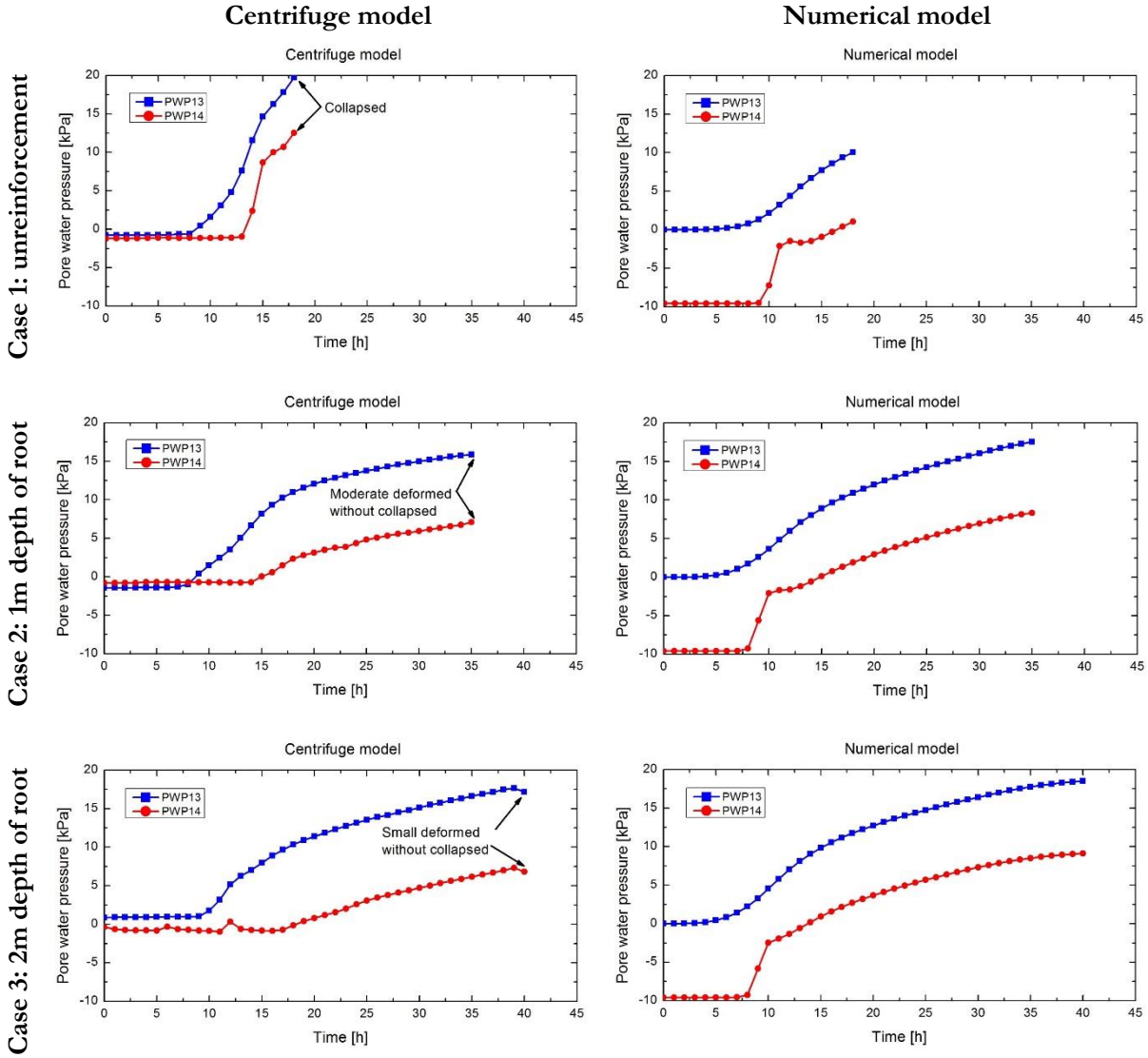

Fig. 6. Comparison of pore water pressure change between centrifuge test and numerical analysis.

4.3. Comparison of Centrifuge and Numerical Modeling Results

Figure 6 shows a comparison of pore water pressure between the centrifuge test and numerical analysis for the unreinforced case, 1-m depth of root case, and 2-m depth of root case. Pore water pressure measured by PWP 13 and PWP 14, which are located near the toe of the slope were plotted with time during the continuous rainfall. The increase of the pore water pressure was used to indicate the triggering time for slope failure as summarized in Table 2. Buildup of pore water pressure for the unreinforced slope is faster than for the root-reinforced slopes. For the unreinforced case, the pore water pressures measured from the centrifuge are much higher than the numerical values. As a result, the factor of safety calculated from the numerical model is higher than expected. This might be due to the fact that the numerical analysis results rely on the input parameters and boundary conditions. In this analysis, assumptions of the SWCC and hydraulic conductivity were made. Despite this, the comparisons show a reasonable agreement between the centrifuge and numerical results with the exception of the negative value measured at PWP 14. This is due to the limitation of pore water pressure transducer installed in the centrifuge test which cannot accurately measure negative pore water pressure. Based on this study, results from both centrifuge and numerical modeling provide good insight into the mechanisms of vegetated root reinforced slope during rainfall. The root-reinforced system delays the rising of the groundwater table and increases the factor of safety of the slope.

5. Conclusions

This research evaluated the effects of vegetation root on slope stability. A series of centrifuge model tests on slopes reinforced by the root model were conducted to illustrate the advantage of the vegetation on the rainfall-induced shallow failure. The results of centrifuge tests were verified by the numerical simulations. Conclusions from this study are as follows.

1) The centrifuge model with rainfall simulator was employed to illustrate the slope instability due to heavy rainfall. The slope failure is triggered by rising of the water table and starts around the toe of the slope. The increase in pore water pressures from water table causes the decrease in the effective stress and shear strength of the soil.
2) The polyester fiber mixed soil can be reasonably used to model the vegetated soil slope in the centrifuge. The results showed that roots in the surface of a slope tie the soil particles together and prevent the formation of cracks on the slope surface. The reinforcement efficiency increases with the root depth and the thicker reinforced zone reduces the slope deformation. In addition, the roots can delay the infiltration of rainfall into the ground to delay the rising of the groundwater table. The delay of slope failure or movement could provide an early warning for evacuation.
3) Results from numerical analyses show an agreement with the results observed in centrifuge model tests. The factor of safety of the slope increases as the depth of root reinforcement increases. The mixture of soil and fiber roots increase the shear strength of soil, hence it provides overall improvement of the slope stability.

Acknowledgements

This research was supported by the Thailand Research Fund under the TRF Research Scholar Award Grant No. RSA-5880023. The work was also carried out under the research and development project on landslide prevention and protection according to Royal Initiatives of the Chaipattana Foundation. The authors would like to thank Dr. Inthuorn Sasanakul for her comments to improve the manuscript.

References

[1] C. W. W. Ng and Q. Shi, "A numerical investigation of the stability of unsaturated soil slope subjected to transient seepage," *Computer and Geotechnics*, vol. 22, no. 1, pp. 1-28, 1998. doi:10.1016/S0266-352X(97)00036-0

[2] D. R. Greenway, "Vegetation and slope stability," in *Slope Stability*, M. G. Anderson and K. S. Richards, Eds. New York, NY: John Wiley and Sons, 1978.

[3] N. J. Coppin and I. G. Richards, *Use of Vegetation in Civil Engineering Construction Industry and Research Information Association (CIRIA)*. London: Butterworths, 1990.

[4] T. H. Wu, "Slope stabilization," in *Slope Stabilization and Erosion Control*, R. P. C. Morgan and R. J. Rickson, Eds. London: E&FN Spon, 1995.

[5] D. H. Gray and R. B. Sotir, *Biotechnical and Soil Bioengineering Slope Stabilization: A Practical Guide for Erosion Control*. New York: John Wiley & Sons, 1996.

[6] F. H. Ali and N. Osman, "Shear strength of a soil containing vegetation roots," *Soils and Foundation*s, vol. 48, no. 4, pp. 587-596, 2008.

[7] T. H. Wu, W. P. McKinnell, and D. N. Swanston, "Strength of tree roots and landslides on Prince of Wales Island, Alaska," *Canadian Geotechnical Journal*, vol. 16, pp. 19-33, 1979.

[8] J. C. Greenfield, "Vegetative vs. mechanical soil conservation system as they affect moisture conservation and sustained production," in *Proceedings of the First International Conference on Vetiver*, Office of the Royal Development Projects Board, Bangkok, 1996, pp. 1-7.

[9] W. Chinapan, A. Sukhasem, and L. Moncharoen, *A Study on the Ecotype Comparison of Vetiver Grass in Thailand*. Land Development Department, Ministry of Agriculture and Cooperatives, Thailand, 1997.

[10] K. H. Eab, S. Likitlersuang, and A. Takahashi, "Laboratory and modelling investigation of root-reinforced system for slope stabilization," *Soils and Foundations*, vol. 55, no. 5, pp. 1270-1281, 2015. doi:10.1016/j.sandf.2015.09.025

[11] R. Sonnenberg, M. F. Bransby, P. D. Hallett, A. G. Bengough, S. B. Mickovski, and M. C. R. Davies, "Centrifuge modelling of soil slopes reinforced with vegetation," *Canadian Geotechnical Journal*, vol. 47, pp. 1415-1430, 2010. doi:10.1139/T10-037
[12] R. Sonnenberg, M. F. Bransby, A. G. Bengough, P. D. Hallett, and M. C. R. Davies, "Centrifuge modelling of soil slopes containing model plant roots," *Canadian Geotechnical Journal*, vol. 49, pp. 1-17, 2012. doi:10.1139/t11-081
[13] H. Chen, C. F. Lee, and K. T. Law, "Causative mechanisms of rainfall-induced fill slope failures," *ASCE Journal of Geotechnical and Geoenvironmental Engineering*, vol. 130, no. 6, pp. 593-602, 2004.
[14] H. Ling and H. Ling, "Centrifuge model simulations of rainfall-induced slope instability," *Journal of Geotechnical and Geoenvironmental Engineering*, vol. 138, no. 9, pp. 1151–1157, 2012. doi:10.1061/(ASCE)GT.1943-5606.0000679
[15] A. Takahashi, K. Nakamura, and S. Likitlersuang, "On the seepage-induce failure of vegetation-stabilised slopes," in *Proceeding of the 8th International Conference on the Physical Modelling in Geotechnic*, Gudin & White, Eds. London: Taylor & Francis Group, 2014, pp. 1233-1239.
[16] K. H. Eab, A. Takahashi, and S. Likitlersuang, "Centrifuge Modelling of root-reinforced soil slope subjected to rainfall infiltration," *Geotechnique Letters*, vol. 4, pp. 211-216, 2014. doi:10.1680/geolett.14.00029
[17] C. W. W. Ng, A. K. Leung, V. Kamchoom, and A. Garg, "A novel root system for simulating transpiration-induced soil suction in centrifuge," *Geotechnical Testing Journal*, vol. 37, no. 5, pp. 1-15, 2014. doi:10.1520/GTJ20130116
[18] C. W. W. Ng, V. Kamchoom, and A. K. Leung, "Centrifuge modelling of the effects of root geometry on transpiration-induced suction and stability of vegetated slopes," *Landslides*, vol. 13, no. 5, pp. 925-938, 2016. doi:10.1007/s10346-015-0645-7
[19] V. Kamchoom, A. K. Leung, and C. W. W. Ng, "Effects of root geometry and transpiration on pull-out resistance," *Géotechnique Letter*, vol. 4, pp. 330-336, 2014. doi:10.1680/geolett.14.00086
[20] R. N. Taylor, *Geotechnical Centrifuge Technology*. Taylor and Francis, 1995.
[21] M. C. Llasat, "An objective classification of rainfall events on the basis of their convective features: Application to rainfall intensity in the northeast of Spain," *International Journal of Climatology*, vol. 21, no. 11, pp. 1385–1400, 2001.
[22] GEO-SLOPE, *Stability Modeling with SLOPE/W 2007 Version—An Engineering Methodology*, 4th ed. Alberta, Canada: GEO-SLOPE International, Ltd., Nov. 2008.
[23] M. Aubertin, M. Mbonimpa, B. Bussière, and R. P. Chapuis, "A model to predict the water retention curve from basic geotechnical properties," *Canadian Geotechnical Journal*, vol. 40, no. 6, pp. 1104-1122, 2003. doi:10.1139/t03-054

Applied Clay Science 146 (2017) 316–324

Contents lists available at ScienceDirect

Applied Clay Science

journal homepage: www.elsevier.com/locate/clay

Research paper

Deformation characteristics and stress responses of cement-treated expansive clay under confined one-dimensional swelling

Sopheap Por[a], Satoshi Nishimura[b], Suched Likitlersuang[c,*]

[a] Department of Civil Engineering, Faculty of Engineering, Chulalongkorn University, Bangkok, Thailand.
[b] Faculty of Engineering, Hokkaido University, Japan.
[c] Geotechnical Research Unit, Department of Civil Engineering, Faculty of Engineering, Chulalongkorn University, Bangkok, Thailand.

ARTICLE INFO

Keywords:
Expansive clay
Cement-treated soil
One-dimensional compression
Lateral coefficient of earth pressure
Swelling pressure

ABSTRACT

This study presents an investigation of the effects of cement addition to expansive clay on its deformation characteristics and stress responses during swelling. The effects were evaluated by focusing on the unconfined compressive strength, swelling-shrinkage strains under various conditions, and the lateral coefficient of earth pressure during one-dimensional deformation for artificial mixtures of two different clays at three different ratios. The clays used in this study were a Na-montmorillonite bentonite and a non-expansive Bangkok clay, mixed at different proportions to simulate naturally encountered expansive clays with different degrees of swelling potential. The experimental programme involved unconfined compression, areal shrinkage strain by unconfined drying, vertical free swelling strain, and confined swelling pressure tests. The experimental results show that the cement addition led to marked decreases in the areal shrinkage strain and vertical free swelling strain in addition to the obvious improvement of strength and stiffness of soils. The confined swelling pressure test results indicated that the cement had a greater effect in reducing vertical swelling pressure than the lateral swelling pressure of the soils during one-dimensional swelling. The measured lateral coefficient of earth pressure and stress paths of untreated and cement-treated soils and their engineering implications are discussed.

1. Introduction

Expansive soils exhibit significant swelling and shrinkage upon changes in water content and stress conditions. The swelling and shrinkage phenomenon of expansive soils is considered as serious and challenging problems in geotechnical engineering due to the potential damages arising from unpredictable upward movements and large settlement of structures founded on such soils undergoing moisture content fluctuations (Nelson and Miller, 1992; Al-Rawas et al., 2005; Puppala et al., 2013). According to Katti et al. (2002), Ferber et al. (2009), and Mohamed et al. (2013), soils' swelling potential depends mainly on nature and state of soils (i.e., clay fraction, mineralogy, dry density, water content, etc.) determining the amount of water intake. The predominant mineral content in an expansive soil is often montmorillonite, which causes the soil to swell and shrink during wetting and drying (Komine and Ogata, 1999; Radhakrishnan et al., 2014). The swelling and shrinkage movement or a change in swelling pressure of expansive ground does not take place only in the vertical direction (Mohamed et al., 2013; Wang et al., 2015). Expansive soils swell laterally as well as vertically. As reported by Andy (1989) the lateral swelling pressure could be 2–10 times larger than the vertical swelling pressure, depending on the conditions. If these pressures are greater than the foundation resistance or retaining wall capacity, then uplifts, often uneven and differential, and/or horizontal movements will occur. This might cause cracks or damage to structures. Retaining structures, in particular, are normally not designed to endure the enormous swelling pressure.

Recently, measuring and assessing the swelling deformation and pressure are given a particular importance in designing foundations on expansive soils. In evaluating the swelling pressure, some researchers suggest a technique that allows soil to heave until attaining the equilibrium and then apply pressure to bring it back to the original volume (Katti et al., 2002), while other researchers propose zero swelling (constant volume) tests and one-dimensional consolidation tests for predicting heaves in swelling soils (Fredlund, 1969; Basma et al., 1995; Al-Shamrani and Dhowian, 2003; Wang et al., 2012; Rao and Ravi, 2015). However, these methods generally concern only the vertical swelling pressure measurement. There is still no systematic knowledge that allows the designer to predict the lateral swelling pressures on geotechnical structures due to swelling soils (Mohamed et al., 2013).

* Corresponding author.
E-mail addresses: nishimura@eng.hokudai.ac.jp (S. Nishimura), fceslk@eng.chula.ac.th (S. Likitlersuang).

http://dx.doi.org/10.1016/j.clay.2017.06.022
Received 22 March 2017; Received in revised form 21 June 2017; Accepted 23 June 2017

For non-swelling soils, on the other hand, the established theory of earth pressure based on force equilibrium and perfect plasticity may be adopted without a particular need to consider the additional pressure due to the mineral swelling. Therefore, many geotechnical projects opt for excavating and replacing the entire expansive soil or to improve them comprehensively. Much more cost-effective measures would be devised, however, if it is understood how the stress responds during swelling, and how the responses may be altered by more modest means such as adding a limited dose of binding agents such as lime or cement.

The lateral coefficients of earth pressure of different soils under various conditions have been investigated by some researchers; e.g. Katti et al. (2002) on the lateral earth pressure of the expansive black cotton soil, Tian et al. (2009) on the coefficients of earth pressure at rest in thick and deep layers of swelling clay. However, research on the lateral coefficient of earth pressure of expansive soils is still limited in number and scope. This research aims to understand and evaluate the effect of cement addition on curbing the undesirable swelling pressure of expansive problematic soils through a variety of readily measurable mechanical quantities as well as close observation of the effective stress path obtained by more elaborate tests. The investigation mainly focuses on the strength-stress-strain characteristics and the earth pressure responses in expansive soils under one-dimensional swelling with and without cement treatment. The latter is expressed in terms of the lateral coefficient of earth pressure (K_s). Artificial expansive soil specimens were prepared for mechanical testing by mixing a Na-montmorillonite bentonite with non-expansive Bangkok clay at different proportions to observe responses of soils with different swelling potentials. In addition to swelling tests in the specially designed oedometer, a number of more conventional laboratory experiments were performed on both cement-treated and untreated soils. Based on the results from these different tests, this paper presents observations on general effects of cement addition on mechanical responses of expansive soils.

2. Experimental programme

2.1. Materials

The expansive soil specimens tested in this study were artificially prepared by mixing a commercially available Na-montmorillonite bentonite with natural non-expansive Bangkok clay, which is locally found in the central of Thailand. Bangkok clay is a soft marine silty clay, characterised by high water content, low shear strength, and high compressibility (Horpibulsuk et al., 2011; Surarak et al., 2012). Na-montmorillonite has low permeability and marked expansibility due to its stacked-lamellar structure (Por et al., 2015). Bangkok clay is a clay with low swelling potential exhibiting physical and engineering properties similar to those of kaolin, while Na-bentonite is a clay with a very high swelling potential. In this study, the Bangkok clay was firstly air-dried for about one week. It was then crushed and sieved through a No. 40 sieve (425 μm). The mixing proportions between the bentonite and Bangkok clay (in the form of powder) were varied at 40:60, 20:80 and 0:100 by dry weight. Ordinary Portland cement was added at 5% and 10% of the dry soil mixture (i.e. bentonite plus Bangkok clay) by weight. Unless specified otherwise, the mixed soils with and without cement treatment were compacted at the optimum moisture content (OMC) and maximum dry density (MDD) of the untreated states, which were obtained from a modified compaction test (ASTM D1557). The compacted specimens were prepared for the unconfined compression, the vertical free swelling strain and the confined swelling pressure tests after 28 days of curing. The index properties and physical properties of compacted untreated soils were determined by following the ASTM standards, as presented in Table 1. Chemical compositions of materials were analysed by X-ray fluorescence (Bruker AXS, Germany model S4 Pioneer Wavelength dispersive X-Ray Fluorescence [WDXRF] Spectrometry). Table 2 lists the chemical composition of bentonite, Bangkok clay and cement obtained by the X-ray fluorescence (XRF) analysis.

Table 1
Experimental conditions and properties of compacted cement-untreated soils.

Sample notation	BKK:B (%)	Initial state: 100% degree of compaction at modified compacted energy				Index properties			
		OMC (%)	ρ_d (Mg/m^3)	e_0	S_{r0} (%)	LL (%)	PI (%)	G_s (−)	A (−)
BKK100B0	100:0	15.50	1.70	0.55	74	72	41	2.64	0.55
BKK80B20	80:20	16.60	1.67	0.61	73	102	65	2.69	0.92
BKK60B40	60:40	20.50	1.60	0.73	78	191	152	2.76	2.23

Remarks: BKK = Bangkok clay content by weight (%); B = Bentonite content by weight (%); OMC = optimum moisture content (%); ρ_d = dry density of a compacted soil at OMC by a modified compacted energy (Mg/m^3); e_0 = initial void ratio; S_{r0} = initial degree of saturation (%); LL = liquid limit (%), PI = plasticity index (%); G_s = specific gravity; A = activity number.

Table 2
Percentage of chemical composition of bentonite, Bangkok clay and cement obtained from XRF.

Chemical composition	Bentonite (%)	Bangkok clay (%)	Cement (%)
SiO_2	50	63	21
Al_2O_3	19	21	5
FeO	15	8	4
CaO	5	–	65
MgO	3	2	1
K_2O	–	3	1
Na_2O	3	1	–
Others	5	3	4

More details on physical properties of these soils are given by Por et al. (2015).

2.2. Testing methods

The experimental programme is summarised along with the sample notation in Table 3. The experimental programme is consisted of unconfined compression (UC), areal shrinkage strain (ASS), vertical free swelling strain (VFSS), and confined swelling pressure (CSP) tests, as well as the index properties tests. A brief summary of the laboratory procedures and equipment used are presented in the following sections.

2.2.1. Unconfined compression (UC) test

The unconfined compressive strength (q_u) and Young's modulus at half the failure stress (E_{50}) of the untreated and cement-treated soils were obtained by performing conventional unconfined compression tests according to ASTM D2166. The specimens were trimmed to 70 mm diameter and 150 mm height and tested at a loading rate of 0.75 mm/min after the 28-day curing.

2.2.2. Areal shrinkage strain (ASS) test

The soils at different mixing proportions, with and without cement as shown in Table 1, were prepared in the form of powder and then uniformly mixed with water content at the liquid limits (w_L) of the cement-untreated states, and placed in a 120 mm × 20 mm × 5 mm mould. The soil specimens were cured for 28 days in advance to allow the cement hydration. The soil specimens in the mould were then firstly air-dried in a controlled temperature room of 30 ± 1 °C and a relative humidity of 50 ± 2% for 7–10 days to reach a stable moisture content. At this stage, cracks formed in the soil specimens in irregular patterns, as shown in Fig. 1. Image analysis was then performed to determine the area (projected to a plane which included the largest cross-section, 120 mm × 20 mm, of the specimens) of the void increment after air-drying (A_c) and the area of the sample before cracking (A_t). The testing

Table 3
Overview of experimental programme.

Sample notation	Proportion		Test performed			
	BKK:B (%)	Cement content (%)	ASS	UC	VFSS	CSP
			Measured parameter			
			ASS, $w_{a.d}$	q_u, E_{50}	ε_v	σ_v', σ_h', K_s, C_s, p', q
			Initial moisture content (set at the untreated soil stage)			
			w_L ± 1%	OMC ± 0.2%		
BKK100B0	100:0	0	✓	✓	✓	✓
BKK100B0C5		5	✓	✓	✓	✓
BKK100B0C10		10	✓	✓	✓	–
BKK80B20	80:20	0	✓	✓	✓	✓
BKK80B20C5		5	✓	✓	✓	✓
BKK80B20C10		10	✓	✓	✓	–
BKK60B40	60:40	0	✓	✓	✓	✓
BKK60B40C5		5	✓	✓	✓	✓
BKK60B40C10		10	✓	✓	✓	–

Materials: BKK = Bangkok clay content; B = Bentonite content.
Tests: UC = unconfined compression; ASS = areal shrinkage strain; VFSS = vertical free swelling strain; CSP = confined swelling pressure.
Measured values: q_u = unconfined compressive strength; E_{50} = Young's modulus at half the failure stress; $w_{a.d}$ = air-dry moisture content (at 30 °C and RH = 50%); w_L = water content of untreated specimen at LL; ε_v = vertical strain; σ_v' = vertical effective stress; σ_h' = horizontal effective stress; K_s = coefficient of lateral earth pressure; C_s = swelling index; p' = mean effective stress; q = deviator stress.

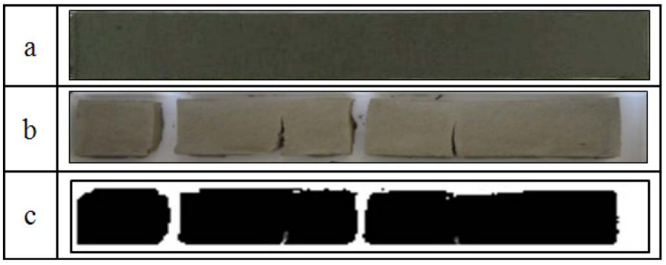

Fig. 1. Typical photograph of soil specimen surface area before and after air-drying; (a) before air-dried, (b) after air-dried, (c) binarised to black and white after image thresholding on air-dried specimens.

procedures and further details on the image analysis technique can be found in Puppala et al. (2004) and Por et al. (2015). The areal shrinkage strain (ASS) can be determined by taking the ratio between A_c and A_t as:

$$ASS = A_c/A_t \quad (1)$$

2.2.3. Vertical free swelling strain (VFSS) test

The vertical free swelling strain (VFSS) tests were performed on all the compacted specimens at the same conditions as for the UC tests. The specimen was trimmed to 60 mm diameter and 24 mm height, and then placed into a rigid mould with an open face at the top. The specimen in the mould was then submerged in water. The specimen was indirect contact with water at the top. The specimen bottom also had a free access to water through a sheet of filter paper laid between the specimen and the percolated mould base. The vertical free swell of the specimen was recorded by using an electronic digital calliper until the deformation reached a stable state. The VFSS was determined by taking the ratio between the increase in height (Δh) to the original height (h_0) of the specimen as:

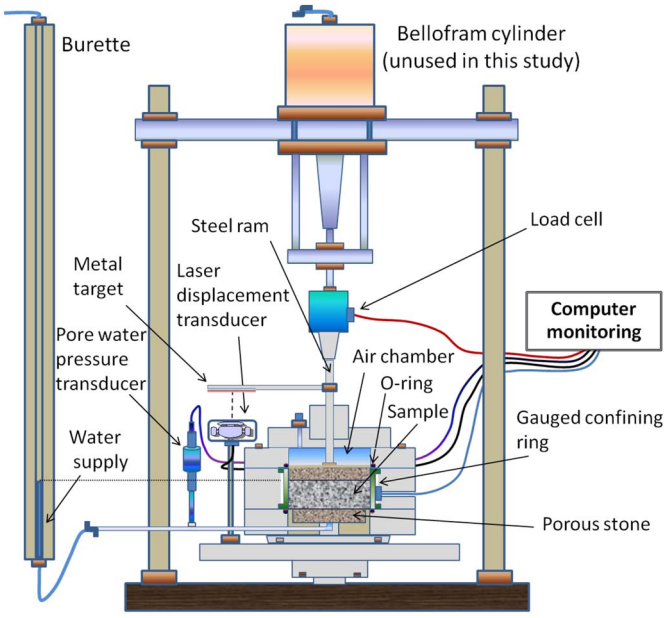

Fig. 2. Confined swelling pressure (CSP) oedometer measuring lateral and vertical swelling pressures.

$$VFSS = \Delta h/h_0 \quad (2)$$

2.2.4. One-dimensional confined swelling pressure (CSP) test

The vertical and lateral swelling pressures of the untreated and cement-treated soils under one-dimensional swelling were measured in a medium-scale oedometer equipped with a gauged confining ring to record the horizontal reaction pressure. The specimen size was 75 mm in diameter and 25 mm in height. The apparatus is illustrated in Fig. 2. The vertical swelling force of the soil specimen was recorded by using a low-compliance load cell with a large capacity (20 kN). The gauged confining ring, manufactured of stainless steel with a thickness of about 2.5 mm, was calibrated by applying air pressure when the chamber was completely sealed. The structure and configuration of the confining ring made it susceptible to offset shifts when the bolts were tightened to assemble the whole apparatus. Through a number of calibration trials; however, it was confirmed that the linearity of the response and the calibration factor were unchanged. The offset were therefore readily corrected simply by noting the shifts. The lateral swelling strain was thus restrained while the vertical strain was allowed to develop by controlling the ram displacement.

The specimen was installed in the apparatus and the swelling strains were initially kept to zero in both lateral and vertical directions (ε_h = 0%, ε_v = 0%) by fixing the vertical ram. Then the specimen in the apparatus was allowed to freely suck the water from a burette connected to the bottom of the specimen through a porous stone, as shown in Fig. 2.

This process guaranteed that the matric suction at the end of each equilibrium stage was always zero. The air pressure in the chamber was always equal to the atmospheric pressure in a temperature-controlled room (25 ± 1 °C). The pressure vent in the chamber was loosely plugged to prevent a humidity loss. The swelling was allowed in 5 steps, in which the lateral swelling strain was always restrained to be zero (ε_h = 0%) and the vertical swelling strain, ε_v, was allowed to develop to 2%, 4%, 6%, and 8% by raising the ram and waiting for swelling. In the first step, the specimen in the apparatus was not allowed to swell (no volume change) until the specimen stopped sucking the water from the burette and reached stable vertical and lateral swelling pressures. This process typically took 7 to 14 days. The swelling pressure of the specimen in the apparatus in the first step was the maximum in both vertical and horizontal directions. For step 2 to step 5 (ε_v = 2, 4, 6 and

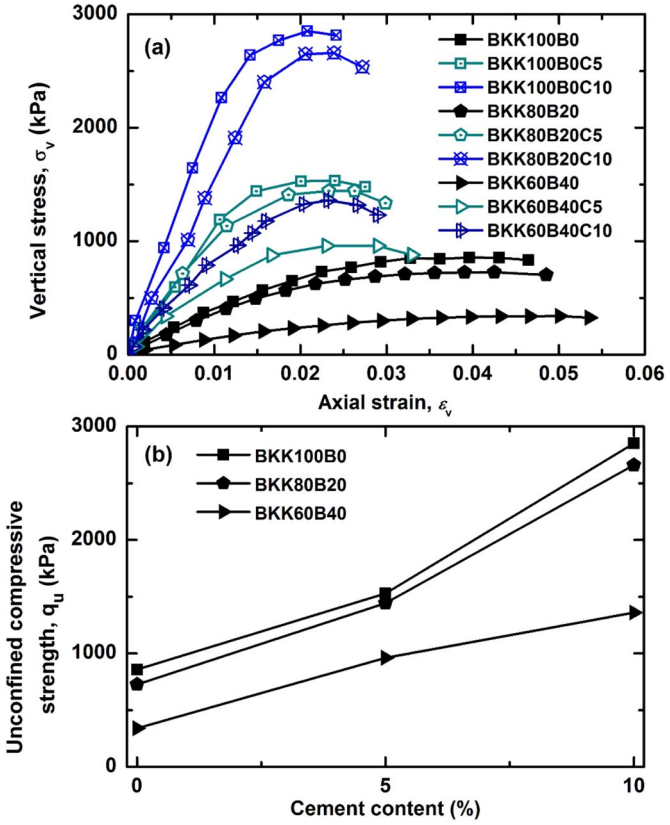

Fig. 3. (a) Relationships between stress and strain from unconfined compression tests; (b) Unconfined compressive strength of untreated and cement-treated soils.

8%, respectively), the procedures were similar.

3. Strength and deformation characteristics

3.1. Strength characteristics

The stress-strain and strength-cement content relationships of the untreated and cement-treated soils from the unconfined compression tests are plotted in Fig. 3. From untreated to cement-treated specimens, the failure pattern changes from ductile to brittle. The stress-strain curves obtained from different BKK:B mix ratios showed a similar contrast between the untreated and cement-treated specimens in terms of shape. All the untreated soil specimen exhibited a ductile behaviour with a continuous strain-hardening until a steady state was reached at a failure strain (ε_f) of 4.0% to 5.5%. All of the stress-strain curves of the cement-treated soils after 28-day curing had a higher peak and smaller ε_f (2.5%–2.8%, and 2.1%–2.5% for 5 and 10% cement content, respectively), compared with those of the untreated soils. The lower liquid limit (LL) soil (i.e. 100% Bangkok clay) presented the highest unconfined compressive strength (q_u) at lower ε_f in both cement-treated and untreated states. The increase of q_u and decrease of ε_f correlated well with the post-hydration reduction of LL and plasticity index (PI) due to the cement addition (Table 4). The reduction in LL and PI caused a significant increase of q_u through reduction of liquidity index as well as formation of inter-particle bonding by the cement hydrates. The strength improvement due to cement addition was greater for the higher LL soils (Table 4). This indicates that, for the soils with higher LL (more bentonite), the cement had a greater effect of improving the strength and decreasing the strain at failure than for the soils with lower LL (Table 4 and Fig. 3). Although the absolute value of strength is smaller for higher LL (lower BKK) specimens (Table 4), the strength improvement ratio is greater for them.

The q_u values of all the specimens are plotted against added cement content in Fig. 3(b). The cement addition led to an increase of the Young's modulus (E_{50}), as summarised in Table 4. Åhnberg (2006) and Åhnberg and Holmén (2008) on stabilised Swedish soils and Raftari et al. (2014) on cement-treated kaolin clays similarly found that, as the strength level increased, the stiffness of the materials also increased. The E_{50} values increased by 3–5 and 4–6 times when 5 and 10% cement was added to the soils, respectively. These results imply that the addition of a modest amount of cement to the expansive soils increases the stiffness, peak strength and brittleness markedly. According to AUSTROADS (2004), for example, a maximum 28-day curing q_u of 1 MPa is specified to be a criterion for a swelling soil improvement in road subgrades. Table 4 shows that q_u values of the BKK100B0 and BKK80B20 specimens treated with 5 and 10% cement and cured for 28 days are all larger than 1 MPa. However, for the 40% bentonite specimens (BKK60B40), only more than 10% cement could increase q_u to fulfil the above strength requirement. This relationship between the treated strength, soil plasticity and added cement content must be more generalised for other swelling soils to obtain a general trend which serves as first guide to estimate necessary cement doses for preliminary design.

Table 4
Results of unconfined compression, areal shrinkage strain, vertical free swelling strain, and Atterberg limits tests of untreated and cement-treated soils.

Sample notation	UC		ASS (after 7 to 10 days air-drying)		VFSS (after 60 days soaking)	Atterberg limits of remoulded specimen after 28 days curing			
	q_u (kPa)	E_{50} (MPa)	$w_{a.d}$ (%)	ASS (%)	ε_v (%)	LL (%)	PL (%)	PI	SL (%)
BKK100B0	857	40	8	20	55.6	72	31	41	14
BKK100B0C5	1529	126	7	15	12.8	52	35	17	21
BKK100B0C10	2850	236	7	6	1.6	48	37	11	25
BKK80B20	725	36	10	34	131.6	102	37	65	16
BKK80B20C5	1443	120	9	26	24.4	65	41	24	18
BKK80B20C10	2659	136	9	10	9.9	57	43	14	26
BKK60B40	339	14	13	49	162.0	191	39	152	12
BKK60B40C5	960	66	12	46	46.6	85	45	40	20
BKK60B40C10	1359	77	12	39	15.4	63	48	15	23

3.2. Shrinkage strain characteristic

Shrinking in expansive soils is interrelated to swelling and thus requires attention in this research. The shrinkage process due to drying may be idealised by two stages; a loss of water without desaturation from the w_L down to the w_s (the water content at shrinkage limit), followed by desatuartion without volume changes from the w_s down to $w_{a.d}$, which is defined as the residual water content after air-drying. The measured values for $w_{a.d}$ are presented in Table 4. The soils with higher LL, when dried from the w_L, showed higher $w_{a.d}$, as shown in Table 4. This is because the ability to retain water after air-drying correlates well with the same ability at the LL. Hence, at a same air-drying condition (temperature and humidity), the soils with higher LL presents higher $w_{a.d}$. Under the above idealisation, the volumetric strain due to air-drying is calculated as $(w_i - w_s)G_s / (1 + w_i G_s)$, where w_i is the initial water content before drying (in this test series, equal to w_L of the untreated specimen). When the strain magnitude is modest, the ASS is calculated as following:

$$ASS = \frac{2(w_i - w_s)G_s}{3(1 + w_i G_s)} \quad (3)$$

The measured areal shrinkage strains (ASS) of the cement-treated and untreated soils are presented in Fig. 4 against the ASS estimated based on the above relationship. As the equation suggests, the ASS of the untreated soils with larger $w_i = w_L$ (i.e. larger bentonite content) is significantly larger, reaching 49% for BKK60B40C0, although the three

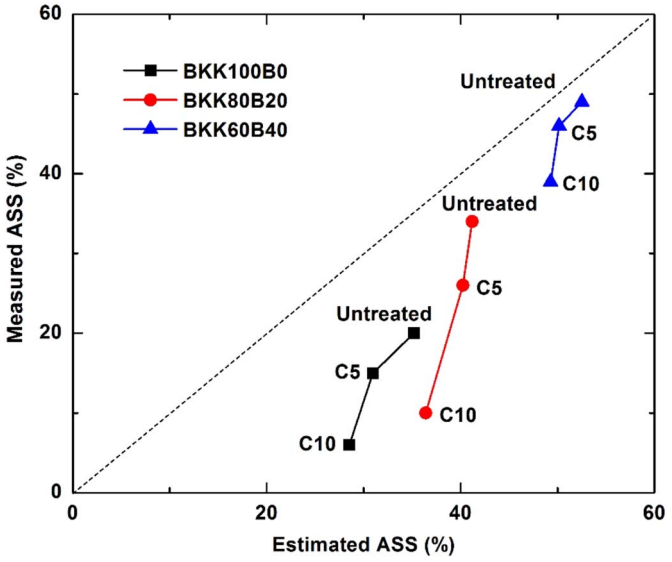

Fig. 4. Areal shrinkage strain (ASS) of untreated and cement-treated soils.

data points for untreated states did not exactly lie on the 1:1 line due possibly to the approximation and idealisation explained above.

When the cement was added, the ASS decreased notably. When the cement-treated mixtures were remoulded and tested for Atterberg limits, the SL significantly increased. This increase explains part of the ASS reduction via Eq. (3). However, the effects of the cement addition seen in Fig. 4 are not fully explained by the SL increase, as the ASS decreased much more than Eq. (3) estimates (i.e. along the 1:1 line in Fig. 4). The inter-particle bonding that developed in the cured cement-treated mixtures and resulting stiffness of the soil skeleton played a significant role in reducing the ASS, possibly by resisting the shrinkage and leading to early desaturation during drying. The bulk stiffness characteristics of the tested specimens is discussed in later sections.

3.3. Vertical free swelling strain characteristic

The vertical free swelling strain (VFSS) was defined as the percentage swell of a laterally confined specimen, which is submerged in water after being compacted to the maximum dry density and optimum moisture content by the modified compaction test (ASTM D1557). The results of the VFSS tests of the untreated and cement-treated soils are summarised in Table 4 and plotted in Fig. 5. Fig. 5(a) shows the variation of VFSS with time for untreated and cement-treated soils. The early swelling strain rate of the higher LL soils was greater than that of the lower LL soils. It was observed that, for the 24 mm-thick specimens, notable swelling lasted up to 30 days in the untreated soils, while the time was significantly reduced by increasing amount of added cement. In general, the time needed for completion of the swelling as well as the maximum swelling strain was closely associated with the swelling clay content (i.e. bentonite content) for both cement-treated and untreated soils.

Different series of tests performed by Por et al. (2015), who studied the same mixtures as reported in this study, are informative. Observing swelling prior to CBR measurements, the specimens also took around 30 days to complete swelling under a small surcharge of 2.5 kPa, although the eventual swelling strains were much smaller than observed in the above VFSS tests (i.e. zero surcharge), converging towards typically less than 20% of the VFSS values quoted in Table 4. On the other hand, swelling (unloading) steps in the standard step-loading oedometer tests on only slightly thinner (20 mm) reconstituted (and hence saturated) specimens indicated that 90% degree of consolidation could be observed within a 24-hour period allowed between the unloading steps for effective vertical stresses of 20–50 kPa, and nominally 100%

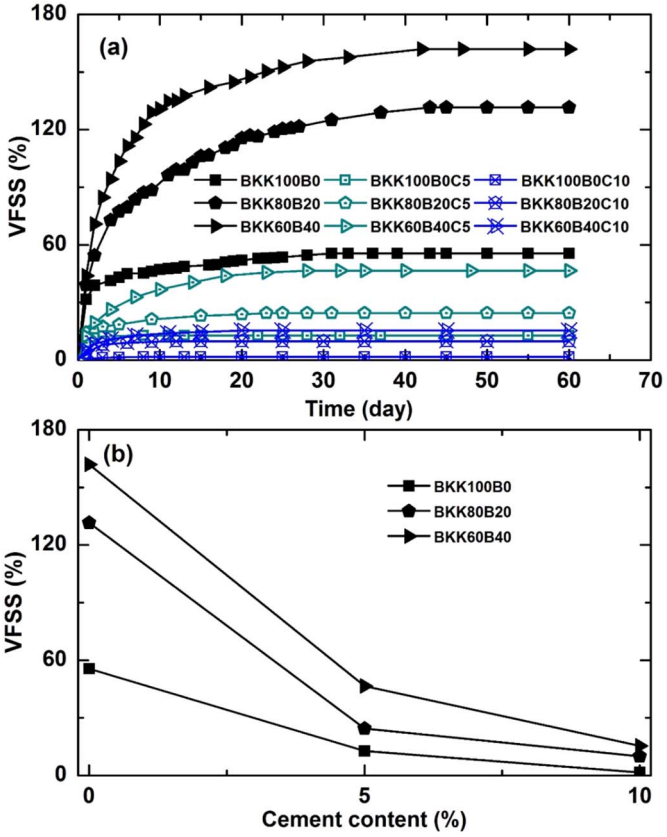

Fig. 5. Results of vertical free swelling strain (VFSS) tests; (a) Relationships between VFSS and time; (b) Relationships between VFSS after 60 days soaking and added cement content.

degree of consolidation could be observed for vertical effective stresses larger than 50 kPa for all the soil specimens. In addition to the lower permeability in the compacted, unsaturated specimens in this study, these significant differences in the swelling rate are explained by decreases of the coefficient of consolidation (c_v) as the effective stresses become smaller. This trend of c_v is confirmed by the oedometer test results (Por et al., 2015) shown in Fig. 6. Summarising the above facts, it is clear that the additional swelling as the effective stress decreases below a few kPa is significant (accounting for some 80% of the VFSS in the tested soils), and it comes with significant delays due to drastically

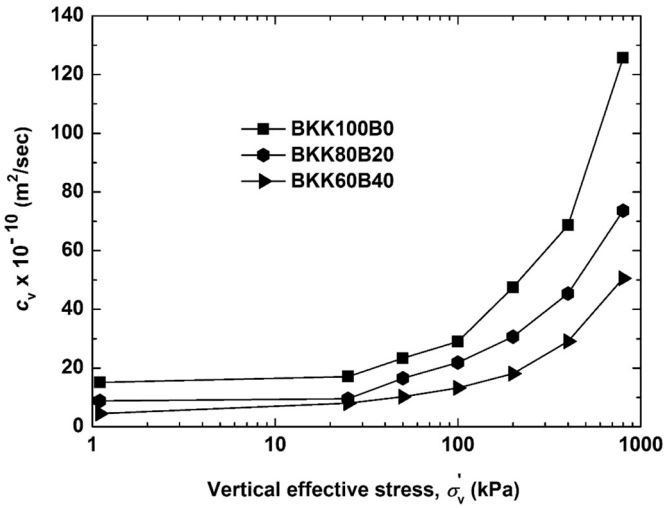

Fig. 6. Coefficient of consolidation (in the unloading stage) (c_v) versus vertical effective stress (σ_v') from step-loading oedometer test.

reduced c_v. Unless the design concerns the very surface of the ground, where the effective stress is indeed close to zero, the VFSS tests will lead to a very pessimistic assessment of swelling magnitude and response rates.

For the untreated soil specimens, the VFSS decreased significantly with the decrease of bentonite content (i.e. decrease in the LL). The specimens with lower LL reached smaller maximum VFSSs in a shorter period (Fig. 5a and Table 4). The longer time required for reaching the eventual strain in the higher bentonite-content specimens is due to the lower c_v values (Fig. 6), resulting both from the higher compressibility and the lower permeability of the bentonite (Komine, 2004 and 2010).

Fig. 5(b) shows the relationship between the cement content and the maximum VFSS, which demonstrates clearly that increasing the cement addition to the mixture dramatically decreases the VFSS for all the specimens. The effect was greater for the first 5% cement addition and less significant for another 5%. In a similar way as for the areal shrinkage strain, the decrease in the VFSS may derive from two different mechanisms. The first is the reduced "inherent" plasticity, pertaining to a change of plasticity at the clay particle level due to a change in the chemical environment caused by cement hydration. This reduction of plasticity could be confirmed by remoulding (see Table 4). The second, and probably more significant mechanism, is presumed to be the increased stiffness of the soil skeleton due to cementation. The cement also reduced the time for the specimen to reach a stable strain, as illustrated in the Fig. 5(a). Deng et al. (2015) reported on cement-treated clays that the cement-treating normally reduces the permeability rather than increases. This is to work in a direction of reducing c_v. However, the reduction of the soil skeleton compressibility can more than compensate the effect, and as a result, c_v must have been made greater.

4. Swelling pressure behaviour under one-dimensional swelling

4.1. Vertical and lateral swelling pressures

The results from the one-dimensional confined swelling pressure (CSP) tests measuring vertical and lateral swelling pressure are summarised in Table 5 and illustrated in Figs. 7 and 8.

All the test results show that, for both untreated and cement-treated specimens, the lateral swelling pressure was higher than the vertical pressure at all the stages. For both treated and untreated specimens, the swelling pressure decreased with a decrease in bentonite content (Fig. 7) at all the stages, showing a correlation with the amount of swelling minerals such as montmorillonite contained in the bentonite.

Table 5
Moisture condition and swelling index of untreated and cement-treated soils from step-loading oedometer and confined swelling pressure tests.

Sample notation	Final moisture and stress condition at vertical swelling strain, ε_v (%)						Swelling index
	–	0	2	4	6	8	C_s
BKK100B0	w (%)	19.8	21.2	22.5	23.8	25.4	0.142
	S_r (%)	95.0	96.3	97.0	97.7	99.5	
	p'(kPa)	286	209	164	131	75	
BKK100B0C5	w (%)	22.4	25.2	25.5	25.8	26.0	0.115
	S_r (%)	107.6	114.6	110.0	105.8	102.0	
	p'(kPa)	132	93	82	56	42	
BKK80B20	w (%)	21.2	22.5	24.3	25.5	27.0	0.180
	S_r (%)	93.5	94.3	96.9	97.1	98.3	
	p'(kPa)	564	463	407	337	286	
BKK80B20C5	w (%)	23.4	24.3	25.5	26.3	27.9	0.150
	S_r (%)	103.1	101.8	101.9	100.0	101.5	
	p'(kPa)	211	192	157	130	116	
BKK60B40	w (%)	24.5	26.0	27.5	29.0	30.5	0.220
	S_r (%)	92.6	93.9	95.0	96.0	96.9	
	p'(kPa)	790	669	583	518	472	
BKK60B40C5	w (%)	26.7	28.6	29.3	–	–	0.185
	S_r (%)	101.0	103.4	101.3	–	–	
	p'(kPa)	367	322	296	–	–	
BKK100B0	σ_v'(kPa)	25–1600					0.122
BKK80B20		25–1600					0.207
BKK60B40		25–1600					0.330

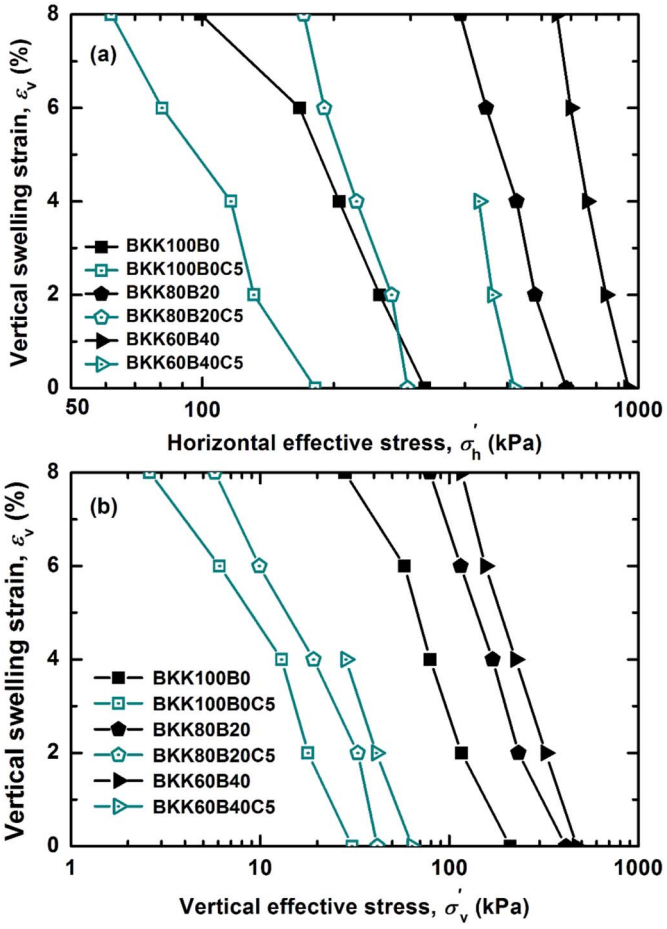

Fig. 7. Variation of vertical swelling strain versus effective stress of untreated and 5% cement-treated soils; (a) Vertical swelling strain versus horizontal effective stress; (b) Vertical swelling strain versus vertical effective stress (the test on BKK60B40C5 was terminated prematurely).

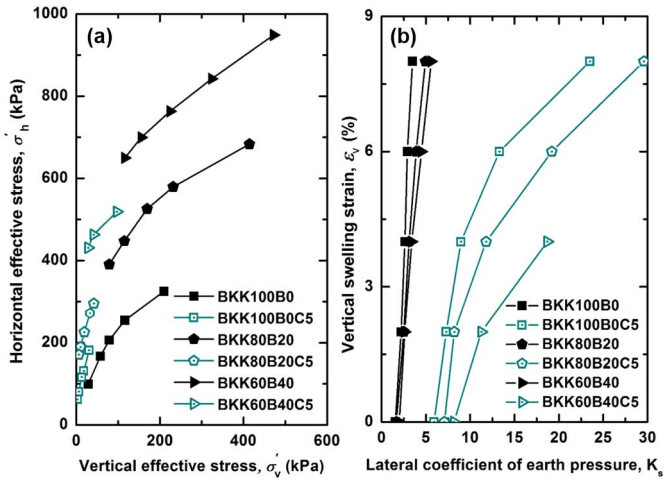

Fig. 8. Effective stresses, vertical strain and lateral coefficient of earth pressure (K_s) of untreated and 5% cement-treated soils; (a) Relationship between vertical and horizontal effective stresses; (b) Variation of lateral coefficient of earth pressure with vertical swelling strain.

Such results are also found for many materials mixed with bentonite or some other expansive soils. For example, Komine and Ogata (1999), Sun et al. (2009) and Cui et al. (2012), who studied bentonite-sand mixtures, reported that the maximum swelling pressure and the maximum swelling strain were lower as the sand content of the mixture became larger. Similar observations were also found in the study on expansive soils treated with lime, cement (Al-Rawas et al., 2005) and fly ash (Nalbantoğlu, 2004). According to Wang et al. (2012), the swelling pressure of soils depends on the montmorillonite content and the type of exchangeable cations.

Being treated by 5% cement, the swelling pressure in both directions, lateral and vertical, decreased significantly. The cement binds the soil particles together and increases the stiffness of the soil (for example, see E_{50} in Table 4). As a result, it leads to reduced swelling under unconfined conditions and, equivalently, reduced swelling pressure during wetting under confined conditions (Tables 4 and 5). Fig. 7(a) and (b) shows that the lateral swelling pressure decreased much less than the vertical swelling pressure when the vertical swelling strain (ε_v) was permitted to develop to 8% in steps. The vertical swelling pressure was reduced to very small values in the cement-treated cases during these steps. Hence, the presence of cement in the soils led to significant increases of the lateral coefficient of earth pressure during one-dimensional swelling (K_s), where $K_s = \sigma_h' / \sigma_v'$. The K_s value of the untreated and cement-treated soils under one-dimensional swelling (ε_h = 0%; ε_v = 0%, 2%, 4%, 6%, and 8%) were plotted in Fig. 8(b). The K_s value became larger when 5% cement was added to the soils at all the stages of swelling, reaching markedly large values at eventual stages. In the cement-treated soils, the increased shear stiffness (as represented by E_{50}) and shear strength (as represented by q_u) mean that, while the vertical strain developed, the deformation to re-adjust the horizontal pressure was significantly subdued, preserving a large part of the initial lateral swelling pressure. Although the K_s value is thus higher for the cement-treated soils, the absolute values of horizontal swelling pressure are still smaller than that in the untreated soils, as shown in Fig. 8(a). In alleviating the lateral pressure exerted from vertically swelling soils on rigid walls, the modest addition of cement is very effective. Although only one-dimensional conditions are considered here, it would not take much imagination to assume that the lateral stress relief is also swift in the treated soils, limiting the active movement towards flexible retaining walls.

4.2. Effective stress paths

The same feature as above can be discussed in a different perspective. Typical $q - p'$ (the deviator stress ($q = \sigma_v' - \sigma_h'$) versus the mean effective stress ($p' = 1/3(2\sigma_h' + \sigma_v')$)) and $(1 + e) - p'$ (the specific volume versus the mean effective stress) diagrams for the untreated and cement-treated specimens are shown in Fig. 9(a) and (b), respectively. By permitting the vertical swelling strain to develop from 0% to 8% with the incremental steps of 2%, the untreated soils' effective stress paths seemed to approach a stress ratio, $\eta = q/p' = 1.0$ while the 5% cement-treated specimens' paths approached the $\eta = 1.4$ line in the $q - p'$ plane. For an axi-symmetric extension, the angle of shearing resistance (φ') can be determined from $\sin\varphi' = 3\eta/(6 - \eta)$, when the effective cohesion is zero. By adding 5% cement to the soils, a significant increase in the calculated value of φ', was observed, from 41° at the untreated states to 52° at the treated states. This feature may seem apparently contradictory to some findings in literature that demonstrated increases of the effective cohesion with broadly constant values of φ' (e.g. Åhnberg, 2006). In this particular study, the observed increase of φ' may be attributed to the produced cementitious materials, which not only binds the clay particles together, contributing to the overall increase of shear stiffness, but may also fill the pore space between the clay particles and imparts a significant friction factor and hence, increase the angle of shear resistance. In the cement treated specimens, the LL and the PI decreased significantly (Table 4). The

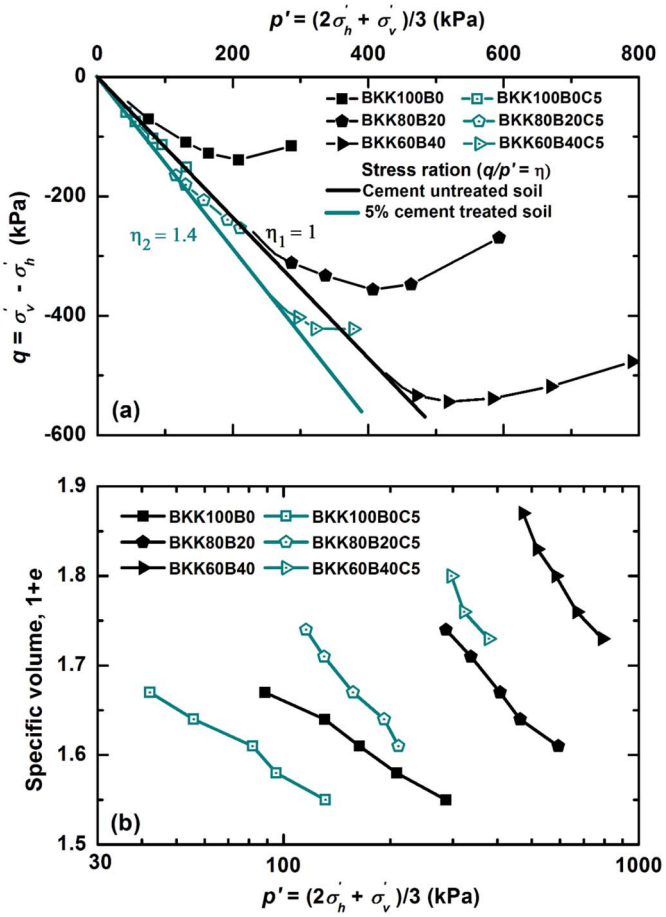

Fig. 9. Deviator stress (q) and specific volume ($1 + e$) versus mean effective normal stress (p') of cement-treated and untreated soils; (a) Effective stress path in the $q - p'$ plane; (b) Mean effective normal stress versus specific volume.

cement added lead to marked decreases of the vertical free swelling strain and hence, the swelling pressure in a confining condition decreased significantly. According to the plasticity chart (ASTM-D2478), initially all the cement untreated soil specimens belonged to a CH (high plastic clay) group, but when it was treated by 5% cement, the soil classification changed to ML (low plastic silt), which implies that the soils changed their intrinsic characteristics from those of a plastic clay to that of a low plasticity silt.

The impression of the behavioural changes during one-dimensional swelling observed in Fig. 9 is that expansive soils treated with a modest amount of cement (5% in this example) still behave in a qualitatively similar manner as untreated soils, although the swelling potential is significantly reduced. Although the inter-particle bonding by cement hydrates and resulting stiffness may play a part, the changes of the intrinsic properties such as plasticity seems to be significant too. The apparent lack of a significant cohesion suggested by the effective stress paths may be one reflection of the latter mechanism.

4.3. Swelling indices

The stiffness against swelling observed in the one-dimensional confined swelling pressure (CSP) tests are evaluated along with the results of the conventional step-loading oedometer tests on reconstituted specimens of the same soils, described in the authors' previous publication (Por et al., 2015). For the step-loading oedometer tests, the specimens were prepared by consolidating slurried clay, not by compaction, as explained earlier. The consolidated specimens were loaded and then unloaded at saturated conditions, while in the CSP tests, the specimen compacted at its optimum moisture content as the initial state

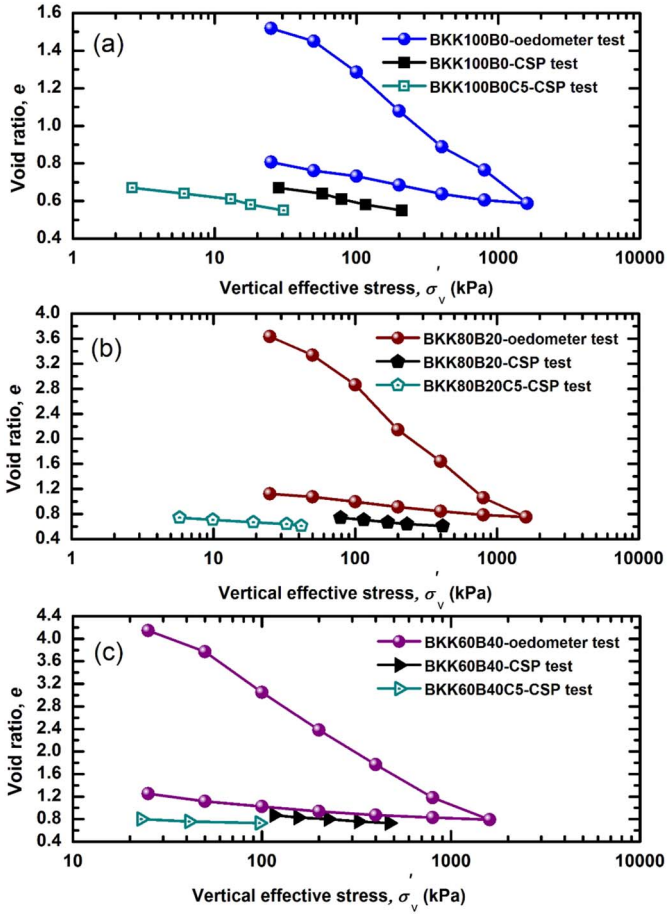

Fig. 10. Void ratio (e) versus vertical effective stress (σ_v') of untreated and 5% cement-treated soils (in conventional step-loading oedometer and confined swelling pressure tests); (a) BKK100B0; (b) BKK80B20; (c) BKK60B40.

was allowed to freely suck the water from its bottom in the confining ring at controlled vertical strains. While the maximum degree of saturation in the initially unsaturated compacted specimens in the CSP tests was slightly lower than 100% for untreated cases, all the 5% cement-treated specimens reached nominally $S_r = 100\%$ for all the specimens (estimation by $S_r = wG_s / e$ led in some cases to values in excess of 100%), as reported in Table 5. It is reiterated that the above experimental arrangement assured that the matric suction was always zero despite the undersaturation in some specimens.

The trend of the swelling lines, defined by the void ratio (e) versus the vertical effective stress (σ_v') of the untreated and cement-treated specimens from both oedometer and CSP tests are compared in Fig. 10.

The swelling lines from the two types of tests are broadly parallel to each other, while the offsets appeared simply due to the arbitrarily set effective stress (1600 kPa) to which the reconstituted specimens were consolidated in the oedometer tests. The two types of tests exhibited good compatibility, despite the difference in specimen preparation methods. By adding 5% cement to the soils, the slope of the swelling line ($C_s = -\Delta e / \Delta \log \sigma_v'$) became smaller by approximately 0.03 than for untreated states in all the cases, as summarised in Table 5. This means a relatively modest reduction of some 15–20% for all the cases, or equivalently, an increase of the bulk modulus by the same percentage, exhibiting a stark contrast against the 3- to 5-fold increases of E_{50}, as discussed earlier. Given the semi-log $e - p'$ relationship, however, its consequences on stress changes under confinement are considerable, as seen in the earlier sections. In addition, the results of the VFSS tests as discussed above suggest that the major difference due to cement addition appears at even lower stress ranges, as illustrated by Fig. 5. Future studies should concentrate more on the behaviour below 10 kPa for further investigation on the swell-curbing effects of cement treatment.

5. Concluding remarks

This study investigated the influence of cement addition on deformation characteristics and stress responses of expansive soils under swelling. The expansive soil specimens in this study were prepared by mixing expansive bentonite and non-expansive Bangkok clay. As well as assessing the effects of cement hydration on mechanical responses through a variety of simple tests, the vertical and lateral swelling pressures were directly measured by elaborate experiments, and the lateral coefficient of earth pressure (K_s) and the stress paths followed during one-dimensional swelling were investigated. The insights obtained from this research can be concluded as following:

1) The swelling-shrinkage strain and swelling pressure of expansive soils seemed to be strongly correlated to the swelling soil content, which also affects the plasticity and the liquid limit (LL) in a similar way. The soil with higher LL presented higher swelling and shrinkage properties during wetting and drying, respectively.
2) The cement treatment not only enhances the strength and stiffness, but also reduces the swelling and shrinkage potential of expansive soils, as confirmed by different kinds of swelling tests (the vertical free swelling and the areal shrinkage tests). For the soils studied in this research. This is likely to be caused not solely by inter-particle bonding deriving from hydrated substances, but also by more intrinsic alteration of the soil – namely, a reduction in the soil plasticity.
3) Equivalently to the above, the swelling pressures of the tested expansive soils markedly decreased when the cement was added. The cement had effect to reduce the horizontal swelling pressure, and even more significantly the vertical swelling pressure under one-dimensional swelling. Due to the more rapidly decreasing vertical swelling pressure, the coefficient of lateral pressure under one-dimensional swelling (K_s) increased more in the cement-treated soils than in the untreated soils.
4) The cement addition led to 15–20% reductions in the swelling index. Although this may seem a modest improvement when compared to the 3- to 5-fold increases seen for Young's modulus (E_{50}) its consequences on the confined swelling pressure are significant. The vertical free swelling strain (VFSS) measurements suggest that the cement-treating has major swell-curbing effects at lower effective stress ranges than explored in the confined swelling tests, possibly below 10 kPa. Obviously more tests on different expansive soils are desired to generalise the above observations on the alteration of expansive soils' behaviour due to cement addition. Although the modest cement treatment leads to a significant improvement of the expansive soils' unfavourable characteristics, it does not turn them into a quasi-rigid mass. A proper understanding of the altered properties still seems important in accurately assessing the reduced swelling strains and pressures.

Lastly, it is suggested that the durability of the cement treatment should be addressed as an interested topic in the future. This suggestion is made, as one might wonder, given the inherent disequilibrium of the hyperalkline cement particles in much lower pH groundwater, will the cement particle suffers leaching that leads to loss of the swelling property alterations.

Acknowledgements

This research was supported by the Thailand Research Fund under the TRF Research Scholar Award Grant No. RSA-5880023. The first author would like to acknowledge the AUN/SEED-Net (JICA) for a Ph.D. sandwich scholarship during his study.

References

Åhnberg, H., 2006. Consolidation stress effect on the strength of stabilised Swedish soils. Proc. ICE-Ground Improv. 10 (1), 1–13.

Åhnberg, H., Holmén, M., 2008. Laboratory determination of small-strain moduli in stabilized soils. In: Burns, S.E., Mayne, P.W., Santamarina, J.C. (Eds.), Proceedings of the 4th International Symposium on Deformation Characteristics of Geomaterials, Atlanta. IOS Press, Amsterdam, the Netherlands, pp. 291–297.

Al-Rawas, A.A., Hago, A.W., Al-Sarmi, H., 2005. Effect of lime, cement and Sarooj (Artificial Pozzolan) on the swelling potential of an expansive soil from Oman. Build. Environ. 40, 681–687.

Al-Shamrani, M.A., Dhowian, A., 2003. Experimental study of lateral restraint effects on the potential heave of expansive soils. Eng. Geol. 69 (2003), 63–81.

Andy, B.F., 1989. Laboratory evaluation of lateral swelling pressure. J. Geotech. Eng. 115 (10), 1481–1486.

ASTM, 2000a. D1557: Standard Test Methods for Laboratory Compaction Characteristics of Soil Using Modified Effort (56,000 ft-lbf/ft3 (2,700 kN-m/m3)). ASTM International, West Conshohocken, PA, USA.

ASTM, 2000b. D2166: Standard Test Method for Unconfined Compressive Strength of Cohesive Soils. ASTM International, West Conshohocken, PA, USA.

ASTM, 2010. D2478: Standard Practice for Classification of Soils for Engineering Purposes (Unified Soil Classification System) ASTM International. West Conshohocken, PA, USA.

AUSTROADS, 2004. New Zealand Supplement to the Document, Pavement Design – A Guide to the Structural Design of Road Pavements. CAPTIF Manager/Roading Engineer, National Office, February 2007 Transit New Zeland.

Basma, A.A., Al-Homoud, A.S., Husein, A., 1995. Laboratory assessment of swelling pressure of expansive soils. Appl. Clay Sci. 9, 355–368.

Cui, S.L., Zhang, H.Y., Zhang, M., 2012. Swelling characteristics of compacted GMZ bentonite-sand mixture as a buffer/backfill material in China. Eng. Geol. 141–142, 65–73.

Deng, Y., Yue, X., Liu, S., Chen, Y., Zhang, D., 2015. Hydraulic conductivity of cement-stabilised marine clay with metakaolin and its correlation with pore size distribution. Eng. Geol. 193, 146–152.

Ferber, V., Auriol, J.C., Cui, Y.J., Magnan, J.P., 2009. On the swelling potential of compacted high plasticity clays. Eng. Geol. 104, 200–210.

Fredlund, D.G., 1969. Consolidometer test procedural factors affecting swell properties. In: The Proceedings, 2nd International Conference on Expansive Clay Soils. Texas A & M Press, College Station, TX, pp. 435–456.

Horpibulsuk, S., Yangsukkaseam, N., Chinkulkijniwat, A., YJ, Du, 2011. Compressibility and permeability of Bangkok clay compared with kaolinite and bentonite. Appl. Clay Sci. 52 (1), 150–159.

Katti, R.K., Katti, D.R., Katti, A.R., 2002. Behaviour of Saturated Expansive Soil and Control Methods. Published by: A.A. Balkema, a member of Swets & Zeitlinger Publishers, Indianpp. 1.

Komine, H., 2004. Simplified evaluation on hydraulic conductivities of sand-bentonite mixture Backfill. Appl. Clay Sci. 26 (2004), 13–19.

Komine, H., 2010. Predicting hydraulic conductivity of sand-bentonite mixture backfill before and after swelling deformation for underground disposal of radioactive wastes. Eng. Geol. 114, 123–134.

Komine, H., Ogata, N., 1999. Experimental study on swelling characteristics of sand-bentonite mixture for nuclear waste disposal. Soils Found. 39 (2), 83–97.

Mohamed, O.Z., Yehia, K., Taha, S.M., El, S.M., Abd, E.A., 2013. Experimental study on the effect of lateral swelling pressure of expansive soil on retaining structure. J. Eng. Sci. 42 (1), 84–92.

Nalbantoğlu, Z., 2004. Effectiveness of class C fly ash as an expansive soil stabiliser. Constr. Build. Mater. 18 (2004), 377–381.

Nelson, J.D., Miller, D.J., 1992. Expansive Soils: Problem and Practice in Foundation and Pavement Engineering. John Wiley & Sons, Inc., Published Simultaneously in Canada, pp. 13.

Por, S., Likitlersuang, S., Nishimura, S., 2015. Investigation of shrinkage and swelling behaviour of expansive/non-expansive clay mixtures. Geotech. Eng. J. SEAGS & AGSSEA 46 (1), 117–127.

Puppala, A.J., Intharasombat, N., Qasim, S.R., 2004. The effects of using compost as a preventive measure to mitigate shoulder cracking: laboratory and field studies. In: Technical Report 0-4573-2. The University of Texas at Arlington, Civil and Environmental Engineering, USA.

Puppala, A.J., Manosuthikij, T., Chittoori, B.C.S., 2013. Swell and shrinkage characterisations of unsaturated expansive clays from Texas. Eng. Geol. 164, 187–194.

Radhakrishnan, G., Kumar, M.A., Raju, G.V.R.P., 2014. Swelling properties of expansive soils treated with chemicals and flyash. Am. J. Eng. Res. 3 (4), 245–250.

Raftari, M., Safuan, A., Rashid, A., Kassim, K.A., Moayedi, H., 2014. Evaluation of kaolin slurry properties treated with cement. Measurement 50, 222–228.

Rao, S.M., Ravi, K., 2015. Influence of initial degree of saturation on swell pressure of compacted Barmer bentonite specimens. Ann. Nucl. Energy 80, 303–311.

Sun, D., Cui, H., Sun, W., 2009. Swelling of compacted sand-bentonite mixtures. Appl. Clay Sci. 43, 485–492.

Surarak, C., Likitlersuang, S., Wanatowski, D., Balasubramaniam, A., Oh, E., Guan, H., 2012. Stiffness and strength parameters for hardening soil model of soft and stiff Bangkok clays. Soils Found. 52 (4), 682–697.

Tian, Q.H., Xu, Z.W., Zhou, G.Q., Zhao, X.D., Hu, K., 2009. Coefficient of earth pressure at rest in thick and deep soils. Min. Sci. Technol. 19, 252–255.

Wang, L.J., Liu, S.H., Zhou, B., 2015. Experimental study on the inclusion of soil bags in retaining walls constructed in expansive soils. Geotext. Geomembr. 43, 89–96.

Wang, Q., Tang, A.M., Cui, Y.J., Delage, P., Gatmiri, B., 2012. Experimental study on the swelling behaviour of bentonite/claystone mixture. Eng. Geol. 124, 59–66.

Arab J Geosci (2017) 10:369
DOI 10.1007/s12517-017-3158-y

ORIGINAL PAPER

Influence of the spatial variability of shear strength parameters on rainfall induced landslides: a case study of sandstone slope in Japan

Thanh Son Nguyen[1] · **Suched Likitlersuang**[2] · **Hiroyasu Ohtsu**[3] · **Takafumi Kitaoka**[3]

Received: 3 February 2017 / Accepted: 10 August 2017

Abstract Rainfall-induced landslides frequently occur in humid temperate regions worldwide. Research activity in understanding the mechanism of rainfall-induced landslides has recently focused on the probability of slope failure involving non-homogeneous soil profiles. This paper presents probabilistic analyses to assess the stability of unsaturated soil slope under rainfall. The influence of the spatial variability of shear strength parameters on the probability of rainfall-induced slope failure is conducted by means of a series of seepage and stability analyses of an infinite slope based on random fields. A case study of shallow failure located on sandstone slopes in Japan is used to verify the analysis framework. The results confirm that a probabilistic analysis can be efficiently used to qualify various locations of failure surface caused by spatial variability of soil shear strength for a shallow infinite slope failure due to rainfall.

✉ Suched Likitlersuang
fceslk@eng.chula.ac.th

Thanh Son Nguyen
nguyensontic@gmail.com

Hiroyasu Ohtsu
ohtsu.hiroyasu.6n@kyoto-u.ac.jp

Takafumi Kitaoka
kitaoka.takafumi.6e@kyoto-u.ac.jp

[1] Department of Civil Engineering, Faculty of Engineering, Chulalongkorn University, Bangkok, Thailand

[2] Geotechnical Research Unit, Department of Civil Engineering, Faculty of Engineering, Chulalongkorn University, Bangkok, Thailand

[3] Department of Urban Management, Graduate School of Engineering, Kyoto University, Kyoto, Japan

Keywords Landslides · Unsaturated soil · Rainfall infiltration · Probabilistic analysis · Shear strength parameters

Introduction

Rainfall-induced slope failure is one of the major causes of natural landslides. The rainfall infiltration could increase unit weight of soil and contribute positive pore water pressure to the soil slope (Ng and Shi 1998; Rahardjo et al. 2007). Mostly, the landslides start taking the form of shallow failure (typically 1–3 m depth) with potential slip surface parallel to original slope surface during heavy rainfall (Lu and Godt 2008; Ray et al. 2010; Li et al. 2013; Kanjanakul et al. 2016). Landslides usually occur because of the shallow impermeable bedrock type of soil slope, in which the water table raising from the rainfall accelerates the slope failure process (Ng and Shi 1998; Cho 2009; Han et al. 2014). Stability analysis of rainfall-induced slope failure generally employs a deterministic analysis, which does not consider the spatial variability of soil properties. However, it is important that the variation of soil properties from one point to another might affect the analysis results, particularly in the case of slope failure caused by reduction in soil shear strength due to rainfall infiltration. Therefore, the spatial variability of soil properties framework of random field to simulate non-homogeneous of soil profiles was proposed (Vanmarcke 1983).

A probabilistic slope stability analysis considered the random field of shear strength parameters was presented by Fenton and Griffiths (2008). There are several studies on seepage analysis using the spatial variability of a saturated permeability in the random field model (Srivastava et al. 2010; Cho 2012). Griffiths et al. (2011) analyzed the failure probability of infinite slope assuming a random field model of the shear strength parameters. The results indicated that the critical failure surface can happen at weak layers where the minimum

Published online: 22 August 2017

factor of safety against sliding occurs. Another study also considered a one-dimensional random field of the saturated permeability combined with transient seepage analysis to study a shallow landslide of an infinite slope of the weathered residual soil (Cho 2014). The slope failure occurs only when pore water pressure reaches a positive value, and the most critical failure surface always take place at the interface between the weathered soil layer and the underlying bedrock. These studies demonstrate the effect of the spatial variability of soil shear strength and the saturated permeability on the slope stability analysis. However, all the studies described above used an assumption of the mean values of shear strength parameters to analyze the slope stability, and the slope failures occur at the critical depth where the soil became fully saturated. In practice, slopes may fail due to reduction in soil shear strength caused by increasing volumetric moisture content; therefore, either positive pore water pressure or rising water table will not necessarily contribute to slope failure.

In this paper, a probabilistic stability analysis considering random fields of shear strength parameters was implemented for a rainfall-induced slope failure problem. Assumptions of reducing soil shear strength and increasing unit weight of the soil were made in the analysis. An infinite slope assumption can be reasonably applied to rainfall-induced slope failure problem because the failure mechanism can be characterized as shallow landside with potential failure surface parallel to slope surface (Cho and Lee 2002; Lu and Godt 2008; Ray et al. 2010; Santoso et al. 2011; Li et al. 2013). A one-dimensional seepage analysis was performed to define variable suction and volumetric moisture content of soil due to rainfall infiltration. This is because of simplicity, and the vertical flow plays a more dominant role than the lateral flow (Lee et al. 2011; Lu and Godt 2013). A case study of rainfall-induced slope failure in Japan was used to verify the framework. Results of analysis were compared with the field data to illustrate the proposed method.

Unsaturated seepage

For seepage analysis in an unsaturated soil layer, Darcy's law originally derived for saturated soil was modified to accommodate the flow of water through unsaturated soil (Richards 1931). The only difference is that under condition of unsaturated flow, the hydraulic conductivity is no longer a constant. The governing equation for one-dimensional flow in unsaturated soil is given by

$$\frac{\partial}{\partial z}\left(k_z\frac{\partial h}{\partial z}\right)+q=\frac{\partial \theta}{\partial t} \tag{1}$$

where z is the depth of soil layer (m), h is the total pressure head (m), k_z is the hydraulic conductivity in the vertical direction (m/h), θ is the volumetric moisture content, q is the applied flux boundary (m/h), and t is time (h).

There are some empirical and semi-empirical functions which have been proposed to present hydraulic conductivity. In this analysis, non-linear functions of the volumetric moisture content and the coefficient of permeability of the unsaturated soil were adopted based on the Mualem-van Genuchten model (van Genuchten 1980) as

$$S_e=\frac{\theta-\theta_r}{\theta_s-\theta_r}=\frac{1}{[1+(\alpha h)^n]^m} \tag{2}$$

where $m=1-\frac{1}{n}$, $n>1$ are dimensionless parameters, and

$$k_z=k_s S_e^{1/2}\left[\left(1-S_e^{1/m}\right)^m\right]^2 \tag{3}$$

in which S_e is the effective water saturation, θ_r is the residual volumetric moisture content, θ_s is the saturated volumetric moisture content, k_s is the saturated permeability (m/h), and α is the fitting parameter (1/m).

In this study, the one-dimensional finite element method was applied using SEEP/W module of Geo-Slope (2012) to solve the Eq. (1). To obtain the result, time step increment and element size should be defined in the advantage (Pan et al. 1996; Van Dam and Feddes 2000; Caviedes-Voullième et al. 2013). Therefore, the small time step increment of 1 s, and element size of 0.05 m were used in the analysis.

Infinite slope stability

The rainfall-induced slope failure is normally categorized as a shallow failure, in which the infinite slope assumption can be reasonably used to analyze the slope stability. Therefore, the infinite slope stability model was adopted in this study, as shown in Fig. 1. The factor of safety of the infinite slope can be expressed as

$$FS=\frac{\tau_f}{\tau_m}=\frac{\tau_f}{W\sin\beta\cos\beta} \tag{4}$$

where τ_f is the shear strength of soil, τ_m is the shear stress at any point along the potential failure surface, W is the weight of the soil slice per unit base area, and β is the slope angle.

The shear strength of unsaturated soil can be expressed based on the extended Mohr-Coulomb failure criterion (Fredlund et al. 1978) as

$$\tau_f=c'+(\sigma_n-u_a)\tan\phi'+(u_a-u_w)\tan\phi^b \tag{5}$$

where c' is the effective cohesion, σ_n is the total normal stress on failure surface, u_a is the pore air pressure, u_w is the pore water pressure, ϕ' is the effective angle of internal friction, and ϕ^b is the contribution to the shear strength due to soil suction.

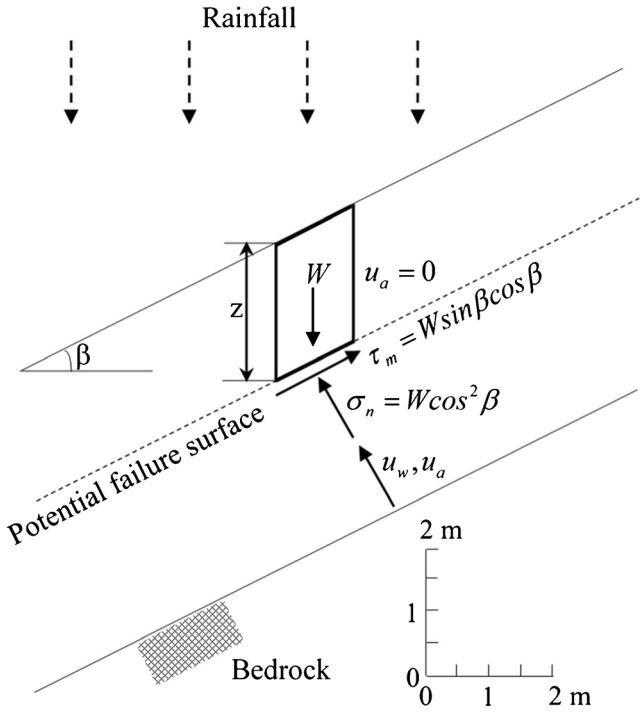

Fig. 1 Stability analysis of an infinite slope model

The equation can be simplified (Fredlund et al. 2012) as

$$\tau_f = C + (\sigma_n - u_a)\tan\phi' \tag{6}$$

where $C = c' + (u_a - u_w)\tan\phi^b$ is the total cohesion under unsaturated soil condition.

The shear strength parameters from the direct shear tests conducted by Matsushi et al. (2006) were adopted in this study. During the test, a single-staged direct shear was performed under different normal stresses. The moisture conditions of soil specimens varied from an oven-dried condition to a capillary saturated condition. The results indicate that the total cohesion can be expressed using an exponential decay function of the apparent soil cohesion at dry condition (c), reduction coefficient (μ), and volumetric moisture content (θ) as

$$C = ce^{-\mu\theta} \tag{7}$$

However, the observations from the direst shear tests indicated that the friction angle is rather constant at the various test conditions from oven-dried to capillary saturated; so in this study, the friction angle is assumed to be constant (i.e., $\phi = \phi'$).

The unit weight of the soil slice increases with the moisture content from rainfall infiltration. The weight of a vertical soil column per unit cross-sectional area (W) from the slope surface to the potential failure surface can be expressed as

$$W = \sum_{i=1}^{m} (\gamma_d + \theta_i\gamma_w)\Delta z \tag{8}$$

where m is the total number of elements, Δz is the thickness of the soil, γ_d is the dry unit weight of soil, and θ_i is the volumetric moisture content of each soil element.

In addition, the unstable slope is still affected by the increase in pore water pressure (Fig. 1) causing a decrease in effective stress. If $u_a = 0$ at atmospheric pressure, the safety factor of the slope can be expressed as

$$FS = \frac{ce^{-\mu\theta}}{\sum_{i=1}^{m} (\gamma_d + \theta_i\gamma_w)\Delta z\sin\beta\cos\beta} + \frac{\tan\phi}{\tan\beta} - \frac{\max(u_w, 0)\tan\phi}{\sum_{i=1}^{m} (\gamma_d + \theta_i\gamma_w)\Delta z\sin\beta\cos\beta} \tag{9}$$

Probabilistic method

Probabilistic slope stability analysis

The probabilistic framework for stability analysis is formulated using a set of random variables. Let x denotes random variables; $f_X(x)$ is the joint probability density function of x, and $FS(x)$ is the factor of safety function of slope. The failure probability can be calculated by the following integral (Baecher and Christian 2003)

$$P_f = P[FS(x) \le 1] = \int_{FS(x)\le 1} f_X(x)dx \tag{10}$$

A Monte Carlo Simulation (MCS) is adopted to calculate the failure probability due to the variability of soil shear strength as (Fenton and Griffiths 2008)

$$P_f \approx \frac{1}{n}\sum_{1=1}^{n} I\left[FS\left(x^i\right)\right] \tag{11}$$

where x_i is the ith sample of random variable x, n is the number of generated samples, and $I[FS(x)]$ is an indicator function characterizing the failure domain defined as

$$I[FS(x)] = \begin{cases} 1 & FS(x) \le 1 \\ 0 & FS(x) > 1 \end{cases} \tag{12}$$

Random field

In order to describe the spatial variability of soil, the Markov correlation function is used in this study (Fenton and Griffiths 2008; Phoon 2008) as follows

$$\rho(\tau) = \exp\left\{-\frac{2|\tau|}{l}\right\} \tag{13}$$

where $\rho(\tau)$ is a correlation coefficient indicating a relationship between two random variables (i.e., $0 \le \rho \le 1$), τ is the vertical

distance between two data points in meter, and l is the actual correlation length in meter. A high correlation length implies a smoothly varying field while a small correlation length indicates a ragged field.

In this study, a normal random field in one-dimensional space was generated using the one-sided spectral approach. A continuous random field can be obtained from Eq. (13) based on calculating the spectral function. In the geotechnical engineering application, the random variable is always positive; thus, the random variables of soil properties are usually assumed to be a lognormal distribution. A transformation approach is used to obtain lognormal random variable. A detailed description of this approach can be found in Fenton and Griffiths (2008).

Case study

The studied site is located in the southwest central Japan, Boso Peninsula including sandstone and mudstone slopes (Fig. 2). A 1989 rainstorm which caused landslides along the sandstone and mudstone slopes was recorded at four meteorological stations (Yokohama, Kisarazu, Sakuma, and Sakahata) within a 30 km radius from the study site (Fig. 3). The sandstone slope S-1, which has an angle of $\beta = 38.4°$, slip depth of 1.6 m, sliding area of 620 m^2, and volume of 990 m^3 was selected in this study (Matsushi et al. 2006). Figure 4 shows the longitudinal section and failure surface of the S-1 slope. It is noted that the shallow failure was a transitional type, so the assumption of infinite slope can be reasonably used in this study. The properties of the upper 1.5 m soil layer were evaluated and summarized in Table 1 (Matsushi 2006). The soil profile of slope S-1 was classified using a dynamic cone penetration test (DCPT) value (N_c) as shown in Fig. 5. According to the ASTM D6951 (2003), the penetrometer consists of a penetration rod with a cone tip of 25-mm diameter and 60° tip angle, guide rods, and a 5-kg weight. When performing the test, the weight falls from a height of 50 cm along the guide rod to the cone. Wakatsuki et al. (2005) classified the ground into four soil layers: $0 \le N_c < 5$ (upper layer), $5 \le N_c < 10$ (middle layer), $10 \le N_c < 30$ (lower layer), and $N_c \ge 30$ (bedrock). In the classification of weathered rock by the Geological Society (1995), the upper layer and the middle layer correspond to "grade V/VI" (completely weathered soil), the lower layer corresponds to "grade IV" (highly weathered rock), and the bedrock corresponds to "grades I-III" (slightly weathered rock and fresh rock). According to the Unified Soil Classification

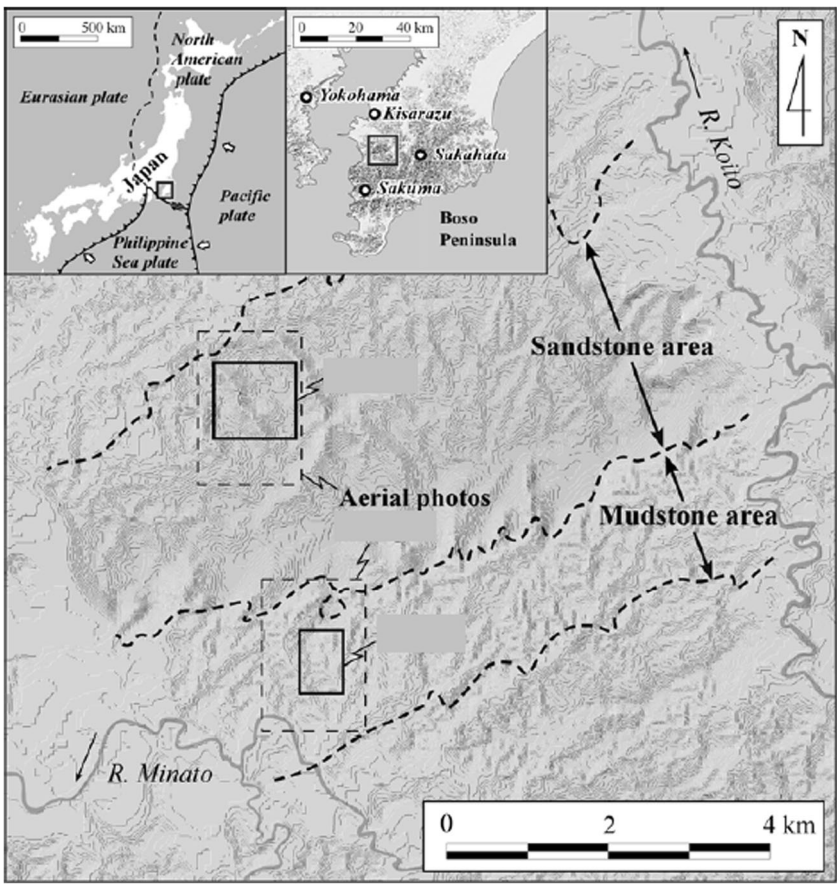

Fig. 2 Site location (after Matsushi 2006)

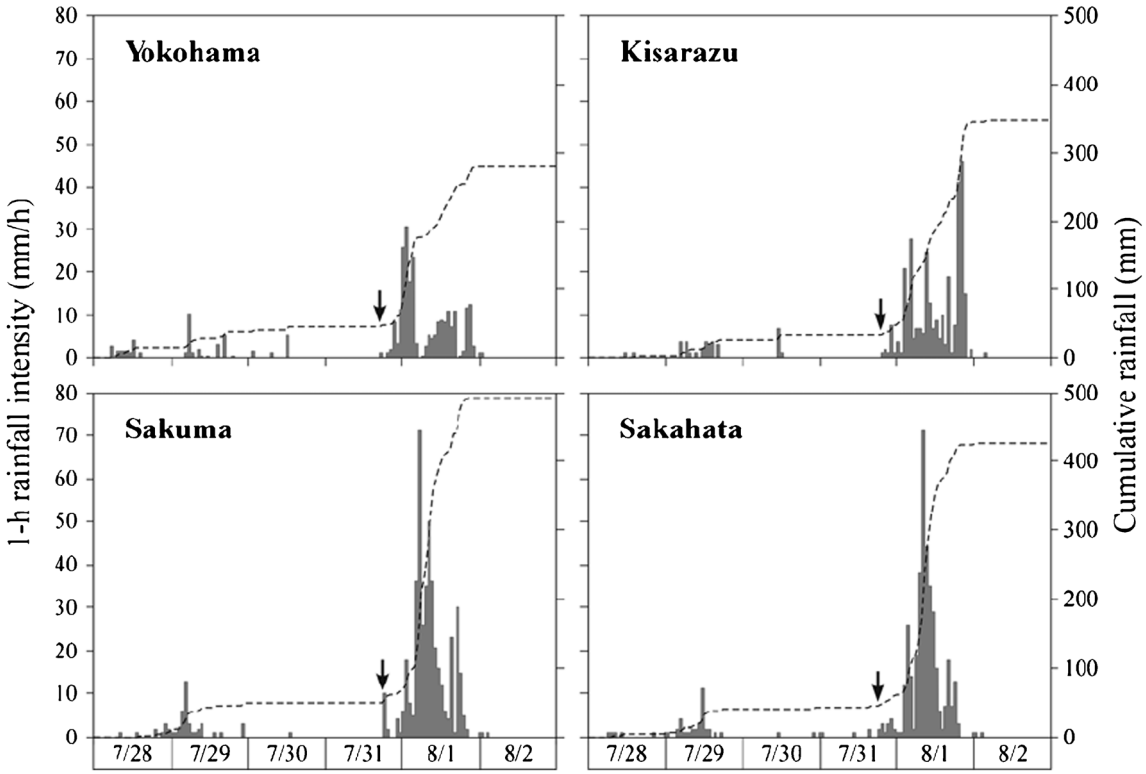

Fig. 3 Rainfall intensity of the 1989 storm recorded at four meteorological stations (after Matsushi 2006)

System (USCS), the upper layer can be classified as silty sand (SM) based on grain-size distribution (Table 1).

The soil suction and volumetric moisture content of the upper layer were obtained from pressure plate tests. The soil water characteristic curve (SWCC) and its curve-fitting van Genuchten model are presented in Fig. 6. In this study, the types of middle and lower layer of soil can be reasonably assumed to be the same as the upper layer based on the DCPT; therefore, the same set of SWCC parameters were used for all soil layers. The saturated permeability was determined from a constant head permeability test with the specimen size of 75 mm in diameter and 260 mm in height (ASTM D2434-68, 2000) which was almost remained from the upper layer down to the bedrock, as shown in Fig. 7. Table 2 summarizes the fitting parameters of the soil-water characteristic curve and the average saturated permeability of all soil layers as input parameters for seepage analysis.

The shear strength of soils determined under four different normal stresses with various volumetric moisture contents (Matsushi et al. 2006) was used in the analysis. The best fitting curves of shear strength versus volumetric moisture content

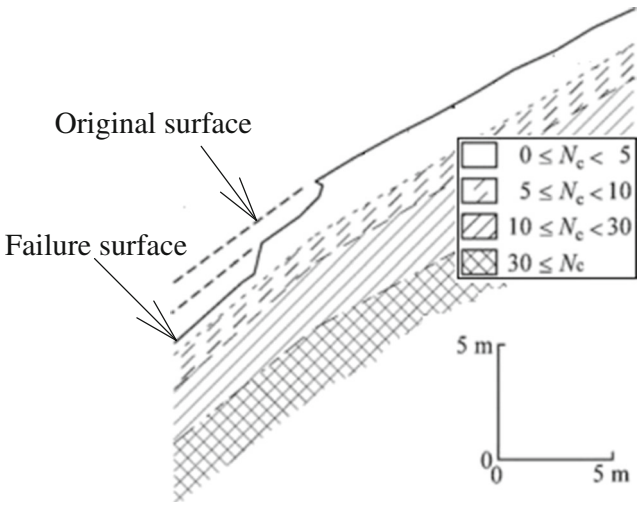

Fig. 4 Longitudinal section and failure surface of slope S-1 (adapted from Matsushi 2006)

Table 1 Physical soil properties

Depth (cm)	Dry unit weight (kN/m^3)	Porosity	Grain-size distribution (%)		
			Clay	Silt	Sand
10	9.8	0.63	3.5	14.6	81.9
30	12.1	0.54	6.2	19.5	74.2
45	12.8	0.52	–	–	–
60	13.3	0.50	3.7	8.0	88.3
75	13.7	0.48	–	–	–
90	13.7	0.48	8.4	7.9	83.6
120	12.9	0.51	7.1	6.5	86.4
150	13.3	0.50	4.7	4.3	91.0
Average	*12.7*	*0.52*	*5.6*	*10.1*	*84.3*

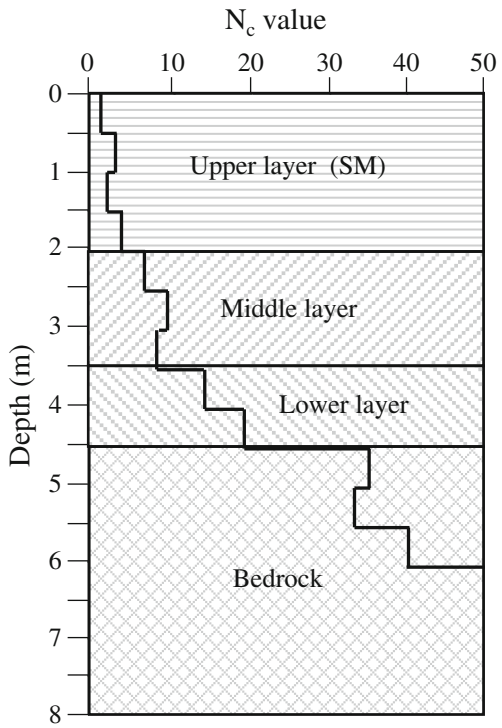

Fig. 5 Soil profile of slope S-1

for normal stress of 10, 20, 30, and 40 kPa are presented in Fig. 8. The apparent soil cohesion (soil cohesion in dry condition), the friction angle, and the reduction coefficient were calculated as the input shear strength parameters for the stability analysis, as summarized in Table 3. It is noted that the direct shear tests were performed for the upper layer (i.e., < 2 m depth). The analysis was then focused on the upper layer.

In this study, a one-dimensional transient seepage analysis was conducted to study the effect of the 1989 rainstorm causing the shallow slope failure in the Japan. For the S-1 slope,

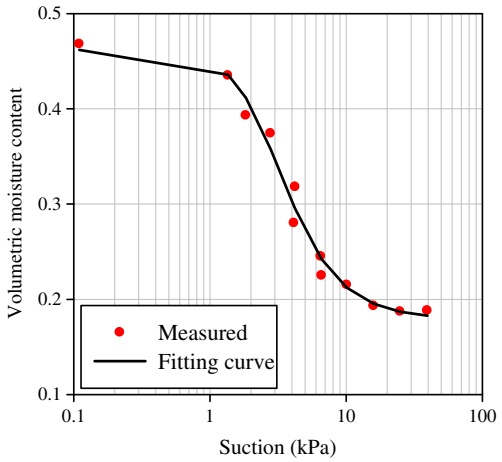

Fig. 6 Soil water characteristic curve of the upper layer

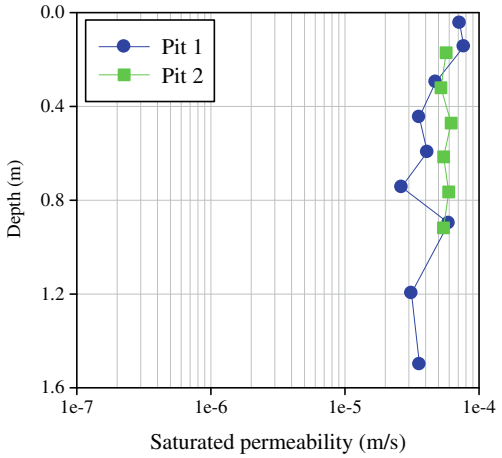

Fig. 7 Saturated permeability varied with depth from a constant head permeability test

the bedrock located at 4.5 m depth (Fig. 5) was designated the bottom undrained boundary (zero flux boundary), while the top boundary of the model should be designated a flux boundary (q), which is equivalent to the desired rainfall intensity. The average rainfall intensity from four recorded stations (Fig. 3) which was equivalent to a flux of 0.032 m/h was defined as the top boundary condition. The linear pressure head (zero at bedrock and − 4.5 m at the surface slope) was set as the initial condition. No ponding on the top surface of the soil column can be reasonably assumed due to the fact that when the rainwater exceeds the infiltration capacity of soil the excess water will drain away as surface runoff. A one-dimensional transient seepage analysis model of the S1-slope is presented in Fig. 9. The volumetric moisture content extracted from the transient seepage analysis was used to calculate the factor of safety using Eq. (9).

To analyze the probability of rainfall-induced slope failure, the total soil cohesion under unsaturated condition (C) and the frictional resistance (tanϕ) were considered as the random fields. The mean values of C and tanϕ were determined from the direct shear test results (Fig. 8). It is noted that the mean value of C is not constant, but it tends to decrease with increasing volumetric moisture content due to rainfall infiltration. According to Retheti (1988), the covariance coefficient of the effective cohesion ($COV_{c'}$) for sandy soils and clayish soils were usually greater than 0.2. Since the effective soil cohesion is the same as the total soil cohesion in the saturated

Table 2 SWCC parameters and saturated permeability

Parameters	Value
θ_r	0.179
θ_s	0.462
α (1/m)	3.73
n	2.598
k_s (m/h)	0.154

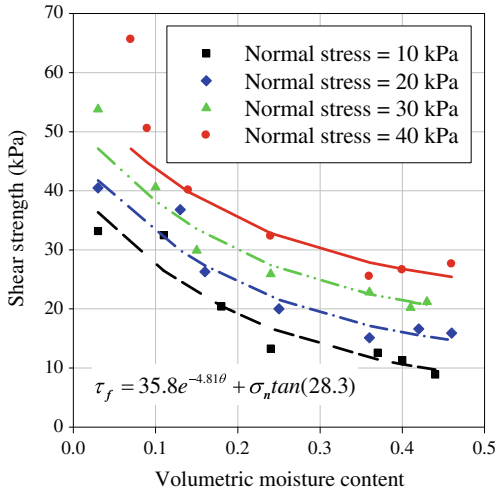

Fig. 8 Best-fitted shear strength versus volumetric moisture content curves for four normal stresses

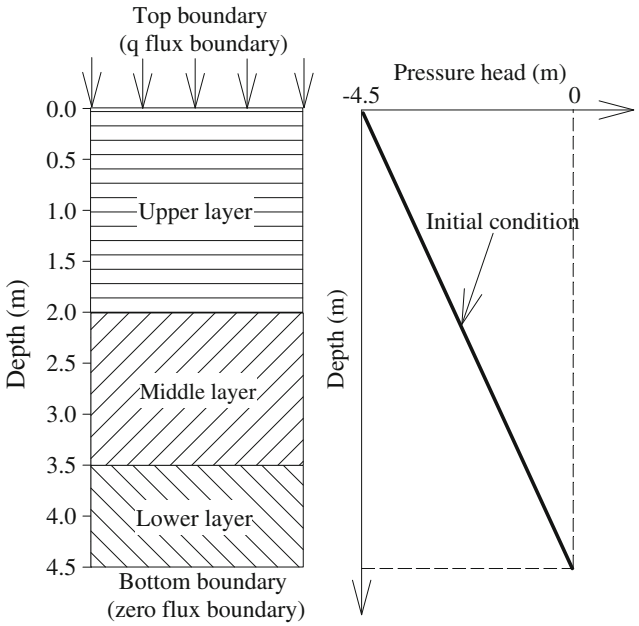

Fig. 9 One-dimensional seepage model of the S1-slope (element size, $\Delta z = 0.05$ m)

condition, the covariance coefficient of the total soil cohesion (COV_C) can be set as the same value of $COV_{c'}$ (Fenton and Griffiths 2008). The covariance coefficient of the frictional resistance ($COV_{tan\phi}$) was between 0.02 and 0.22 (Phoon and Kulhawy 1999). In order to verify slope failure during the rainstorm and evaluate the effect of each shear strength parameter, the slope failure probability was calculated using the same value of covariance coefficient corresponding to $COV_C = COV_{tan\phi} = 0.2$. In addition, to simulate the effect of heterogeneous soil characteristics on the probabilistic calculation, the correlation length l is varied from 0.02 to 2.0 m for the description of the spatial correlation length of random fields C and tanϕ. Table 4 summarizes the statistical characteristics of soil shear strength parameters used for probabilistic analysis.

A series of random fields of C and tanϕ are carried out using the random model and MCS. Figure 10 shows the convergence of the estimated probability of failure for the slope, which indicates that the failure probability can be converged when the generated samples exceed 2000. In this study, 5000 sets of the random fields C and tanϕ were used as input shear strength parameters for probabilistic stability analysis. Then, the factor of safety and critical depth were recorded for each generated random fields C and tanϕ; the failure probability was approximated based on Eq. (11).

Table 3 Soil shear strength parameters

Parameters	Meaning	Value
c (kPa)	Apparent soil cohesion	35.8
ϕ (°)	Friction angle	28.3
μ	Reduction coefficient	4.81

Remark: $C = ce^{-\mu\theta}$ is total soil cohesion under unsaturated condition

Analysis results

Deterministic analysis

In this section, a deterministic seepage and slope stability analysis was performed to investigate slope stability during rainfall. The resulting volumetric moisture content calculated from SEEP/W was then used with the infinite slope stability model to determine the corresponding factor of safety. Figure 11a shows the vertical distribution of volumetric moisture content with the duration of rainfall. The results show that the volumetric moisture content of ground surface rapidly increased at the beginning of rainfall. Then, the volumetric moisture content increased with depth as rainfall infiltrated the soil. When infiltration remained constant after 12 h, the volumetric moisture content nearly reached saturation, and there was no generation of positive pore water pressure in the upper layer. Figure 11b shows that the factor of safety varied with depth for the different rainfall durations. It can been seen that by increasing volumetric moisture content with depth, the factor of safety first decreased dramatically, increased slightly, and then decreased again. For the case of the 6 h rainfall, the factor of safety decreased due to soil shear

Table 4 Statistical properties of soil shear strength parameters used for probabilistic analysis

Parameters	Mean value	COV	Correlation length (m)
C (kPa)	$35.8e^{-4.81\theta}$	0.2	$0.02 \le l \le 2.0$
tanϕ	0.5384		

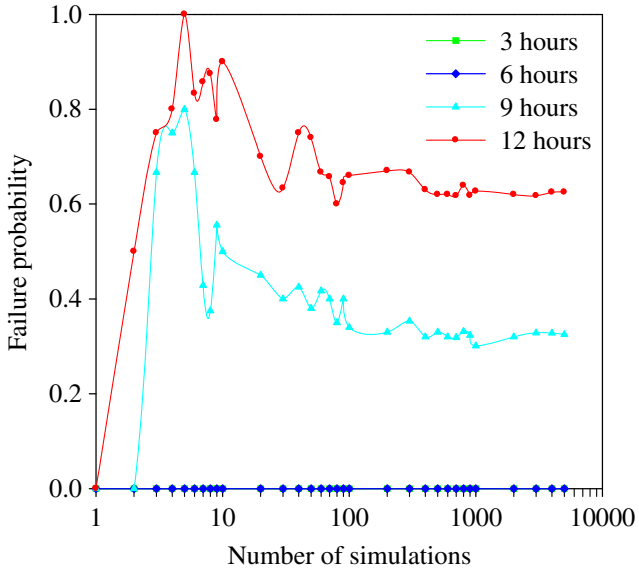

Fig. 10 Convergence of the failure probability at different times

strength deceased and the unit weight of the soil slice increased with increasing depth. The minimum factor of safety, close to 1.21, occurred at the depth of 1.05 m. However, as shown in Fig. 11a, the volumetric moisture content decreases at a depth of approximately 1.1–1.3 m; therefore, the factor of safety began to increase slightly. Subsequently, the unit weight of the soil slice increases with increasing depth, and the factor of safety began to decrease. This is because the main factor controlling the factor of safety is the reduction in soil shear strength at the early stage of rainfall. A similar phenomenon can be observed at 3 and 9 h of rainfall. The factor of safety only continuously decreases with depth after 12 h of rainfall because the increase in volumetric moisture content is almost constant in the upper layer (the top 2 m) (Fig. 11a). A factor of safety of less than one can be observed from a depth below 1.7 m. The slope stability analysis demonstrates that failure of the S-1 slope occurred during the 1989 rainstorm with failure surfaces below 1.6 m in the upper layer. Results indicate that the simulation of the failure surface agrees well with the observation of actual slip surface.

Probabilistic analysis

Effect of correlation length

In this section, probabilistic analysis of rainfall-induced slope failure is illustrated. The correlation lengths between 0.02 to 2.0 m were implemented for both random fields of C and tanϕ in this study. Figure 12 shows the histogram of frequency of each critical failure surface which occurred at different depth for the correlation lengths of 0.02 and 2.0 m at 9 and 12 h of rainfall duration. Figure 12a, b indicates that the critical failure surface most likely occurred at a depth of approximately 1.0–1.7 m after 9 h of rainfall. This finding means that the wetting front due to rainfall infiltration only decreases the shear strength of soil at the slope's upper portion in the early stage of infiltration. As infiltration progresses and the wetting front moves down, the critical surface continuously increases in depth until the wetting front reaches the base of the upper layer. Finally, the highest frequency of critical surface failure occurred at the base of the upper layer, as shown Fig. 12c, d. Since the highest frequency of critical surface failure took place between 1.5 and 2.0 m depths of the upper layer after 9 h of rainfall, as seen Fig. 12, the failure mechanism can be characterized as a shallow failure, where the critical failure surfaces were located above the interface between the weathered soil and bedrock. Comparing the previous studies of Cho (2014) and Dou et al. (2015), the failure mechanism always occurs at the interface between the weathered soil and bedrock during rainfall infiltration. Figure 12 also indicates that the frequency of the critical surface failure was

Fig. 11 Results of deterministic analysis. **a** Volumetric moisture content profiles. **b** Variation of the factor of safety with time

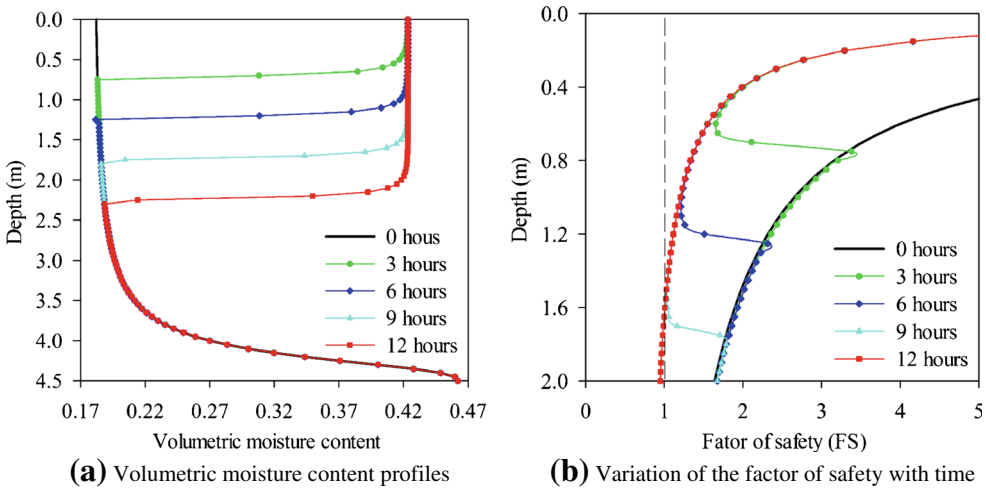

(a) Volumetric moisture content profiles **(b)** Variation of the factor of safety with time

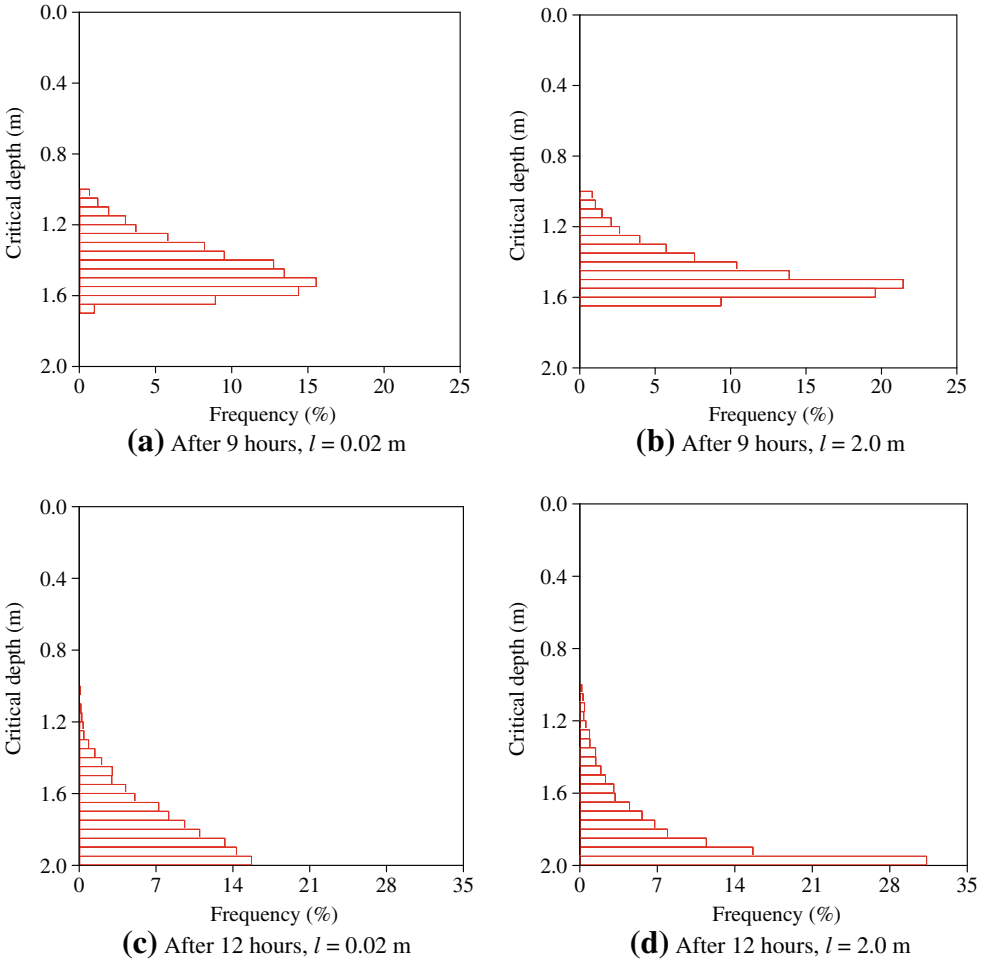

Fig. 12 Histogram of the critical depth at two different times (COV_C = 0.2; $COV_{tan\phi}$ = 0.2). **a** After 9 h, l = 0.02 m. **b** After 9 h, l = 2.0 m. **c** After 12 h, l = 0.02 m. **d** After 12 h, l = 2.0 m

affected by the correlation length. In the histogram shown in Fig. 12a, c, l = 0.02 m displays smaller frequencies at the critical failure surface than the histogram in Fig. 12b, d for l = 2.0 m. This is because the lower correlation length, which exhibits highly non-homogeneous soil, has the critical surface moving upward. Conversely, the higher correlation length provided an increased frequency probability that the critical failure surface would be

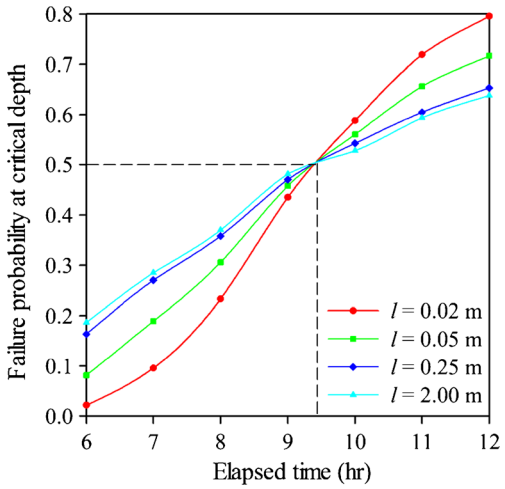

Fig. 13 Effect of l on failure probability at critical depth (COV_C = 0.2; $COV_{tan\phi}$ = 0.2)

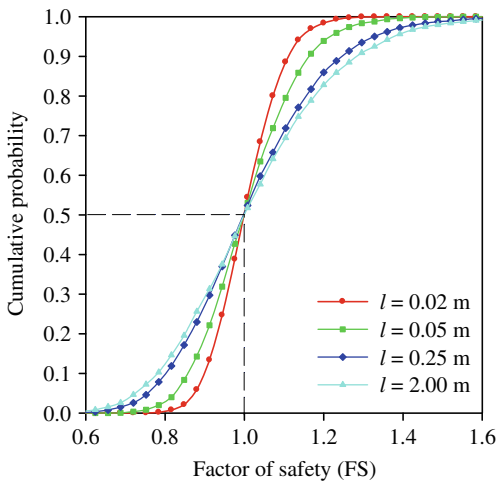

Fig. 14 Cumulative probability of FS at critical rainfall duration (COV_C = 0.2; $COV_{tan\phi}$ = 0.2)

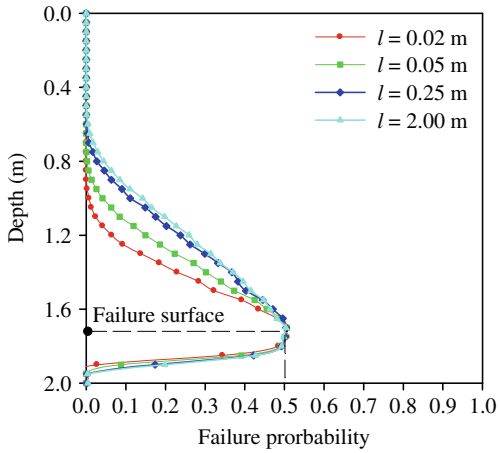

Fig. 15 Failure probability distribution at critical rainfall duration ($COV_C = 0.2$; $COV_{tan\phi} = 0.2$)

located at the weakest part of the upper layer as the random field becomes more spatially uniform.

Figure 13 shows the influence of correlation length l in the range of $0.02 \le l \le 2.0$ m on the failure probability at different points in rainfall duration. The failure probability was calculated at the critical failure surface corresponding to the minimum factor of safety of the deterministic analysis. The results indicate that the failure probability increases dramatically as infiltration progresses, and soil slope with smaller values of correlation length has a smaller failure probability at the early stages of infiltration. However, the failure probability for cases with smaller values of correlation length is greater than those with larger values of correlation length after the rainfall duration exceeded approximately 9.5 h. This can be referred to as a critical rainfall duration causing slope failure. It should be emphasized that all curves cross over at the failure probability of $P_f = 0.5$ occurring at the critical rainfall duration. This is because the cumulative probability of FS for all correlation lengths equal to 0.5 at the corresponding safety factor of FS = 1.0, as shown Fig. 14. Therefore, the location of the failure surface can be derived from probabilistic analysis, in which $P_f = 0.5$.

In order to obtain the failure surface, the failure probability distributions were calculated at the point of critical rainfall duration. Figure 15 shows the distribution of failure probability with depth for all correlation lengths. The corresponding failure surface was also obtained at the failure probability of $P_f = 0.5$, with the failure surface located at the depth of 1.7 m

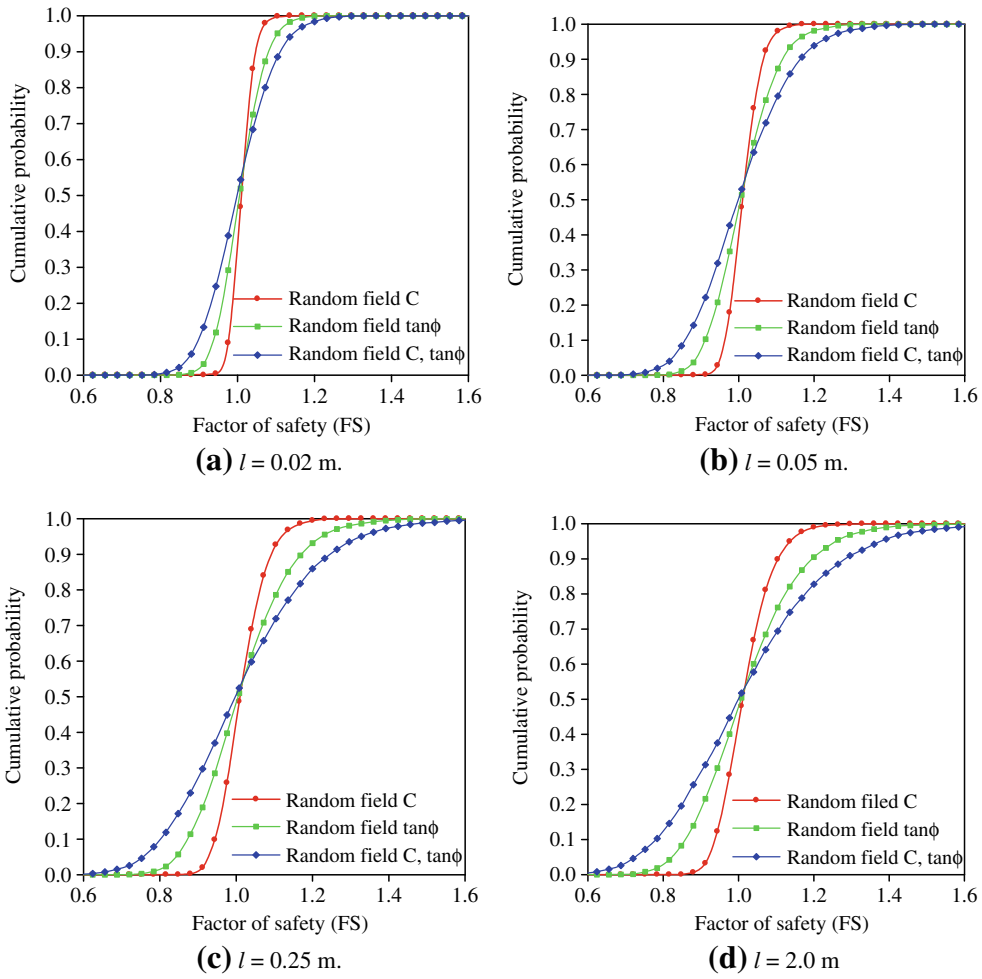

Fig. 16 Effect of random field C and tanϕ on the slope failure at the critical rainfall duration ($COV_C = 0.2$; $COV_{tan\phi} = 0.2$). **a** $l = 0.02$ m. **b** $l = 0.05$ m. **c** $l = 0.25$ m. **d** $l = 2.0$ m

of slope while the actual failure surface during the 1989 storm occurred at the depth of 1.6 m, which approximates the analysis result indicating that the probabilistic analysis with random fields is an effective predictor to locate critical failure surfaces and determine critical rainfall durations.

Effects of random field of shear strength parameters

In the previous assessment, two random fields of C (total soil cohesion under unsaturated condition) and tanϕ (frictional resistance) were considered for the failure probability calculation. One might want to identify which random field greater effect on the slope failure. In order to evaluate the influence of each random field, a series of FS for each random field alone and both random fields were calculated at the failure surface which occurred at the critical rainfall duration, and the cumulative probability curves of FS for these cases were obtained at a different correlation lengths. Figure 16 compares the cumulative probability curve of FS considering two random fields together with the curve obtained by ignoring one random field at a different correlation length. The difference between the curves considering two random fields and the curve neglecting one random field reflects the importance of that random field for failure probability calculation. As shown in Fig. 16, when random field tanϕ was ignored, the difference of probability was more than the difference by neglecting random field C. It turns out that shallow failure is mainly caused by reduction in soil cohesion during rainfall infiltration. In addition, this difference tends to increase with the increase of correlation length. This finding indicates that the influence of each random field for non-homogeneous soil is somewhat important.

Conclusion

This paper examined the spatial variability of shear strength parameters on rainfall-induced landslides. A case study of a sandstone slope with deep impermeable bedrock in a site in Japan was selected for comparison. An unsaturated seepage and infinite slope stability analysis were applied using a probabilistic method. To simulate shallow failure, the reduction in soil shear strength due to the increase in volumetric moisture content was considered. A series of Monte Carlo simulations were conducted to investigate the effect of a random field on C and tanϕ parameters. The analysis results were then compared to an actual occurrence of slope failure during a storm in 1989. The study results can be concluded as follows

1. The probabilistic analysis results indicate that the critical failure surface was located at the depth of approximately 1.0–2.0 m belowground surface depending on the rainfall duration. The failure surface occurred at 1.7 m depth at the critical rainfall duration of 9.5 h. The actual soil slope also failed at 1.6 m depth belowground in the period of the 1989 storm. However, the deterministic approach with infinite slope assumption reported the location of the failure surface at the base of the upper layer (i.e., 2.0 m in this study).
2. The critical failure surface is not necessarily fixed at the base of the upper layer but changed due to the migration of wetting front as rainfall progressed. The results show that the frequency of the critical failure surface that occurs at the weakest part of the upper layer increase with increased correlation length. This also agrees well with previous studies by Cho (2014) and Dou et al. (2015).
3. The probability framework can be used to find the critical rainfall duration corresponding to the location of the slip surface occurring at a depth of 1.7 m of the upper layer. In this study, the critical rainfall duration was obtained to indicate the slope failure during the 1989 rainstorm. The results confirm that the random field model is an essential technique to predict the slope failure due to rainfall.
4. A probabilistic stability analysis of rainfall-induced slope failure depends on the contribution of random fields on the shear strength parameters *C* and tanϕ. However, the study found that the random field of *C* is more important than the random field of tanϕ for failure probability estimation of shallow landslides. This finding can be used to verify the significance of effect of uncertain shear strength parameters of a shallow failure.

Acknowledgements The first author would like to acknowledge the AUN/Seed-Net (JICA) for a Ph.D. sandwich scholarship during his study. The authors would like to thank William L. Dam, Hydrogeologist, who assisted with editing the manuscript.

Compliance with ethical standards

Funding information This research was supported by the Thailand Research Fund Grant No. RSA-5880023 and the Ratchadaphiseksomphot Endowment Fund.

References

ASTM D2434-68 (2000) Standard test method for permeability of granular soils (constant head). ASTM International, West Conshohocken, PA

ASTM D6951 (2003) Standard test method for use of the dynamic cone penetrometer. ASTM International, West Conshohocken, PA

Baecher GB, Christian JT (2003) Reliability and statistics in geotechnical engineering. Wiley, New York

Caviedes-Voullième D, Garcı P, Murillo J (2013) Verification, conservation, stability and efficiency of a finite volume method for the 1D Richards equation. J Hydrol 480:69–84. doi:10.1016/j.jhydrol.2012.12.008

Cho SE (2009) Infiltration analysis to evaluate the surficial stability of two-layered slopes considering rainfall characteristics. Eng Geol 105(1):32–43. doi:10.1016/j.enggeo.2008.12.007

Cho SE (2012) Probabilistic analysis of seepage that considers the spatial variability of permeability for an embankment on soil foundation. Eng Geol 133:30–39. doi:10.1016/j.enggeo.2012.02.013

Cho SE (2014) Probabilistic stability analysis of rainfall-induced landslides considering spatial variability of permeability. Eng Geol 171: 11–20. doi:10.1016/j.enggeo.2013.12.015

Cho SE, Lee SR (2002) Evaluation of surficial stability for homogeneous slopes considering rainfall characteristics. J Geotech Geoenviron 128(9):756–763. doi:10.1061/(ASCE)1090-0241(2002)128:9(756)

Dou HQ, Han TC, Gong XN, Qiu ZY, Li ZN (2015) Effects of the spatial variability of permeability on rainfall-induced landslides. Eng Geol 192:92–100. doi:10.1016/j.enggeo.2015.03.014

Fenton GA, Griffiths DV (2008) Risk assessment in geotechnical engineering. John Wiley & Sons, New York

Fredlund D, Morgenstern NR, Widger R (1978) The shear strength of unsaturated soils. Can Geotech J 15(3):313–321. doi:10.1139/t78-029

Fredlund DG, Rahardjo H, Fredlund MD (2012) Unsaturated soil mechanics in engineering practice. John Wiley & Sons, New York

Geo-Slope (2012) Seepage modeling with SEEP/W. Geo-Slope International Ltd, Canada

Griffiths DV, Huang J, Fenton GA (2011) Probabilistic infinite slope analysis. Comput Geotech 38(4):577–584. doi:10.1016/j.compgeo.2011.03.006

Han TC, Dou HQ, Gong XN, Zhang J, Ma SG (2014) A rainwater redistribution model to evaluate two-layered slope stability after a rainfall event. Environ Eng Geosci 20(2):163–176. doi:https://doi.org/10.2113/gseegeosci.20.2.163

Kanjanakul C, Chub-uppakarn T, Chalermyanont T (2016) Rainfall thresholds for landslide early warning system in Nakhon Si Thammarat. Arab J Geosci 11(9):1–11. doi:10.1007/s12517-016-2614-4

Lee LM, Kassim A, Gofar N (2011) Performances of two instrumented laboratory models for the study of rainfall infiltration into unsaturated soils. Eng Geol 117(1):78–89. doi:10.1016/j.enggeo.2010.10.007

Li WC, Lee LM, Cai H, Li HJ, Dai FC, Wang ML (2013) Combined roles of saturated permeability and rainfall characteristics on surficial failure of homogeneous soil slope. Eng Geol 153:105–113. doi:10.1016/j.enggeo.2012.11.017

Lu N, Godt J (2008) Infinite slope stability under steady unsaturated seepage conditions. Water Resour Res 44(11):W11404. doi:10.1029/2008WR006976

Lu N, Godt JW (2013) Hillslope hydrology and stability. Cambridge University Press, New York

Matsushi Y (2006), Triggering mechanisms and rainfall thresholds of shallow landslides on soil-mantled hillslopes with permeable and impermeable bedrocks. Dissertation, University of Tsukuba

Matsushi Y, Hattanji T, Matsukura Y (2006) Mechanisms of shallow landslides on soil-mantled hillslopes with permeable and impermeable bedrocks in the Boso Peninsula, Japan. Geomorphology 76(1):92–108. doi:10.1016/j.geomorph.2005.10.003

Ng CWW, Shi QA (1998) A numerical investigation of the stability of unsaturated soil slopes subjected to transient seepage. Comput Geotech 22(1):1–28

Pan L, Warrick A, Wierenga PJ (1996) Finite element methods for modeling water flow in variably saturated porous media: numerical oscillation and mass-distributed schemes. Water Resour Res 32(6):1883–1889. doi:10.1029/96WR00753

Phoon KK (2008) Reliability-based design in geotechnical engineering: computations and applications. Taylor & Francis, London & New York

Phoon KK, Kulhawy FH (1999) Characterization of geotechnical variability. Can Geotech J 36(4):612–624. doi:10.1139/t99-038

Rahardjo H, Ong TH, Rezaur RB, Leong EC (2007) Factors controlling instability of homogeneous soil slopes under rainfall. J Geotech Geoenviron 133(12):1532–1543. doi:10.1061/(ASCE)1090-0241(2007)133:12(1532)

Ray RL, Jacobs JM, de Alba P (2010) Impacts of unsaturated zone soil moisture and groundwater table on slope instability. J Geotech Geoenviron 136(10):1448–1458. doi:10.1061/ASCEGT.1943-5606.0000357

Retheti L (1988) Probabilistic solutions in geotechnics. Developments in Geotechnical Engineering Vol. 46, Elsevier

Richards LA (1931) Capillary conduction of liquids through porous mediums. J Appl Phys 1(5):318–333. doi:10.1063/1.1745010

Santoso AM, Phoon K-K, Quek S-T (2011) Effects of soil spatial variability on rainfall-induced landslides. Comput Struct 89(11):893–900. doi:10.1016/j.compstruc.2011.02.016

Society (1995) Geological Society Engineering Group Working Party Report: the description and classification of weathered rocks for engineering purposes. Q J Eng Geol 28:207–242. doi:10.1144/GSL.QJEG.1970.003.01.01

Srivastava A, Babu GS, Haldar S (2010) Influence of spatial variability of permeability property on steady state seepage flow and slope stability analysis. Eng Geol 110(3):93–101. doi:10.1016/j.enggeo.2009.11.006

Van Dam JC, Feddes RA (2000) Numerical simulation of infiltration, evaporation and shallow groundwater levels with the Richards equation. J Hydrol 233(1):72–85. doi:10.1016/s0022-1694(00)00227-4

van Genuchten MT (1980) A closed-form equation for predicting the hydraulic conductivity of unsaturated soils. Soil Sci Soc Am J 44(5):892–898. doi:10.2136/sssaj1980.03615995004400050002x

Vanmarcke E (1983) Random fields: analysis and synthesis. The MIT Press, Cambridge

Wakatsuki T, Tanaka Y, Matsukura Y (2005) Soil slips on weathering-limited slopes underlain by coarse-grained granite or fine-grained gneiss near Seoul, Republic of Korea. Catena 60(2):181–203. doi:10.1016/j.catena.2004.11.003

Computers and Geotechnics 95 (2018) 68–81

Contents lists available at ScienceDirect

Computers and Geotechnics

journal homepage: www.elsevier.com/locate/compgeo

Research Paper

Underground excavation behaviour in Bangkok using three-dimensional finite element method

Chhunla Chheng[a], Suched Likitlersuang[b,*]

[a] Department of Civil Engineering, Faculty of Engineering, Chulalongkorn University, Bangkok, Thailand
[b] Geotechnical Research Unit, Department of Civil Engineering, Faculty of Engineering, Chulalongkorn University, Bangkok, Thailand

ARTICLE INFO

Keywords:
Deep excavation
Finite element modelling
Bangkok clays
Hardening soil model
Wall movement
Surface settlement

ABSTRACT

This study provides evidence that three-dimensional finite element modelling can be effectively applied for deep excavation analysis in Bangkok. The Bangkok subsoils were modelled using the hardening soil model and their parameters were calibrated against the results of laboratory and field tests. A study of a MRT station excavation was initially used to validate the model. The predicted wall movements and surface settlements were compared with the instrument data and two-dimensional analysis from a previous study. Another deep excavation project was selected as an independent study. The result shows that the model can be confidently used for deep excavation analysis.

1. Introduction

Bangkok, the capital city of Thailand, is a densely conglomerated metropolitan centre with a rapidly growing population resulting in limited space for residential and transportation infrastructure development. Hence, developing underground space to fulfil people's needs is a current trend. Importantly, Bangkok metropolis is also located on a large river deposit which consists of a thick soft clay layer deposited on the top [1]. Excavations in soft soils are usually associated with substantial difficulties. Since these types of soils are sensitive to deformations and possess low shear strength, they may lead to structural damage during the construction as well as throughout the life of projects [2]. In particular, deep excavations in soft clays, which could induce soil movements, need to be assessed thoroughly. Due to advancement of computational tools, most of the complex geotechnical problems including deep excavation employ finite element analysis. However, the results of finite element analysis are influenced by many input factors such as simplified geometry and boundary conditions, mesh generation, choice of constitutive soil model and its parameters, modelling of construction sequences, and structural modelling.

Ou et al. [3] employed non-linear three-dimensional finite element analysis (3D FEA) to evaluate the wall performance of an irregular excavation site of the Hai-Hua Building in Guangzhou, China. Similarly, Hou et al. [4] successfully modelled the excavation of the north square underground shopping centre in the Shanghai South Railway Station using 3D FEA. Those studies show that 3D FEA provided better results that were closer to the instrument data than predicted from 2D FEA for modelling wall deformation. Hsieh et al. [5] utilised 3D numerical analysis to study the deformation of a D-wall with and without cross wall. The results show that the cross wall effectively reduced lateral wall movement. Recently, Dong et al. [6] modelled the highly irregular geometry of the North Square shopping centre of the Shanghai South Railway Station with a 3D finite element model. The 12.5 m deep excavation was adjacent to a metro line, a metro underground station and other surrounding public infrastructure. Numerical analysis can be reasonably used to predict the wall deformation and ground surface settlement of the complex excavation. Dong et al. [7] also studied several effects on diaphragm deflection of deep excavation in Shanghai using 3D FEA. They concluded that much care must be taken in the FEA. For one, the corner effect was inherent in the 3D analysis of diaphragm wall deflection. Furthermore, Hsiung et al. [8] modelled deep excavation in Taiwan with 3D finite element modelling. They emphasised the corner effect and the results showed good agreement with the measured lateral wall deformation. Hence, the 3D effect shares much with ground movement analysis in deep excavation. Nowadays, the shape of excavation becomes more complicated and it leads to be very far from the assumptions used in 2D FEM as in Dong et al. [6] and Lin et al. [9].

In Bangkok, the numerical studies of deep excavation are often conducted using two-dimensional finite element analysis with the Mohr-Coulomb model. Many researchers [10–12] concentrated their work on back-calculating the ratio of undrained elastic modulus and undrained shear strength (E_u/s_u). Recently, Likitlersuang et al. [13] conducted a 2D FEA of a Bangkok MRT station considering the

* Corresponding author.
E-mail addresses: chhunla.ch@student.chula.ac.th (C. Chheng), fceslk@eng.chula.ac.th (S. Likitlersuang).

http://dx.doi.org/10.1016/j.compgeo.2017.09.016
Received 10 July 2017; Received in revised form 24 September 2017; Accepted 25 September 2017
Available online 04 October 2017

influence of constitutive soil models. The results revealed that the advanced soil models, the Hardening Soil Model (HSM) and Hardening Soil Model with small strain (HSS), provided better results compared to instrument data on the long side of the excavation. Due to the simplified assumptions of the 2D FEA, the effect of 3D cannot be included, such as wall movement predictions at the short side or near corner of an excavation. Moreover, the study was extended to predict ground surface settlements due to tunnel excavations in Bangkok [14]. This study was an extension of previous studies [13,14] but employing the 3D finite element method to model deep excavation problems in soft ground in Bangkok. The 3D finite element model was initially validated with the case study of a MRT station excavation by comparing the results with the instrument data and 2D analysis from the previous study [13,14]. In addition, an independent underground excavation was selected to make predictions. This study aims to provide necessary information to model the deep excavation problem using 3D FEA.

2. Challenges in deep excavation

2.1. Wall deformation

The most challenging issue in deep excavation is inward movement of retaining walls. Wall deformation can lead to catastrophic consequences when the deformation is excessive and has not been controlled effectively. Hence, this is a problem drawing much attention from geotechnical engineers. The finite element method is capable of modelling and predicting such stresses on retaining walls. Wall deflection results from lateral earth pressure and surcharge adjacent to the wall. Clough and O'Rourke [15] demonstrated the behaviour of wall deformation in response to excavation stages, as shown in Fig. 1. They concluded there are two types of deformation: cantilever and deep inward. Cantilever type appears at the early stages of excavation when struts or slabs have yet to be installed. In contrast, the deep inward pattern is usually exhibited after bracing systems have been installed and the excavation has advanced to deeper depths. These two types of deformation lead to the different ground settlement profiles as depicted in Fig. 1. Similar findings were presented by Ou et al. [16]. They also added that maximum lateral wall movement (δ_{hm}) often occurs near the surface of an excavation and falls within the range of 0.002–0.005 of excavation depth.

2.2. Ground surface settlement

In general, wall deformation is associated with surface ground settlement. The larger the wall deformation, the more ground surface settlement. Substantial degrees of settlement can be harmful to surrounding structures or public facilities. Ou et al. [16] conclude that there are two types of ground surface settlement: spandrel and concave type, as illustrated in Fig. 1. Spandrel type corresponds to cantilever type retaining wall deformation while concave type corresponds to the deep inward wall deformation pattern. Mana and Clough [17] and Hsieh and Ou [18] showed that maximum ground surface settlement (δ_{vm}) fell in the envelope of (0.5–1) of δ_{hm}. Hsieh and Ou [18] proposed an empirical trilinear relationship to estimate a ground surface settlement pattern as a function of distance from the wall, as shown in Fig. 2. It is noted that the maximum ground surface settlement (δ_{vm}) must be known. However, Ou and Hsieh [19] have suggested a new ground surface settlement pattern which takes the width of the excavation and depth to hard stratum into account.

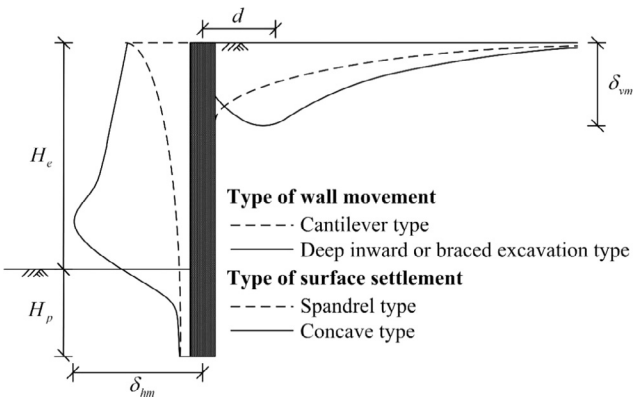

Fig. 1. Types of wall movement and ground surface settlement [13,18].

3. Finite element modelling

The numerical method has become a very powerful tool in geotechnical engineering in recent years. At present however, only two-dimensional (2D) finite element analysis (FEA) has been extensively employed in practice. Simplified assumptions are made in 2D FEA, for instance, plane strain or axisymmetry. In fact, only a few cases of deep excavation can be reasonably simplified as in 2D FEA. For example, the 3D effect could be neglected only in excavations whose length-to-width ratio is larger than 6 [20]. Furthermore, some features cannot be modelled in 2D FEA such as corner effects, complex conditions, and irregular shapes of excavation. Ou et al. [3] indicated that the degree of accuracy of 2D plane strain FEA was affected by the presence of corners. The existing corners can reduce the deformation of the wall especially on the short side. Therefore, this study focuses on utilisation of 3D finite element modelling in deep excavation analysis and evaluates its performance. Commercial software PLAXIS 3D AE (Anniversary Edition) was used in this study. A 10-noded tetrahedron element with a quadratic displacement function was selected to discretise soil volume. In 3D FEA, many parameters must be considered carefully including geological conditions, the constitutive soil model and its parameters, soil-structure interface modelling, and boundary conditions as well as construction sequences.

3.1. Bangkok subsoils

Bangkok is situated on a thick soft layer of clay consisting of marine deposits formed during the Quaternary period. Most deep excavation projects in Bangkok have been constructed in this layer. The soft layer

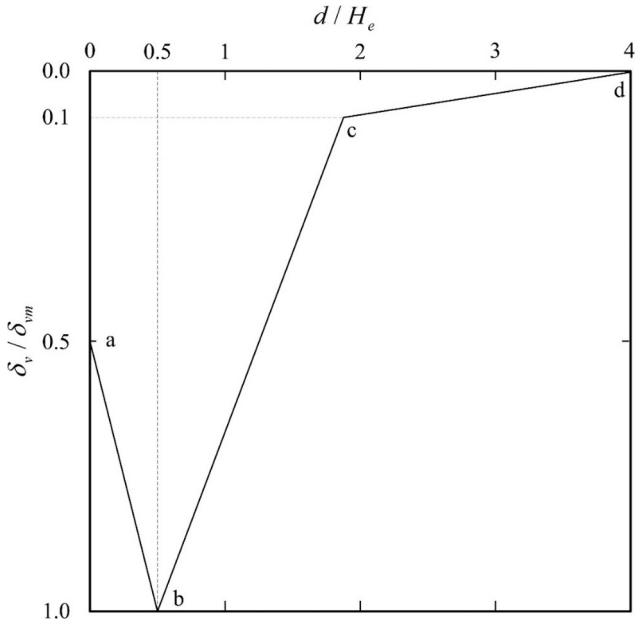

Fig. 2. Estimation of ground concave surface settlement [18].

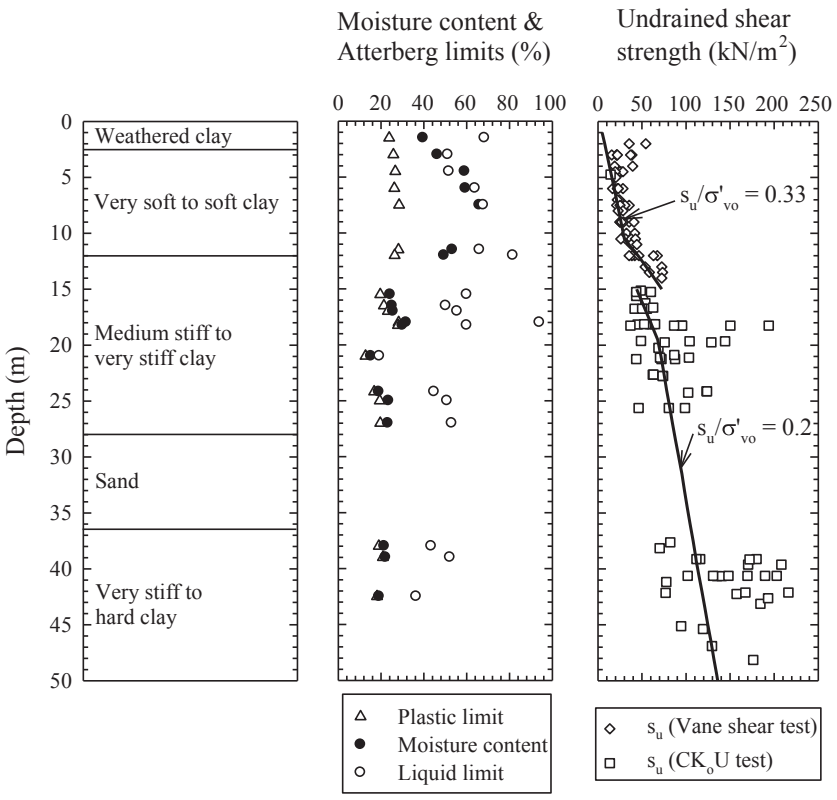

Fig. 3. Typical Bangkok subsoil condition [24].

of clay is overlaid by a terrestrial deposit of a few meters thickness. The underlying layers alternate clay and sand forming a broad sedimentary basin while the depth of the bedrock is still undetermined [21]. Fig. 3 presents a typical subsoil condition after Likitlersuang et al. [24]. The subsoil layers can be divided into 7 different layers including Made Ground (MG), Bangkok Soft Clay (BSC), Medium Clay (MC), First Stiff Clay (1st SC), Clayey Sand (CS), Second Stiff Clay (2nd SC) and Hard Clay (HC) after Likitlersuang et al. [13]. Many studies have been conducted to explore and investigate Bangkok's subsoils. For instance, Likitlersuang et al. [21] investigated the Bangkok subsoils extending from the MRT Blue Line extension project using pressuremeters. The results were interpreted for geotechnical parameters including coefficient of earth pressure at rest (K_0), undrained shear strength (s_u) and soil moduli. Moreover, it was reported that Bangkok's groundwater conditions have suffered from deep well pumping for the past 50 years which has led to the significant drawdown of water pressure [13,14,21].

3.2. Soil constitutive models

Soil constitutive modelling is an important procedure in finite element analysis. Advanced constitutive models are able to accurately describe soil behaviour. For example, the Hardening Soil Model (HSM) is an advanced soil model which can be used to describe both soft and stiff soils. The HSM was also shown capable of predicting behaviours of Bangkok clays by Likitlersuang et al. [13]. The HSM adopts a well-known hyperbolic model developed by Duncan and Chang [22] and the Mohr-Coulomb failure criterion. Soil stiffness is assumed to be stress-dependent while loading and unloading/reloading stiffness behave differently. Isotropic strain hardening and non-associated flow is adopted for frictional hardening, while associated-flow is employed for volumetric hardening. All required input parameters in PLAXIS 3D are shown in Table 1. Further detail on the Hardening Soil Model (HSM) can be found in Schanz et al. [23]. Surarak et al. [1] re-analysed the experimental data on soft and stiff Bangkok clays in order to obtain

Table 1
HSM parameters explanation.

Parameter symbol	Parameter description	Parameters evaluation
ϕ'	Internal friction angle	Slope of failure line from Mohr–Coulomb failure criterion
C'	Cohesion	y-intercept of failure line from Mohr–Coulomb failure criterion
ψ'	Dilatancy angle	Ratio of $d\varepsilon_v^p$ and $d\varepsilon_s^p$
E_{50}^{ref}	Reference secant stiffness from drained triaxial test	y-intercept in $\log(\sigma_3/p^{ref})$–$\log(E_{50})$ curve
E_{oed}^{ref}	Reference tangent stiffness for oedometer primary loading	y-intercept in $\log(\sigma_1/p^{ref})$–$\log(E_{oed})$ curve
E_{ur}^{ref}	Reference unloading/reloading stiffness	y-intercept in $\log(\sigma_3/p^{ref})$–$\log(E_{ur})$ curve
v_{ur}	Unloading/reloading Poisson's ratio	0.2 (default setting)
m	Exponential power	Slope of trend-line in $\log(\sigma_3/p^{ref})$–$\log(E_{50})$ curve
K_0^{nc}	Coefficient of earth pressure at rest (NC state)	$1-\sin\phi'$ (default setting)
R_f	Failure ratio	$(\sigma_1-\sigma_3)_f/(\sigma_1-\sigma_3)_{ult}$

Remarks: σ_1 is major principle stress (kN/m^2).
σ_3 is minor principle stress (kN/m^2).
p^{ref} is reference pressure (100 kN/m^2).

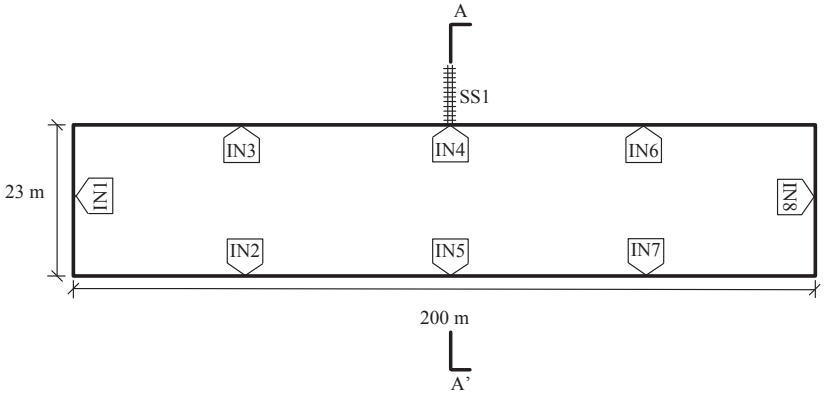

Fig. 4. Sukhumvit MRT station (top view): geometry and location of inclinometers.

stiffness and strength parameters of the HSM for finite element modelling. Numerical calibration was carried out and the conclusion drawn that drained moduli are required for HSM. Likitlersuang et al. [24] determined the small strain stiffness characteristics for Bangkok clay focusing on two parameters, the small strain shear modulus (G_{max}) and reference shear strain ($\gamma_{0.7}$), based on laboratory and field tests carried out at various locations throughout Bangkok.

3.3. Diaphragm wall modelling

A diaphragm wall (D-wall) is a concrete structure of finite thickness commonly designed as elastic material. In this study, the D-wall was modelled by plate elements (non-volume). The rigidity of concrete is mainly controlled by the modulus of elasticity (E), Poisson's ratio (v), thickness (t), and the unit weight of plate elements (γ) (the subtraction

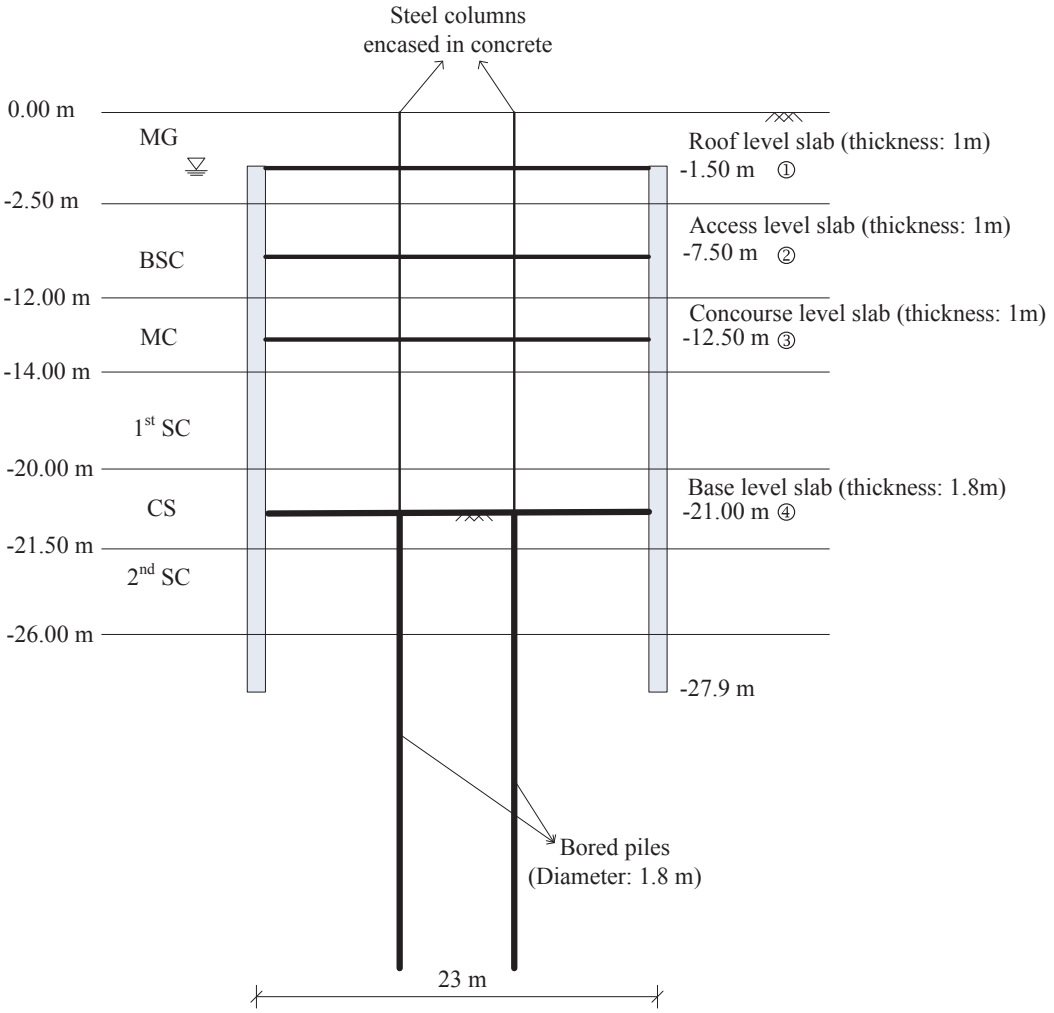

Fig. 5. Sukhumvit MRT station.

Table 2
Hardening soil model parameters.

Soil type	γ_b (kN/m^3)	C' (kPa)	ϕ' (°)	ψ' (°)	E_{50}^{ref} (MPa)	E_{oed}^{ref} (MPa)	E_{ur}^{ref} (MPa)	v_{ur}	m	K_0^{nc}	R_f	R_{inter}	Analysis type
MG	18	1	25	0	45.6	45.6	136.8	0.2	1	0.58	0.9	0.7	Drained
BSC	16.5	1	23	0	0.8	0.85	8.0	0.2	1	0.7	0.9	0.7	Undrained
MC	17.5	10	25	0	1.65	1.65	5.4	0.2	1	0.6	0.9	0.7	Undrained
1st SC	19.5	25	26	0	8.5	9.0	30.0	0.2	1	0.5	0.9	0.7	Undrained
CS	19	1	27	0	38.0	38.0	115.0	0.2	0.5	0.55	0.9	0.7	Drained
2nd SC	20	25	26	0	8.5	9.0	30.0	0.2	1	0.5	0.9	0.9	Undrained
HC	20	40	24	0	30.0	30.0	120.0	0.2	1	0.5	0.9	0.9	Undrained

between the unit weight of concrete and unit weight of soil) to account for non-volume elements [8].

3.4. Interface modelling

Soil-structure interaction in finite element modelling is another crucial matter to be carefully modelled. The nodal compatibility must endure the soil elements and the structure must move together [25]. PLAXIS 3D models interface by setting the distance between the two nodes of a node pair to zero. Each node has three translational degrees of freedom in three-dimensional space [26]. Like the behaviour of soils, interface behaviour can also be represented by the advanced soil models [2]. In this study, the HSM was employed. The properties of the interface model incorporate the behaviour of adjacent soil; however, shear strength parameters (c,ϕ) are reduced by the reduction factor (R_{inter}). The reduction factors were in the range from 0.7 to 0.9 depending on the soil profile to simulate the amount of ground disturbance [27]. The effect of ground disturbance is normally high on the top soil layer and lower for the deeper soil layer. In this study, the interfaces were modelled with the same constitutive modelling as adjacent soil with the strength reduction factors of 0.7 for MG, BSC, MC, 1st SC and CS layers and 0.9 for 2nd SC and HC layers [13].

4. Finite element analysis of deep excavations

4.1. Sukhumvit MRT station

4.1.1. General information

The Mass Rapid Transit (MRT) Blue line project is the first underground transportation system in Bangkok, which began service in 2004. The project includes approximately 20 km long tunnels and 18 cut-and-cover stations. The Sukhumvit MRT station is located in the centre of Bangkok. The station is 200 m long and 23 m wide with a length-to-width ratio of 8.7. Eight inclinometers were installed to record wall movement at different stages of excavation and documented with good quality. Inclinometer 4 (IN4) and inclinometer 8 (IN8) employed in this study were at the centre of the long and short sides respectively. A surface settlement array 1 (SS1) was installed behind the diaphragm wall to record the amount of surface settlement induced by excavation.

Table 3
Parameters for structural materials of Sukhumvit MRT station.

Parameters	d (m)	γ (kN/m^3)	E (MPa)	v	A (m^2)	I (m^4)	Element type
D-wall	1.0	16.5	28,000	0.15	–	–	Plate element
Base slab	1.8	25	28,000	0.15	–	–	Plate element
Platform slab	1.0	25	28,000	0.15	–	–	Plate element
Steel column	–	25	200,000	–	0.5	0.02	Plate element
Bored piles (massive circular pile)	1.8	25	28,000	–	–	–	Embedded pile

The layout and locations of inclinometers and surface settlement array are presented in Fig. 4. In addition, the cross section A-A′ is shown in Fig. 5.

According to Finno et al. [28], the 2D FEA could be used to roughly predict wall movement at the middle of the long wall. Due to the plane strain assumption used in the 2D FEA, it was not possible to model wall movement on the short side with confidence. The amount of wall movement and ground surface settlement during construction at this station was predicted and compared with monitoring data using 2D FEA by Likitlersuang et al. [13] with HSM input parameters as shown in Table 2. Therefore, at the long side of the excavation, it was expected that 3D FEA would exhibit the same results as 2D FEA since the geometry could be assumed to be a plane strain condition.

The excavation was supported by a 1 m-thick D-wall to a depth of 28 m. A top down method was adopted for underground construction in which concrete slabs were used to provide permanent lateral support to the D-wall. Bored piles were constructed before the soil was excavated and steel columns were placed on top of the concrete bore piles to provide vertical support for working loads. The structural input properties are given in Table 3. The construction sequences were divided into 4 different stages consecutively as summarised and illustrated in Table 4 and Fig. 5. The finite element mesh used in this study, as shown in Fig. 6, consisted of 295,081 10-noded tetrahedron elements with an

Table 4
Construction sequences of Sukhumvit MRT station.

Stage	Construction activities
1	Wish-in-place of D-wall, bored piles, steel columns and excavation to the depth of 1.5 m
2	Finish roof floor concrete casting and excavation to depth of −7.5 m
3	Finish second floor concrete casting and excavation to the depth of −12.5 m
4	Finish third floor concrete casting and excavation to the depth of −21 m

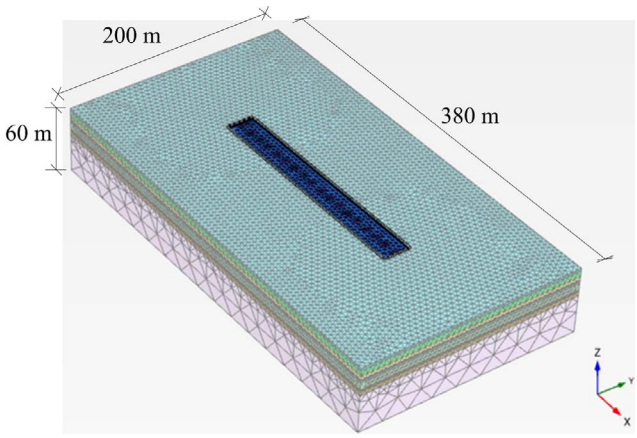

Fig. 6. Sukhumvit MRT station: Finite element mesh (295,081 10-noded tetrahedron elements with the average size of 3.96 m).

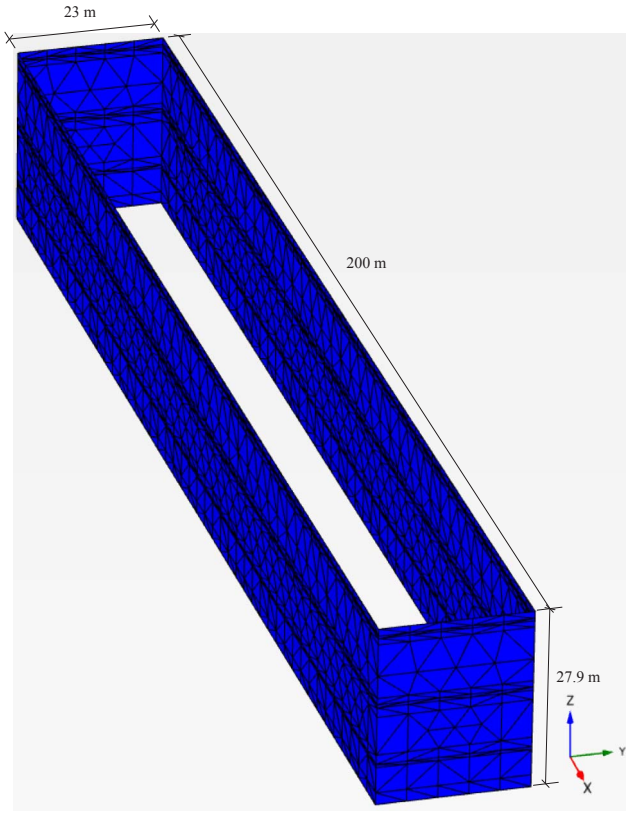

Fig. 7. Sukhumvit MRT station: Finite element mesh of D-wall.

average size of 3.96 m. In addition, the D-wall modelled with plate elements in PLAXIS 3D was discretised as triangular elements as illustrated in Fig. 7. It is noted that the effect of boundary conditions was studied by observing the deformation near the left, right and bottom boundaries at stage 4 of the excavation. The result revealed that the boundary effects were very small.

4.1.2. Results and discussion

A shading view of wall deformation at stage 4 obtained from 3D FEA is shown in Fig. 8. Cross sections were cut to observe the behaviour of wall movement at both the long and short sides at specific locations as depicted in Fig. 9. From observation of Fig. 10, a cantilever deformation pattern can be seen at the early stage on both sides of the wall because no bracing system had been installed yet. From the second stage to the final stage, the wall movement profiles on both long and short sides changed shape to the deep inward type. Fig. 10(a) plots the values of lateral wall movement at the middle of the long side against the measured values from IN4. The prediction almost overlaps at stage 1 and stage 4. However, the prediction agrees well with the measured values for stage 2 and stage 3. Maximum lateral wall movement at the final stage on the long side, as modelled from 3D FEA, was 95% of maximum lateral wall movement from recorded data from IN4. Fig. 10(b) presents the prediction from 3D FEA at the middle of the short side wall against the measured values from IN8. The prediction provides fair agreement with data from stage 1 to stage 3. However, the prediction at stage 4 almost coincides with the measured values. Specifically, maximum lateral wall movement at stage 4 on the short side agrees well with IN8, the difference being as little as 10%. These results suggest that 3D FE modelling accurately reflects the behaviour of wall deformation during excavation.

Compared to the previous study of Likitlersuang et al. [13], which modelled the station two-dimensionally, lateral wall movements at all stages of the current study greatly overlap as shown in Fig. 11(a). Maximum values from 3D FEA and the maximum values from 2D FEA are exactly the same except for stage 1 which varies slightly. An interesting phenomenon from 3D FEA is depicted in Fig. 11(b). Lateral wall deformation of the long side is twice the lateral wall movement of the short side corresponding to the observational data from IN4 and IN8. The difference is due to the corner effect. In addition to wall movement, ground surface settlement behind the wall can be observed from 3D FEA, as well. As seen in Fig. 12(a), ground surface settlement from the first stage, corresponding to the cantilever wall movement pattern, shows a spandrel shape as explained by Ou et al. [16]. From stage 2 to 4, ground surface settlements exhibit concave curves corresponding to deep inward wall movement patterns as explained in Ou et al. [15]. The maximum ground surface settlement at stage 4 agrees

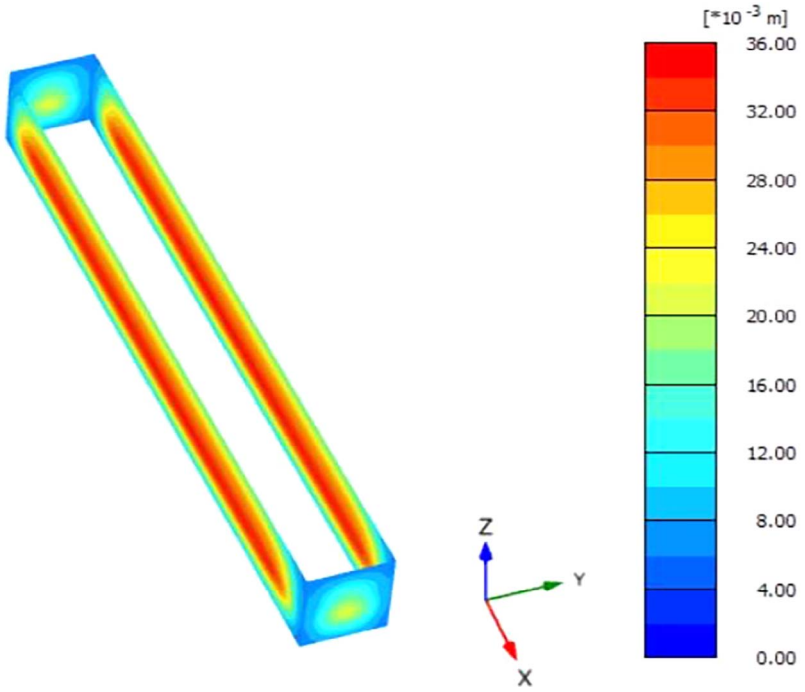

Fig. 8. Sukhumvit MRT station: Shading view of wall deformation station at Stage 4.

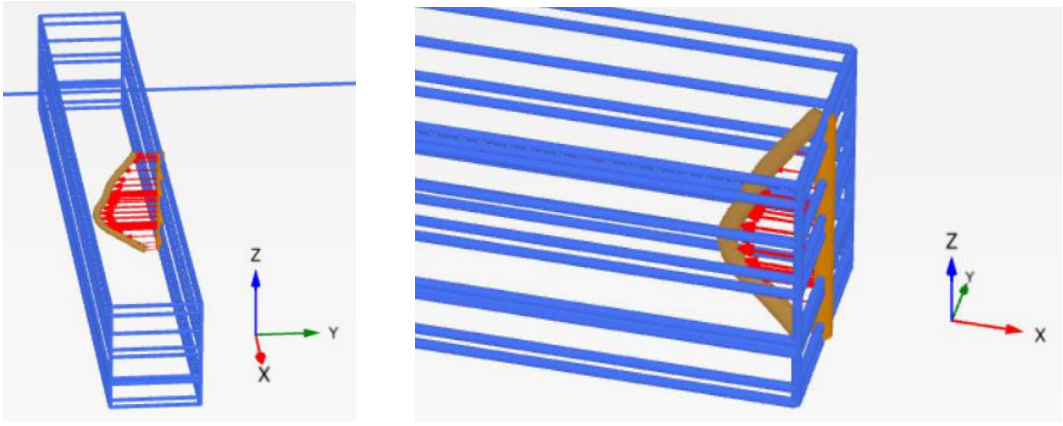

Fig. 9. Sukhumvit MRT station: Lateral wall movement at stage 4 by PLAXIS 3D [movement × 500]: (a) On the long side (IN4); (b) On the short side (IN8).

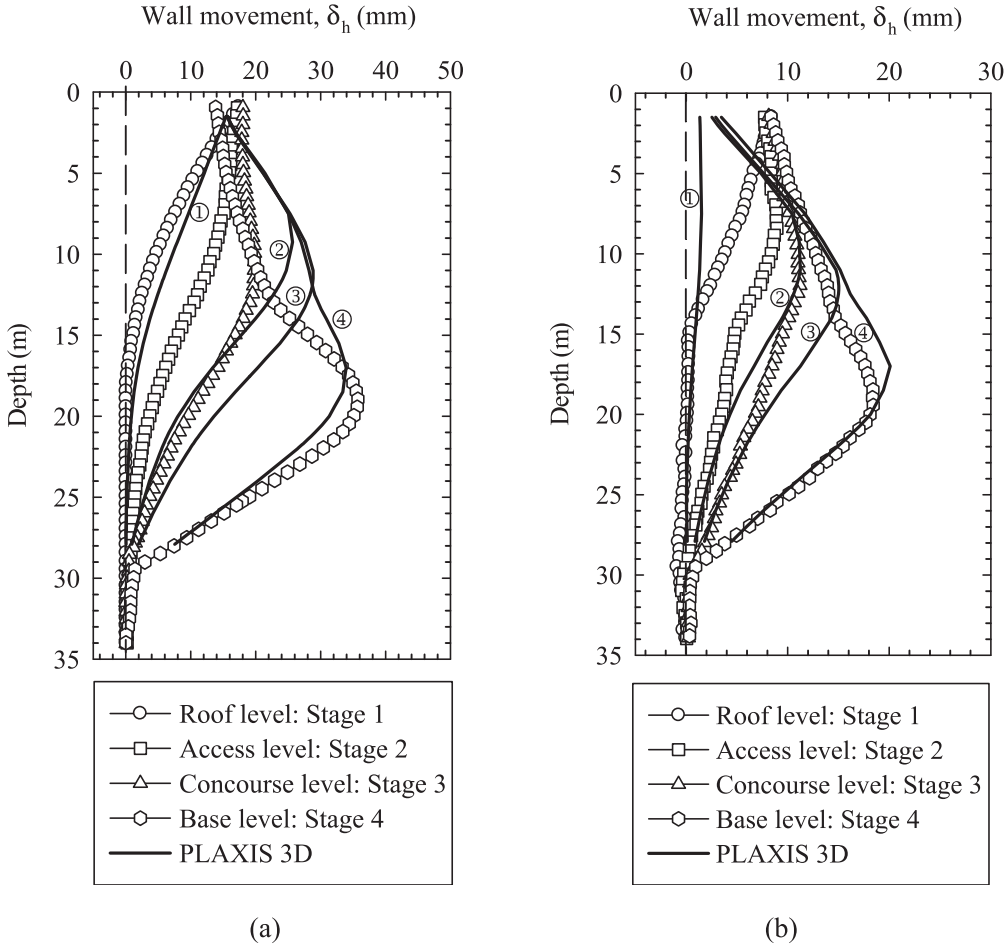

Fig. 10. Sukhumvit MRT station: Lateral wall movements: (a) PLAXIS 3D vs. IN4; (b) PLAXIS 3D vs. IN8.

well with the field data from a surface settlement array (SS1) as well as the empirical formulation by Hsieh and Ou [18]. Comparison between 2D FEA, 3D FEA and empirical relationships of Hsieh and Ou [18] are summarised in Fig. 12. As can be seen, maximum ground surface settlements from these three methods coincide at stage 4 which is the most critical stage of excavation.

In this section, the results of comparisons confirm that the proposed 3D finite element modelling is valid for deep excavation in Bangkok. In general, 3D FEA provides lateral movement and ground surface settlement predictions at all sides of the excavation. Moreover, the corner effect can be observed clearly as a significant feature in the 3D FEA. The wall movement and ground surface settlement prediction agree not only with the measured data but also with the empirical relationship.

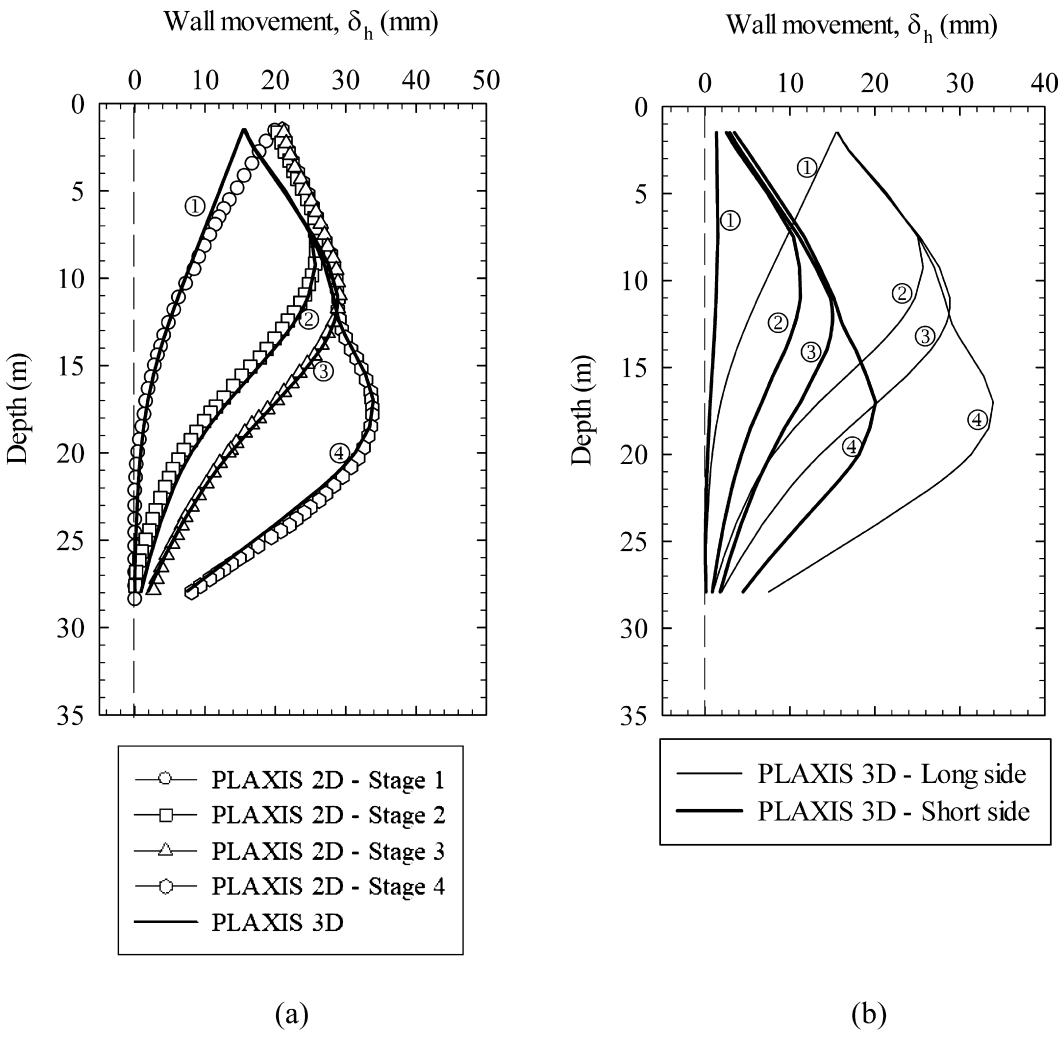

Fig. 11. Sukhumvit MRT station: Lateral wall movements: (a) PLAXIS 2D vs. PLAXIS 3D on long side; (b) PLAXIS 3D on long side vs. PLAXIS 3D on short side.

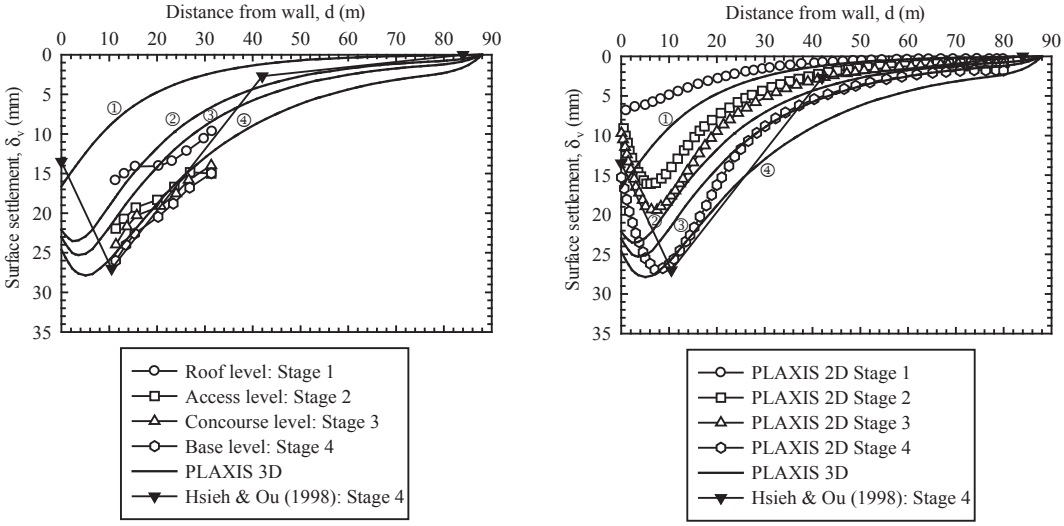

Fig. 12. Sukhumvit MRT station: Ground surface settlement profile comparison: (a) PLAXIS 3D vs. SS1; (b) PLAXIS 2D vs. PLAXIS 3D.

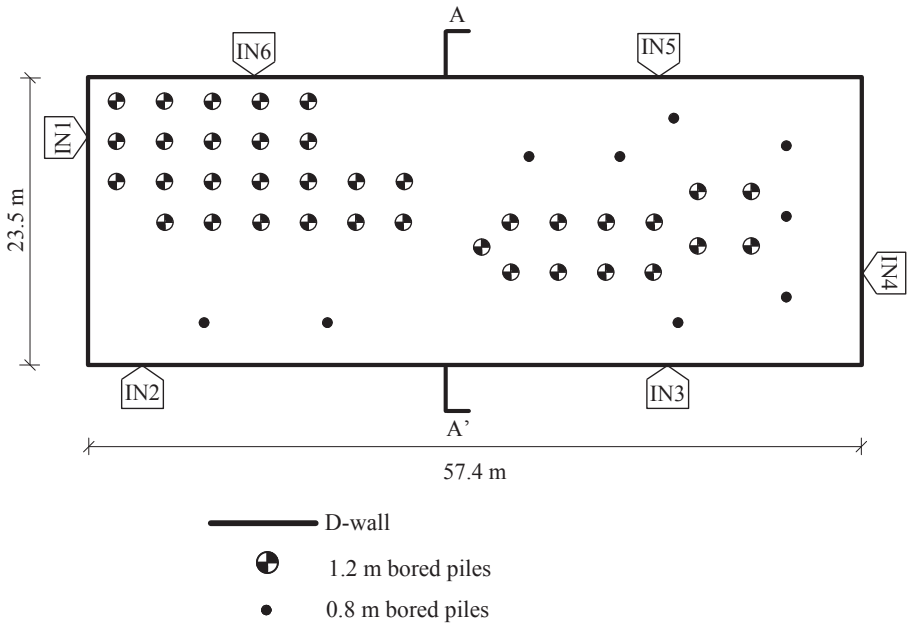

Fig. 13. Silom residential tower (top view): geometry, location of inclinometers and bored piles.

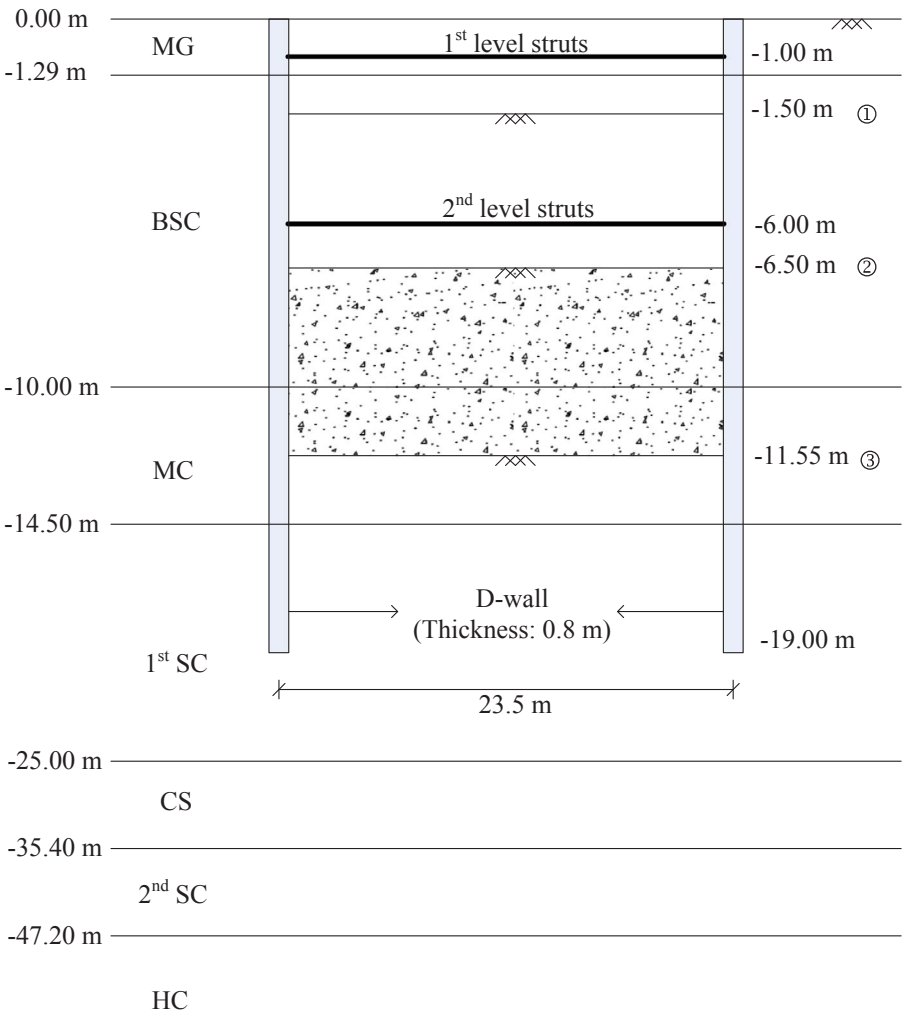

Section A-A'

Fig. 14. Silom residential tower.

Table 5
Construction sequences of the underground works of Silom residential tower.

Sequences	Construction activities
1	Wish-in-place of D-wall, bored piles, and excavation to the depth of 1.5 m
2	Install the 1st level of bracing system at −1.00 m and preloading excavation to the level of −6.5 m
3	Install the 2nd level of bracing system at −6.00 m and preloading and excavation to the level of −11.55 m
4	Finish lean concrete and mat foundation
5	Remove 2nd level of bracing system and cast B2 slab at −5.85 m
6	Cast B1 slab at −3.05 m and remove the 1st level of bracing system

Table 6
Parameters for soil retaining structures of Silom residential tower.

Parameters (plate element)	d (m)	γ (kN/m^3)	E (MPa)	v
D-Wall	0.8	16	24,800	0.15

4.2. Silom residential tower

4.2.1. General information

To confirm the consistency of the 3D FEA, another monitored deep excavation of a residential tower in Silom was selected as an independent case study. Silom is one of the most densely populated areas of Bangkok consisting of many commercial and residential towers. An underground construction site of a residential tower in the Silom road area was selected for this study. The excavation area has a rectangular shape 57.4 m long and 23.5 m wide. The length-to-width ratio is about 2.44. The layout and cross section A-A′ of the excavation area are depicted in Figs. 13 and 14, respectively, while the construction stages are summarised in Table 5. To obtain wall deformation information, 6 inclinometers were installed at 6 different locations. In this study, 2 inclinometers (IN1 and IN2) were used to compare with a 3D FEA. The residential project consists of 3 ground floors with a maximum excavation depth of 11.55 m below ground level. A bottom-up construction method was adopted for underground construction. Surrounding soil was supported with 0.8 m thick diaphragm walls (D-walls) with barrette piles. D-walls and barrette piles were modelled with plate elements with input properties summarised in Table 6. Two levels of

Table 7
Parameters for bracing system of Silom residential tower.

Parameters (beam element)	A (m^2)	γ (kN/m^3)	E (MPa)	I_3 (m^4)	I_2 (m^4)
Steel struts (400 × 400 × 172 kg/m)	2.19×10^{-2}	77.15	210,000	2.24×10^{-4}	6.66×10^{-4}
Steel wailings (400 × 400 × 172 kg/m)	2.19×10^{-2}	77.15	210,000	6.66×10^{-4}	2.24×10^{-4}

Remarks: Preloading was 30% of designed load.

Table 8
Parameters for bored piles of Silom residential tower.

Parameters (embedded pile)	E (MPa)	γ (kN/m^3)	Type	Diameter (m)
Bored piles	24,800	23	Massive circular pile	1.20
Bored piles	24,800	23	Massive circular pile	0.80

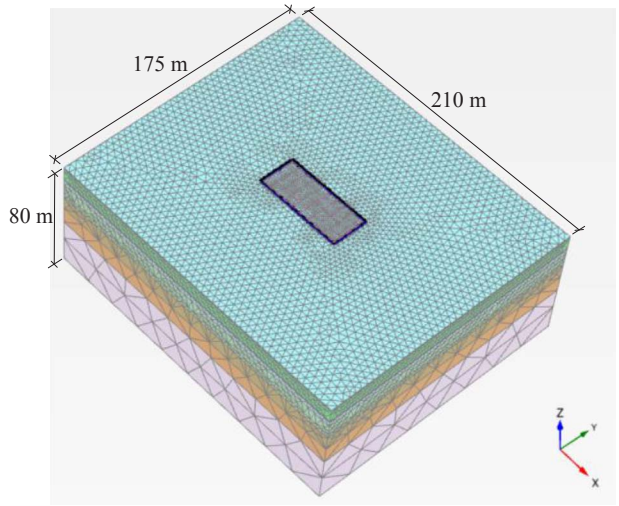

Fig. 15. Silom residential tower: Finite element mesh (236,424 10-noded tetrahedron elements with the average size of 3.54 m).

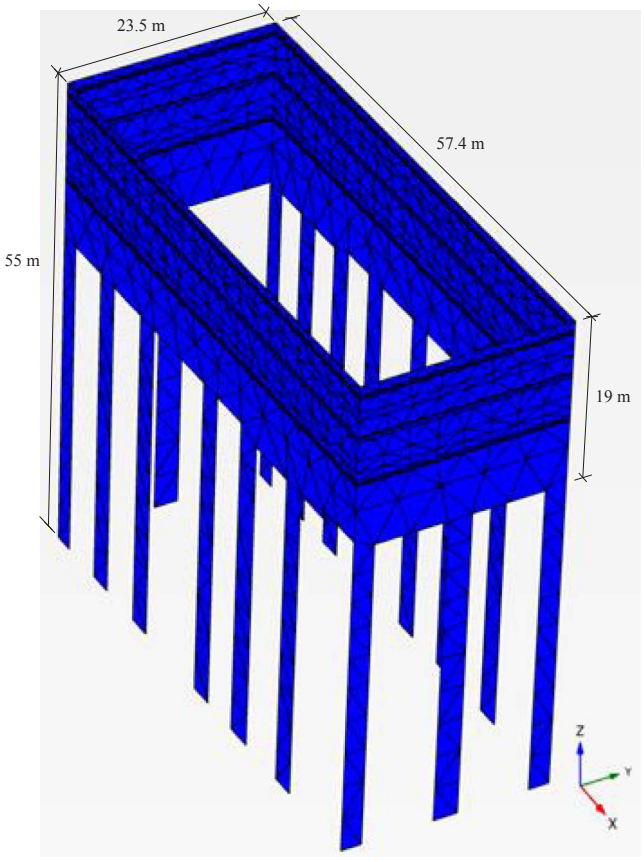

Fig. 16. Silom residential tower: finite element mesh of D-wall.

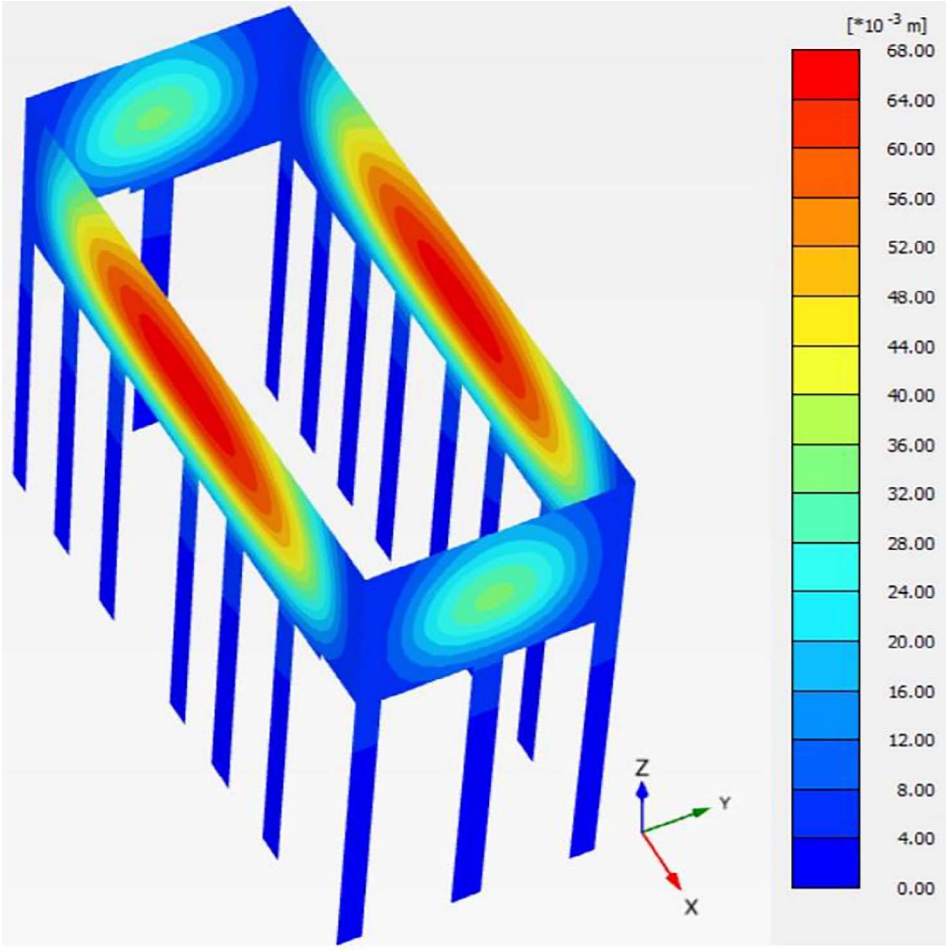

Fig. 17. Silom residential tower: Shading views of wall deformation at final stage.

bracing system were used to laterally support the walls. Struts and wailings were modelled as beam elements in which axial and flexural stiffness play important roles. The properties of struts and wailing are presented in Table 7. Moreover, these 2 levels of struts were preloaded to 30% of the load acting on each strut to provide the axial forces to the shore to reduce the inward movement of the wall. In addition, the input properties of existing bored piles are given in Table 8. The finite element model illustrated in Fig. 15 consists of 236,424 elements with an average size of 3.54 m while the finite element mesh of the D-wall is depicted in Fig. 16.

4.2.2. Results and discussion

A shading view of wall deformation at the final stage is displayed in Fig. 17. Maximum total movement of the wall occurs at the middle of the wall and reduces toward the corners. All wall panels show interconnection in which the deformation on the short sides of the excavation is smaller than the deformation along the long sides of excavation. Moreover, the cross-sections of both sides of wall are depicted in Fig. 18 to make the distinction clear from the original position. Here, a deep inward type of wall movement can be observed. Values of wall movement extracted from 3D FEA are compared with inclinometers 1 (IN1) and 2 (IN2) as plotted in Fig. 19. The continuous curves represent results from 3D FEA while the marked curves represent the instrument data. The maximum lateral wall movements from 3D FEA are 19 mm and 12 mm compared to 22 mm and 8 mm from IN1 and IN2 respectively. However, the movements at IN1 and IN2 are much less than the movements at the middle of the walls which is about 58 mm as illustrated in Fig. 20(a). This observation suggests that the corner effect is inherent and is therefore significant in the 3D FEA. Following the empirical relationship described by Ou et al. [16] as shown in Fig. 2, the input maximum lateral wall movement from observation is 58 mm, which is the same as given by the 3D FEA. The maximum lateral wall movement is 0.005 times the maximum excavation depth which is 11.55 m. In terms of surrounding soil movement, corresponding ground surface settlement is captured in Fig. 20(b) with comparison to the empirical relationship. After Hsieh and Ou [18], maximum ground surface settlement (δ_{vm}) is 60 mm while δ_{vm} from 3D FEA is 59 mm. The result shows that maximum ground surface settlement is 0.9 of maximum lateral wall movement which falls under the upper limit line of Mana and Clough [17].

To confirm the consistency of the 3D modelling for deep excavation in Bangkok soft soil, the second case was selected as an independent case study. The same set of parameters for Bangkok subsoils can be used. This indicated that the proposed 3D finite element modelling with the set of soil parameters can be reasonably used for the analysis of deep excavation in Bangkok. In this section, the results also confirm that 3D FEA provides reasonable wall movement and ground surface settlement predictions. The modelling clearly shows the difference of deformation near the corner and at the middle of the wall. 3D FEA shows good agreement with empirical and measured values for lateral wall movement as well as ground surface settlement.

5. Concluding remarks

This study presents three-dimensional finite-element analysis of deep excavations in soft ground. The 3D modelling and a set of Bangkok subsoil parameters were proposed for the deep excavation analysis. Two case studies from different locations in Bangkok were selected to model and analyse. The first case of the Sukhumvit MRT station was utilised for model validation by comparing the 3D FEA results with the

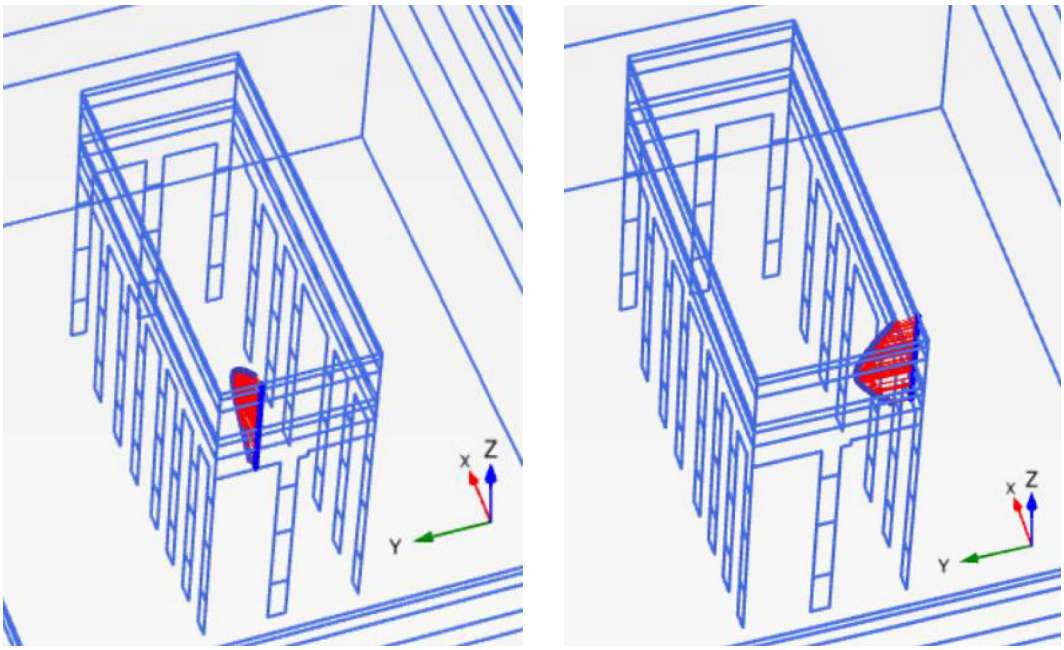

Fig. 18. Silom residential tower: Lateral wall movement at stage 3 by PLAXIS 3D [movement × 500]. (a) On the long side. (b) On the short side.

results from the previous 2D analysis. The second case of deep excavation was used to confirm the proposed 3D model and the set of Bangkok subsoil parameters. Several significant conclusions can be drawn:

(1) Though 2D FEA has been extensively used, the simplified plan strain analysis could be reasonably applied for large length-to-width ratio excavations. Unlike the Sukhumvit MRT station case, most of the projects in Bangkok do not possess such dimensions. In addition, the 2D assumption did not take the corner effect into account. Therefore, the main purpose of using 2D FEA is to reduce complexity and time in application.

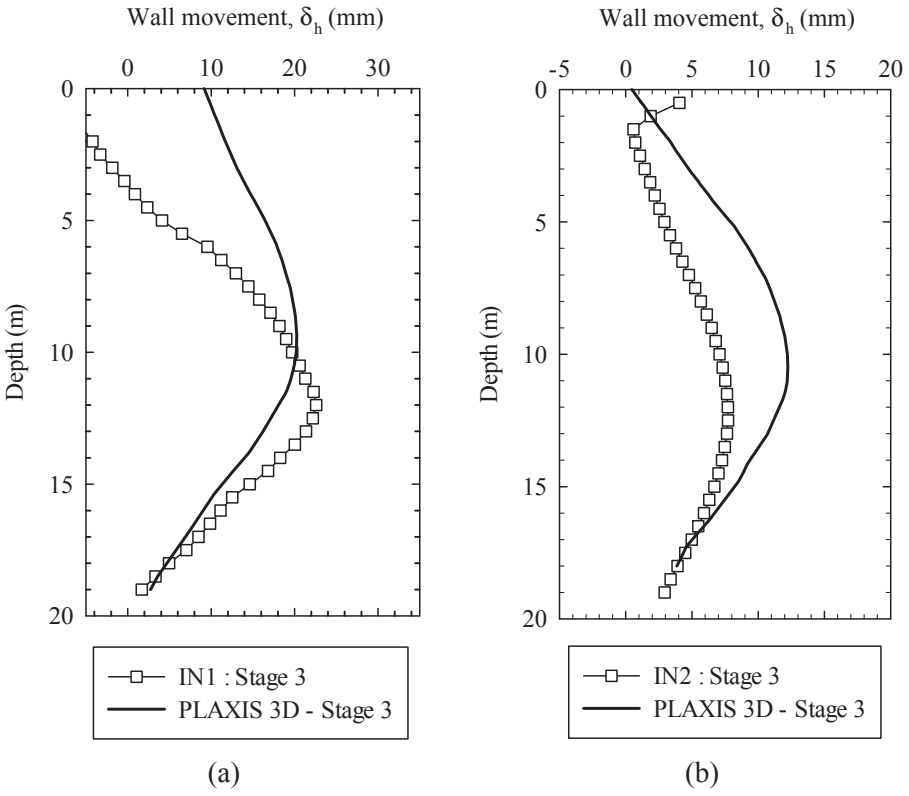

Fig. 19. Silom residential tower: Lateral wall movements: (a) PLAXIS 3D vs. IN1. (b) PLAXIS 3D vs. IN2.

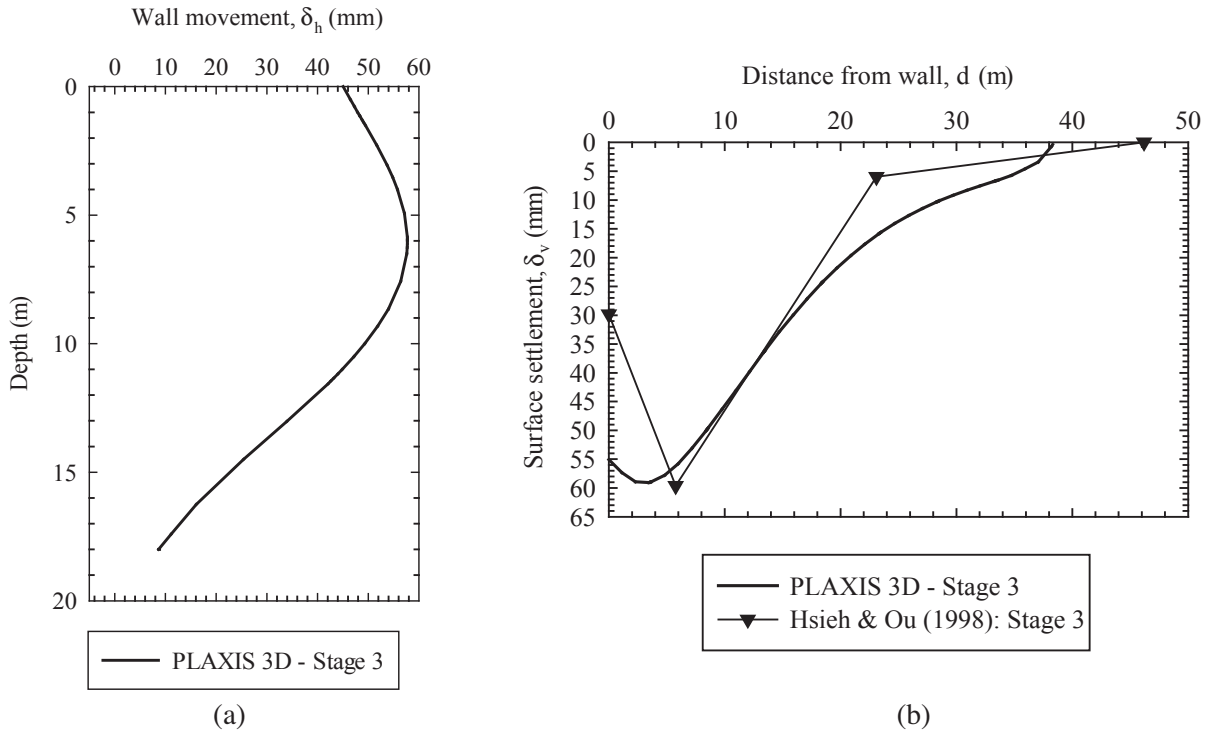

Fig. 20. Silom residential tower: (a) Wall deformation at the middle of the long side. (b) Corresponding ground surface settlement profile.

(2) 3D FEA provided wall deformation and ground surface settlement estimates at all sides of excavation pits. The corner effect was inherent in the simulation providing the different lateral wall movements on the long and short sides. Furthermore, lateral wall movements tended to be smaller near the corner.
(3) 3D FEA provided better agreement between predicted lateral wall movements and measurements from the sites along the long and short sides of the retaining walls; the differences were 10% on average in this study.
(4) Hardening soil model (HSM) parameters adopted from Likitlersuang et al. [13] characterised fairly accurately the soft and stiff Bangkok subsoils. Based on 3D FEA, the HSM parameters provided accurate wall deformation and ground surface settlement predictions compared to measurement data from the field.
(5) Another advantage of the 3D FE model is in simulating construction sequences. It can accurately reflect the real construction process at the excavation site. As a result, ground movement can be sequentially assessed.
(6) Meanwhile, applying 3D FE modelling for excavation means high costs. The 3D FE modelling requires a lot more time for calculation and engineering experience to analyse the results. For the Sukhumvit MRT station case, the 2D PLAIXS model takes around 30 min for calculation, while the 3D PLAXIS model requires up to 8 h. It is noted that the calculations were carried out on Intel® Core™ i7-6500U CPU@2.50 GHz.
(7) Based on the cases done in this study and experience learned from other 3D FE models, the advantage of applying 3D FE modelling would be more significant when the construction and excavation domain is more complex. It is recommended that more complex projects, in terms of geometry and construction processes, shall be tested with the proposed 3D FE modelling and the set of Bangkok soil parameters in the future.

Acknowledgements

This research was supported by the Thailand Research Fund, Grant No. RSA-5880023 and the Ratchadaphiseksomphot Endowment Fund. The authors would like to thank Lt. Col. Dr. Chanaton Surarak for providing useful suggestions throughout the research. The first author wishes to thank the AUN/SEED-Net (JICA) for a scholarship during his period of study.

References

[1] Surarak C, Likitlersuang S, Wanatowski D, Balasubramaniam A, Oh E, Guan H. Stiffness and strength parameters for hardening soil model of soft and stiff Bangkok clays. Soils Found 2012;52:682–97. http://dx.doi.org/10.1016/j.sandf.2012.07.009.
[2] Kempfert H-G, Gebreselassie B. Excavations and foundations in soft soils. Berlin, Heidelberg, Germany: Springer-Verlag; 2006.
[3] Ou CY, Chiou DC, Wu TS. Three-dimensional finite element analysis of deep excavations. J Geotech Eng, ASCE 1996;122:337–45. http://dx.doi.org/10.1061/(ASCE)0733-9410(1996) 122:5(337).
[4] Hou Y, Wang J, Zhang L. Finite-element modeling of a complex deep excavation in Shanghai. Acta Geotech 2009;4:7–16. http://dx.doi.org/10.1007/s11440-008-0062-3.
[5] Hsieh P-G, Ou C-Y, Lin Y-L. Three-dimensional numerical analysis of deep excavations with cross walls. Acta Geotech 2012;8:33–48. http://dx.doi.org/10.1007/s11440-012-0181-8.
[6] Dong Y, Burd H, Houlsby G, Hou Y. Advanced finite element analysis of a complex deep excavation case history in Shanghai. Front Struct Civ Eng 2014;8:93–100. http://dx.doi.org/10.1007/s11709-014-0232-3.
[7] Dong YP, Burd HJ, Houlsby GT. Finite-element analysis of a deep excavation case history. Géotechnique 2015;66:1–15. http://dx.doi.org/10.1680/jgeot.14.P.234.
[8] Hsiung B-CB, Yang K-H, Aila W, Hung C. Three-dimensional effects of a deep excavation on wall deflections in loose to medium dense sands. Comput Geotech 2016;80:138–51. http://dx.doi.org/10.1016/j.compgeo.2016.07.001.
[9] Lin P-Y, Chang T-K, Ho S-K, Ho SP. Excavation without internal support and its implications in construction management: a case study. J GeoEng 2017;12(2):81–8. http://dx.doi.org/10.6310/jog.2017.12(2).4.
[10] Teparaksa W, Thasnanipan N, Tanseng P. Analysis of lateral wall movement for deep braced excavation in Bangkok subsoils. Proceedings of the civil and environmental engineering conference, Bangkok, Thailand. 1999. p. 67–76.
[11] Phienwej N, Gan CH. Characteristics of ground movements in deep excavations with concrete diaphragm walls in Bangkok soils and their prediction. Geotech Eng J SEAGS 2003;34:167–76.
[12] Phienwej N. Ground movements in station excavations of Bangkok first MRT. Proceedings of the geotechnical aspects of underground construction in soft ground: proceedings of the 6th international symposium (IS-Shanghai 2008). 2008. p. 181.
[13] Likitlersuang S, Surarak C, Wanatowski D, Oh E, Balasubramaniam A. Finite element analysis of a deep excavation: a case study from the Bangkok MRT. Soils Found 2013;53:756–73. http://dx.doi.org/10.1016/j.sandf.2013.08.013.
[14] Likitlersuang S, Surarak C, Suwansawat S, Wanatowski D, Oh E, Balasubramaniam A. Simplified finite-element modelling for tunnelling-induced settlements. Geotech Res 2014;1:133–52. http://dx.doi.org/10.1680/gr.14.00016.

[15] Clough GW, O'Rourke TD. Construction-induced movements of insitu walls. Proceedings of the design and performance of earth retaining structures. 1990. p. 439–70.
[16] Ou CY, Hsieh PG, Chiou DC. Characteristics of ground surface settlement during excavation. Can Geotech J 1993;30:758–67. http://dx.doi.org/10.1139/t93-068.
[17] Mana AI, Clough GW. Prediction of movements for braced cuts in clay. J Geotech Eng Div, ASCE 1981;107:759–77.
[18] Hsieh P-G, Ou C-Y. Shape of ground surface settlement profiles caused by excavation. Can Geotech J 1998;35:1004–17. http://dx.doi.org/10.1139/t98-056.
[19] Ou CY, Hsieh PG. A simplified method for predicting ground settlement profiles induced by excavation in soft clay. Comput Geotech 2011;38:987–97. http://dx.doi.org/10.1016/j.compgeo.2011.06.008.
[20] Faheem H, Cai F, Ugai K. Three-dimensional base stability of rectangular excavations in soft soils using FEM. Comput Geotech 2004;31:67–74. http://dx.doi.org/10.1016/j.compgeo.2004.02.005.
[21] Likitlersuang S, Surarak C, Wanatowski D, Oh E, Balasubramaniam A. Geotechnical parameters from pressuremeter tests for MRT Blue Line Extension in Bangkok. Geomech Eng: Int J 2013;5:99–118. http://dx.doi.org/10.12989/gae.2013.5.2.099.
[22] Duncan JM, Chang CY. Nonlinear analysis of stress and strain in soils. J Soil Mech Found Div, ASCE 1970;96:637–59.
[23] Schanz T, Vermeer P, Bonnier P. The hardening soil model: formulation and verification. Beyond 2000 in computational geotechnics; 1999. p. 281–96.
[24] Likitlersuang S, Teachavorasinskun S, Surarak C, Oh E, Balasubramaniam A. Small strain stiffness and stiffness degradation curve of Bangkok Clays. Soils Found 2013;53:498–509. http://dx.doi.org/10.1016/j.sandf.2013.06.003.
[25] Potts DM, Zdravkovic L. Finite element analysis in geotechnical engineering: application vol. 2. Thomas Telford; 2001.
[26] Brinkgreve RBJ, Kumarswamy S, Swolfs WM, Waterman D, Chesaru A, Bonnier PG, et al. PLAXIS 2015. The Netherlands: PLAXIS bv; 2015.
[27] Schweiger H. Influence of constitutive model and EC7 design approach in FEM analysis of deep excavations. Proceedings of the proceeding of ISSMGE international seminar on deep excavations and retaining structures, Budapest. 2009. p. 99–114.
[28] Finno RJ, Blackburn JT, Roboski JF. Three-dimensional effects for supported excavations in clay. J Geotech Geoenviron Eng 2007;133:30–6. http://dx.doi.org/10.1061/(ASCE)1090-0241(2007) 133:1(30).

Cite this article
Nguyen TS, Likitlersuang S and Jotisankasa A (2018)
Stability analysis of vegetated residual soil slope under rainfall conditions.
Environmental Geotechnics **XXXX(XXXX)**: 1–XX,
https://doi.org/10.1680/jenge.17.00025

Research Article
Paper 1700025
Received 08/04/2017; Accepted 19/06/2018

Keywords: landslides/permeability/seepage

Environmental Geotechnics

ice publishing

Stability analysis of vegetated residual soil slope under rainfall conditions

Thanh Son Nguyen BEng, MEng, PhD
Lecturer, Department of Civil Engineering, Faculty of Engineering, Mien Trung University of Civil Engineering, Tuy Hòa, Vietnam

Suched Likitlersuang BEng, MEng, DPhil
Professor, Geotechnical Research Unit, Department of Civil Engineering, Faculty of Engineering, Chulalongkorn University, Bangkok, Thailand (corresponding author: fceslk@eng.chula.ac.th) (Orcid:0000-0001-8289-3647)

Apiniti Jotisankasa BEng, MSc, DIC, PhD
Associate Professor, Geotechnical Innovation Laboratory, Department of Civil Engineering, Faculty of Engineering, Kasetsart University, Bangkok, Thailand



The effects of climate change including intense rainfalls have resulted in many slope failures. The bioengineering method using vegetation is an environmentally friendly alternative for slope stabilisation. This paper presents the effect of root reinforcement on the stability of vegetated slope under rainfall condition. A transient seepage and slope stability analysis was conducted based on the finite-element and limit equilibrium methods. Field monitoring on a residual soil slope in Thailand was numerically modelled. In transient seepage analysis, the soil-water characteristic curve and the saturated permeability measured from laboratory and in situ tests were used, and the results are comparable with the monitored values from the site. For slope stability analysis, the effective shear strength parameters from direct shear tests were used to model the well-compacted and non-compacted soil slopes. The additional shear strength of soil from the root cohesion was modelled for vegetated soil slope. The results show that the contribution of root cohesion to slope stability was more significant for the non-compacted soil condition than for the well-compacted one. Both modelled and monitored pore-water pressure reached the highest values about 1 d after the daily rainfall had reached its peak. This finding has a significant implication for landslide warning based on rainfall.

Notation

A_r	root area
A_s	cross-sectional area of soil
c'	effective soil cohesion
c_r	root cohesion
h	total pressure head
k	hydraulic conductivity function
k_s	saturated permeability
k_x	hydraulic conductivity in the horizontal direction
k_y	hydraulic conductivity in the vertical direction
l	length of slice
n, m	soil-water characteristic curve (SWCC) parameters
q	applied flux boundary
S_e	effective water saturation
T_r	tensile strength of root
t	time: d
u_a	pore-air pressure
u_w	pore-water pressure
W	weight of slice per unit base area
α	fitting parameter for SWCC
β	slice base inclination
γ	unit weight of soil
θ	volumetric moisture content
θ_r	residual volumetric moisture content
θ_s	saturated volumetric moisture content
σ	total stress
σ'	effective stress
σ^s	suction stress
τ_f	shear strength
ϕ'	effective friction angle

Introduction

Shallow landslides usually occur due to heavy rainfall and mostly involve completely weathered rock or residual soil slopes. Heavy rainfall and the subsequent infiltration can cause a reduction in soil shear strength due to a decrease in soil suction and/or an increase in pore-water pressure as well as moisture content, which can ultimately lead to slope failure (Ng and Shi, 1998; Rahardjo *et al.*, 2007). The stability of natural and fill slopes can be significantly influenced by the vegetation condition. The contributions of vegetation to slope stability are well recognised for both their hydrological effects and mechanical effects (Cecconi *et al.*, 2015;

Chirico *et al*., 2013; Fatahi *et al*., 2014; Jotisankasa *et al*., 2014; Leung *et al*., 2015; Pathirage *et al*., 2017; Schmidt *et al*., 2001; Wu *et al*., 1979). For the hydrological effects, the increase in soil suction due to the moisture extracted by plant roots from soil is known as evapotranspiration. The presence of roots in the soil can also affect the soil's permeability and soil-water retention behaviour (Jotisankasa and Sirirattanachat, 2017). One of the major mechanical effects of roots on slope stability is the process of increase in soil shear strength provided by additional root reinforcement (Coppin and Richards, 1990; Eab *et al*., 2015; Likitlersuang *et al*., 2017; Rahardjo *et al*., 2018; Wu, 2013). During heavy rainfall, the air humidity is generally high; evapotranspiration would thus be negligible and of minor influence on infiltration and slope stability.

Wu *et al*. (1979) developed a simple root reinforcement model with the assumption of elastic roots which extended to a potential failure surface in a slope. Schmidt *et al*. (2001) measured root cohesion in the field, and their results indicate that the variability in root cohesion depends on the species of vegetation present. They found that root cohesion ranges from 6·8 to 23·2 kPa in industrial forests and from 25·6 to 94·3 kPa in natural forests. Eab *et al*. (2015) studied the increase in soil shear strength by a vetiver root system by using direct shear tests. The results can be used to correlate the root area ratio with the increase in soil shear strength. Vetivers with root area ratios of 2·44–4·37% can increase root cohesion by around 6·0–6·8 kPa. In addition, the fact that root cohesion tends to decrease with depth was observed from typical shrub and tree roots in Hong Kong and China by Ji *et al*. (2012) and Leung *et al*. (2015). The results of these studies on root cohesion were then employed in slope stability analysis, which suggests that vegetation significantly contributes to shallow failures at depths of around 1·0–2·0 m only.

Several researchers have investigated the influence of rainfall on slope stability by using numerical modelling (Fredlund and Zhang, 2004; Ng and Shi, 1998). Most results indicate that the critical pore-water pressure triggering slope instability is significantly influenced by rainfall intensity and rainfall duration. Oh and Lu (2015) conducted a field study of two cut slopes in Korea and investigated the hydromechanical properties of soils, aiming to predict failure events. They found that the shape of the predicted failure surfaces matched those of actual failure. The slope failures occurred as a result of the decrease in soil suction due to heavy rainfall of about 100 mm/d. Nguyen *et al*. (2017) conducted a case study of a rainfall-induced slope failure to verify the effect of spatial variability of soil shear strength. However, most previous researches on vegetated soil slope lacked comparisons between monitoring data and model prediction (Leung, 2014; Zhan *et al*., 2007). This may lead to the proposed model being less convincing. In addition, the contribution of vegetation to slope stability during heavy rainfall has not been studied yet.

In this study, full-scale field monitoring on an unsaturated soil slope in Nakorn Nayok Province, Thailand (Jotisankasa *et al*., 2009) together with rainfall records and pore-water pressures were employed in an analysis. The soil slope was rebuilt, compacted and grown with vetiver grass after failure in 2004. A two-dimensional (2D) seepage analysis was performed using the finite-element method to simulate the pore-water pressure and volumetric moisture content. The results of seepage model were verified against the field data. Transient stability analysis was conducted for two cases: well-compacted soil condition and non-compacted soil condition. To study the influence of vegetation on slope stability, the extended Mohr–Coulomb model with the unified effective stress concept for unsaturated soils was applied in the limit equilibrium analysis. The method of slices was used to calculate the factor of safety (FS) for the soil slope considering the effect of root reinforcement. The analysis results can be used to explain the influence of root reinforcement on vegetated slope.

Theoretical framework

Unsaturated–saturated seepage analysis

For seepage analysis of an unsaturated soil layer, Darcy's law originally derived for saturated soil was modified for the flow of water through unsaturated soil (Richards, 1931). The numerical codes were developed based on the theory of unsaturated flow. The governing equation for 2D transient flow in unsaturated soil is given by

$$1.\quad \frac{\partial}{\partial x}\left(k_x\frac{\partial h}{\partial x}\right)+\frac{\partial}{\partial y}\left(k_y\frac{\partial h}{\partial y}\right)+q=\frac{\partial \theta}{\partial t}$$

where h is the total pressure head (m); k_x and k_y are the hydraulic conductivities in the horizontal direction (x) and vertical direction (y) (m/d), respectively; θ is the volumetric moisture content, defined as the ratio of the volume of soil water to the total volume of soil; q is the applied flux boundary (m/d); and t is time (d).

Several empirical and semi-empirical functions have been proposed to define the hydraulic conductivity of the unsaturated soil. In this analysis, the non-linear functions of the volumetric moisture content and the coefficient of permeability of the unsaturated soil were adopted based on the Mualem–van Genuchten model (van Genuchten, 1980) as

$$2.\quad S_e=\frac{\theta-\theta_r}{\theta_s-\theta_r}=\frac{1}{[1+(\alpha h)^n]^m}$$

where $m = 1 - 1/n$ and $n > 1$ are dimensionless parameters and

$$3.\quad k=k_s S_e^{1/2}\left[\left(1-S_e^{1/m}\right)^m\right]^2$$

in which S_e is the effective water saturation, θ_r is the residual volumetric moisture content, θ_s is the saturated volumetric

moisture content, k_s is the saturated permeability (m/d) and α is the fitting parameter (1/m).

The transient-state non-linear partial differential equation (Equation 1) was solved using an iterative finite-element scheme in the Seep/W module of GeoStudio software (Geo-Slope, 2007). To obtain reliable results, the time step and element size should be defined in advance (Caviedes-Voullième *et al*., 2013; Smith and Griffiths, 2004; Van Dam and Feddes, 2000). In this analysis, a small time step increment of 300 s and a global element size of 0·2 m were employed.

Root cohesion of vegetation

The contribution of vegetation to slope stability analysis is usually characterised by root cohesion through root reinforcement. Wu *et al*. (1979) modified the root reinforcement model to define the root cohesion from the tensile strength of an individual root T_{ri} and the root area ratio (A_{ri}/A_s) as follows

$$c_r = 1{\cdot}2\sum_{i=1}^{n} T_{ri}\left(\frac{A_{ri}}{A_s}\right) \quad (4)$$

where the root area ratio is defined as the ratio between the area of each root (A_{ri}) and the cross-sectional area of soil (A_s) and n is the number of roots in the area.

There are several researchers who investigated and statistically compared the distribution of roots and root area ratio with depth, the relationship between root tensile strength and root diameter and the variation of root cohesion with depth (i.e. Eab *et al*., 2015; Ji *et al*., 2012; Leung *et al*., 2015). The laboratory investigation on the vetiver root system by Eab *et al*. (2015) was employed in this study. The investigation programme included root observation and direct shear tests of vetiver root-reinforced soils. The results showed that a vetiver root could grow up to 1·8 m with an average root area ratio of 4%. The root cohesions observed from the direct shear tests were approximately 3–6 kPa within 3–6 months of growth.

Stability analysis of vegetated slope

FS is defined as the ratio of the available shear strength to the shear stress calculated along the failure surface. Normally, the traditional limit equilibrium is used to determine the FS of a slope under the transient infiltration condition (Lu and Godt, 2013). Therefore, the method of slices was adopted to calculate the FS along the potential failure surface and to search for the critical surface. FS can be expressed as

$$\mathrm{FS} = \frac{\sum_i^n \tau_f l_i}{\sum_i^n W_i \sin \beta_i} \quad (5)$$

where n is the total number of slices, τ_f is the shear strength, i is the slice index, l_i is the length of each slice, W_i is the weight of each slice per unit base area and β_i is the slice base inclination.

For a vegetated slope under unsaturated–saturated condition, the shear strength can be expressed by using the primary influence of root reinforcement, as suggested by Wu *et al*. (1979), in combination of the Mohr–Coulomb failure criterion (Fredlund *et al*., 1978). The shear strength is given by

$$\tau_f = c' + c_r + \sigma' \tan \phi' \quad (6)$$

where c' is the effective soil cohesion, c_r is the root cohesion, σ' is the effective stress and ϕ' is the effective friction angle. The effective stress can be computed by using the suction stress-based equation (Lu and Likos, 2006)

$$\sigma' = \sigma - u_a - \sigma^s \quad (7)$$

where σ is the total stress due to the self-weight of the soil; u_a is the pore-water pressure, which is zero at the atmospheric condition; and σ^s is the suction stress, which can be expressed as a function of matric suction ($u_a - u_w$) (Fredlund *et al*., 2012; Lu *et al*., 2010)

$$\sigma^s = -\frac{\theta - \theta_r}{\theta_s - \theta_r}(u_a - u_w) \quad (8)$$

where θ is volumetric water content. θ_r and θ_s are the saturated and residual volumetric water contents of soil, respectively.

In the incorporation of Equations 6–8, the shear strength of the vegetated slope can be defined under the soil–root composite for unsaturated–saturated condition as follows

$$\tau_f = c' + c_r + \left[(\sigma - u_a) + \frac{\theta - \theta_r}{\theta_s - \theta_r}(u_a - u_w)\right] \tan \phi' \quad (9)$$

Since the weight of grass was considered negligible and there was no traffic load on the slope, the weight of each slice per unit base area (W_i) from the slope surface to the potential failure surface was contributed by soil only, which can be expressed as

$$W_i = \sum_{i=1}^{n} \gamma A_{si} \quad (10)$$

where γ is the unit weight of soil. To simplify the calculation in the transient slope stability analysis, γ can be approximated as the saturated unit weight for both unsaturated and saturated

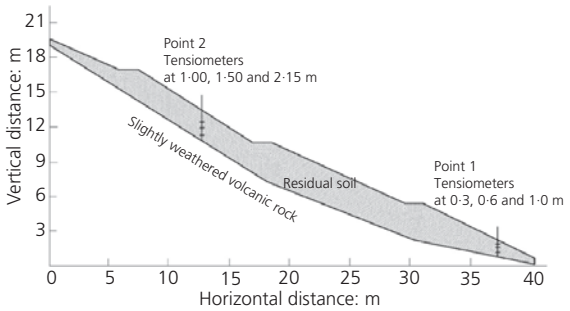

Figure 1. Field instruments and finite-element model of study site (after Jotisankasa *et al*. (2009))

conditions during the rainy season. A_{si} is the cross-sectional area of each slice.

Finally, the FS with consideration of vegetation effects on slope stability during rainfall infiltration can be written as

$$\mathrm{FS} = \frac{\sum_i^n \left(c' + c_r\right) l_i + W_i \cos \beta_i \tan \phi' - \left(\frac{\theta - \theta_r}{\theta_s - \theta_r}\right) u_w l_i \tan \phi'}{\sum_i^n W_i \sin \beta_i} \quad (11)$$

The computed field of volumetric moisture content and soil suction (pore-water pressure) from transient seepage analysis are then used as hydrological parameters to input in the Slope/W module (Geo-Slope, 2007) for calculating FS. The results are verified whether or not slope failure occurs within periods of heavy rainfall.

Site description

Location, geometry and historical failure

The study site is located near the Khundan Prakanchon dam (formerly known as the Thadan dam) in Nakorn Nayok Province, Thailand (hereafter referred to as the Thadan slope) about 200 km north-east of Bangkok. A shallow failure in 2004 was triggered by a heavy rainfall spanning over 3 d which amounted to a total rainfall of about of 300 mm or an average of about 100 mm/d. After failure, the slope was redesigned and constructed with compacted residual soil available on-site. The repaired soil slope was investigated by using a lightweight dynamic penetrometer (Jotisankasa *et al*., 2009), which indicated the thickness of the residual soil layer to be around 2–3 m. Below the residual soil lies the slightly weathered volcanic rock, which can be defined to be impermeable bedrock. Figure 1 displays the cross-section of the study site considering the residual soil layer. The slope angle of 26° with respect to the horizontal plane was averaged along the ground surface. Field instrumentation was conducted on the slope using tensiometers, which were installed at point 1 (lower station) and point 2 (upper station) to monitor pore-water pressure at depths varying from 0·3 to 2·15 m during rainfall, as depicted in Figure 1.

Geological conditions

The geology in the area of the slope consists of undifferentiated Permo-Triassic volcanic rock, including rhyolite, andesite, tuffs and agglomerate (Royal Irrigation Department, 2004). The undisturbed samples were collected using a thin-walled tube sampler with a diameter of 63 mm from the depths of about 0·5–1·0 m. The basic properties of the residual soil were determined and are summarised in Table 1. According to the Unified Soil Classification System, the residual soil can be classified as silty soil with medium plasticity (MH/ML).

The relationships between soil suction and volumetric moisture content (soil-water characteristic curve (SWCC)) of the residual soil were obtained from Kasetsart University (KU) tensiometers for both drying and wetting conditions of the samples (Jotisankasa and Vathananukij, 2008). The KU miniature tensiometers were developed by Jotisankasa *et al*. (2007) at KU, using microelectromechanical system (Mems) pressure sensors. Each device is able to measure pore-water pressure in the range of −100 to 600 kPa both in conventional laboratory tests and in the field. The SWCC test involved suction measurement of a soil sample at different moisture contents. After each suction measurement, the sample is either wetted or dried, corresponding to the test path in progress, by about 2% water content in order to obtain suction values at different moisture contents. The sample was simply left exposed in the air for gradual drying, while wetting was realised by directly spraying very fine droplets of water onto the sample. After the moisture content was changed to the desired value, the sample was carefully wrapped and cured for about 2–3 d to allow for suction equilibration in the sample. The SWCC and its curve-fitting van Genuchten model are presented in Figure 2. It is noted that the wetting points only slightly lie below the drying points and the hysteresis loop (shown as dashed lines) is minimal for this range of suction. The explanation for this small hysteresis could be that the wetting SWCC represents a scanning curve and the suction range involved is rather limited. Due to the

Table 1. Physical properties of residual soil

Soil type	Saturated unit weight: kN/m^3	Liquid limit: %	Plasticity index: %	Grain-size distribution: %			
				Clay	Silt	Sand	Gravel
MH/ML	17·61	46–51	6–18	31·9–36·7	38·9–53·9	13·7–18·9	0·5–5·5

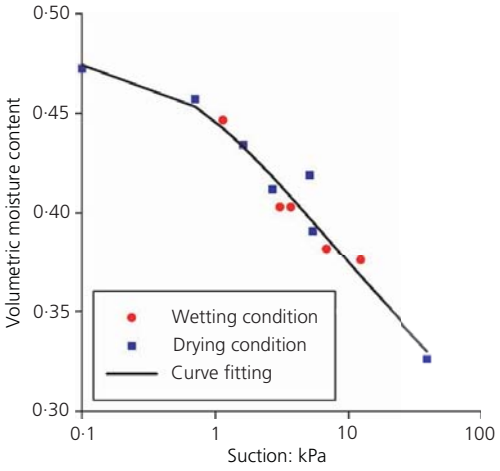

Figure 2. SWCC of residual soil (data from Jotisankasa and Vathananukij (2008))

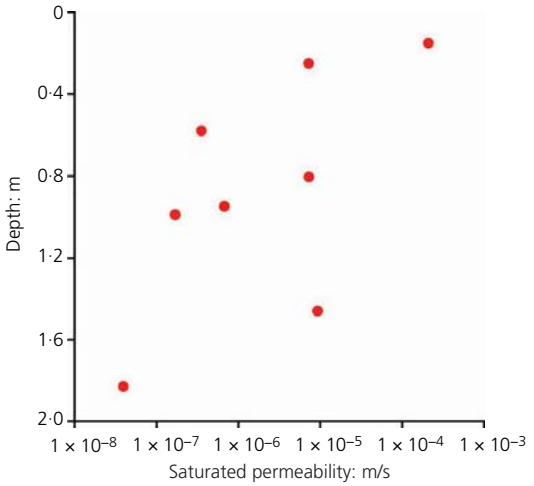

Figure 3. Saturated permeability variation with depth from field permeability tests

small suction range involved, the variation in void ratio during wetting appears to be negligible. Upon redrying, only a slight decrease in void ratio was observed corresponding to a volumetric strain of about 1·6%. The change in void ratio was taken into account when interpreting the SWCC, although the magnitude of this was considered marginal and did not largely affect the hysteresis of the SWCC. An average SWCC curve fitting was thus reasonably assumed for the data points on wetting and drying paths.

The saturated permeability was determined from a constant-head in situ borehole permeability test at different depth at the study site, using the method described by Garga and Blight (2012). As shown in Figure 3, the field test results exhibit larger values of hydraulic conductivity at the topsoil (0–0·3 m depth) varying from 7×10^{-6} to 2×10^{-4} m/s. This large variation was expected to relate to the effect of vegetation root rather than the compacted state of the soil. The permeability then decreases to 4×10^{-8} m/s at a depth of about 1·8 m, most likely to due to the effect of overburden stress. The average saturated permeability of $2{\cdot}9 \times 10^{-5}$ m/s was reasonably used as a first approximation to define the hydraulic conductivity function (Equation 3). Table 2 summarises the fitting parameters of SWCC and the average saturated permeability of residual soil as input parameters in seepage analysis. Of course, a more sophisticated permeability as a function of effective stress or depth could also be used at a higher computational cost. As will be shown later, this simplified constant permeability could be used to reproduce the pore pressure response accurately enough for the purpose of this study.

The effective shear strength parameters were measured on the undisturbed specimens using the drained direct shear test under the saturated condition. It is noted that the undisturbed samples were obtained from the slope recompacted after failure in 2004, which would represent a denser state than it would have been before failure in 2004. Both single-stage and multistage shearing tests were performed, which mainly showed a strain hardening behaviour. The effective soil cohesion c' and the effective friction angle ϕ' are 12·8 kPa and 33·1°, respectively. In this study, the effective soil cohesion $c' = 12{\cdot}8$ kPa was applied for the well-compacted soil slope case, while $c' = 0$ was assumed for the worst-case scenario of non-compacted soil condition. The effective cohesion intercept ($c' > 0$) of the well-compacted soil was expected to be due to grain interlocking and dilatancy (e.g. Bolton, 1986; Xiao *et al.*, 2014) as well as natural cementation that would likely increase over time due to thixotropy (Doglioni and Simeone, 2013; Jeong *et al.*, 2015) and bacterial/fungal activities (Molope, 1987; Wood *et al.*, 1995). Table 3 presents the values of shear strength for both cases as the input parameters in stability analysis during the rainfall infiltration.

Table 2. SWCC parameters and saturated permeability

Type	Parameter	Value
Residual volumetric moisture content	θ_r	$2{\cdot}1 \times 10^{-4}$
Saturated volumetric moisture content	θ_s	0·473
Fitting parameters	α (1/kPa)	0·902
	n	1·101
Saturated permeability	k_s (m/s)	$2{\cdot}9 \times 10^{-5}$

Table 3. Soil shear strength parameters

Type	Parameter	Value	Remark
Effective soil cohesion	c' (kPa)	12·8	Well-compacted soil
		0	Non-compacted soil
Effective friction angle	ϕ' (°)	33·1	—

Monitoring data

Rainfall records

In order to simulate the effect of heavy rainfall that can lead to the slope failure, the rainfall intensity within the period of 3–24 September 2008 was chosen in this study as shown in Figure 4. This was the period with maximum pore pressure readings observed during the monitoring programme starting from 2007. No rain was recorded at the beginning of the period, and the rainfall intensity slightly increased a few days later. The maximum rainfall intensity of this period was observed on 12 September 2008 and found to be over 120 mm/d. The rainfall intensity dropped rapidly after the highest rainfall had occurred and remained about 25 mm/d within 6 d. Then, the rainfall intensity suddenly increased to about 100 mm/d on 19 September 2008 and quickly decreased, and no rain occurred at the end of this period.

Measured pore-water pressure

The pore-water pressures were monitored at two different locations along the slope (i.e. upper and lower stations) by using the miniature tensiometers developed at KU (Jotisankasa *et al*., 2007). These devices are based on the Mems pressure sensor technology and are capable of measuring both positive and negative pore-water pressures ranging from −80 to 600 kPa. The Mems sensor used was a Freescale-NXP piezoresistive absolute pressure transducer. In order to avoid the cavitation problem, the tensiometer and the porous ceramic tube were submerged in water under vacuum pressure for about 1 h to saturate the space within the sensor body and porous ceramic with de-aired water. Each tensiometer was installed at depths of 0·3, 0·6 and 1·0 m at point 1 and at depths of 1·0, 1·5, 2·15 m at point 2 as shown in Figure 1. The pore-water pressures corresponding to the rainfall intensity record during the period of 3–24 September 2008 were also obtained as presented in Figure 4. The pore-water pressure at point 1 appears to be greater and more positive than those at point 2. In the lower station of the slope, the pore-water pressure was close to zero at shallow depth (0·3 m) and became values at deeper depth (0·6 and 1·0 m) during rainy days, while at every depth in the upper station of slope, the pore-water pressure remained negative and slightly fluctuated throughout most of rainy days and only became positive when the rainfall intensity exceeded about 100 mm/d on 19 September 2008.

Analysis and results

Seepage analysis

In this section, the unsaturated–saturated flow model as explained in the section headed 'Unsaturated–saturated seepage analysis' was simulated for both steady-state analysis and transient-state analysis. The SWCC parameters and the saturated permeability from laboratory and field tests were used as input parameters in the seepage model to calculate pore-water pressure and volumetric moisture content during the period of rainfall. To define the initial condition, an infiltration rate is assumed as the annual average rainfall intensity during the period of data record (i.e. 1 January to 31 December 2008). So the infiltration rate of 7·54 mm/d was assigned on the ground surface of the slope. This was meant to simulate the initial condition of pore-water pressure in the ground before simulation of the major heavy rainfall event. A zero-flux boundary was imposed at the bottom of the domain where slightly weathered volcanic rock is in place. In order to simulate the transient infiltration analysis, a flux boundary condition can be applied at the ground surface where the flux corresponds to the recorded rainfall (Lan *et al*., 2003; Oh and Lu, 2015; Yeh *et al*., 2008). In this study, the transient flux boundary was simulated using the rainfall data during the period of 3–24 September 2008. Since the ground surface was close to interacting with the bottom of residual soil at the crest and toe of slope, a zero-flux condition

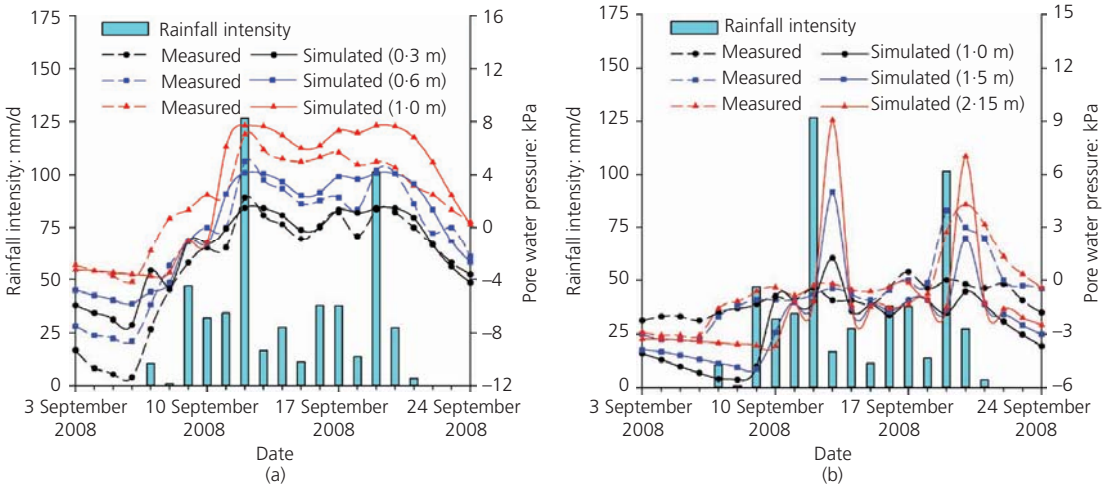

Q14 Q15 **Figure 4.** Comparisons between measured and simulated pore-water pressures

can thus be also set for the left and right boundary conditions. The model ignored the effect of evapotranspiration, in which it is not a major contribution to slope stability within the rainy season (Coppin and Richards, 1990; Greenway, 1987). No ponding (when rainfall is more than infiltration) on the top surface of the soil slope can be reasonably assumed due to the fact that when the rainwater does not exceed the infiltration capacity of soil, the excess water will not drain away as surface run-off.

Predicted against observed rainfall-induced effects

Figures 4(a) and 4(b) present the results of the transient seepage analysis at the various depths at points 1 and 2, respectively. The pore-water pressure at the lower part (point 1) gradually changed in response to the rainfall process at shallow depths, while the change appeared more sudden in the upper part (point 2) at deeper depths when rainfall intensity exceeded 100 mm/d. At point 1, the positive pore-water pressure appeared at different depths at 1 d before the highest rainfall intensity and was almost constant until the finishing period of rainfall. This was expected as the free-draining saturated surface was located near the toe slope. At point 2, however, the positive pore-water pressure could be observed at different depths only at 1 d after the highest rainfall intensity and reappeared at the deeper depths (1·5 and 2·15 m) after 19 September 2008. This demonstrated a kind of delayed infiltration behaviour or time lag at a deeper depth. This finding has a significant implication for landslide warning based on rainfall (e.g. Mairaing *et al*., 2012). In other words, slope instability could take place quite sometime after the daily rainfall reaches its peak. Failure could be triggered by the delayed rise in pore-water pressure even when there was only minimal rainfall at the time. The measured pore-water pressures at different depths are also drawn on these figures to demonstrate the accuracy of the proposed seepage model. As shown in Figure 4(a), the pore-water pressures obtained from simulation are higher than those from measurement at the shallow depths (0·3 and 0·6 m) at the first period of rainfall (no rainfall). This is because the assumed initial flux boundary condition of 7·54 mm/d, based on long-term rainfall measurement, was set to the ground surface and therefore may not represent the short-term distribution of the pore-water pressure that would be affected by some daily climate effects (e.g. evapotranspiration), particularly at a shallow depth. Subsequently, the simulation curves and the measurement curves become more consistent from the beginning rainfall to the finishing period of rainfall. At 1·0 m depth of the lower station (Figure 4(a)), the pore-water pressure from simulation was slightly greater than those from measurement after a few days of rainfall (9 September 2008). This slight difference can be explained by the fact that in the analysis, the undrained flux boundary at the bottom domain and consequently a small part of rainwater would still be remaining in the soil slope. In reality, however, a small part of seepage may occur out of the bottom domain.

Unlike the results in Figure 4(a), the pore-water pressure responses at the upper station in Figure 4(b) indicate that the loss of soil suction in the first period of rainfall affected not only the initial infiltration but also the downslope seepage from the crest to the toe slope. In the same way, the modelled downslope seepage can occur more easily than the actual response because the modelled soil was assumed as homogeneous in this analysis. This would explain why the measured pore-water pressure was greater than the simulated value. However, 1 d after the highest rainfall record (13 September 2008), the results at different depths show a better consistency between the modelled and measured pore-water pressures. In addition, the pore-water pressure response characteristics are also expected to be strongly affected by other factors, such as geomorphological and geological condition.

Predicted pore-water pressure

Figures 5(a) and 5(b) show the prediction of pore-water pressure distribution with depth at points 1 and 2, respectively, during the

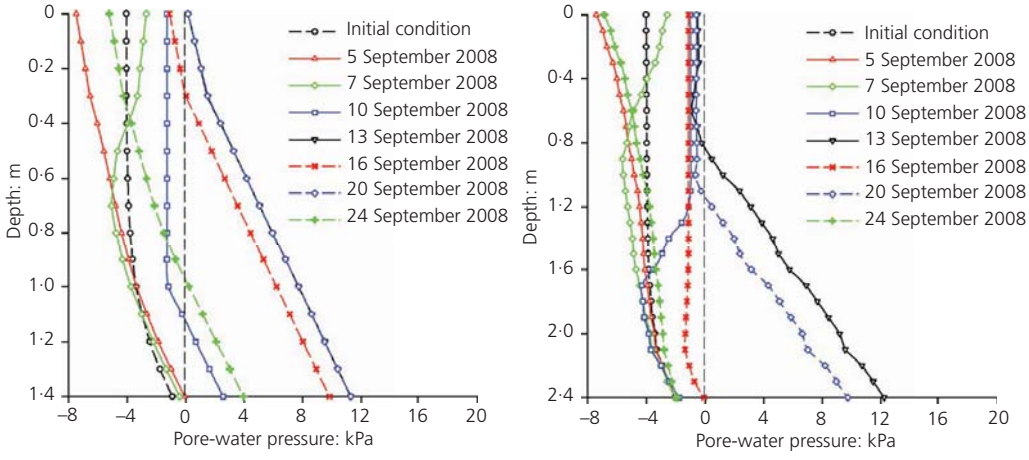

Q16 **Figure 5.** Prediction of pore-water pressure distribution with depth

period of rainfall. As seen in Figure 5(a), at the beginning of rainfall (before 5 September 2008), a decrease in pore-water pressure occurred at shallow depth, which tended to increase because of water redistribution during the period of no rain, while pore-water pressure remained almost unchanged at the deeper depth. It is noteworthy that this decrease in pore-water pressure could be also attributed to evapotranspiration. Nevertheless, since no measurements of meteorological data such as air temperature, solar radiation, air humidity and wind speed were available at this site to derive evapotranspiration fluxes, such effects were not taken into account in the current analysis. On 7 September 2008, pore-water pressure exceeded the initial condition only at a depth above 0·4 m as a consequence of limited rainfall infiltration. Below 0·4 m depth, the pore-water pressure curve tends to be similar to the pore-water pressure curve on 5 September 2008. Since rainfall had continuously increased up to 10 September 2008, pore-water pressure reached a positive value at a depth below 1·1 m. On the other hand, the ground above 1·1 m depth was still unsaturated. After the highest rainfall intensity had occurred (13 September 2008), the saturated zone was up to the bedrock (1·4 m depth) and the pore-water pressure linearly increased with depth. The rainfall intensity declined rapidly on 16 September 2008' pore-water pressure decreased with the same range of values along depth, and this tendency remained until no rainfall was recorded on 24 September 2008. In addition, it was noted that the pore-water pressure distributions on 13 and 20 September 2008 were nearly identical even though the rainfall intensities of these days were different. This can be explained that when rainfall intensity exceeded an amount of about 100 mm/d, those rainwaters in excess of the infiltration capacity cannot infiltrate through the ground surface and thus were converted to run-off. It can be implied that rainfall at that particular time caused the flow rate to be over the infiltration capacity of the soil. A similar explanation can be provided for pore-water pressures at the upper station (before 7 September 2008), as shown in Figure 5(b). However, on 10 September 2008, pore-water pressure increased to approximately −1·5 kPa and soil slope became saturated only near bedrock because the rainfall amount and duration were not sufficient for inducing pore-water pressure rise to a higher part. When the highest rainfall intensity happened (125 mm/d), the soil profile was completely saturated below 0·8 m depth and was almost saturated above this level on 13 September 2008. Rainfall intensity dropped to 37 mm/d on 16 September 2008, which caused an obvious decrease in pore-water pressure at a deeper depth since seepage happened downslope by gravity. Unlike the case of the lower station, pore-water pressure on 20 September 2008 was smaller than the value on 13 September 2008 below 0·8 m depth and the soil slope had not been completely saturated above 0·8 m. This can be explained by the fact that soil thickness at the upper station is larger than that at the lower station. It can be demonstrated that the highest rainfall intensity assumed in this analysis cannot make the whole soil profile completely saturated at the upper station. Therefore, run-off might not appear at the upper location as the infiltration and seepage progressed.

Stability analysis

Slope without root cohesion

In this section, analysis method as explained in the section headed 'Stability analysis of vegetated slope' was performed to investigate slope stability during the period of rainfall. The resulting pore-water pressure and volumetric moisture content calculated from Seep/W were then used as input in Slope/W to determine the corresponding FS. FSs were determined for both well-compacted soil condition and non-compacted soil condition. Figure 6 illustrates the variation in FS during the rainfall period of 3–24 September 2008. For the well-compacted soil condition, the slope remained stable according to the FS (FS > 1·0). For the non-compacted soil condition, slope instability appeared to happen after the rainfall intensity exceeded 100 mm/d, in which FS was less than 1·0 after 13 September 2008. At the beginning of rainfall (before 7 September 2008), FS was almost constant for both conditions, which indicated the minor effect of suction on slope stability analysis. From 7 to 12 September 2008, the FS of the well-compacted soil condition gradually decreased, while the FS of the non-compacted soil condition fluctuated. It can be implied that FS variability was not affected in the case of greater soil cohesion in the first period of rainfall. However, the distribution of FS with time for well-compacted sand the non-compacted soil conditions (Figure 6) showed some discrepancy after the highest rainfall intensity had occurred on 12 September 2008.

In order to illustrate the influence of the heavy rainfall event and failure mechanism of slope for the non-compacted soil condition, Figure 7 presents the distribution of pore-water pressure in the soil slope and the corresponding failure surface on 13 September 2008 as shown in Figure 8. As seen in Figure 7, the water table (where the pore-water pressure was zero) was up to the upper half

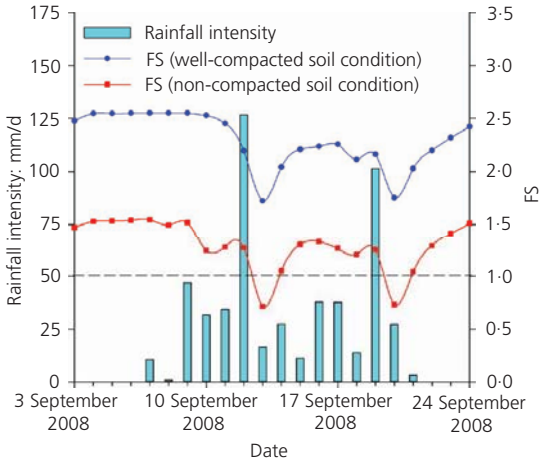

Figure 6. FS variation with time for soil slope without root cohesion **Q17**

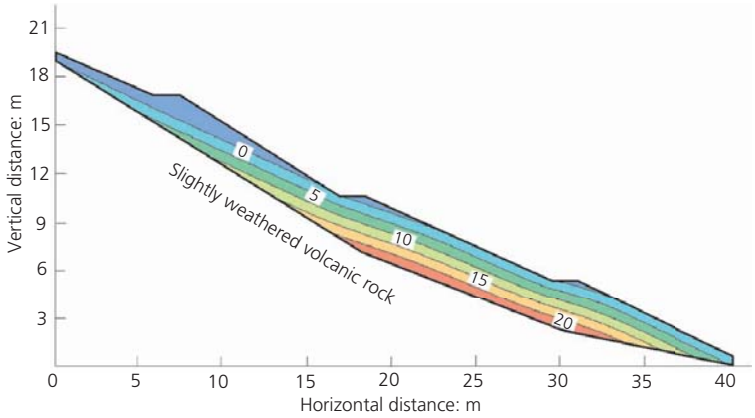

Figure 7. Pore-water pressure distribution on 13 September 2008

of the slope, and pore-water pressures linearly increased from ground surface to the interface between the residual soil and bedrock. The failure surface took on the region of the lower half of the slope, in which the residual soil slope was fully saturated (Figure 8). The simulated failure surface implied that the failure mechanism of slope was shallow failure, which could occur only at the lower depth of 1·0 m in the residual soil. The slope would fail as a result of the decrease in the effective stress due to the increase in pore-water pressure, while the slope failure might not be affected by a great reduction in soil shear strength (an assumption of $c' = 0$ for non-compacted soil condition).

Slope with root cohesion

To assess the influence of vegetation on slope stability, the worst-case scenario (non-compacted soil condition) was only performed to calculate FS using Equation 11 from 3 to 24 September 2008. Vegetation with typical vetiver grass in Thailand was employed as a special case of the Thadan slope. In the literature, the majority of root cohesion of vegetation species fall within the range of 1·0–20·0 kPa depending on different environments (Abernethy and Rutherfurd, 2001; Kazutoki and Iwamoto, 1986; O'Loughlin, 1974; Simon and Collison, 2002). Furthermore, according to Lynch (1995), the root distribution of some grasses was observed and can be approximately uniform at the shallow depth, while the researches of Ji *et al*. (2012); Leung *et al*. (2015) presented that the root distribution tends to decrease with depth at deeper zones. In this section, root cohesion was assumed based on the research of Eab *et al*. (2015), which presented a condition near the ground surface. The average value of root cohesion corresponding to c_r = 3·0 kPa and the root cohesion of c_r = 6·0 kPa are used to simulate the effect of variability of root vegetation on slope stability, as shown in Table 4. As seen in Figure 1, the thickness of the

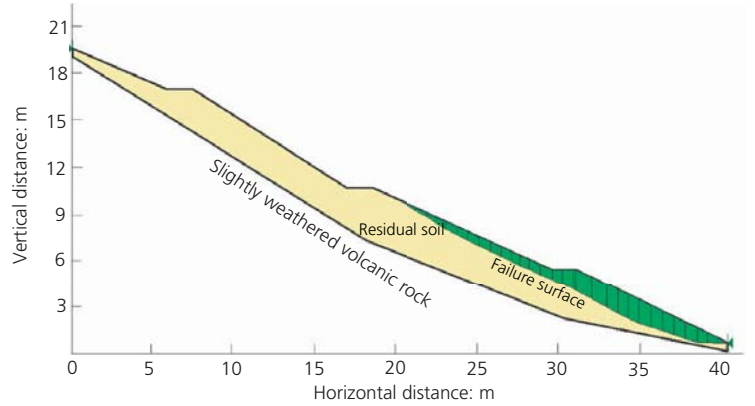

Figure 8. Corresponding failure surface for non-compacted soil slope without root cohesion on 13 September 2008 (the worst-case scenario)

Table 4. Characteristics of vetiver grass

Type	Parameter	Value
Root cohesion	c_r (kPa)	3·0, 6·0
Depth of root	l_r (m)	1·8

residual soil changes from 0·3 m at the crest and toe slope to 2·5 m at the middle of slope. However, the depth of the root system varies significantly with vegetation species and their growing environments. For example, root depths of trees and shrubs were reported to be in the range of 1·0–3·0 m (Kozlowski, 1971). In North America, the root depth is usually constrained by the bedrock (less than 2·0 m) in many slopes (Schmidt *et al.*, 2001). Therefore, an assumption of the extended depth of roots which reach the bedrock can be performed for the whole soil slope in this study.

Figure 9 shows FSs during the rainfall period of 3–24 September 2008 considering the contribution of vegetation for both of the root cohesions c_r = 3·0 and 6·0 kPa. It can be seen that the FSs of the vegetated slope are higher than those of the worst-case scenario of without root cohesion (Figure 8). In all cases, FSs are higher than 1·0 even though the highest rainfall intensity happened on 12 September 2008. The results in Figure 9 also indicate the discrepancy in the distribution of FS considering the smaller value of root cohesion and that of FS considering the greater value of root cohesion. For cases of root cohesion c_r = 3·0 and 6·0 kPa, the lowest FSs are 1·03 and 1·24 (45 and 75% increments from the case of without root cohesion), respectively. This finding suggests that a uniform distribution of roots can effectively increase the stability of a slope during heavy rainfall. Thus, the contribution of vegetation to stabilisation of slopes can be readily seen that the slope would not fail even under the worst-case scenario if it was rebuilt and grown with vegetation.

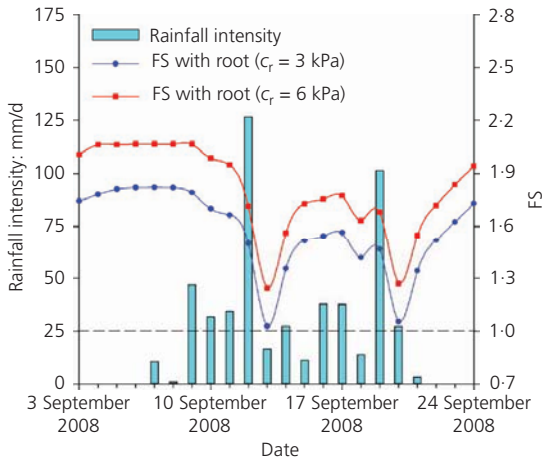

Q18 Figure 9. FS variation with time for vegetated slope

Concluding remarks

This paper presents a case study of a seepage model for slopes subjected to rainfall in Thailand and the influence of vegetation on slope stability. The rainfall intensity, the soil-water characteristics and the saturated permeability recorded and/or measured from the field were used in the seepage analysis. The pore-water pressure and volumetric moisture content obtained from the seepage model were then employed in a transient unsaturated–saturated slope stability analysis. The influence of root cohesion on slope stability was considered by means of root cohesion. FSs in transient seepage and slope stability analysis were computed for the cases of without and with root cohesion. The research conclusion can be highlighted as follows.

- The proposed seepage model indicated that there is a better agreement between the simulated and measured pore-water pressures at the shallower depths than between those at the deeper depths. The positive pore-water pressures showed more discrepancy at point 1 (lower part), while a conversion occurred at point 2 (upper part). The prediction of pore-water pressure pointed out that the whole soil slope was almost completely saturated in intense storms.
- The non-vegetated slope with well-compacted soil condition was stable during the period of rainfall, while slope instability occurred in the non-compacted soil condition (the worst-case scenario) when rainfall intensity exceeded the amount of 100 mm/d. The failure mechanism of slope under the worst-case scenario was characterised as shallow failure, in which the failure surface was located at a depth above 1·0 m, in the saturated region.
- Slope stabilisation by vegetation was adopted through additional soil shear strength by root cohesion. Typical characteristics of the vetiver grass in Thailand were assumed to specify due to root in the analysis. The results showed that FS was greater than 1·0 for both root cohesions of c_r = 3·0 kPa and c_r = 6·0 kPa during the period of rainfall, and the slope with the non-compacted soil condition considering vegetation became stable in the assumed heavy rainfall condition. This finding demonstrated the effectiveness of bioengineering for shallow slope stabilisation.
- The highest positive pore-water pressure could be observed at different depths 1 d after the highest rainfall intensity. This demonstrated a kind of delayed infiltration behaviour at a deeper depth. This finding has a significant implication for landslide warning based on rainfall. In other words, slope instability could take place several days after daily rainfall has reached its peak. Failure could be triggered by the delayed rise in pore-water pressure even when there was hardly any rainfall at the time.

Q19

Acknowledgements

This research was supported by the Thailand Research Fund Grant Number RSA-5880023, the Ratchadapisek Sompoch Endowment Fund (2017) and Chulalongkorn University (760003-CC). Field instrumentation and monitoring works were funded by

the Kasetsart University Research and Development Institute. The work was also carried out under the research and development project on landslide prevention and protection according to Royal Initiatives of the Chaipattana Foundation. The first author would like to acknowledge Asean University Network/Southeast Asia Engineering Education Development Network (Japan International Cooperation Agency) for a PhD sandwich scholarship during his study.

REFERENCES

Abernethy B and Rutherfurd ID (2001) The distribution and strength of riparian tree roots in relation to riverbank reinforcement. *Hydrological Processes* **15(1)**: 63–79, https://doi.org/10.1002/hyp.152.

Bolton M (1986) The strength and dilatancy of sands. *Géotechnique* **36(1)**: 65–78, https://doi.org/10.1680/geot.1986.36.1.65.

Caviedes-Voullième D, Garcı P and Murillo J (2013) Verification, conservation, stability and efficiency of a finite volume method for the 1D Richards equation. *Journal of Hydrology* **480**: 69–84, https://doi.org/10.1016/j.jhydrol.2012.12.008.

Cecconi M, Napoli P and Pane V (2015) Effects of soil vegetation on shallow slope instability. *Environmental Geotechnics* **2(3)**: 130–136, https://doi.org/10.1680/envgeo.13.00110.

Chirico GB, Borga M, Tarolli P *et al.* (2013) Role of vegetation on slope stability under transient unsaturated conditions. *Procedia Environmental Sciences* **19**: 932–941, https://doi.org/10.1016/j.proenv.2013.06.103.

Coppin NJ and Richards IG (1990) *Use of Vegetation in Civil Engineering*. Construction Industry Research and Information Association, London, UK.

Doglioni A and Simeone V (2013) Recovery of strength along shear surfaces in clay soils. In *Landslide Science and Practice* (Margottini C, Canuti P and Sassa K (eds)). Springer, Berlin, Germany, pp. 183–188.

Eab KH, Likitlersuang S and Takahashi A (2015) Laboratory and modelling investigation of root-reinforced system for slope stabilisation. *Soils and Foundations* **55(5)**: 1270–1281, https://doi.org/10.1016/j.sandf.2015.09.025.

Fatahi B, Khabbaz H and Indraratna B (2014) Modelling of unsaturated ground behaviour influenced by vegetation transpiration. *Geomechanics and Geoengineering* **9(3)**: 187–207, https://doi.org/10.1080/17486025.2014.880520.

Fredlund D and Zhang L (2004) Numerical study of soil conditions under which matric suction can be maintained. *Canadian Geotechnical Journal* **41(4)**: 569–582, https://doi.org/10.1139/t04-006.

Fredlund D, Morgenstern NR and Widger R (1978) The shear strength of unsaturated soils. *Canadian Geotechnical Journal* **15(3)**: 313–321, https://doi.org/10.1139/t78-029.

Fredlund DG, Rahardjo H and Fredlund MD (2012) *Unsaturated Soil Mechanics in Engineering Practice*. Wiley, New York, NY, USA.

Garga V and Blight G (2012) Steady and unsteady flow of water and air through soils – permeability of saturated and unsaturated soils. In *Mechanics of Residual Soils* (Blight GE and Leong EC (eds)). CRC Press, London, UK, p. 119.

Geo-Slope (2007) *Seepage Modeling with SEEP/W and Slope Stability Analysis with SLOPE/W*. Geo-Slope International Ltd, Calgary, AB, Canada.

Greenway D (1987) Vegetation and slope stability. In *Slope Stability: Geotechnical Engineering and Geomorphology* (Anderson MG and Richards KS (eds)). Wiley, Chichester, UK.

Jeong SW, Locat J, Torrance JK and Leroueil S (2015) Thixotropic and anti-thixotropic behaviors of fine-grained soils in various flocculated systems. *Engineering Geology* **196**: 119–125, https://doi.org/10.1016/j.enggeo.2015.07.014.

Ji J, Kokutse N, Genet M, Fourcaud T and Zhang Z (2012) Effect of spatial variation of tree root characteristics on slope stability: a case study on Black Locust (*Robinia pseudoacacia*) and Arborvitae (*Platycladus orientalis*) stands on the Loess Plateau, China. *Catena* **92**: 139–154, https://doi.org/10.1016/j.catena.2011.12.008.

Jotisankasa A and Sirirattanachat T (2017) Effects of grass roots on soil-water retention curve and permeability function. *Canadian Geotechnical Journal* **54(11)**: 1612–1622, https://doi.org/10.1139/cgj-2016-0281.

Jotisankasa A and Vathananukij H (2008) Investigation of soil moisture characteristics of landslide-prone slopes in Thailand. *Proceedings of the International Conference on Management of Landslide Hazard in the Asia-Pacific Region*, p. 12.

Jotisankasa A, Porlila W, Soralump S *et al.* (2007) Development of a low cost miniature tensiometer and its applications. *Proceedings of the 3rd Asian Conference on Unsaturated Soils (Unsat-Asia), Nanjing, China.*

Jotisankasa A, Takahashi A, Takeyama T *et al.* (2009) A study of deformation behaviour of an instrumented slope subject to rainfall near Thadan dam Thailand. *Proceedings of the 14th National Convention in Civil Engineering, Nakhon Ratchasima, Thailand.*

Jotisankasa A, Mairaing W and Tansamrit S (2014) Infiltration and stability of soil slope with vetiver grass subjected to rainfall from numerical modeling. *Proceedings of the 6th International Conference on Unsaturated Soils, UNSAT*, pp. 1241–1247.

Kazutoki A and Iwamoto M (1986) Preliminary experiment on shear in soil layers with a large-direct-shear apparatus. *Journal of the Japanese Forestry Society* **68(2)**: 61–65, https://doi.org/10.11519/jjfs1953.68.2_61.

Kozlowski T (1971) *Growth and Development of Trees, Volume II: Cambial Growth, Root Growth, and Reproduction Growth*. Elsevier, Amsterdam, the Netherlands.

Lan H, Zhou C, Lee CF, Wang S and Wu F (2003) Rainfall-induced landslide stability analysis in response to transient pore pressure – a case study of natural terrain landslide in Hong Kong. *Science in China Series E: Technological Sciences* **46**: 52–68.

Leung AK (2014) Grass evapotranspiration-induced suction in slope: case study. *Environmental Geotechnics* **3(3)**: 155–165, https://doi.org/10.1680/envgeo.14.00010.

Leung FT, Yan W, Hau BC and Tham LG (2015) Root systems of native shrubs and trees in Hong Kong and their effects on enhancing slope stability. *Catena* **125**: 102–110, https://doi.org/10.1016/j.catena.2014.10.018.

Likitlersuang S, Takahashi A and Eab KH (2017) Modeling of root-reinforced soil slope under rainfall condition. *Engineering Journal* **21(3)**: 123–132, https://doi.org/10.4186/ej.2017.21.3.123.

Lu N and Godt JW (2013) *Hillslope Hydrology and Stability*. Cambridge University Press, New York, NY, USA.

Lu N and Likos WJ (2006) Suction stress characteristic curve for unsaturated soil. *Journal of Geotechnical and Geoenvironmental Engineering* **132(2)**: 131–142, https://doi.org/10.1061/(ASCE)1090-0241(2006)132:2(131).

Lu N, Godt JW and Wu DT (2010) A closed-form equation for effective stress in unsaturated soil. *Water Resources Research* **46(5)**, https://doi.org/10.1029/2009WR008646.

Lynch J (1995) Root architecture and plant productivity. *Plant Physiology* **109(1)**: 7–13.

Mairaing W, Jotisankasa A and Soralump S (2012) Some applications of unsaturated soil mechanics in Thailand: an appropriate technology approach. *Geotechnical Engineering Journal of the SEAGS & AGSSEA* **43(1)**: 1–11.

Molope M (1987) Soil aggregate stability: the contribution of biological and physical processes. *South African Journal of Plant and Soil* **4(3)**: 121–126, https://doi.org/10.1080/02571862.1987.10634957.

Ng C and Shi Q (1998) A numerical investigation of the stability of unsaturated soil slopes subjected to transient seepage. *Computers and*

Geotechnics **22(1)**: 1–28, https://doi.org/10.1016/S0266-352X(97)00036-0.

Nguyen TS, Likitlersuang S and Ohtsu H and Kitaoka T (2017) Influence of the spatial variability of shear strength parameters on rainfall induced landslides: a case study of sandstone slope in Japan. *Arabian Journal of Geosciences* **10(16)**: 369, https://doi.org/10.1007/s12517-017-3158-y.

Oh S and Lu N (2015) Slope stability analysis under unsaturated conditions: case studies of rainfall-induced failure of cut slopes. *Engineering Geology* **184**: 96–103, https://doi.org/10.1016/j.enggeo.2014.11.007.

O'Loughlin C (1974) The effect of timber removal on the stability of forest soils. *Journal of Hydrology (New Zealand)* **13(2)**: 121–134.

Pathirage U, Indraratna B, Pallewattha M and Heitor A (2017) A theoretical model for total suction effects by tree roots. *Environmental Geotechnics*, https://doi.org/10.1680/jenge.15.00065.

Rahardjo H, Ong TH, Rezaur RB and Leong EC (2007) Factors controlling instability of homogeneous soil slopes under rainfall. *Journal of Geotechnical and Geoenvironmental Engineering* **133(12)**: 1532–1543, https://doi.org/10.1061/(ASCE)1090-0241(2007)133:12(1532).

Rahardjo H, Satyanaga A, Wang CL, Wong JLH and Lim VH (2018) Effects of unsaturated properties of soil with *Caesalpinia crista* roots on slope stability. *Environmental Geotechnics*, https://doi.org/10.1680/jenge.17.00031.

Richards LA (1931) Capillary conduction of liquids through porous mediums. *Journal of Applied Physics* **1(5)**: 318–333, https://doi.org/10.1063/1.1745010.

Royal Irrigation Department (2004) *Report on Source Areas for Rock and Aggregates in Klong Thadan Dam Construction Project*. Royal Irrigation Department, Bangkok, Thailand.

Schmidt K, Roering J, Stock J *et al.* (2001) The variability of root cohesion as an influence on shallow landslide susceptibility in the Oregon Coast Range. *Canadian Geotechnical Journal* **38(5)**: 995–1024, https://doi.org/10.1139/t01-031.

Simon A and Collison AJ (2002) Quantifying the mechanical and hydrologic effects of riparian vegetation on streambank stability. *Earth Surface Processes and Landforms* **27(5)**: 527–546, https://doi.org/10.1002/esp.325.

Smith I and Griffiths D (2004) *Programming the Finite Element Method*. Wiley, New York, NY, USA.

Van Dam JC and Feddes RA (2000) Numerical simulation of infiltration, evaporation and shallow groundwater levels with the Richards equation. *Journal of Hydrology* **233(1)**: 72–85, https://doi.org/10.1016/s0022-1694(00)00227-4.

van Genuchten MT (1980) A closed-form equation for predicting the hydraulic conductivity of unsaturated soils. *Soil Science Society of America Journal* **44(5)**: 892–898, https://doi.org/10.2136/sssaj1980.03615995004400050002x.

Wood DM, Meadow A, Murray J and Meadows PS (1995) Effect of fungal and bacterial colonies on slope stability. In *Vegetation and Slopes* (Barker D (ed.)). Thomas Telford, London, UK, pp. 46–51.

Wu TH (2013) Root reinforcement of soil: review of analytical models, test results, and applications to design. *Canadian Geotechnical Journal* **50(3)**: 259–274, https://doi.org/10.1139/cgj-2012-0160.

Wu TH, McKinnell WP III and Swanston DN (1979) Strength of tree roots and landslides on Prince of Wales Island, Alaska. *Canadian Geotechnical Journal* **16(1)**: 19–33, https://doi.org/10.1139/t79-003.

Xiao Y, Liu H, Chen Y and Chu J (2014) Strength and dilatancy of silty sand. *Journal of Geotechnical and Geoenvironmental Engineering* **140(7)**: 06014007, https://doi.org/10.1061/(ASCE)GT.1943-5606.0001136.

Yeh HF, Lee CC and Lee CH (2008) A rainfall-infiltration model for unsaturated soil slope stability. *Journal of Environmental Engineering and Management* **18(4)**: 261–268.

Zhan TL, Ng CW and Fredlund DG (2007) Field study of rainfall infiltration into a grassed unsaturated expansive soil slope. *Canadian Geotechnical Journal* **44(4)**: 392–408, https://doi.org/10.1139/t07-001.

How can you contribute?

To discuss this paper, please submit up to 500 words to the editor at journals@ice.org.uk. Your contribution will be forwarded to the author(s) for a reply and, if considered appropriate by the editorial board, it will be published as a discussion in a future issue of the journal.